

A Novel Method for the Bottom-Up Microstructuring of Silicon and Patterning of Polymers

DISSERTATION

zur Erlangung des akademischen Grades

**Doctor rerum naturalium
(Dr. rer. nat.)**

vorgelegt

dem Bereich Mathematik und Naturwissenschaften
der Technischen Universität Dresden

von

M.Sc. Christopher Schutzzeichel

geboren am 18.12.1992 in Werl

Eingereicht am 23. Februar 2021

Verteidigt am 15. Juni 2021

Gutachter:

Frau Prof. Dr. Brigitte Voit

Herr Prof. Dr. Stefan Mannsfeld

Die Dissertation wurde in der Zeit von Januar 2018 bis Februar 2021 am
Leibniz-Institut für Polymerforschung Dresden e.V. angefertigt.

*„Ein guter Forscher
muss nach der Wahrheit streben und wissen,
dass er ihr immer nur nahe kommen kann.“*

LISE MEITNER

Acknowledgments

First and foremost, I want to thank my supervisors Prof. Dr. Brigitte Voit and Dr. Anton Kiriy for the opportunity to work on this interesting and challenging, but fruitful topic. The continuous support over the last three years helped me tremendously with the research resulting in this dissertation.

I also want to extend my gratitude towards my project partners within the e²SABA project at Infineon Dresden, in particular Marcus Dankelmann, Heiko Aßmann and Stefan Döring, who provided the silicon substrates used in this work. Their feedback during numerous project meetings and calls helped to find the right direction and I benefited greatly from their knowledge in semiconductor physics and processing. In connection with the e²SABA project I thank the Sächsische Aufbaubank for funding the project and my position at the IPF.

Without the scientific and instrumental knowledge of a number of people at the IPF, this work would not have been possible. I want to thank Dr. Nataliya Kiriy for an uncountable number of AFM measurements, as well as Andreas Janke for the introduction and support for my own measurements, Dr. Petr Formanek for the SEM and TEM measurements and their evaluation, special thanks to Takuya Tsuda (津田さん、ありがとうございます!) for further SEM measurements, LED light sources and general help with the experimental setup and Olha Aftenieva for lending me the LED power meter. For the design and manufacturing of the custom setups, I want to thank the department Research Technology at IPF. I also thank Roland Schulze and Claudia Marschelke for support with ellipsometric measurements, Anja Caspari for the extensive Zeta potential measurements and their analysis and Bettina Pilch for UV/VIS measurements. Even though I did not have many NMR samples myself, I want to thank Dr. Hartmut Komber for the cooperation during my duties as one of the responsible students for the NMR automation.

I also want to thank all the other coworkers at the IPF, in particular the organisational team of the IMC, Carmen Krause, Mandy Faulhaber and Gina Seltsmann and the administration of the IPF for keeping the research going. Thank you to my lab colleagues over the years, who made the long work hours more enjoyable: Dr. Johanna Zessin, Fabian Borrmann, Christoph Horn, Wenhui Dong, Dr. Ningwei Sun, Kajari Mazumder and Lisa Ehrlich. I also thank my colleagues from the departments PS and RP, in particular in my office Jennifer Daeg, Peng Wang and Dishu Wang, but also Dr. Silvia Moreno Pinilla, Christiane Effenberg, Dr. Franziska Obst, Robin Zinke, Andreas Korwitz, Andreas Schurig, Dr. Xueyi Wang, Andrei Mitrofanov, Bettina Keperscha and Dr. Jens Gaitzsch, as well as all other colleagues at the IPF.

For help during writing and proofreading this thesis I am very grateful to Dr. Anton Kiriya, Dr. Uwe Schröder and Sandra Heckel.

Without the continuous support of my family and friends, this work and my way towards it would not have been successful. Special mention must be made of my parents for their love and support and for enabling me to pursue my education in the first place and of my sisters for being there for me, even when I were an annoying brother. I also want to thank my friends, in particular the Lausers, with whom I shared the great deal of chemical difficulties during our education. They helped me take my mind of work, enjoy life and find new energy and motivation.

To finish, thank you Sandra for sharing your life with me, always supporting me and pushing me to be the best version of myself.

Contents

1	Theoretical background	1
1.1	Introduction	3
1.2	Silicon Microstructuring Technology	4
1.2.1	Photolithography	4
1.2.2	Etching	10
1.2.3	Silicon doping	21
1.3	Semiconductor Device Physics	21
1.3.1	pn-Junction	21
1.3.2	Photo Effects in Semiconductors	24
1.4	Electropolymerisation	26
1.5	Selective Polymer Deposition on Surfaces	28
1.5.1	Polymer Dewetting	28
1.5.2	Surface Initiated Polymerisation	29
2	Motivation and Aim	33
3	Results and Discussion	37
3.1	Sample Description	39
3.2	Surface Property Investigation	42
3.3	Pyrrole Electropolymerisation	47
3.3.1	Introduction	47
3.3.2	Cyclovoltammetric Electropolymerisation	47
3.3.3	Light Induced Electropolymerisation	50
3.3.4	Summary	57
3.4	Light Induced Selective Etching - LISE	59
3.4.1	Introduction	59
3.4.2	Self-Replication of Implant Structure through Selective Etching	61
3.4.3	Self-Replication via Etching with Implant Structure Buried Under a Homogeneous Epitaxial Layer	68
3.4.4	Mechanism Hypothesis	76

3.4.5	Process Parameters	78
3.4.6	Investigation of the Mechanism	96
3.4.7	Summary	109
3.5	Selective Polymer Deposition according to etched structure	111
3.5.1	Introduction	111
3.5.2	Deposition of Films	111
3.5.3	Surface Initiated Polymerisation	115
3.5.4	Summary	117
4	Conclusion and Prospects	119
5	Experimental Part	135
5.1	Chemicals	137
5.2	Silicon Substrates	138
5.3	Instrumentation	138
5.4	Synthetic Procedures	140
5.4.1	Allylpyrrole	140
5.5	Substrate Cleaning	140
5.5.1	Solvent Clean	141
5.5.2	Standard Clean-1	141
5.6	Surface Modifications	141
5.6.1	Silanisation Reactions	141
5.6.2	Si-H Modification	142
5.7	Polypyrrole Experiments	142
5.7.1	Electropolymerisation	142
5.7.2	Light Induced Polymerisation	143
5.8	Selective Etching Experiments	143
5.8.1	Polymer Film Deposition	143
5.8.2	Photocurrent Measurements	145
A	Appendix	147
	List of Abbreviations and Symbols	155
	Bibliography	157
	Versicherung	171

1 Theoretical background

1.1 Introduction

The development of the first Integrated Circuits (ICs) by Jack Kilby in 1958 (hybrid IC)^[1] and Robert Noyce in 1960 (silicon planar IC, using Kurt Lehovec' method of pn-junction isolation)^[2,3], essentially served as the starting signal for the semiconductor industry. As the digitalization of nearly every part of life, be it in personal devices or other approaches like Industry 4.0, proceeds, the importance of the semiconductor industry increases as well^[4,5]. As of 2018, this industry has grown to over \$481 billion, making it one of the largest industries worldwide^[6]. This growth can be attributed to the large number of innovations, driving the progress in device design and manufacturing, of which the latter is the topic with which this work is concerned.

The manufacturing of semiconductor devices relies heavily on a large number of process steps in order to produce functioning transistors and other device elements^[7,8]. These steps include the formation of films^[9–11], selective removal of material^[12–15], introduction of impurity dopants^[7,16,17] and other processes^[18]. In particular, this work is concerned primarily with the structuring of silicon through lithography and etching as a key step in modern semiconductor manufacturing. For the production of ICs, microstructuring is essential for the controlled formation of the different device layers, such as silicon itself, dielectrics or conductive vias^[7]. Over time, the feature sizes on semiconductor devices are shrinking, in order to enable higher performance with less power consumption, as predicted by Gordon Moore already in 1965, now known as Moore's law^[19]. Innovative fabrication methods are necessary to sustain this decrease in size and increase in performance, currently driven in particular by progress in areas like artificial intelligence, powering inventions such as autonomous cars or factories which require enormous amounts of computational power^[20–22]. Besides the need for more computational power, applications such as autonomous cars and factories require increased awareness of the surrounding world, enabled by a multitude of sensors, integrated into everyday articles^[22]. For this, Micro-Electro-Mechanical Systems (MEMS) and Micro-Opto-Electro-Mechanical Systems (MOEMS), whose fabrication relies heavily on microstructuring, i. e. etching methods, are frequently used as the basis for the production of microscopic sensors and actuators for the next generation of data collection^[13,23]. A number of devices utilizing MEMS are already in use, such as pressure sensors, e. g. in car tyres^[24,25], accelerometers for airbag deployment or control systems^[26,27], gyroscopes for navigation and control purposes in various flying vehicles^[28], micromirrors for Light Detection and Ranging (LIDAR) systems^[29] or microphones in smart home devices^[30,31]. The small size and low cost of such devices allows for the easy integration also in any production environment, avoiding the need for time consuming manual

process control^[13]. As MEMS and MOEMS device production relies heavily on silicon etching, innovation to improve capabilities and availability in this area is a significant part of current research.

1.2 Silicon Microstructuring Technology

In the production of silicon-based devices, structuring is one of the key steps in achieving down to nanometer-sized features in the substrate. Generally, structuring describes the controlled removal of substrate material. In the case of Very Large Scale Integration (VLSI) processes, this is essentially a planar process, as generally the structure depth is below 1 μm . In contrast, in the case of microsystem technology, the depth can reach up to 100 μm ^[32].

A typical microstructuring process requires two main methods: Photolithography, in order to create a mask of the pattern, which is to be transferred into the substrate, and etching, used to transfer the mask structure into the substrate as a topography variation^[32].

1.2.1 Photolithography

Photolithography is the central process during the fabrication of a silicon device, taking up 40 to 50 % of the total wafer processing time. Even the simplest Metal-Oxide-Semiconductor (MOS)-based chip needs five lithographic steps, whereas more complex devices can require more than 30^[7]. As photolithography is the process needed to create nearly all structures for silicon devices, this step is of great importance in the fabrication of semiconductor devices^[33].

Photolithography consists of three main parts (see Figure 1.1), which aim to create a patterned sacrificial layer on the surface, which serves as a guide for the following process of etching or doping^[7]:

1. The sacrificial layer, based on a photosensitive polymer, called photoresist, is initially homogeneously deposited on the surface.
2. The substrate is illuminated through a photomask or reticle, representing the desired structure as opaque and transparent areas. The areas of the photoresist which are illuminated through the transparent parts of the reticle are chemically altered by photochemical reactions. This chemical alteration leads to a lateral variation in the properties of the photoresist layer.

3. The chemical variation is then used to selectively remove parts of the photoresist in the development-process. Two main types of resists can be differentiated here: positive resists, for which the light-exposed parts can be removed and negative resists, which show the inverse behaviour.

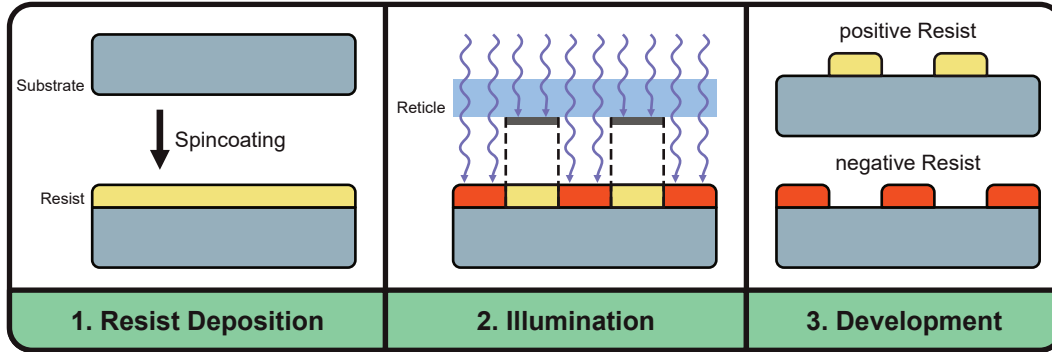


Figure 1.1: General process steps for photolithography. Depending on the resist tone, resulting structure is either a positive or negative image of the photomask. (Adapted from^[7])

Special care must be taken with all three steps and their components in order to be able to fabricate devices with nm-range feature sizes with high yield. Following, the most important parts of photolithography, namely the photomask, light source and photoresist will be described further.

Photomasks

The first step necessary to perform photolithography is the fabrication of a photomask, often called reticle, with an image of the structure to be transferred to the substrate. The layout on the reticle is created from a digital representation of the finished device by splitting it into the necessary fabrication steps and creating the appropriate layout for every lithography step. Most masks are not fabricated with a 1:1 dimensional reproduction of the structure, as this would sometimes already require nanometer resolution, but instead are magnified, usually four times. This magnification reduces the complexity during fabrication of the reticle, as larger features are easier to create on the mask. Furthermore, the magnification reduces the impact of contaminations on the reticle, as they are demagnified and can possibly fall below the resolution limit of the lens, preventing defects in the structure^[33]

The usual way of fabricating reticles starts with a piece of fused silica (SiO_2) covered with a thin layer of chromium. Into this layer, the desired structure is patterned, based on the design data. An electron-sensitive resist is coated onto the chromium layer and

selectively irradiated with an electron beam (e-beam lithography) writing the desired layout. After removal of the irradiated resist parts, the structure can then be transferred into the chromium layer with an etch step. This yields a reticle with an absorbing layer patterned according to the desired structure. Finally, the reticle is protected with a thin polymer film, called pellicle, suspended above the chromium layer in order to prevent particles from contaminating the surface. As the pellicle is not in the focal plane during lithography, contaminations that deposit on it are not transferred to the substrate (see Figure 1.2)^[18,33].



Figure 1.2: Model layout of a typical photolithography reticle.

Light Sources

The light source for lithography is the most important part in regards to the achievable resolutions, as only short wavelengths can be used to resolve small details, due to the diffraction limit. Depending on which wavelength of light is to be used, different types of illumination sources are employed, which can be split into three categories: mercury arc lamps, excimer lasers and plasma sources. Classic arc discharge lamps with mercury are used for g- and i-line (436 and 365 nm, respectively) illumination, as well as Deep Ultra Violet (DUV) with 240 to 255 nm. The emission spectrum of the lamp, mainly due to mercury emission, is filtered according to the needed wavelength before illuminating the sample^[10,33].

For shorter wavelengths used in DUV lithography, laser sources are used, based on KrF for 248 nm and ArF for 193 nm light. In these laser devices, electric discharges with voltages over 10 kV lead to the formation of excited dimers like KrF^* and ArF^* which can undergo quenching, spontaneous or stimulated emission to return to the ground state. The stimulated emission provides the required optical output and is used for sample illumination^[10,33].

Plasma sources constitute the third group of light sources, used for Extreme Ultra Violet (EUV) lithography. The principle behind these sources is to generate a plasma containing highly charged ions, which can recombine with electrons under emission of high-energy photons. The necessary plasma can be produced in two ways, by laser irradiation (Laser-produced-plasma, LPP) or electric discharge (discharge-produced-plasma, DPP) of a fuel droplet, usually tin. Nowadays, mostly LPP sources are used, as they

produce higher intensities, necessary for high resolution lithography^[7,33].

Photoresists

The photoresist, as the layer transferring the structure into the substrate, plays an immensely important role during the lithography process. It needs to be able to react to the light exposure through the reticle and reproduce the structure with high fidelity. Resists are multi-component systems and consist of different organic compounds: a solvent for application during spincoating, a base polymer as the film matrix and a photosensitive compound, as most polymers are not inherently sensitive to the exposure during illumination^[18].

Photoresists are classified as either negative or positive, depending on the way the exposure to light changes its chemical properties. Negative resists are initially soluble in the developer solution and are rendered insoluble upon irradiation of photons with the appropriate wavelength. In contrast, positive resists are insoluble, but can be chemically altered to be soluble in the developer solution upon illumination. Depending on the exposure wavelength, different resist systems are used.

g- and i-line Resists For applications with critical dimensions down to 350 nm, typically novolak/diazanaphthoquinone (DNQ)-based positive resists are used for g- and i-line lithography. Novolaks are phenolic resins polycondensated from phenol and formaldehyde (see Figure 1.3a for general structure). They are generally soluble in the aqueous basic developers, but can be made insoluble if mixed with a diazanaphthoquinone-derivative as a dissolution inhibitor. DNQs themselves are insoluble in basic solutions and, if mixed into a novolak resin, decrease the solubility of the resin in basic developer greatly. DNQs are also photoactive and react to soluble indenecarboxylic acids upon illumination (see Figure 1.3b). The reaction proceeds via a Wolff rearrangement to an intermediate ketocarbene under nitrogen elimination. The intermediate then reacts under water addition to the carboxylic acid. Due to this change in structure and solubility, the effect of the DNQ dissolution inhibitor on the base polymer is reversed, leading to a greater solubility value for the illuminated resist compared to the pure novolak resin^[9,33,34]. Therefore, if a layer of novolak/DNQ based resist is illuminated through a mask, i.e. only specific parts are irradiated by photons, the solubility of the resist material increases locally, according to the mask pattern. This can be used during the development process to remove the illuminated areas, creating a copy of the used photomask in the resist.

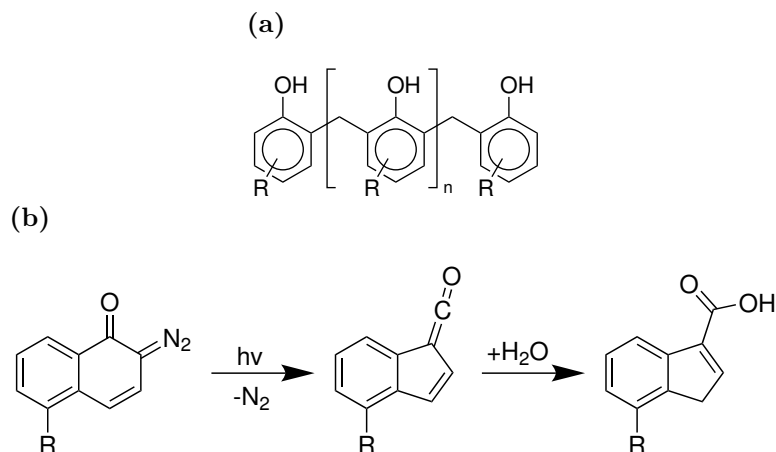


Figure 1.3: (a) General novolac structure (b) Photoreaction of DNQs, leading to a reversal in the solubility-modifying properties, i. e. illuminated resist areas are more soluble than pure novolac.

DUV Resists With the development towards smaller feature sizes on modern semiconductor devices, different light sources with shorter wavelengths are used, as they enable higher resolution. This poses a problem, as typical novolac materials show high optical absorption in the DUV, which leads to incomplete penetration of photons through the resist, preventing the removal of the resist in some areas during development. To overcome this problem, a different base polymer needs to be used, which is transparent to wavelengths ≤ 260 nm. One such polymer is poly(4-vinylphenol), which is transparent to DUV and also soluble in aqueous bases. For such polyphenol resins, the photo sensitive part of the resist mixture is modified to use *chemical amplification* as the solubility altering process. For this, a base polymer with protecting groups, such as *t*-Boc is necessary, rendering the polymer insoluble in the basic developer. The protecting groups can then be removed, reversing the insolubility, by acid-catalysed cleavage of the C-O bond between the phenolic group and the *t*-Boc group. In order to achieve the localized dissolution of the resist needed for lithography, photoacid generators like triphenylsulfonium triflate or bis(cyclohexylsulfonyl) methane are mixed into the resist. These compounds dissociate under illumination, releasing protons available for catalytic deprotection, enabling the localized modulation of solubility (see Figure 1.4). As the deprotection step is acid-catalysed, each proton photogenerated from a single exposure event is potentially able to deprotect multiple polymer side chains, giving this method the name *chemical amplification*^[9,33,35].

EUV Resists Moving further towards even smaller feature sizes, another kind of light source and matching resist chemistry is necessary. Currently the cutting edge technology

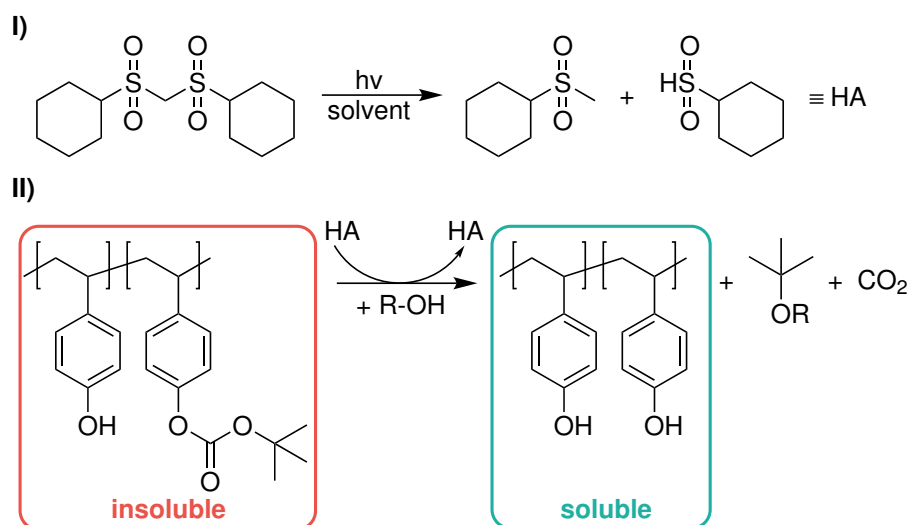


Figure 1.4: Components and photoreaction of positive-tone chemically amplified resists. Upon irradiation, an acid environment is generated, which can deprotect the polymer, making it soluble in the developer solution.

in regards to light sources is the usage of EUV light with a wavelength of 13.5 nm^[36]. Even though very similar materials can be used the mechanism of the radiation induced change in structure is very different from DUV resists. Instead of direct absorption of photons on a molecular level, followed by photoacid generation, EUV resists generate secondary electrons upon irradiation with EUV light, which in turn react with acid generators, which are identical to those in DUV resists^[33,37]. One advantage arising from the difference in absorption properties of EUV light is in the reduced restrictions on which kinds of bonds may be present in the polymer matrix. As these bonds have only a very small effect on absorption in the EUV, polymers which are not usable for DUV can be used in the EUV case.

Development

After the photoresist has been illuminated through the photomask, inducing chemical variation inside the resist according to the desired pattern, the next step is to develop the resist. In this process the illuminated (positive) or unilluminated (negative) areas are removed to yield the structured mask layer. In the case of positive tone resists, like novolak/DNQ or chemically amplified resists, the de facto industry standard for development nowadays is tetramethylammonium hydroxide (TMAH). A solution with a concentration of 0.26 mol L⁻¹ is used to dissolve the illuminated areas^[7,33]. For negative tone resists organic solvents like xylene are generally used to remove the unchanged areas of the resist^[7].

For the development process, the substrate is immersed in the developer solution, usually by dispensing a large volume on the slowly rotating wafer. After the specified development time, the substrate is rinsed with a clean solvent and finally dried^[7,33].

After this the substrate wafer is covered with a thin layer of photoresist which has been patterned according to the photomask and can now be used for further processing, for example etching of the underlying layer or ion implantation to introduce dopant ions into the substrate^[32].

1.2.2 Etching

In the context of semiconductor manufacturing, etching describes the controlled removal of material on a surface. It can be used to create structures in the semiconductor material necessary for the device functionality. The material removal is controlled, as the rate of removal has to be precisely directed in all three dimensions. For the lateral dimensions, this is achieved by an appropriate etch mask, as fabricated with photolithography. For the vertical dimension, control over the etch parameters, such as concentration and temperature allows for the necessary precision. Two major types of etching processes can be distinguished: Wet etching, i. e. etching in a solution of the etchant, and dry etching, where the substrate is etched with a gaseous etchant under plasma influence. Both of these types can be further divided based on whether the etchant exhibits orientation dependent etch rates. An etchant is labelled isotropic, if all crystal orientations are etched with the same rate. Anisotropic etchants on the other hand etch specific crystal planes faster than others^[7,12,32,38].

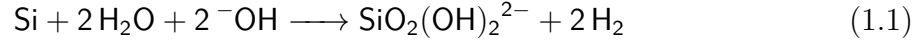
Wet Etching

Until around the 1980s wet etching processes were the dominant way to pattern silicon substrates, but were mostly replaced with dry processes due to feature size limitations with wet etching. Nevertheless wet etching plays an important role today, for example in stripping of layers and analysis tasks^[7]. Furthermore, in the realm of MEMS and MOEMS, wet etching is an extensively used process for devices such as pressure sensors, accelerometers, micro motors or cantilevers^[12,13]. The production of these devices utilizes the anisotropic etching effect certain etchant solutions exhibit.

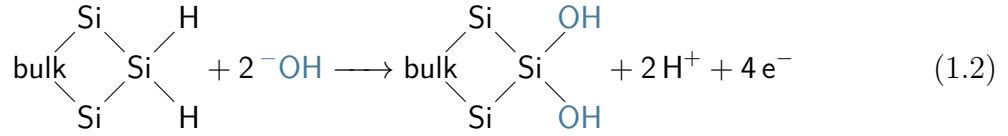
Besides this, certain isotropic wet etch solutions are used, mainly for removal of layers or when undercutting of masked areas is wanted, e. g. in the fabrication of pointed needle tip structures^[12].

Anisotropic Etchants

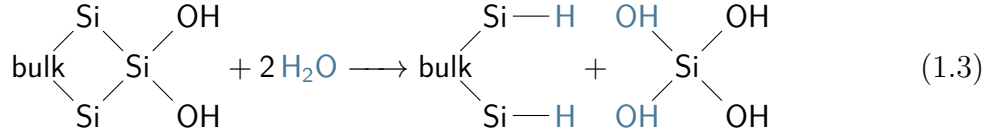
Anisotropic etching of silicon is performed with aqueous alkaline solutions, such as KOH, TMAH, NH_4OH , ethylenediamine or other bases. Of these, KOH and TMAH are the most used candidates in device manufacturing today^[12,39,40]. These alkaline solutions etch bulk silicon via oxidative dissolution of silicon atoms under hydrogen evolution^[12]:



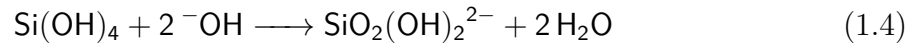
This reaction proceeds over several steps, starting from the successive binding of two hydroxide ions to a surface silicon atom with two hydride terminated free bonds under injection of four electrons into the conduction band:



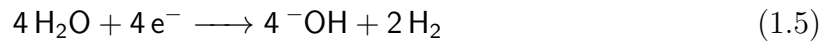
The now partially hydroxylated silicon atom is still bound to the Si-bulk, but both backbonds are weakened due to the electronegativity of the oxygen atoms. Consequently, the atom can be fully dissolved from the Si-bulk as a silicate, leaving behind two hydride terminated Si-atoms:



The dissolved neutral silicate species is not stable in the high pH environment and reacts to a charged silicate under loss of two protons, which are neutralised by two hydroxide ions:



Finally the four injected electrons per Si-atom are transferred from the conduction band to water molecules in the electrolyte, reducing four protons to two hydrogen molecules and releasing four hydroxide ions:



Summed up, these steps will give the overall reaction, as shown in equation 1.1^[12,39]. Besides the same etch mechanism, all previously mentioned etchants exhibit strong anisotropy, i. e. different crystal planes of silicon etch with dramatically different etch rates. The exact ratios are dependent also on the etchant composition, but for the three

main crystallographic faces (100), (110) and (111) the general rule is that (111) etches the slowest and can almost be considered stable against alkaline solutions, (100) etches up to 150 times faster in KOH, while (110) is the fastest etching orientation which can be up to 250 times faster than (111)^[12]. This stark contrast in etch rates can be explained by analysing the number and types of bonds the surface Si-atoms exhibit in each crystal orientation. As silicon crystallises in a face-centred cubic diamond-type crystal structure, the atomic arrangement along the face is different for the three basic lattice planes (100), (110) and (111), as can be seen in Figure 1.5.

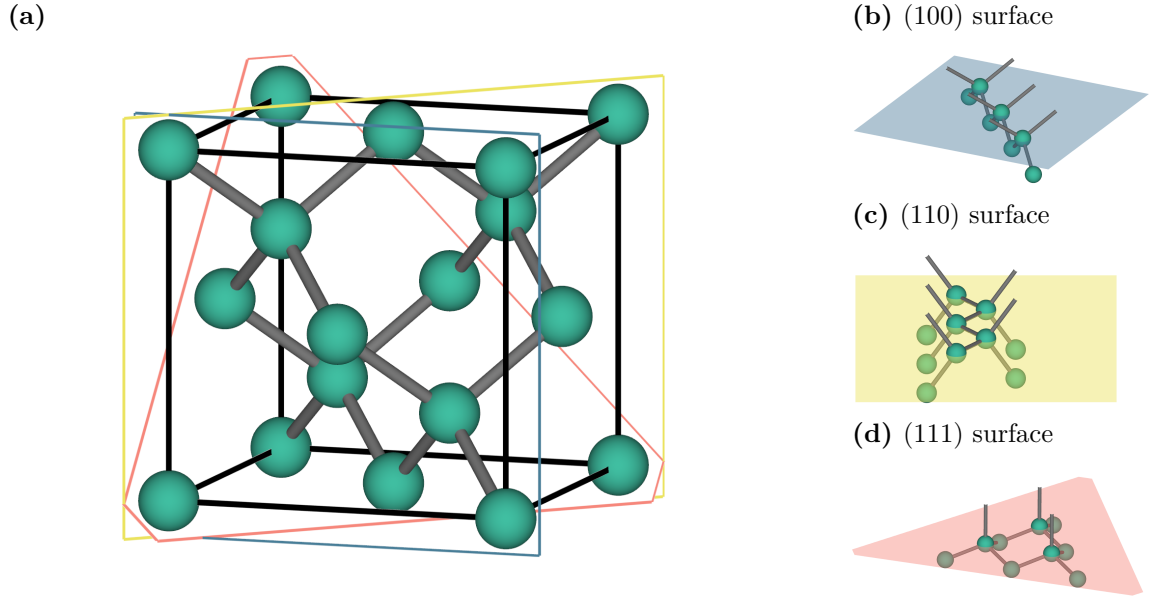


Figure 1.5: (a) Unit cell of silicon with (100), (110) and (111) planes drawn (b),(c),(d) Surface atoms of (100), (110) and (111) crystal planes.^[40]

Surface atoms, which are all those atoms which have at least one free bond, usually saturated with hydrogen, have the most significant impact on etch characteristics^[40]. Besides free bonds, the surface atoms can have volume bonds, which connect to other Si-atoms inside the bulk crystal, or surface bonds which connect to other surface atoms, which is only the case for the (110) plane. In Table 1.1 the values for each base plane are listed, together with the free bond density σ . Considering the previously described mechanism, the density of free bonds should have a significant influence on the etch rate, as a higher number means fewer backbonds that need to be broken. From this, taking the free bond density into account, the etch rates should follow the relation (100) > (110) > (111), which is not observed in experimental results. To explain this discrepancy the number of volume and surface bonds needs to be considered as well. Looking at the (111) plane first, the surface-atoms have only one free bond and three volume

Table 1.1: Table of types and numbers of Si-bonds for the base planes

Crystal plane	Free bond density $\sigma^{[41]}$ / $\cdot 10^{15} \text{ cm}^{-2}$	Bonds		
		Volume	Surface	Free
(100)	1.36	2	0	2
(110)	0.96	1	2	1
(111)	0.78	3	0	1

bonds, making this face almost stable against alkaline etchants. The atoms in the (110) plane are etched fastest, even though they have the same number of free bonds as in the (111) plane. This difference is due to two easily breakable surface bonds, leaving the atom with only one volume bond, leading to quick dissolution. Lastly, atoms in the (100) plane etch slower compared to (110), as they don't have any surface, but two volume bonds, which is also the configuration described in the mechanism^[40]. Due to this strong anisotropy the morphology of the etched area is strongly dependent on the crystal plane that is being etched. On (100)-silicon surfaces, this leads to the formation of rectangular holes with V-shaped profiles on the sidewalls, as the slow etching {111} planes are inclined at 54.7° relative to the (100) surface, as is shown in Figure 1.6a. The {110} planes etch faster than the (100) surface, progressing to the very slowly etching {111} planes. This results in the V shaped cross section of the rectangular features. All mask hole shapes lead to rectangular features, as the intersections of the {111} with the (100) surface form a rectangle. Due to this anisotropy, it is not possible to etch perfectly vertical sidewalls with alkaline etchants on (100) surfaces. These observations for concave features, i. e. holes, also apply for convex structures, such as lines or columns etched out of silicon^[40,42,43].

On (110)-silicon surfaces the resulting etch morphology differs due to the varying orientation of the {111} planes to the surface. Etched holes take on a hexagonal shape with two sides inclined at 35.3° and the remaining four vertical at 90° , as is illustrated in Figure 1.6b. This allows, given the right orientation of masked features, the etching of perfectly vertical walls, enabling the manufacturing of for example needle-like structures. As before this hexagonal form is etched into the crystal even when using a circular or irregular mask. Also here these principles apply for concave as well as convex features^[12,40,42,43].

Influence of Etchant Parameters Besides the crystal structure the etching result is strongly influenced by other parameters, especially etchant temperature and composi-

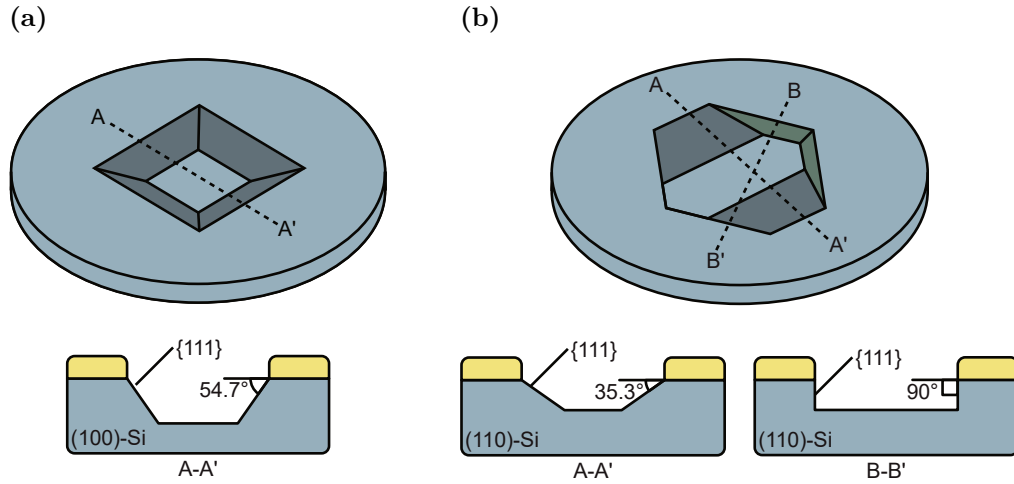


Figure 1.6: Illustration of etching anisotropy as observed on (100)-Si and (110)-Si. (a) On (100)-Si a V-shaped profile on the sidewalls is etched, as the 54.7° inclined $\{111\}$ faces etch much slower. (b) On (110)-Si a hexagonal hole is etched with four 90° sidewalls and two inclined at 35.3° . (Adapted from^[42])

tion. For etching experiments at different solution temperatures it can be observed that the etch rate increases with increasing temperature. This dependence is due to the reaction limitation of the etching, i. e. the slow process of OH-attachment to the hydrogen terminated silicon atoms, which requires a large activation energy. This activation energy is supplied by thermal energy, which is why the reaction rate is strongly dependent on etching temperature^[12,39,44].

The dependence on the concentration of the etchant is more diverse and does not follow a simple relation. It differs for each etchant and will be exemplified here with KOH and TMAH. For KOH, a concentration dependence with global maximum at around 6 mol L^{-1} can be observed (see Figure 1.7a). The decrease in etch rate for concentrations larger than 6 mol L^{-1} is due to the decreased availability of water molecules which are needed for the reaction to proceed. This is true for all crystal orientations, but with varying extent of etch rate change, so that the anisotropy ratio between Si(110) and Si(100) is greatest around 6 mol L^{-1} . In this way the extent of anisotropy can be controlled via the KOH concentration and it is possible to vary the shape of the etched feature, for example changing the bottom shape of trenches on a Si(110) surface^[12,40]. For TMAH, the behaviour differs in that not all crystal orientations follow the same dependence: $\{110\}$ planes follow a curve of increasing etch rate with increasing TMAH concentration, whereas $\{100\}$ planes exhibit the inverse behaviour and etch slower with increasing concentration (see Figure 1.7b). To explain this phenomenon the etching model needs to be modified, as it only takes water molecules and hydroxide ions into account. For TMAH, it appears that the TMA^+ -ion plays a significant role and needs

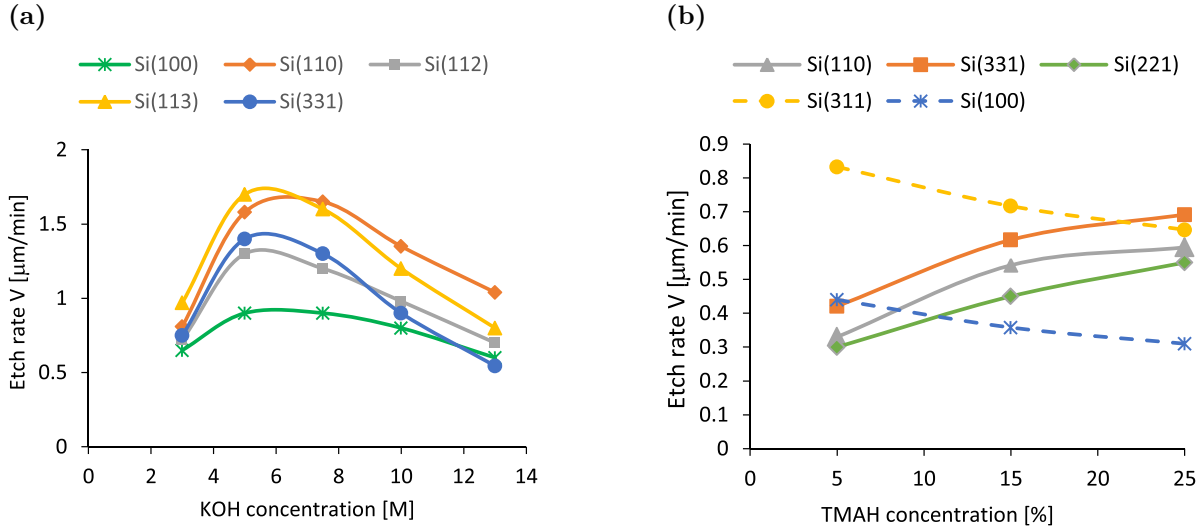


Figure 1.7: Etch rate dependence for different crystal orientations and etchants. (a) KOH etch rate, exhibiting a global maximum around 6 mol L^{-1} . (b) TMAH etch rate, with varying dependence for different crystal orientations. (Taken from^[40])

to be taken into account as well. It appears that the TMA^+ -ion interacts with the two hydride terminated bonds which are present on $\{100\}$ planes and thereby reduces the etch rate despite the increasing concentration of hydroxide ions. As these bonds are not present on the other crystal orientations they exhibit the expected behaviour of increasing etch rate with increasing TMAH concentration. This special behaviour of the $\{100\}$ planes also leads to a cross point in the etch rates, where the rate relation changes from $\{110\} > \{100\}$ to the inverse. This allows for very good control over the resulting etch morphology, as the fastest etching plane can be varied according to the needs^[12,40].

Similar changes in the anisotropy ratio can be achieved by adding tensioactive compounds, such as alcohols or surfactants. Using a mixture of KOH with *i*-propanol as the etchant solution an inversion of the anisotropy ratio can be observed so that $\{100\}$ faces etch faster than $\{110\}$ for KOH concentrations up to around 10 mol L^{-1} . Again this allows very good control over the resulting morphology of etched features, making it possible to selectively etch certain crystal faces. A similar effect can be achieved for TMAH with the addition of a nonionic surfactant containing a polyethylene glycol chain (Triton X-100). With the addition of 150 ppm of the surfactant to a 25 wt% solution of TMAH the etch rate of $\{110\}$ faces can be reduced below the value of $\{100\}$ faces. These effects are due to the preferred adsorption of *i*-propanol and the Triton surfactant to the $\{110\}$ faces because of their bond orientation. The adsorbed layer of tensioactive compound then slows the diffusion of the etching compound to the silicon surface, which in turn reduces the etch rate^[40].

Isotropic Etchants

For specific application where anisotropy is not desired, isotropic etchant solutions can be used instead. With these etchants, the substrate is etched in a uniform way regardless of crystal structure. This can be useful for the removal of entire layers of silicon, for post processing to remove sharp corners or damaged surfaces or when concave, hemispherical features are desired. With isotropic etching, mask undercutting always has to be taken into account, but can also be implemented as a design feature, e.g. in the production of sharp needle tips. Figure 1.8 illustrates various structures that can be realised with isotropic etching and mask undercutting^[12].

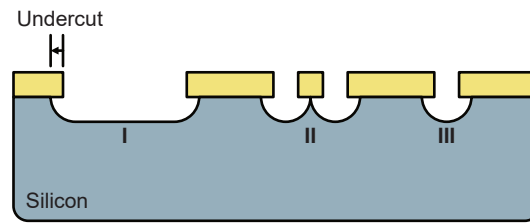
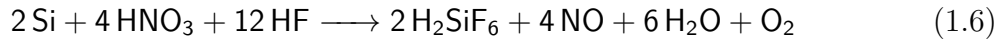


Figure 1.8: Possible features achievable by isotropic etching of silicon: **I** Wide area etching with mask undercutting, **II** Small, closely spaced mask apertures leading to a needle tip structure, **III** pinhole mask aperture for hemispherical feature (Adapted from^[12]).

The most common etching solution for this type of etching is a mixture of hydrofluoric acid, nitric acid and acetic acid, commonly called HNA acid. The overall etching reaction of silicon in this mixture can be expressed as:



Generally, the etching proceeds over the oxidation of silicon by nitrogen dioxide, created in-situ from nitric acid, and the subsequent dissolution of the silicon oxide in hydrofluoric acid. Acetic acid is added to the mixture as a buffer and dilutant to maintain a stable etch rate. The exact ratios of the three components needs to be adjusted to the task at hand, with 2:3:3 (HF:HNO₃:CH₃COOH) being a frequently used ratio which gives good isotropy and surface smoothness^[12,32].

Dry Etching

With the need for ever smaller feature sizes, most wet etching processes were replaced with dry etching processes as small features might not be properly resolved with wet processes, especially isotropic etching. With dry etching the substrate is not immersed in a solution of etchant but instead the etchant is applied to the surface in gaseous form.

Most of these processes are plasma based and can act either on a physical basis via sputtering, or chemically. Physical processes are anisotropic, but unselective, whereas chemical processes are selective, but isotropic. To use the best of both worlds, most dry etching processes nowadays use a combination method called reactive ion etching (RIE). In these methods the substrate is bombarded with ions like Ar^+ for sputtering while being subjected to a reactive gas like XeF_2 , which chemically etches the surface. This allows for a highly controllable etching, but with greatly increased equipment costs and reduced throughput^[7,12].

Etch Stop Techniques

As photolithography is a highly complex, time consuming process during device fabrication, a multitude of methods replacing some lithography steps have been proposed and are actively used today. This allows for a simpler, faster production process, increasing production yield while decreasing production cost^[7,45,46]. In particular, various techniques for enhanced control have been developed. These allow lateral control, similar to lithographically prepared etch mask, and vertical control, in order to stop the etching at a specified etch depth. As the dissolution of silicon atoms during anisotropic etching proceeds under injection of electrons into the crystal, as shown in section 1.2.2, a change in the charge accumulation zone should show a strong influence on the etching behaviour. Commonly used techniques for achieving this change are doping control and bias control.^[12,32]

Doping control For wet etching processes in MEMS and MOEMS processes, the most commonly used technique is doping control, specifically an etch stop effect due to a very high p-type boron doping (p^+ -etch stop). When investigating the influence of boron doping concentration on etch rate a sharp drop can be found for concentrations around $10 \cdot 10^{19} \text{ cm}^{-3}$. Above this threshold, the etch rate is only around 1% of the value for intrinsic silicon and the etching is effectively stopped (see Figure 1.9a). As a dopant concentration of around $10 \cdot 10^{19} \text{ cm}^{-3}$ coincides with the onset of degeneracy of p-silicon, the reduction in etch rate can be easily explained electrochemically. At such high doping concentrations the p-doped silicon behaves not like a semiconductor, but like a metal. This results in a greatly reduced space charge layer on the surface, which allows electrons to more easily leave the confinement at the surface and penetrate deeper into the crystal. Here, the chance for recombination with holes is increased so that these electrons are not available for the subsequent reduction reaction on the silicon surface (equation 1.5). As this reaction provides the new hydroxide ions close to the negatively

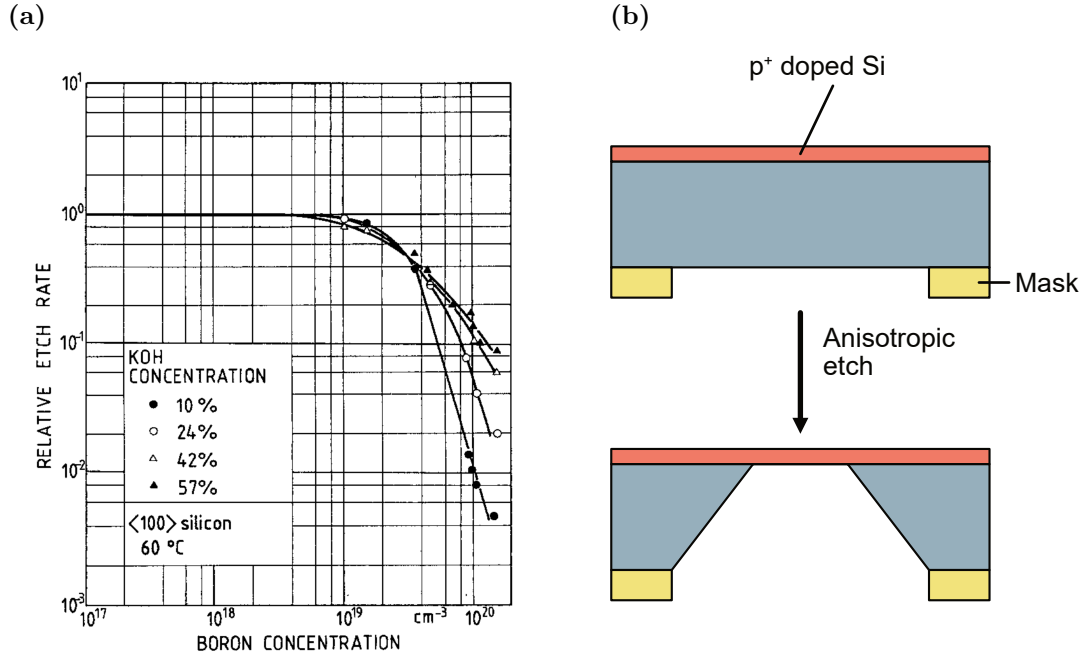


Figure 1.9: (a) Diagram of etch rate vs. boron concentration for (100)-Si in KOH. A large drop in etch rate above $10 \cdot 10^{19} \text{ cm}^{-3}$ can be seen (taken from^[47]), (b) Illustration of fabrication of thin membrane from layer of highly boron doped p-Si.

charged surface, necessary for further etching, the etching comes to a stop^[32,47].

The primary use of this technique is the application as a stop layer, preventing further etching at a specified depth. A good example for this is the fabrication of thin silicon membranes, as illustrated in Figure 1.9b. A silicon substrate is modified with a p-Si layer by impurity doping with boron of sufficiently high concentration. The thickness of the layer is chosen to coincide with the desired membrane thickness. On the opposite side of the substrate an etch mask is deposited and structured according to the desired feature. Finally, an anisotropic etch step is employed to etch a cavity up to the p^+ etch stop layer. The reaction will stop itself, for one due to the etch stop layer in vertical direction and due to etch mask and unreactive crystal orientations in lateral dimensions^[12,32,48–50]. Besides vertical control, other applications with lateral etch control have also been realised: Ma *et al.* have demonstrated the fabrication of silicon nanowires with dimensions of $55 \times 280 \text{ nm}$ from a patterned, highly boron doped layer^[51]. Similarly, Hsieh *et al.* used p^{++} boron doped sidewalls in the fabrication of free standing micromachined devices, such as gyroscopes or actuators^[52].

Problematic with this kind of etch control is the high doping concentration, as it changes the material properties so significantly, that it might not be suitable anymore for use in MEMS or MOEMS applications. Similarly, the onset of degeneracy from

semiconductor to metal prevents the use in Complementary Metal-Oxide Semiconductor (CMOS) applications^[12].

Bias controlled Besides the p^+ etch stop, selectivity can also be induced by applying a bias to the substrate. This can be used for homogeneously p- or n-doped samples or on samples with structured doping. Basis for a bias dependent etching is the passivation potential (PP) of silicon. When a silicon sample is biased with a potential more positive than this threshold, etching can not take place, because the anodic oxidation process leads to a passivating oxide layer. As illustrated in Figure 1.10a, for applied voltages above the passivation potential the etch rate decreases sharply to a near zero value^[53,54]. This can be exploited by using a layered structure, with a thin n-doped layer on a p-Si bulk, creating a pn-junction. Similar to the p^+ etch stop sample, the thin layer is of the thickness that should remain after etching. Such a sample is then biased with a potential larger than the passivation potential at the n-Si side, with only the p-Si side immersed into the alkaline etchant solution, as illustrated in Figure 1.10b. As the pn-junction is in reverse bias, no current flow is possible between n- and p-Si, meaning that only the n-Si is positively biased, with the p-Si being at open circuit potential. Accordingly, the p-Si is etched, constrained by the etch mask, until the etch front reaches the n-Si layer. Here the etching stops, because this layer is still biased above the passivation potential and therefore passivated. The resulting thin layer is now much lower doped than in the case of p^+ etch stop and retains its material properties for use in MEMS and MOEMS, as well as CMOS technology^[12,53]. Besides anodic passivation, p- and n-doped silicon show a strong difference in etch rate for applied potentials below -1.5 V. Under these conditions, p-Si still exhibits an etch rate similar to the value at open circuit potential, whereas n-Si is again passivated and shows a near zero etch rate (see Figure 1.10a). This can be used very similar to the previous example with an identical sample and setup. The difference is that in this case the pn junction is in forward bias so that the p-Si is not at open circuit potential, but is also biased to around -1.5 V or lower, where it still is etched. As soon as the etching reaches the n-Si layer the reaction stops, as n-doped silicon is passivated under this bias^[53].

These bias controlled etching processes can further be influenced by illumination of the substrate with light of energy greater than the band gap of silicon (>1.1 eV, <1000 nm). For n-type silicon such illumination shifts the passivation potential to more negative values, enabling substrates that are etched with bias slightly below the PP to be passivated upon illumination. On p-type silicon the effect is inverted and passivated substrates slightly above the PP can be etched upon illumination^[55,56].

Bias controlled etching is not only applied for alkaline etching, but is also frequently

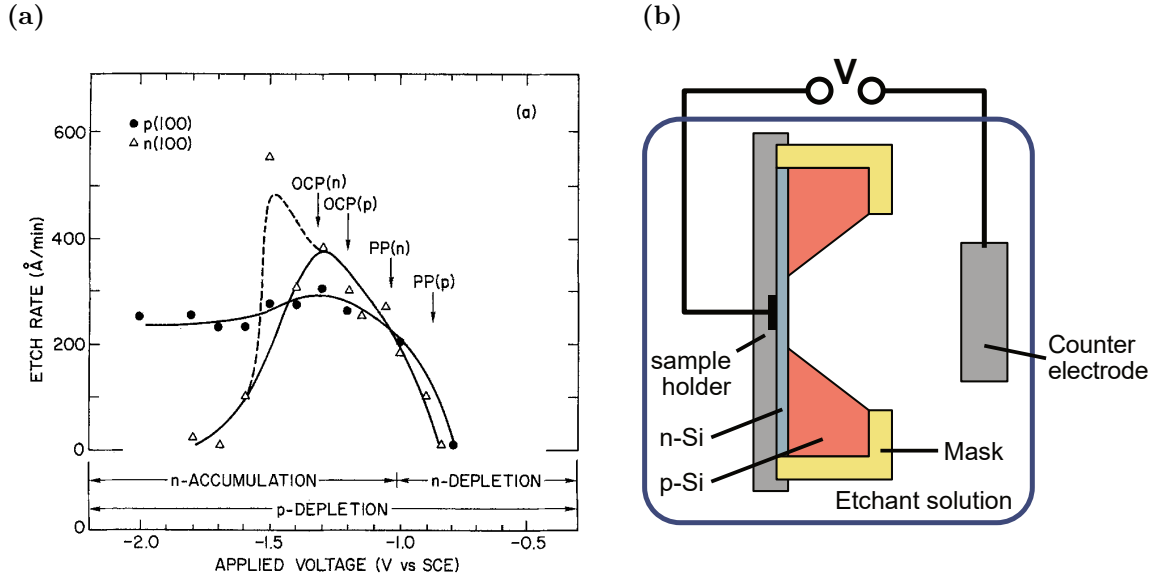


Figure 1.10: (a) Diagram of etch rate vs. applied bias for n- and p- doped Si in KOH (taken and adapted from^[53]), (b) Illustration of fabrication of thin membrane from layer of n-doped Si on p-bulk with bias control. The applied bias to the n-Si layer can either be positive and higher than the passivation potential or negative and low enough to inhibit n-Si etching (compare left side of (a)).

used in the creation of porous silicon in hydrofluoric acid etchant solutions. This process is based on the oxidation by holes and dissolution of silicon in HF-containing solutions. For p-doped silicon, this is possible without any external influence, as holes are the majority charge carrier. For n-doped silicon on the other hand, external generation of holes by high electric fields or illumination is necessary. The reason for the formation of pores during this process is the concentration of electric field lines on surface irregularities, which locally enhances dissolution. These irregularities act as seed sites for pore formation and the electric field stays concentrated at the pore tip, protecting the sidewalls from dissolution. This positive feedback leads to a deepening of the pores over time^[57,58]. The resulting morphology can be controlled by doping concentration and process parameters. By pre patterning the surface it is furthermore possible to control the location of pore formation. By creating pyramidal notches on the surface through masked anisotropic etching defect sites are introduced, determining the position of pore formation^[58].

1.2.3 Silicon doping

Besides the application as a method of directing an etch process, thereby creating the desired structure as a topography variation, the mask generated with photolithography can also be applied for the selective doping of silicon, i. e. the introduction of impurities into the semiconductor crystal. Historically, this goal was achieved with diffusion processes using a dopant oxides on the surface which are transformed to dopants inside the substrate via several high-temperature processes^[7,59,60]. Due to this, a number of disadvantages arise, specifically the codependence of dopant concentration and diffusion depth, and the isotropic dopant profile^[7]. Accordingly, modern production processes rely on ion implantation as the primary means of introducing dopant atoms into the substrate in controlled manner^[61]. During ion implantation, a high energy beam of dopant ions, generated from an ion source and accelerator, is directed at the substrate, leading to the penetration of these ions into the crystal lattice. Due to elastic (nuclear) and inelastic (electronic) collisions, the ions lose energy and are slowed gradually^[7,16,17]. Via variation of the beam properties, such as ion energy and dose, the penetration depth and dopant concentration can be precisely controlled^[7,62–65]. Following the ion penetration, a final annealing step is necessary, as the ions implanted into the substrate create defects, such as atom displacements and lattice defects^[16,66].

After annealing, the substrate is topographically unchanged, but now contains surface areas with varying doping type, controlled by the mask introduced via photolithography.

1.3 Semiconductor Device Physics

A number of the previously described etch control processes rely on fundamental silicon physical properties, which allow for a high level of control in the fabrication and application of semiconductor devices. The following section aims to elucidate on some basic principles of semiconductor device physics, in particular related to pn-junctions and their electric characteristics, as well as their behaviour under illumination.

1.3.1 pn-Junction

A pn-junction exists at the boundary between a volume of p-doped and n-doped silicon. If two such pieces of differing doping state are brought into contact, for example by ion implantation or diffusion of p-dopants of sufficient concentration into an n-doped substrate, a concentration gradient between the two areas forces the diffusion of majority charge carriers to the opposing substrate area. Specifically, electrons diffuse from n-Si

to p-Si, as the electron concentration is much higher in the n-type area, compared to the p-type area. Here, the electrons recombine with holes, leaving behind the negatively charged dopant atoms. Conversely, holes diffuse from p-Si to n-Si and recombine with electrons, resulting in the evolution of a positive charge, due to uncompensated positively charged dopant atoms. The area with fixed negative charges in the p-Si and the area with fixed positive charges in the n-Si are depleted of mobile charges, which is why the combined area is known as depletion region. Inside the depletion region, a potential difference and thus an electric field develops. The value of the potential difference, the built-in potential V_0 , is dependant on dopant concentrations and temperature. It can be calculated as

$$V_0 = \frac{kT}{q} \ln \left(\frac{N_A N_D}{n_i^2} \right) \quad (1.7)$$

with k being the Boltzmann constant, T the temperature, q the elemental charge, N_A the acceptor doping concentration, N_D the donor doping concentration and n_i the intrinsic carrier concentration of silicon.

The electric field across the junction exerts a force on the remaining charge carriers, which is opposite to the diffusion force due to carrier concentration gradients. Accordingly, an equilibrium is established between the forces, leading to a constant width W_d of the depletion region. To calculate this value in equilibrium state, the built-in potential and doping concentrations need to be known

$$W_d = \sqrt{\frac{2\epsilon}{q} V_0 \left(\frac{1}{N_A} + \frac{1}{N_D} \right)} \quad (1.8)$$

with ϵ being the permittivity^[67]. Besides the overall width of the depletion region, the extent to which the depletion extends into each region can be calculated based on the doping concentration as

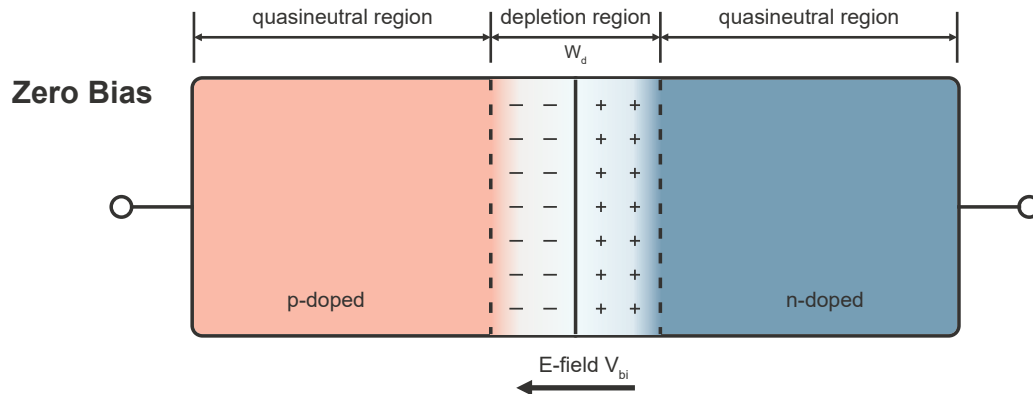
$$x_n = W \frac{N_A}{N_A + N_D} \quad (1.9)$$

$$x_p = W \frac{N_D}{N_A + N_D} \quad (1.10)$$

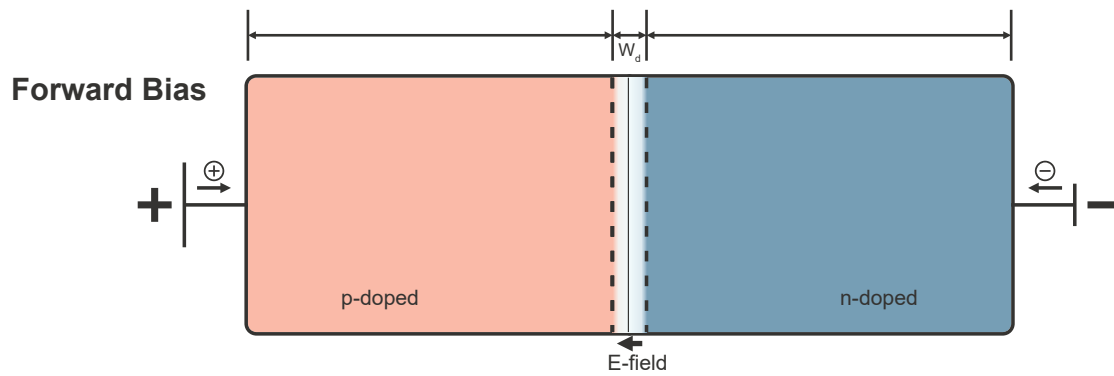
with x_n and x_p being the width of the depletion region in the n-doped and p-doped region, respectively. Essentially, this means that with increasing doping concentration the width of the depletion region in that area decreases, as less volume supplies the same number of dopant atoms. From this also follows, that the depletion region is not necessarily symmetrically distributed over p- and n-Si.

An illustration of a pn-junction in thermal equilibrium is given in Figure 1.11a.

(a)



(b)



(c)

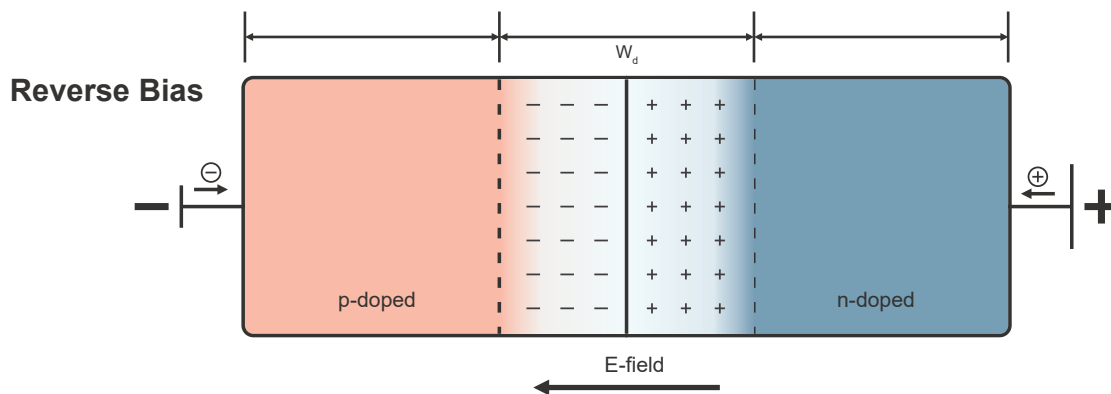


Figure 1.11: Illustration of pn-junction under different biases: (a) Zero bias, no external voltage is applied, the junction is in thermal equilibrium. (b) Forward bias, the positive terminal is applied to the p-side, reducing the depletion region width and electric field, making the device conductive. (c) Reverse bias, the positive terminal is applied at the n-Si, increasing depletion region width and electric field. No current can flow through the device.

The depletion region is the reason for the rectifying character of pn-diodes, as it lets current pass only in one direction. If a current source is connected with the positive terminal to the p-doped side and the negative terminal to the n-doped side, the diode is in forward bias mode. In this case, the electrons pushing towards the depletion region from the n-doped side neutralize the fixed positive charges, while the holes pushing in from the p-doped side neutralize the fixed negative charges. With a bias larger than the built-in potential applied this way, the depletion region becomes so small that it no longer inhibits the movement of charge carriers, enabling the external current to flow through the device, as illustrated in Figure 1.11b. On the other side, if the negative terminal is connected to the p-doped side and the positive terminal to the n-doped side, the diode is in reverse bias mode. Here, the electrons in the n-doped region are pulled away from the junction by the external bias, leading to an increase in depletion width, due to more of the fixed, positively charged dopant atoms being left without compensating electrons. Similarly, the bias pulls away the holes from the junction in the p-Si side, also increasing the width of the depletion region there. The electric field is effectively increased, preventing current flow across the device (see Figure 1.11c). Still, a small current will flow under reverse bias conditions, due to diffusion of thermally generated minority carriers. This means that a very small amount of holes in the n-doped side will diffuse to the positive terminal and likewise, a very small amount of electrons in the p-doped side will diffuse to the negative terminal. This reverse current is mostly independent of bias voltage and only increases abruptly once the diode reaches breakdown condition at its specific breakdown voltage. At this point, the rectifying characteristic breaks down, usually either due to the Zener effect or avalanche breakdown. In the case of the Zener effect, a very high electric field leads to the tunneling of electrons from the valence band to the conduction band, which generates a large amount of free charge carriers and in turn a high conductivity. On the other hand, the diode can break down due to the avalanche effect, where thermally excited charge carriers are accelerated by the high electric field of the depletion region and collide with other bound carriers, freeing them as well. This leads to an avalanche like increase in free carriers and therefore current flow^[67–69].

1.3.2 Photo Effects in Semiconductors

Semiconductors, like any other material, are perceptible to light illumination in a way that can give rise to specific effects taking place in the material. Mainly this is due to the photoelectric effect, leading to the excitation of electrons inside the material from a lower to a higher energy state.

1.3.2.1 Photoelectric Effect

The photoelectric effect, as discovered by Heinrich Hertz in 1887 and explained by Albert Einstein in 1905, earning him the 1921 Nobel Prize in physics, can be differentiated into the outer and inner photoelectric effect. In the case of the outer effect, which affects all materials, the excited electrons are emitted from the illuminated material. This emission of photoelectrons leaves the material positively charged^[70–72]. Contrary to this, in the case of the inner photoelectric effect, the electrons are not emitted from the material, but instead excited from the lower energy valence band to the higher energy conduction band. This leads to mobile charge carriers, electrons in the conduction band and holes in the valence band, increasing the materials conductivity (photo conductivity). For this to occur it is necessary for the semiconductor to be illuminated with light of a sufficiently short wavelength in order to overcome the band gap.

A simple type of device, based on the photoelectric effect, is the photo resistor. Here, a piece of semiconductor material is used as a conductor with known resistance. As the conduction process is based on mobile charge carriers, the conductivity increases proportionally with temperature and doping state, due to an increase in available charge carriers. Additionally, the carrier concentration can be influenced by the aforementioned charge carrier generation under illumination. The increase in mobile carriers is furthermore proportional to the intensity of the incident light, allowing photo resistors to be used as simple light sensors^[67].

1.3.2.2 Photovoltaic Effect

In more complex semiconductor structures, for example diodes or transistors, charge carrier generation takes place like described before, but the doping structure gives rise to another effect, called photovoltaic effect. This is the basis for solar cells and allows for the harnessing of the energy of incident photons. For this, a device structure with depletion region is necessary. If the charge carriers are generated within or within one diffusion length of the depletion region the built-in potential will separate holes and electrons by sweeping the holes into the p-type region and the electrons into the n-doped silicon, as illustrated in Figure 1.12. If no external circuit is connected, this will lead to the charging of the regions, generating the open circuit potential V_{oc} . This potential effectively biases the junction in forward bias mode, leading to a small forward current opposite to the photo current. If now the n- and p-doped sides are connected over an external circuit containing a load (e.g. a lamp or motor), the photo generated electrons swept to the n-doped side by the built-in potential can exit the semiconductor over the contact, power the load and return to the p-doped side of the semiconductor

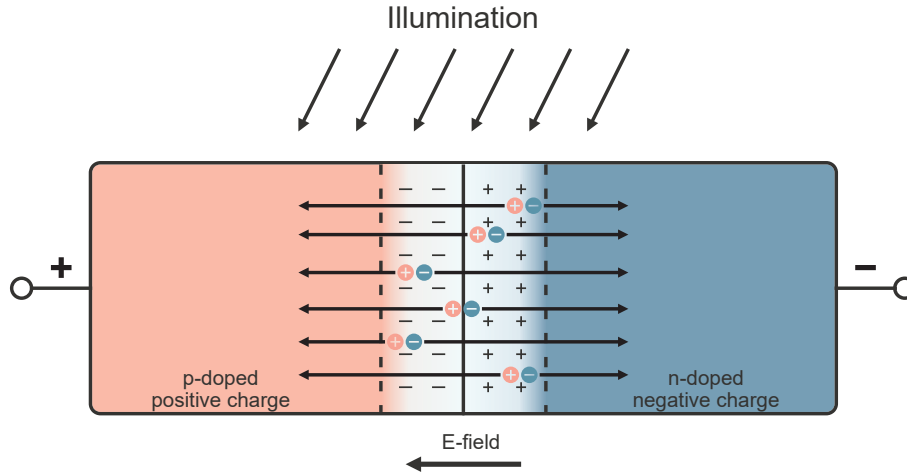


Figure 1.12: Illustration of the behaviour of a pn-junction under illumination, leading to charging of the p- and n-area, generating the open circuit potential.

where it can recombine with a hole, which might have been swept across the junction as well. In this way, the diode can generate a voltage and current from the incident light, enabling the usage as a solar cell^[67–69,73,74].

Alternatively, the diode can be used as a photo sensor, in order to detect and quantify the incident light. This is frequently used for fiber-optic data transmission. Here, the sensor needs to have a fast response time and be very sensitive and reliable. In order to achieve this, such sensors are operated in reverse bias mode with relatively high bias voltages below the breakdown voltage. This decreases the carrier transit time and capacitance, increasing response time. Light generated carriers are swept into the corresponding areas and allow the flow of current through the external circuit, creating a signal proportional to the incident light.^[67]

1.4 Electropolymerisation

Multiple literature sources describe the electrochemical polymerisation of monomers, such as pyrrole^[75–80], thiophene^[81–83] or aniline^[84–86] from electrolyte solutions on electrodes. In particular pyrrole is a extensively investigated monomer, with reports of successful polymerisation on semiconductor surfaces, such as homogeneously doped silicon^[77,87–90]. The current flow through the sample leads to the oxidation of pyrrole, which then polymerises via radical intermediates^[75,91]. A number of mechanisms have been hypothesised, with the route proposed by Genies *et al.* assumed to be the most probable^[92]. A simple scheme of the reaction is shown in Figure 1.13. In the first step (I), a pyrrole monomer is oxidized, leading to three possible conformations of the

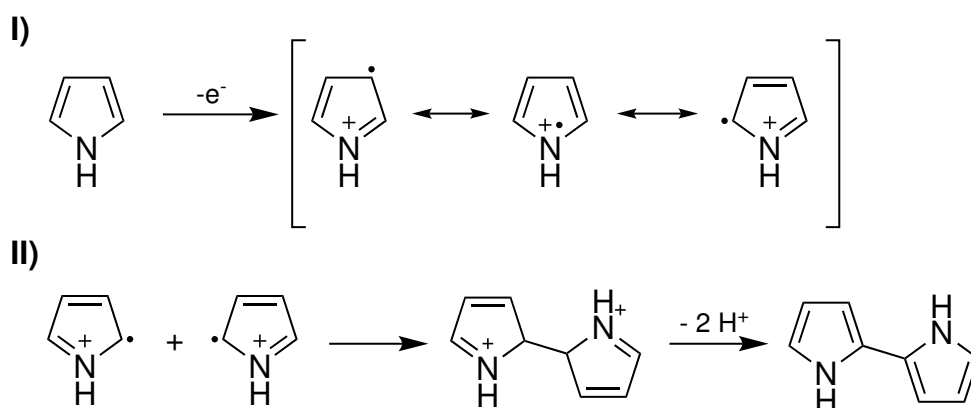


Figure 1.13: Initial steps of pyrrole electropolymerisation mechanism. After the proton elimination, the dimer can again be oxidized and react with further oxidized monomers, leading to chain growth.

radical cation. Two such cations can then react (II), forming a double cationic dimer, which, under elimination of two protons, becomes a pyrrole dimer. In subsequent steps, such dimers can again be oxidized and react with other oxidized monomers, leading to chain growth^[75,92]. In a typical experiment employing a silicon sample as the electrode in a potentiostat setup, the sample is connected to a Pt-rod and submerged in an organic electrolyte solution containing the pyrrole monomer, together with a Pt-counter electrode and a reference electrode, allowing for control over the applied voltage while measuring the current. The schematic setup is illustrated in Figure 1.14. Upon applying an anodic potential of around 1 V, the monomer is then oxidized, leading finally to the formation of a polymer, which is insoluble in the electrolyte solution and therefore

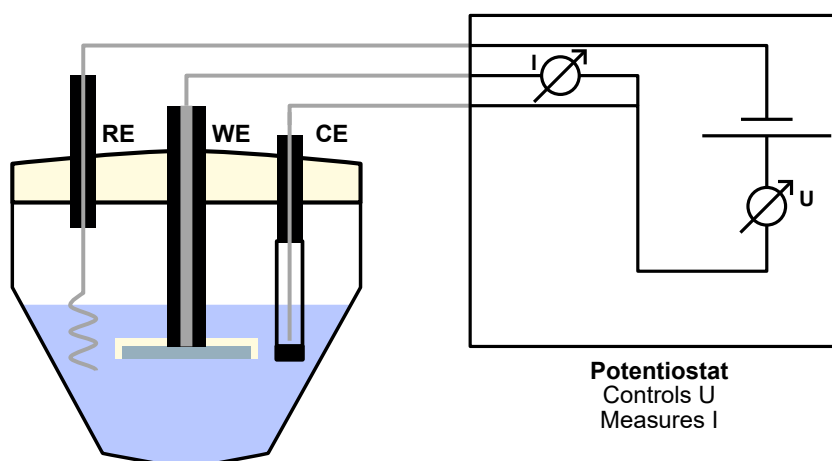


Figure 1.14: Schematic representation of a typical setup used for electropolymerisation of pyrrole using a potentiostat: CE: Counter electrode, WE: Working electrode: RE: Reference electrode.

deposited immediately on the electrode surface^[93–97].

As the oxidation is the initial step for the polymerisation, and each monomer has to be oxidized, the polymerisation rate depends directly upon current flow. Several approaches for the patterned deposition of polypyrrole have been investigated, making use of introduced variations in the substrate. For example, Gorman *et al.* used a Self-Assembled Monolayer (SAM), patterned via micro-contact printing to prevent polymerisation on some surfaces^[98]. In a different approach, Fabre *et al.* controlled the polymerisation by employing a conductive AFM tip as an electrode, scanning the areas on which polypyrrole is aimed to be deposited^[99].

1.5 Selective Polymer Deposition on Surfaces

As shown for photolithography, the deposition of polymer films plays an important role in device fabrication. Here, the aim is to create a smooth, even layer on the substrate for further processing. In contrast to this, several methods can be used to exploit existing variations in surface properties in order to selectively deposit polymer films. Here, the aim is to only cover certain areas with the layer, gaining precise control over the behaviour of the polymer film.

Two often used methods include polymer dewetting directed by surface inhomogeneities and the selective polymerisation from surface sites.

1.5.1 Polymer Dewetting

For the case of surface directed polymer dewetting, a number of literature sources demonstrate the use of variations in surface properties, such as surface energy^[100,101], roughness^[102,103] or the presence of self-assembled monolayers^[104–107] in order to direct a thin polymer film to only cover certain areas of the substrate. For this, the polymer is usually spin-coated and then annealed or deposited via drop-casting. As the evaporation of the solvent during spin-coating is relatively fast, the polymer initially deposits homogeneously on the surface, regardless of variations in the surface properties. To induce the dewetting, an annealing step is performed, during which the sample is heated above the T_g of the polymer, enabling it to flow. In this state, the surface inhomogeneities induce dewetting due to favorable and unfavorable interactions. Upon cooling, the polymer solidifies again and a selectively dewetted sample is yielded. In contrast, in the case of drop-casting, the relatively slow evaporation of the solvent allows the mobile polymer chains to immediately be influenced by the surface properties, directing their deposition. The overall process is illustrated in Figure 1.15. Zhang *et al.* described a process for

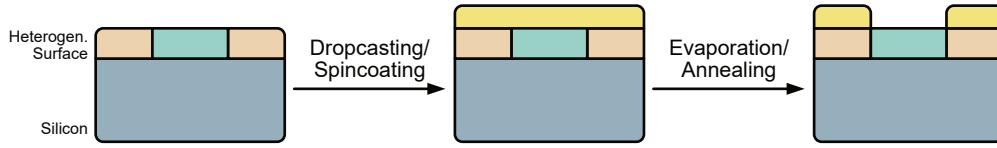


Figure 1.15: Illustration of selective dewetting of polymers. First, a polymer film or solution is deposited via spincoating or dropcasting on an inhomogeneous substrate. This deposit is then annealed or evaporated, depending on the deposition method, in order to align the polymer chains.

the selective dewetting of polystyrene (PS) from a modified silicon oxide surface. Via microcontact printing, a structure of octadecyl trichlorosilane (OTS) was patterned on the SiO_2 -surface, creating a spatially inhomogeneous surface. After spincoating of PS and annealing, the polymer dewetted preferably from the OTS areas, leading to the structuring of the film, according to the surface, as illustrated in Figure 1.16a^[107].

Lee *et al.* showed that PS films can also be selectively dewetted on silicon samples with varying silicon oxide thickness. By modifying the substrates three variations were created: H-Si after etching in hydrofluoric acid, generating H-bonds, P-Si after plasma activation of the oxide surface and N-Si without further modification, i.e a native surface. It was demonstrated, that PS selectively dewets from more oxidized surfaces (see Figure 1.16b), enabling a possible route for film structuring^[108].

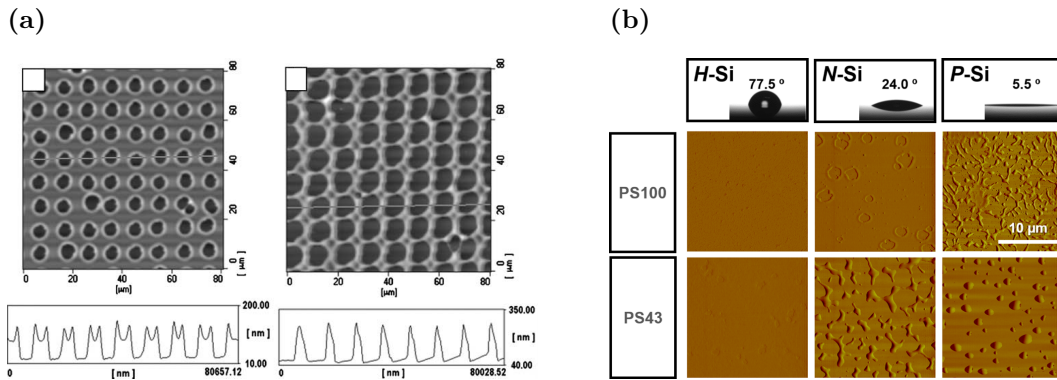


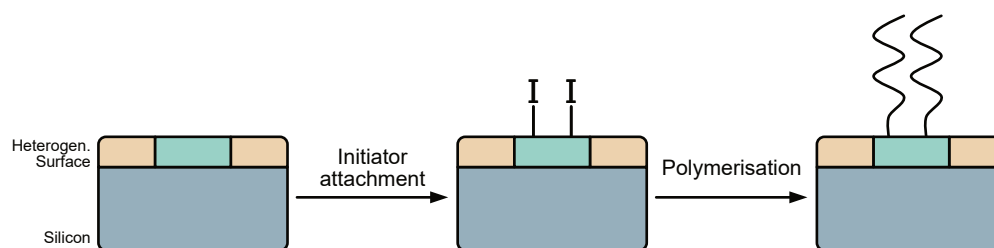
Figure 1.16: (a) AFM images showing the selective dewetting of a PS film on silicon substrate structured with an OTS-monolayer after 1 min (left) and 14 min (right) of annealing (taken and adapted from^[107]). (b) AFM images the dewetting of PS films on silicon surfaces with varying surface energy, due to the presence of silicon oxide (adapted from^[108]).

1.5.2 Surface Initiated Polymerisation

An alternative approach enables not only the selective deposition of polymer chains onto the substrate, but also their covalent attachment. Particularly, the polymers are

synthesised directly on the substrate in a 'grafting-from'-approach^[109–113], starting from initiator groups which are bound to surface functions. Widely employed are gold or silicon oxide surfaces, as they allow for easy attachment via sulfide-bonds or silanization, respectively^[114]. Given that a sample exhibits a spatially varying distribution of such surface functions, the initiator can be attached selectively only on some areas of the sample, generating initiation sites according to the structuring of the surface. Starting from these, polymer brushes can then be synthesised, leading to the patterning of the substrate, as illustrated in Figure 1.17a^[115].

(a)



(b)

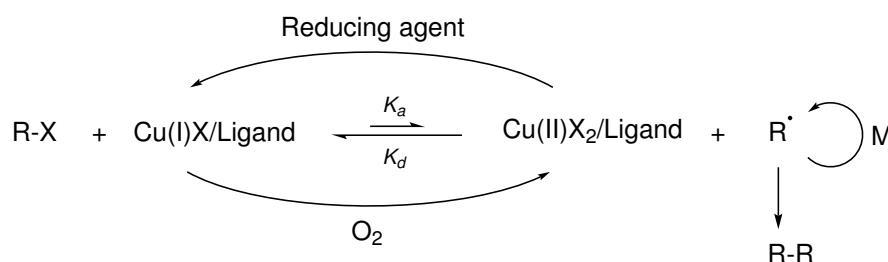


Figure 1.17: (a) Schematic process of selective surface initiated ATRP after modification of only one surface group (B) with a suitable initiator(I). (b) Mechanism scheme for ARGET-ATRP, illustrating the reasons for good molecular weight control ($k_a \ll k_d$) and process simplicity (reduction of Cu-species, allowing for air to be present).

In the literature, a relatively new approach is based on controlled radical polymerisation using Activators Regenerated by Electron Transfer (ARGET) - Atom Transfer Radical Polymerisation (ATRP), enabling simple processes and good control over polydispersity, while allowing for the usage of a number of functional groups^[116–119]. ARGET-ATRP is desirable, as the rapid activation/deactivation cycles of the controlled radical polymerisation allow for low stationary radical concentration, minimizing termination reactions. The general mechanism scheme is shown in Figure 1.17b. In ATRP, the initiation is based on the abstraction of a halogen atom from the initiator by the metal complex catalyst, usually a copper species, creating a radical for the polymerisation

reaction. The catalyst undergoes a reversible oxidation upon abstraction so that an equilibrium, which is shifted to the side of low radical concentration, is reached. Accordingly, the low radical concentration allows for controlled polymer growth^[117,120]. Furthermore, due to the added reducing agent in the case of ARGET-ATRP, a very simple process is possible, as the reaction does not need oxygen free conditions. The problem of oxygen-induced oxidation and subsequent deactivation of the catalyst is circumvented by the addition of a reducing agent, which restores the original +I oxidation state^[110,121].

As demonstrated by Ma *et al.*, this process allows for the selective polymerisation on a suitable surface, in this case the surface was structured by the micro contact printing of a polymeric mask. The final, structured POEGMA film was then used for directing the adsorption of proteins, measurable with confocal microscopy, as illustrated in Figure 1.18a^[115].

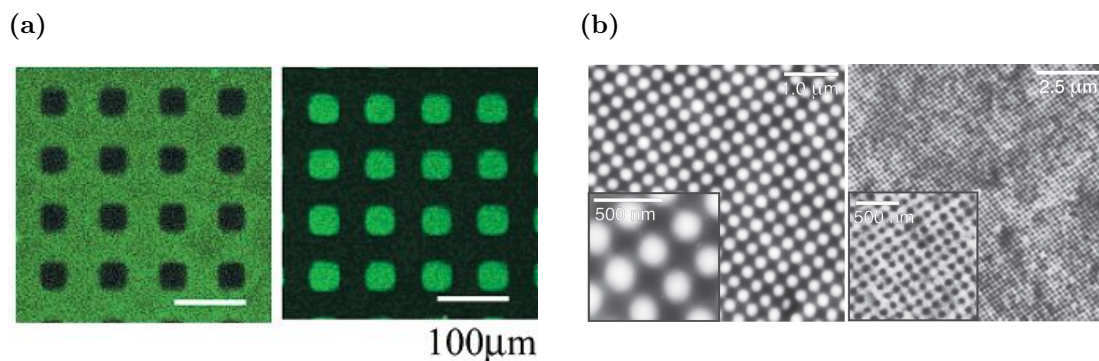


Figure 1.18: (a) Confocal microscopy images showing the selective adsorption of marked proteins (green) with only a micro-contact printed polymeric mask (left) and after the unprinted areas were modified with POEGMA through ATRP (taken and adapted from^[115]). (b) AFM images showing nanometer-sized structures generated with selective surface initiated ATRP after lithographic structuring of the surface (adapted from^[122]).

Similarly, Benetti *et al.* used imprint lithography to create nanometer-sized structures used to direct the polymerisation and subsequently pattern the polymer brushes in nanometer dimension as well. AFM images of such patterned PEGMA films are shown in Figure 1.18b.

2 Motivation and Aim

Motivation

As described in the theoretical part, photolithography for the fabrication of semiconductor devices is a central process, taking up a large part of the overall fabrication time. Accordingly, a great interest exists in the reduction of the number of necessary lithography steps, in order to improve yield and efficiency. One particular topic for this is the simplification of the fabrication of superjunction transistors, as manufactured via the Multi-EPI process. Superjunction transistors, such as the CoolMOS™ power transistor, first demonstrated by Siemens Halbleiter (now Infineon Technologies), are used frequently in high voltage applications, gaining importance due to increasing electrification, in particular in the transportation sector^[123,124]. These types of transistors are desirable, as they greatly improve the electrical characteristics, such as the On-Resistance $R_{DS(on)}$, by using columns of p-doped silicon inside an n-doped substrate^[125–127].

In the production of such devices, the columns are created inside the substrate by repeated masking, implantation and epitaxy steps. This creates separated volumes of p-Si buried inside the n-silicon bulk, which are finally joined through thermal diffusion, as illustrated in Figure 2.1a^[128].

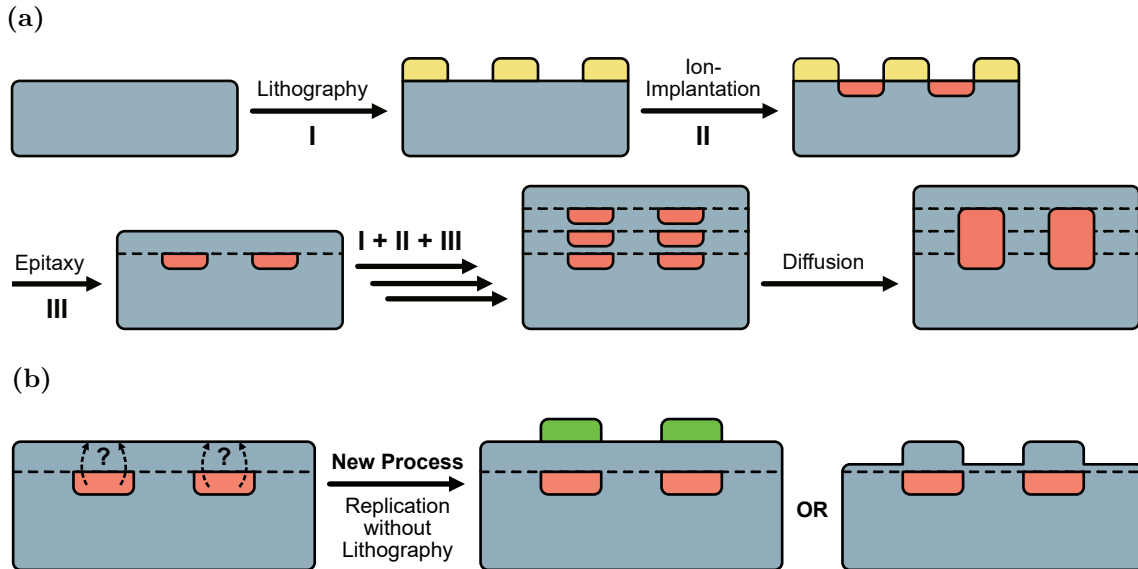


Figure 2.1: (a) Schematic illustration of Multi-EPI process. Over multiple steps layers with separated implantations are created, requiring the repetition of identical lithography steps. (b) Illustration of the envisioned process to be developed in this work. The buried implants induce an effect on the homogeneous surface, allowing for the reproduction of the implant structure as a surface heterogeneity.

Although this is an established process, improvements are desired, as the repeated fabrication of identical implantation structures with perfect alignment and dimensionality

is no trivial task, as even small deviations render a device unusable. This further complicates the process with a large number of additional steps, for example measurements of critical dimensions and overlay.^[129–131]

Improvements can be made by finding a method for the self-alignment of the implantation mask on the epitaxial layer, according to the implantations of the previous step. This would eliminate all but the first lithography step, greatly simplifying the fabrication.

Aim of this Work

The aim of this work is the development of a process for the replication of the p-implant structure buried beneath a layer of n-doped epitaxial silicon, as illustrated in Figure 2.1b. Specifically, the task is to establish a method which is able to generate features, e. g. height or material variations, directly above the buried implants on the homogeneous silicon surface, without the need for conventional lithography steps. This self-alignment process is envisioned to be directed by the influence of the buried implants on the silicon surface directly above.

1. Sample analysis for suitable surface properties

To achieve this goal, the first task is the comprehensive analysis of the samples with deeply buried p-implants in order to detect changes in surface properties, induced by the buried implants. Candidates for a suitable property are for example surface energy, surface potential, surface charge or resistance.

2. Generation of surface heterogeneities self-aligned above buried implants

If the analysis defines a surface property which is sufficiently influenced by the buried implants, the next step is the employment of this property for the generation of a significant surface heterogeneity as an alteration in the sample topography or change of the surface composition, e. g. by deposition or removal of a material selectively above the buried implants.

3. Analysis of the established process

Lastly, the established self-alignment process has to be investigated with regard to the mechanism of the self-alignment in order to further improve the new process.

3 Results and Discussion

3.1 Sample Description

The samples used for this work were provided by Infineon Technologies in pre-structured form. Generally, all samples consist of bulk silicon wafer pieces, cut to 20×10 mm. The wafer substrate is n-doped and cut to (100) crystal orientation. On all provided samples, an epitaxial n-doped silicon layer, denoted as n-Si, with $17 \mu\text{m}$ thickness was deposited. On most wafers, ion implants were introduced into this layer, according to different structures. Finally, on all but one sample type another epitaxial layer, denoted as $n_t\text{-Si}$, with varying thickness between 250 to 1000 nm was deposited, burying the implants beneath a homogeneous silicon layer. This results in a layered structure as illustrated in Figure 3.1.

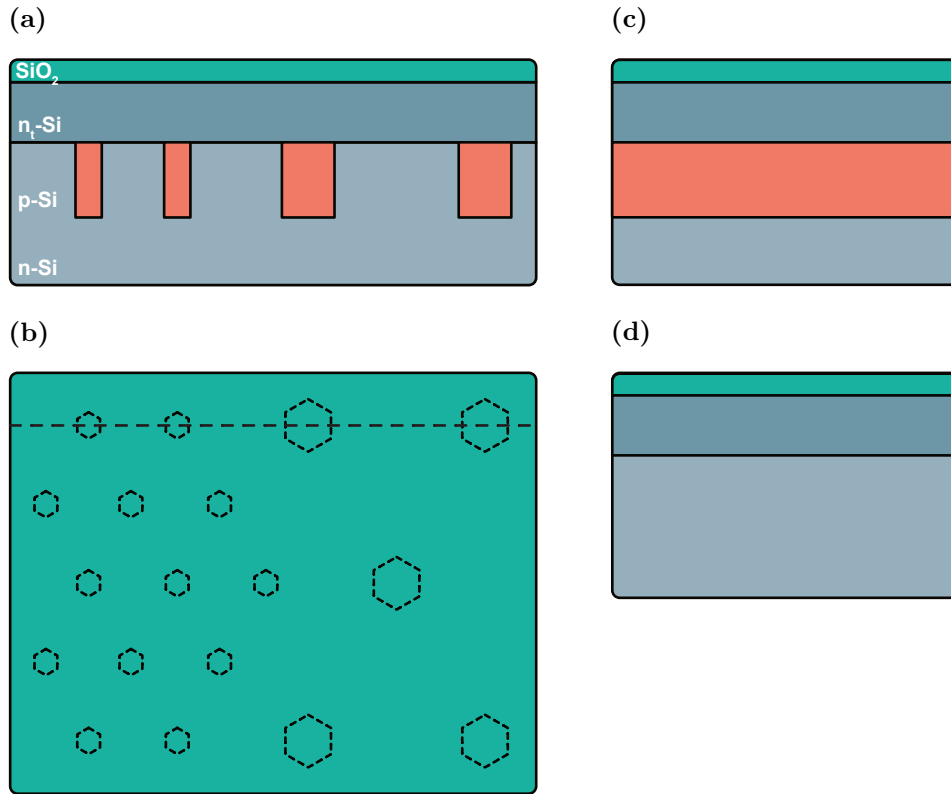


Figure 3.1: Illustrations of the sample structure and mask layout for the typically used samples. (a) Cross-section view of the layered sample structure with buried p-implants. (b) Top view of sample with the mask layout of hexagonal p-implants marked. (c) Cross-section view of sample with full-surface p-implant. (d) Cross-section view of sample with no p-implant.

Figure 3.1a shows the schematic cross-section for samples with structured implants, for which the mainly investigated structure of hexagons in a hexagonal pattern can be seen in top view in Figure 3.1b. The implants have a circumscribed circle diameter range of 2 to $5 \mu\text{m}$, whereas the larger implants are twice the size of the smaller ones.

Figure 3.1c and Figure 3.1d show the cross-section of samples with full area and no implant, respectively. Also shown in the cross-section images is the native oxide layer present on all samples. From ellipsometric measurements the thickness of this layer after cleaning was determined as (1.29 ± 0.03) nm.

Figure 3.2 collects further mask information for different implantation structures. In Figure 3.2a the macroscopic overview of the arrangement of the different implant sizes for the mainly investigated structure with hexagonal implants is shown.

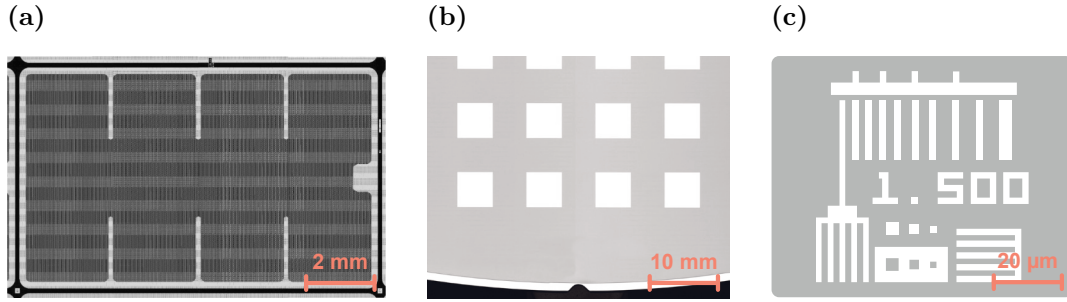


Figure 3.2: Mask overview images for the additionally provided samples. (a) Arrangement of the different hexagonal structures into a single device chip. (b) Overview image of the mask used for large area implants. The holes and distances between measure 5 mm. (c) General mask layout for resolution test samples. The number in the centre represents the single line width of the structures, but needs to be increased by 20 %, due to a different optical reduction.

Here, the lighter outlines consist of the smaller implants, the darker infill of the larger implants and the black border around each chip structure has no implants at all. On samples with this implantation structure, the deposited top epitaxial layer thicknesses are 0 nm, 250 nm, 500 nm and 1000 nm. Figure 3.2b shows the mask layout for another type of sample with macroscopically large implant sizes. Here, the holes in the mask (white squares) used for ion implantation are squares with 5 mm edge length. With this layout, only one wafer with 1000 nm top epitaxial layer was provided. For additional resolution investigations, a wafer with a 500 nm top epitaxial layer with continually smaller structures from around 7 to $0.35 \mu\text{m}$ with the mask layout shown in Figure 3.2c was provided. The number in the centre denotes the single line width, reduced by 20 %, due to the usage of a differing optical reduction, as intended for this mask.

In order to determine the real size of the hexagonal p-implants on the typically used samples, measurements were taken from Scanning Spreading Resistance Microscopy (SSRM) images, which were provided by Infineon Technologies together with the samples (Figure 3.3). This image was taken on a sample without the top epitaxial layer in order to measure the implant dimension with no disturbance due to this layer. SSRM measures the spreading resistance of the sample, which varies laterally with doping type. The

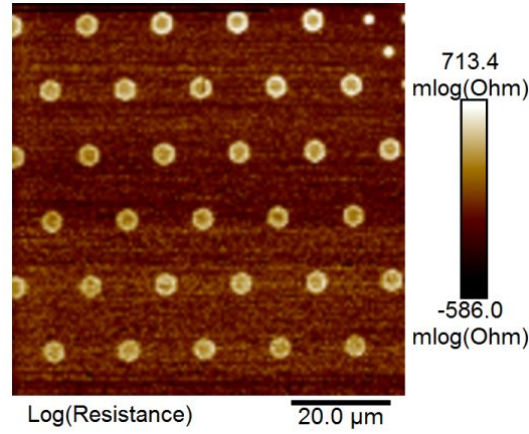


Figure 3.3: SSRM image of sample without top epitaxial layer, used to determine the real dimension of the implants.

analysis yields a mean diameter of $(4.36 \pm 0.18) \mu\text{m}$ for the larger implants. Not enough image data was available for the smaller implants, but as their size is exactly half of the larger ones, their dimensions can be assumed to be $(2.18 \pm 0.09) \mu\text{m}$.

The doping parameters for the three different doping regions are listed in Table 3.1.

Table 3.1: Doping parameters of the provided samples

Region	Type	Resistivity	Concentration	Thickness
		$\Omega \text{ cm}$	cm^{-3}	μm
Top layer ($n_t\text{-Si}$)	n	3.19	$8 \cdot 10^{14}$	0, 0.25, 0.5, 1
Initial layer (n-Si)	n	6.15	$4 \cdot 10^{14}$	17
Implants	p	6.83	$2 \cdot 10^{15}$	≈ 1.5

The concentration values were provided by Infineon Technologies for the the n-Si from the epitaxy process parameters and for the p-Si from Time of Flight-Secondary Ion Mass Spectroscopy (ToF-SIMS) measurements as the value at the interface between bottom and top epitaxial layer. The resistivity values were then calculated from the dopant concentrations^[132].

3.2 Surface Property Investigation

From initial measurements, such as AFM height and phase images, it was obvious, that the sample surface is completely homogeneous and shows no signs of the buried implants, as seen in Figure 3.4.

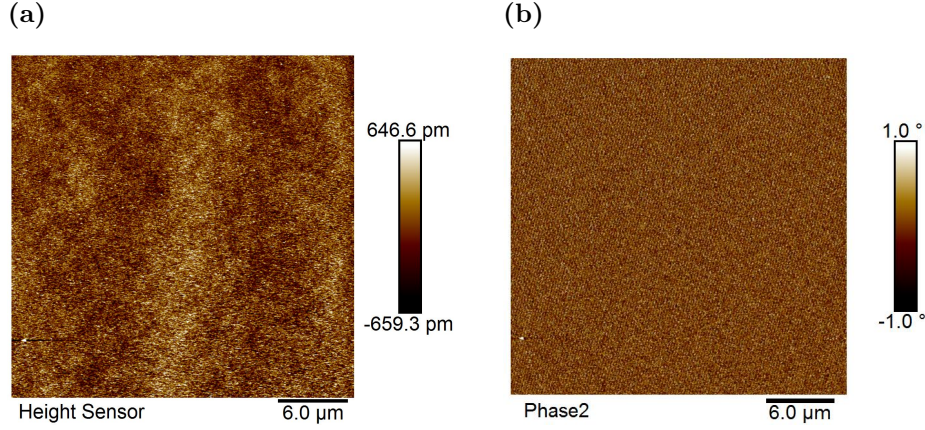


Figure 3.4: AFM images of a cleaned sample with 500 nm top epitaxial layer thickness. (a) AFM height image. (b) AFM phase image.

This is to be expected, as the implants are covered by a completely homogeneous, n-doped layer, which screens any influence of the buried implants usually measurable with standard techniques. Only recently, Gramse *et al.* developed a nondestructive technique for the spatial and electrochemical analysis of buried implant structures, using a technique called Scanning Microwave Microscopy (SMM). Otherwise, analysing buried implants is mostly only possible destructively^[133,134], e.g. via ToF-SIMS, as used for the determination of the doping parameters. This also means, that finding a surface property, which is influenced by the implant structure is no easy task. The presumably suitable surface properties, as described in the aim of this work, are surface potential or work function, surface charge, surface energy and sample conductivity, which were further explored, as follows.

Surface Potential The surface potential or work function of the surfaces can be measured using Kelvin Probe Force Microscopy (KPFM), a modified AFM technique^[135,136]. With this method, changes in the surface potential, induced by the buried implants can be visualized. For silicon, literature reports show a difference in surface potential, depending on the bulk doping type of the substrate^[137]. It is therefore conceivable, that doping variation due to buried implants can also influence the surface, especially if the implants are close to the surface, e.g. below 250 nm of epitaxial silicon.

To test this hypothesis, samples with 0 nm, 250 nm and 500 nm top epitaxial layer were cleaned and measured with KPFM, yielding the results shown in Figure 3.5.

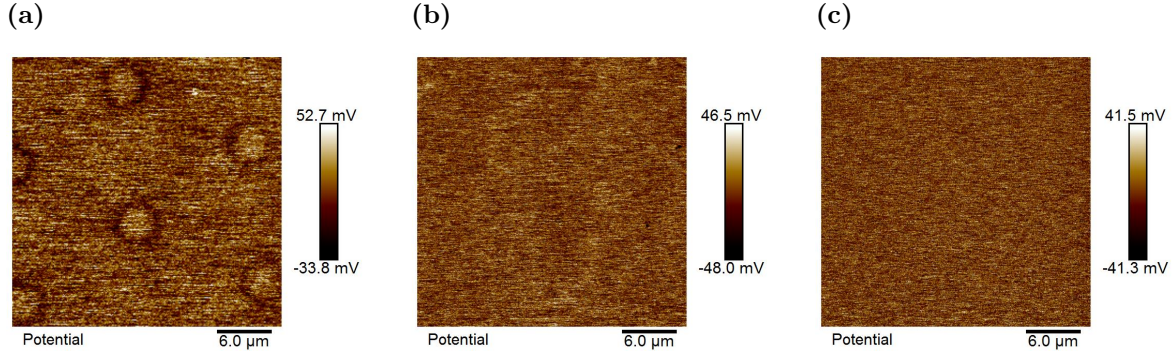


Figure 3.5: Kelvin Probe Force Microscopy (KPFM) images for samples with varying top epitaxial silicon layer thickness. (a) no epitaxial layer, (b) 250 nm, (c) 500 nm.

On samples without the epitaxial layer, i.e. with the implants immediately at the sample surface, the results show an image of the implants, as variation in the surface potential. Furthermore, on such samples the implants were visible in height and phase images as well (see Figure A.1). The measured height difference is very small at only around 100 pm and is likely due to interactions between the AFM cantilever and sample and not an actual height difference. The phase image shows a small contrast below 1° , indicating a small, but measurable interaction. For the samples with epitaxial layer, i.e. buried implants, no difference in surface potential was measurable, the surface was completely homogeneous in potential mode, as well as height and phase contrast.

These results indicate, that the buried implants are likely too far from the surface in order to induce a measurable effect on the surface potential. Accordingly, this property was precluded as a suitable inhomogeneity for self-aligning resists.

Surface Charge Another possibly suitable property is the surface charge, which could allow for selective adsorption of other charged materials, if a sufficient difference due to buried implants can be found. Especially interesting here are samples with native oxide layer, as silicon oxide already exhibits a pH-dependent surface charge, which decreases with increasing pH. The isoelectric point of native silicon oxide is around pH 2.6^[138,139]. If a pH value can be found at which surfaces with and without underlying p-implants have opposite surface charges, or at which one is uncharged while the other has a non-zero surface charge, this difference could be exploited for self-alignment.

In order to measure the surface charge, a zeta-potential method was employed. Here, the potential at the slipping plane (zeta-potential, ζ) of the solid-liquid interface is

measured using the streaming potential/current. As the method requires a large, homogeneous surface, instead of samples with structured implants, samples with either full surface or no p-implants under 1000 nm of epitaxial silicon were investigated (see Figure 3.1c and Figure 3.1d). With these samples, the difference between both sample types gives direct conclusions about the influence of the implant on the surface charge. Figure 3.6 depicts the measured zeta potentials for such samples with and without native silicon oxide layer.

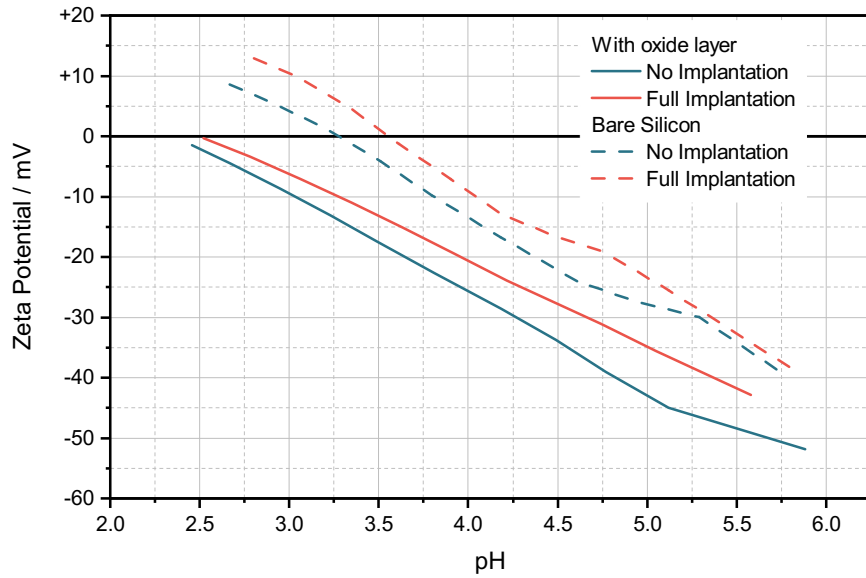


Figure 3.6: Zeta potential versus pH for samples with and without full area buried implant. Only a small difference is visible on samples with and without native silicon oxide layer.

For samples with native oxide layer, both sample types, with and without buried implants, show a very similar surface charge versus pH behaviour in that at around pH 2.5, the charge is close to neutral, while it decreases with increasing pH. Samples with full surface p-implant are offset in positive direction, but only by a small value, which furthermore decreases closer to the neutral value. This effectively means that no pH value can be determined at which both sample types have opposite surface charges with a significant difference, or at which one is neutral while the other has a large enough non-zero surface charge. A similar behaviour is measurable for samples on which the native oxide layer was removed immediately prior to the experiment using hydrofluoric acid. Here, all values are shifted in positive direction, leading to an isoelectric point around pH 3.5. Even though a point exists, where opposite charges are measured, the difference of below 5 mV is too small to be useful for application in a self-alignment process. Experiments investigating the selective adsorption of a negatively charged

surfactant were not successful as well, leading to the preclusion of surface charge as a suitable surface property for self-alignment.

Surface Energy A third possibly suitable surface property is the surface energy, in particular concerning the wettability of the surfaces. If this parameter is influenced significantly by the buried implants, it could be used to selectively deposit materials on the surface, exactly in alignment with the buried implant structure. In the literature, a number of reports describe the selective deposition of materials, according to the surface energy, for example using thin homogeneous polymer films^[100,101,105,106,108] or a blend of two polymers^[140–143]. Here, the surfaces were modified in way that they exhibit areas with varying surface interfacial energy, allowing for the polymer to deposit only on one type, or only one part of the blend to deposit, respectively.

In order to test this idea for samples with buried implants, contact angle measurements were taken, again on samples with and without full area implants, as not to disturb the results due to microscopic structuring. The measurement results are shown in Figure 3.7.

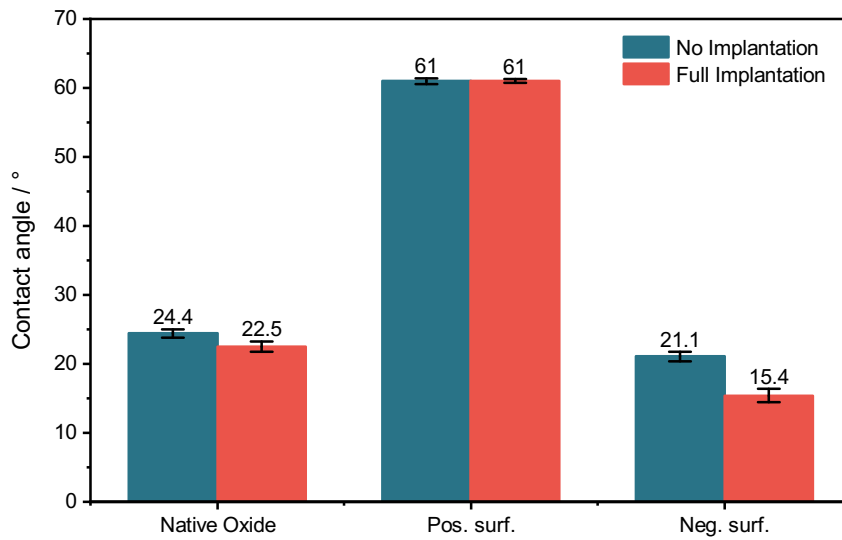


Figure 3.7: Contact angle measurements on samples with and without full area buried implant. Some samples were treated with surfactants in order to achieve selective adsorption.

The left side shows the measured contact angle for a sample with native oxide layer after cleaning. The values for both sample types are very close to each other within 2, indicating that no difference in surface energy is induced by the buried implant. This was further investigated under addition of surfactants, in a similar way as proposed in the previous section about surface charge. If a surfactant would selectively attach to one

sample type, the resulting change in surface energy should be reflected in the contact angle. Here, it could be found that a positively charged surfactant (hexadecyltrimethylammonium bromide, CTAB), which would attach to a negative surface, resulted in a significant change in the contact angle. This was to be expected, as the native oxide surface is negatively charged under the experimental conditions ($\text{pH} \approx 7$). In contrast, a negatively charged surfactant (sodium dodecyl sulfate, SDS) did not attach to the surface at all, leading to no significant change in contact angle. Both sample types showed identical behaviour, i. e. the buried implant did not change the surface energy significantly. Consequently, surface energy was not further taken into consideration as a suitable surface property for self-alignment.

Conductivity Another possible sample property to be used for self-alignment is the conductivity of the substrate in vertical direction, i. e. through the cross section. It stands to reason that a sufficient difference in conductivity is possible due to the electrical characteristics between p- and n-Si regions. As pn-junctions are formed at the interfaces, the current flow through areas with underlying buried implants should be reduced, in comparison to the sample areas which are fully n-type.

To measure such an effect, SSRM was again employed to determine the resistance with nanometer spatial resolution. In addition to the result shown in Figure 3.3, samples with 250 nm and 500 nm top epitaxial layer were investigated as well, depicted in Figure 3.8. As observed before, a strong variation in resistance is measurable on samples with no top epitaxial layer, i. e. with the implants directly at the surface. This is to be expected, as the pn-interface acts as diode, blocking electron flow in the direction from p to n-Si (see the description of pn-junctions in section 1.3.1). On samples with an epitaxial layer, even with a thickness of 500 nm, a difference is also measurable, albeit with a smaller

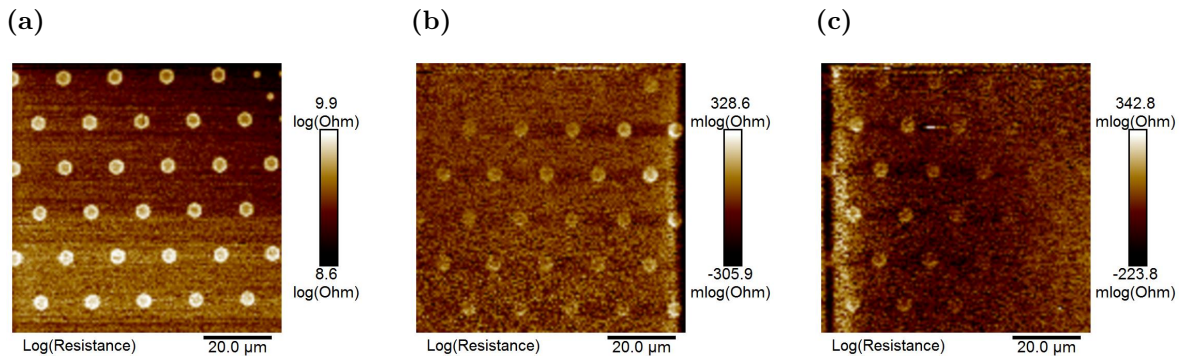


Figure 3.8: Scanning Spreading Resistance Microscopy (SSRM) images for samples with varying top epitaxial silicon layer thickness. (a) no epitaxial layer, (b) 250 nm, (c) 500 nm.

magnitude. The shape and orientation of the buried implants is still visible, indicating a sufficiently high difference in the conductivity to possibly be suitable for the application in a self-alignment process.

To exploit the conductivity difference, electrochemical reactions leading to the deposition of material can be used. Here, the product of the electrochemical reaction on the surface has to be insoluble in the electrolyte, so that it will deposit at the reaction site. One such reaction is the oxidation and subsequent polymerisation of pyrrole.

3.3 Pyrrole Electropolymerisation

3.3.1 Introduction

As described in the theoretical part (see section 1.4), pyrrole can be polymerised electrochemically on silicon substrates of homogeneous doping, resulting in the deposition of a polymer film. The polymerisation rate of this process is directly dependent upon the current flowing^[75,91], allowing control over the polymer structure. On homogeneously doped substrates, the current is controlled externally via the experimental setup, whereas the samples shown here exhibit a resistance variation, induced by the buried implants, which potentially allows for the spatial control over the pyrrole polymerisation in alignment with the structure of the buried implants. A schematic illustration of the envisioned process is shown in Figure 3.9. On areas with lower cross-sectional resistance, i. e. with no underlying buried implants, an increased amount of pyrrole should be oxidized and consequently polymerised. This would yield a surface structuring reproducing the buried implant structure as height difference in the polymer layer.

3.3.2 Cyclovoltammetric Electropolymerisation

Electrochemical polymerisation experiments were conducted via cyclic voltammetry, by sweeping the applied sample bias while measuring the current flowing through the sample. This allows for precise control and also information about what kind of electrochemical processes take place on the sample surface. Such experiments were carried out using a potentiostat, enabling good control over the electrical parameters. A sample was attached to a platinum working electrode in a custom PTFE holder, using silver paste or Ga-In eutectic as a conductive interface layer (see Figure 1.14). With the custom holder, it was possible to only submerge the polished front surface of the sample in the electrolyte solution. This solution consisted of acetonitrile as solvent, 0.1 mol L^{-1} Tetrabutylammonium hexafluorophosphate (TBAFP) as electrolyte salt and 0.05 mol L^{-1} pyrrole as

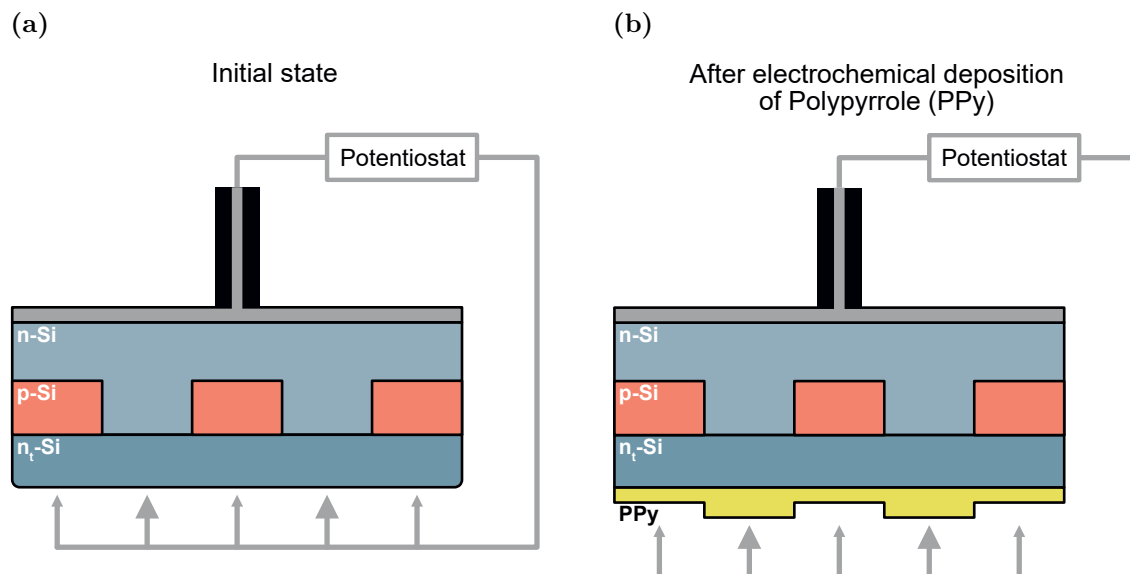


Figure 3.9: Schematic illustration of electrochemical material deposition on samples with buried implants. (a) Prior to the electrochemical reaction the sample is connected to the setup. No surface inhomogeneity is visible. (b) After the process, a layer of material is deposited with variations in layer height or another property, according to the buried implants.

the redox active species. Via a platinum wire counter electrode and a Ag/AgCl reference electrode the electrical parameters could be measured and controlled using the potentiostat. In order to improve polymer film adhesion and the electrical junction behaviour, all experiments were carried out on samples modified with a pyrrole containing monolayer^[77,90]. This provides an anchor point for the polypyrrole, covalently binding it to the surface. Initially the modification consisted of a treatment with a pyrrole silane, reacting with the native oxide layer and forming a pyrrole-containing Self-Assembled Monolayer (SAM).

Literature sources describe oxidation potentials of pyrrole below 1 V, which leads to a peak in current flowing through the sample at such voltages^[93–97]. Accordingly this peak should be visible in measurements taken for samples investigated with a voltage sweep from -0.5 V and 1.5 V with a scanrate of 50 mV s^{-1} . The resulting voltammogram for one sample is shown in Figure 3.10a, measured on a sample with 1000 nm top epitaxial layer. Around 0.5 V in the positive sweep direction, one can observe a small increase in current, indicating successful oxidation and subsequent polymerisation of pyrrole. These increases are visible for all cycles, except for the first, indicating that some induction is necessary before the actual oxidation can take place. Figure 3.10b shows an AFM height image of the sample after cyclovoltammetry. The height of the polymer layer was determined by scratching the surface and measuring the difference, resulting in a

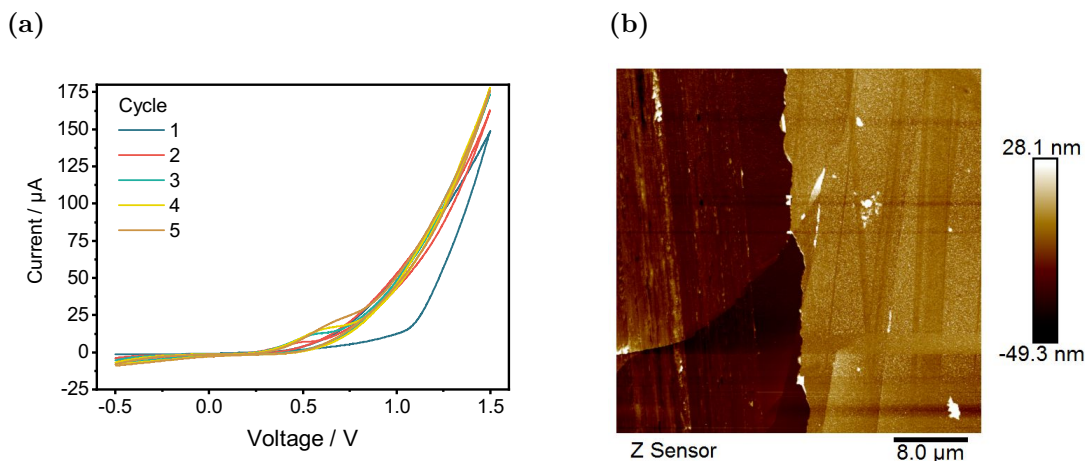


Figure 3.10: CV curve (a) and AFM height image (b) for a sample modified with pyrrole silane and electropolymerised with 5 cycles between -0.5 V and 1.5 V , scanrate 50 mV s^{-1} .

value of 26.4 nm , while the roughness of the layer was measured as 6.5 nm (R_q). With ellipsometry a comparable value of 31.0 nm was measured. As is visible, no reproduction of the implant regions was possible, but initial experiments confirmed the possibility of electrochemical polymerisation of pyrrole on the samples.

To improve the electrochemical selectivity, the native oxide layer was removed on all subsequent samples, as it acts as a dielectric layer, blocking current flow. In order to still provide anchoring pyrrole moieties on the surface, a different surface modification protocol was used. From the literature it is known that hydride terminated silicon can be modified with unsaturated compounds via a photochemical or thermal process^[77,144]. By cleaving the hydride from the silicon surface, either induced via UV irradiation or heat, a highly reactive surface is generated which quickly reacts with any unsaturated hydrocarbons, yielding a Si-C bonded monolayer. In the present work, the hydride surface was generated by oxygen-free etching of samples in ammonium fluoride solution, followed by UV irradiation of the samples covered with allyl pyrrole. This led to the formation of covalently bound pyrrole units on the surface of the samples. Figure 3.11a shows the voltammogram of a sample modified this way. Here, a sample without the top epitaxial layer was used in order to increase the sensitivity, as the resistance difference measurable from SSRM is much larger (compare Figure 3.8). The sample was submitted to the same electropolymerisation scheme with 5 cycles between -0.5 V and 1.5 V . The overall curve shape is similar to the sample with pyrrole silane, although the achieved current at the oxidation peak of pyrrole is increased, indicating better current flow. The visible plateau is due to device limits during this experiments. From AFM height images (see Figure 3.11b) a smooth layer with 6.76 nm (R_q) roughness and 27.4 nm thickness can

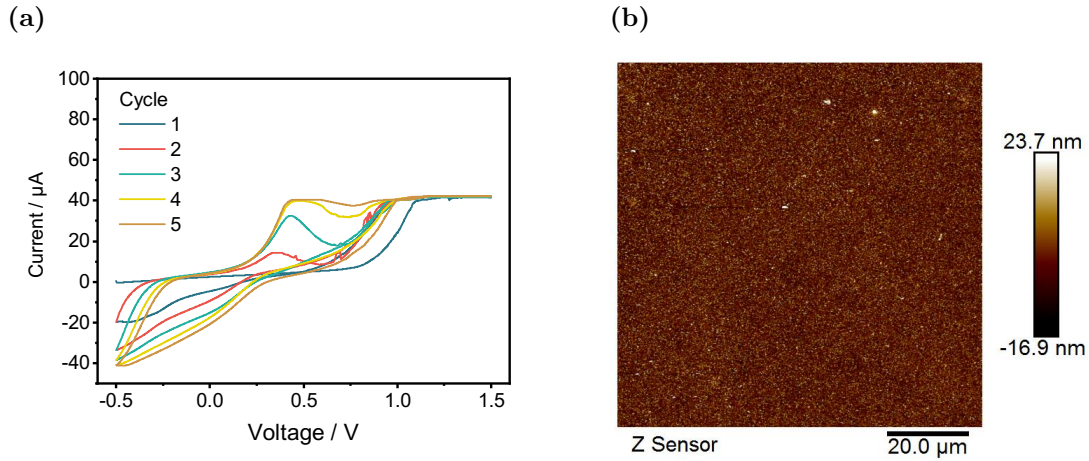


Figure 3.11: CV curve (a) and AFM height image (b) for a sample modified with allyl pyrrole and electropolymerised for 5 cycles between -0.5 V and 1.5 V, scanrate 50 mV s^{-1} .

be determined. Generally, the resulting polypyrrole layer was very similar to samples with silane modification and did not show any sign of selectivity due to the difference in Si doping. The electropolymerisation process was further extensively studied in order to find optimal parameters for the selective deposition of polypyrrole in alignment with the implants. Primarily the voltage sweep width and number of cycles was varied in order to achieve minimal polymerisation with maximum sensitivity, but none of these changes led to a successful structuring.

3.3.3 Light Induced Electropolymerisation

Based upon the previous results, a different approach making use of photoinduced polymerisation was pursued. In short, the photosensitive pn-junctions inside the provided samples should induce current flow upon illumination, similar to how photovoltaic cells generate current. Under the correct conditions, this current could be utilized to grow polypyrrole on the sample without any external current source. Besides the oxidizable pyrrole, a reducible species needs to be present during such experiments to equalize charges. In the literature, Kobayashi *et al.*^[145] and Yoneyama *et al.*^[146] reported successful oxidation of pyrrole and subsequent deposition of polypyrrole on illuminated samples of homogeneously doped n-Si using the reduction of Ag^+ -ions to elemental silver as the counter reaction. They report the simultaneous deposition of polypyrrole on the illuminated surface and silver on any defect sites on the substrate. This technique was subsequently adapted in this work as a means to selectively deposit either polypyrrole or silver, self-aligned to the buried implants. As the provided samples consist mainly of

epitaxial n-doped silicon, the general process is expected to be similar, while the buried implants induce additional effects upon illumination, leading to a change in the deposition behaviour, as illustrated in Figure 3.12. Illustrated is an increased deposition rate in areas without buried implants beneath.

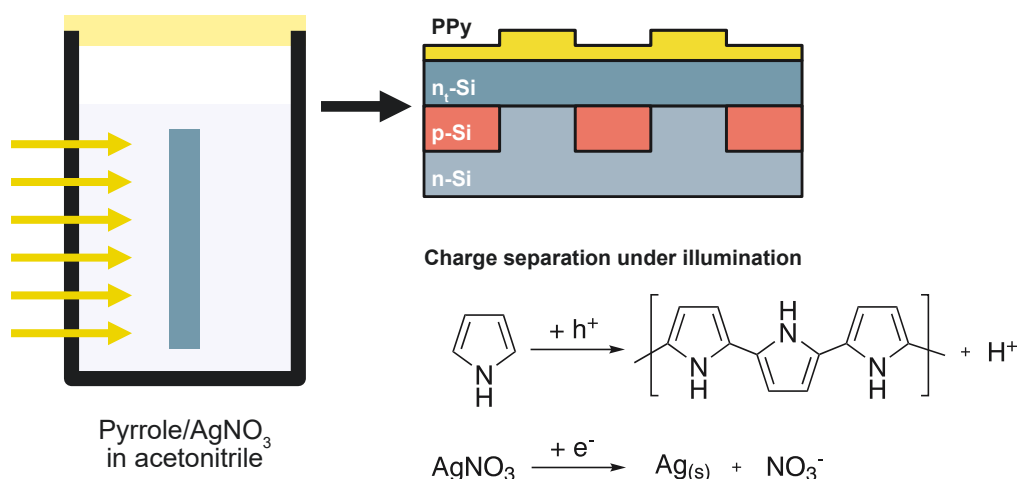


Figure 3.12: Illustration of the proposed light induced electropolymerisation of pyrrole, leading to variations in the polypyrrole deposition, in accordance with the buried implants. Besides polypyrrole, elemental silver is expected to be deposited, likely on unilluminated surfaces^[145,146].

The reaction was carried out initially on samples without top epitaxial layer, again to maximize any effect. The native oxide was removed and the samples immersed in a deoxygenated solution of 0.1 mol L⁻¹ AgNO₃ and 0.1 mol L⁻¹ pyrrole monomer in acetonitrile, while being illuminated. A photograph and light microscope image of one such sample after illumination from a fluorescent tube lamp for 60 min are shown in Figure 3.13a and Figure 3.13b, respectively. Immediately after removal of the sample from the reaction solution, a structure was visible on the surface in the form of darker

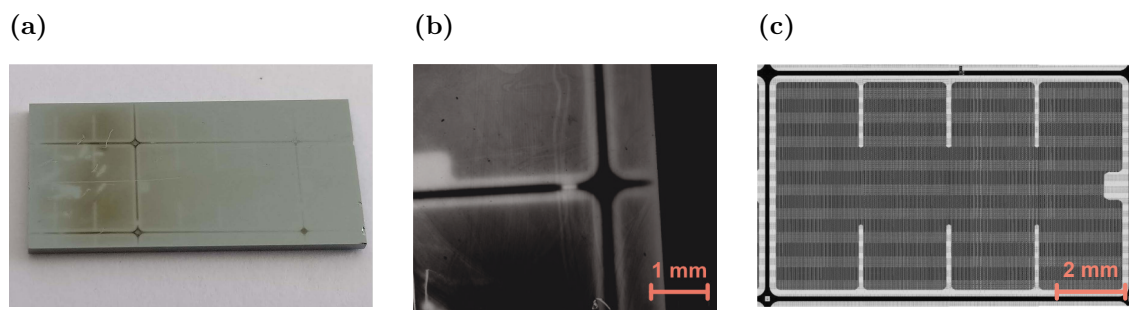


Figure 3.13: Photograph (a) and light microscope image (b) of a sample illuminated for 60 min with light from a fluorescent tube in a pyrrole/Ag⁺ solution in acetonitrile. (c) Mask layout showing the chip structure visible on the samples.

and lighter parts of a thin film. Overall three different shades are visible: a grid of dark lines, very light lines surrounding the grid lines and protruding into the grid interspace and lastly an area of medium shade filling the remaining area inside the grid. The same shading is clearly visible in light microscope images, as shown in Figure 3.13b. Each of these three regions can be matched to the different regions implanted into the sample and the overall structure fits the mask layout (see Figure 3.13c). The darkest grid lines represent the areas without any implant, i. e. only n-Si, the light lines immediately next to the dark lines coincide with those areas with small implants of $2.18\text{ }\mu\text{m}$ diameter, whereas the medium dark area represents all areas with the larger $4.36\text{ }\mu\text{m}$ diameter implants. As there is no other modification of the original samples with this structure besides the implant, this variation in the deposited film could only be induced by the differently doped silicon areas.

Besides the deposited polypyrrole film, residues of a silverish compound were visible on the edges of the substrates. As the polymerisation needs the reduction of Ag^+ as the counter reaction the most likely explanation for this is the deposition of elemental silver on these surfaces. This is in good agreement with the literature reporting silver deposition on defect sites^[145,146]. These initial results confirmed the general idea of deposition of polypyrrole via a photo-electropolymerisation. In further experiments, the optimal reaction conditions with regard to solution composition were determined. By separately varying the concentration of pyrrole as well as silver nitrate it could be shown that both are indeed necessary for a successful polymer formation. Without either no polymer is deposited on the surface and no patterning is visible.

The successfully patterned sample was investigated further with AFM in order to characterize the structure formed during polymerisation and why the differently shaded areas exist. One exemplary AFM image is shown in Figure 3.14a. From multiple images across the sample the layer thickness was determined as ranging from 12 nm in the areas with lighter deposition (right side in Figure 3.13a) to 35 nm where an overall darker layer was deposited (left side). Over the whole sample the roughness of the layer is $(3.8 \pm 0.7)\text{ nm}$, indicating a very smooth layer. In none of the three macroscopically different regions a height difference in accordance to the implant areas could be measured, despite the visually different layer properties. In order to achieve a successful structuring as a height difference, the experimental method was varied, mainly by using a different light source. The initially used fluorescent tube source was replaced with a 50 W halogen lamp which emits a continuous spectrum instead of the line spectrum of the fluorescent tube. This enables a higher activation of the apparent process, as the sample is illuminated by all possibly active wavelengths. Figure 3.14c

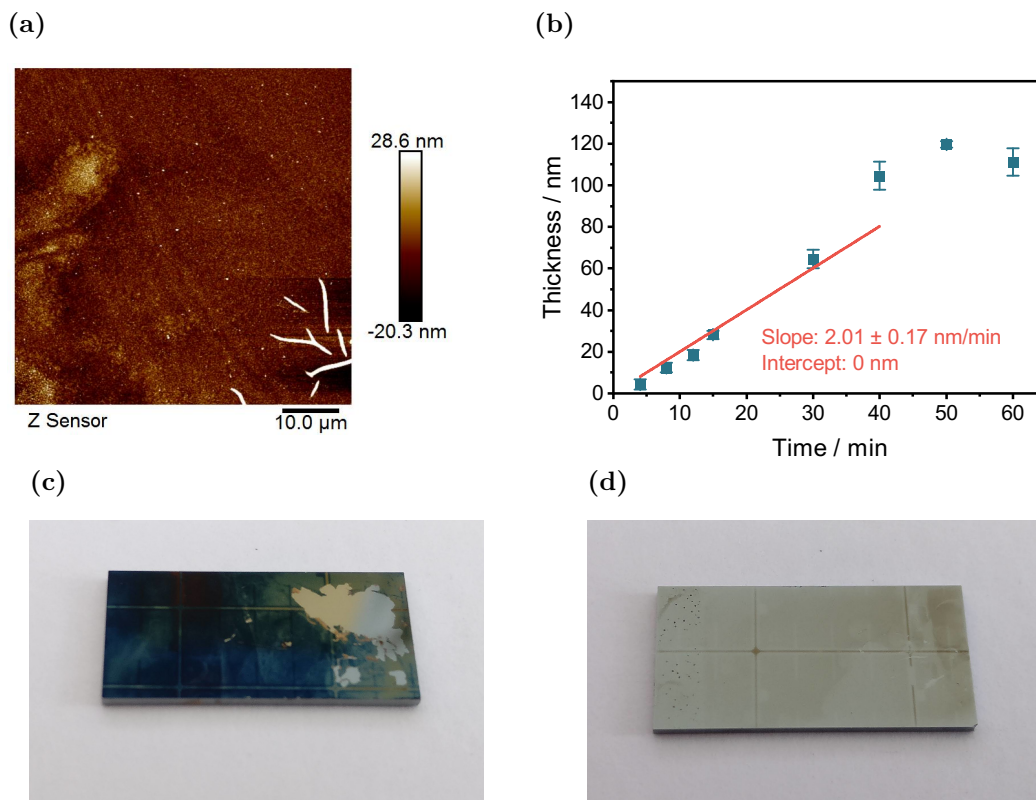


Figure 3.14: (a) AFM micrograph of a sample illuminated for 60 min with light from a fluorescent tube in a pyrrole/Ag⁺ solution in acetonitrile. (b) Graph of ellipsometric layer thickness over time for samples illuminated in pyrrole/Ag⁺ solutions. (c) Photograph of sample illuminated by halogen light in a pyrrole/Ag⁺ solution in acetonitrile for 60 min, (d) 15 min.

shows a photograph of a sample on which polypyrrole was deposited under the same conditions like before with the exception of the change in illumination source. As can be seen, this results in a much darker film, due to an increased thickness, which was measured from AFM as (104.5 ± 7.3) nm (Ellipsometry: (111.2 ± 6.6) nm). Notable on such samples was the tendency of the thicker film to detach from the surface during washing steps after the polymerisation. Apparently, a too large thickness decreases the adhesion, as is visible from the area of detached film in Figure 3.14c, revealing the bare silicon surface below. In order to yield samples closer to the previous realised results, the time of irradiation was reduced stepwise. One such sample with a irradiation time of 15 min is shown in Figure 3.14d. This sample is again much closer in visual appearance to the initial results with light from a fluorescent tube, showing the higher efficiency of the illumination with a halogen source due to a broader wavelength spectrum and an overall higher irradiance.

From the experiments with varying irradiation time some kinetic information can be

gained. Figure 3.14b shows a graph plotting the thickness of the polypyrrole layer, as measured with ellipsometry, against the irradiation time. The results show a linear increase in thickness of 2.01 nm min^{-1} for irradiation times of up to 40 min. Afterwards, the thickness remains constant, which can be explained by the decreasing adhesion of the film to the surface, leading to the detachment of thicker films.

During investigations of samples which were irradiated for 30 min or longer it became apparent that the samples did not only show structuring in accordance to the three different shades, as described before, but also shows smaller spots of varying shade corresponding in size and layout to the buried implants. Two light microscope images of such features are shown in Figure 3.15.

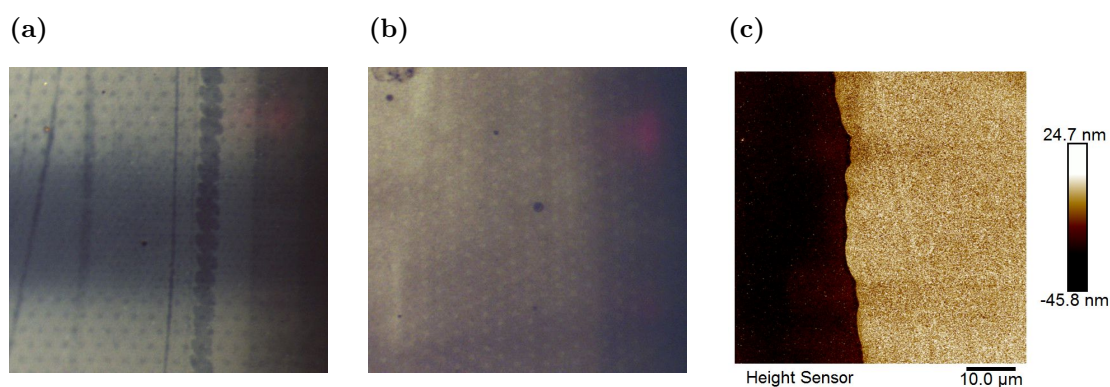


Figure 3.15: (a) Photograph of samples after polymerisation for 60 min, showing the reproduction of the implant layout, (b) 30 min. (c) AFM micrograph of a sample illuminated for 120 min showing minute height differences according to the implants.

These spots were not apparent on the whole surface, but only visible in some parts. Furthermore the appearance varied, specifically regarding if the spots are darker (Figure 3.15a) or lighter (Figure 3.15b) than the surrounding polypyrrole film. Upon AFM investigation it became clear that this structuring is again not due to a significant height difference in the polymer film. On most AFM images no difference at all was measurable, only some images showed a very minute height difference of 1 to 2 nm over the implant regions (see Figure 3.15c). To further analyse the film and determine the cause of the implant dependant colour deviation experiments with Scanning Electron Microscopy (SEM) and Transmission Electron Microscopy (TEM) were carried out.

SEM measurements showed that there is a visible patterning according to the implants in the film, recognizable as a darker ring on the perimeter of the implant area, as shown in Figure 3.16a. When using secondary electrons or back scattered electrons no contrast was visible, indicating no significant topography and material contrast, confirming the results from AFM height and phase images^[147]. The visible contrast in the InLens

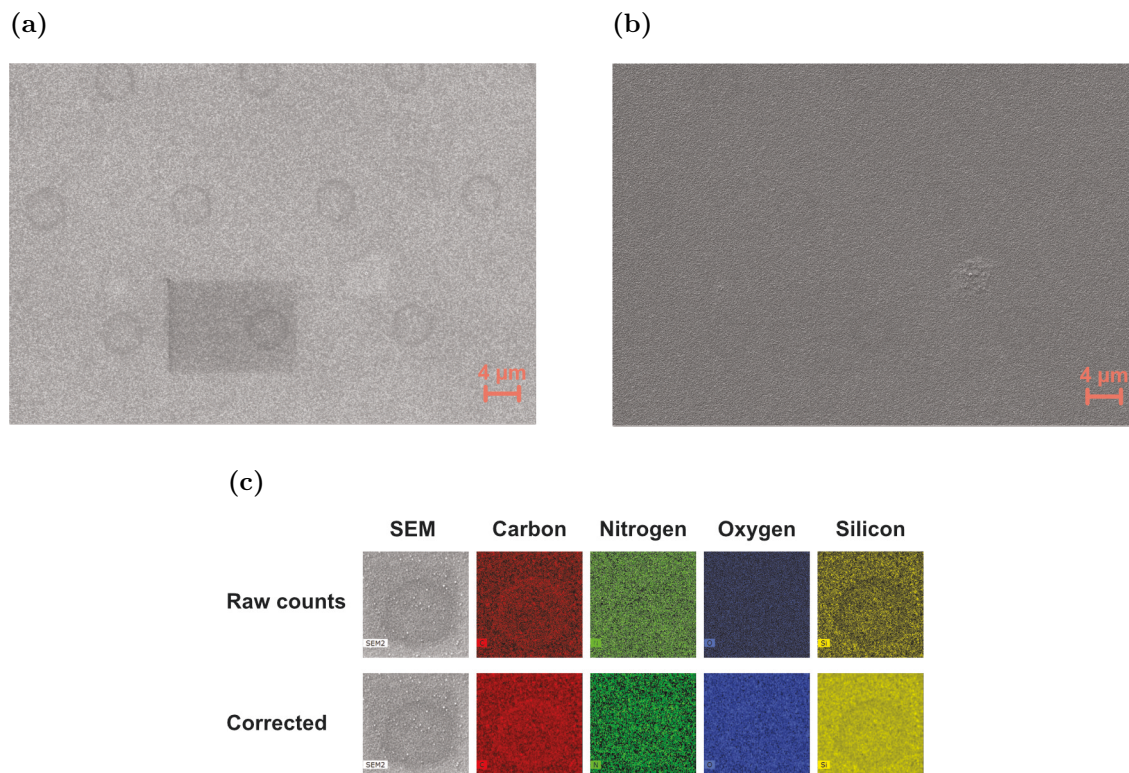


Figure 3.16: SEM and EDX mapping results for samples after light induced pyrrole polymerisation for 120 min. (a) SEM micrograph with InLens detector. (b) SEM micrograph with secondary electron detector. (c) EDX results for the same sample, showing detection for carbon, nitrogen, oxygen and silicon. The corrected measurement has been smoothed and the background was subtracted.

image can be due to differences in composition, electrical potential or conductivity, but no definite answer can be given from the SEM images alone. To test for differences in the composition of the polymer layer, Energy-dispersive X-ray spectroscopy (EDX) mapping was used. Such measurements are displayed in Figure 3.16c, showing detection for carbon, nitrogen, oxygen and silicon. A small difference in the carbon signal is visible, showing an increased signal in the ring above the implant. The silicon signal on the other hand was decreased inside the ring. For nitrogen and oxygen no significant difference is detectable. These results are most likely due to the slight difference in height that was measurable with AFM and which is barely visible in the secondary electron SEM image (Figure 3.16b). In the elevated regions the content of the interaction volume of the electron beam inside the sample is shifted upwards, therefore containing less silicon and more carbon. This can explain the visible contrast on some SEM images, but does not elucidate on the differences seen in light microscopy and by bare eye.

For further investigations of the material properties, TEM measurements were carried out. As TEM can not be done on the full thickness samples, the polymer film needed

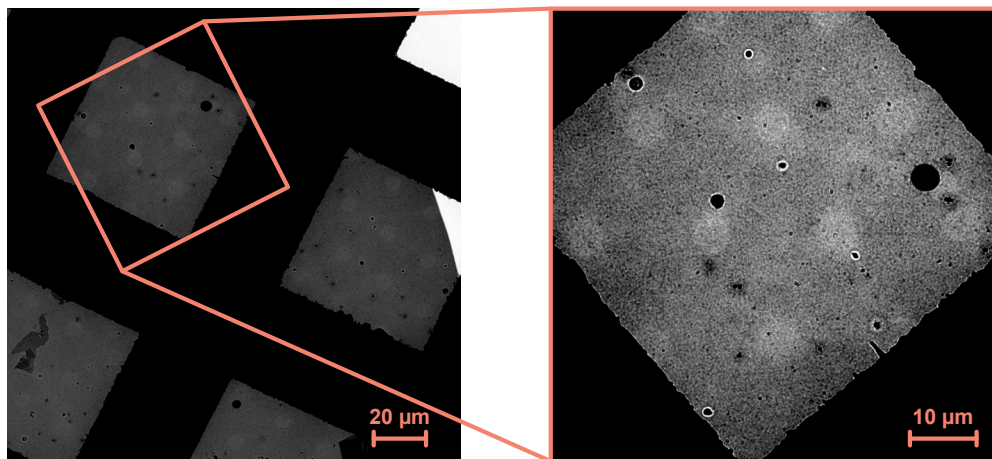


Figure 3.17: TEM micrographs of polypyrrole films removed from the silicon substrate showing the implant structure as bright circles. Contrast enhanced for clarity.

to be removed from the substrate. This was done either by washing samples, which partially removed the film on some samples and placing the washed off film flakes on a TEM grid, or, for stronger adhering films, by placing the sample in a KOH etch bath to partially remove the silicon and free the polymer film. The recovered film was then gently washed and placed on TEM grids. Two images taken from samples illuminated for 60 min are shown in Figure 3.17. These are of the same sample region at different magnifications. Both show evidence of the reproduction of the silicon implant region inside the polymer film. Specifically, lighter circles in the correct layout and size are visible. This indicates either a reduced thickness, contrary to SEM results, or reduced density, leading to a larger number of transmitted electrons. In combination with the SEM results it seems most probable that the visible difference reproducing the implant layout is due to variations in mostly density with a small contribution due to thickness. One explanation for this variation can be a different doping of the conductive polymer layer during the electrochemical reaction. Depending on the underlying Si-doping the resulting doping level of the polymer layer varies. This difference in doping would in turn lead to variations in conductivity, manifesting as image contrast in SEM InLens measurements (see Figure 3.16a). Furthermore, this would alter the absorption properties of the polymer film, explaining the visible variation in shading, as shown in photographs and light microscopy images.

Following these explanatory investigations, the photo-electropolymerisation was carried out on samples with top epitaxial layer to investigate the suitability of the patterning process for the application of self-alignment over buried implants. Unfortunately, no selectivity could be established on these samples, even at the lowest epitaxial layer thickness of 250 nm. It was again possible to nicely deposit polypyrrole on the illuminated

surface, as well as silver particles on the edges of the sample, but no sample showed the reproduction of the macroscopic or even microscopic structure. For two such samples light microscopy images are shown in Figure 3.18.

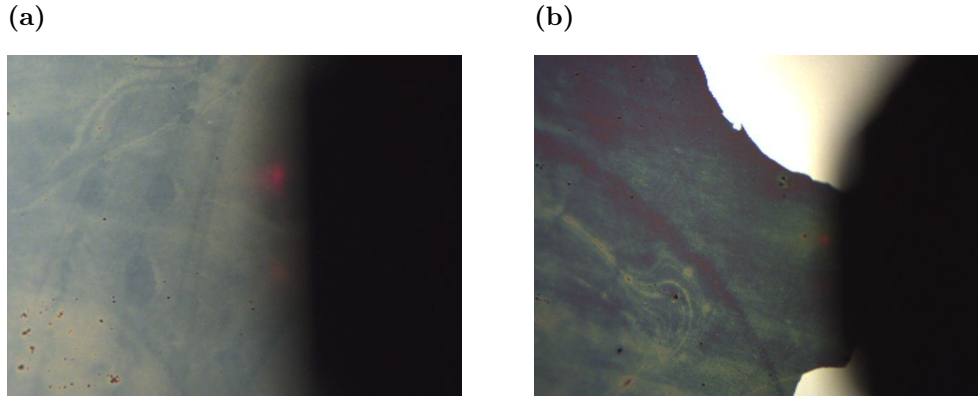


Figure 3.18: Micrographs of samples with 250 nm top epitaxial layer after polymerisation, showing no implant layout reproduction. (a) 60 min, (b) 120 min.

As can be seen, the film is similar to the result on samples without top epitaxial layer, differing only in the fact that no structuring is visible. Various samples were prepared in order to realise structuring, but no further improvements were possible. It appears, that the epitaxial layer prevents the selective process by screening the effect, so that the polymerisation takes place like it would on completely homogeneously doped samples.

3.3.4 Summary

In summary, even though the goal of selective deposition could not be achieved, the electropolymerisation of pyrrole enabled the homogeneous covering of the sample surface with covalently attached polypyrrole via a relatively simple process. A thick layer of the polymer was detected in AFM images (Figure 3.19a) and the results are overall in good agreement with experiments reported in the literature^[78,79,93]. For covalently attached films, the results even show improvements in the film roughness, compared to previously reported results^[77]. It appears though, that the measured resistance difference in the samples is not high enough to pattern the polymer film in accordance with the structure of the buried implants. In further experiments it was possible to repeat results reported in the literature regarding the photo-electropolymerisation of polypyrrole on doped silicon substrates. The reaction leads to the formation of a homogeneous film over the whole surface and the deposition of silver particles on the edges. On samples without the top epitaxial layer, where the p-implants are immediately at the sample surface, a clear structuring of the polymer layer was possible, directly reproducing the layout

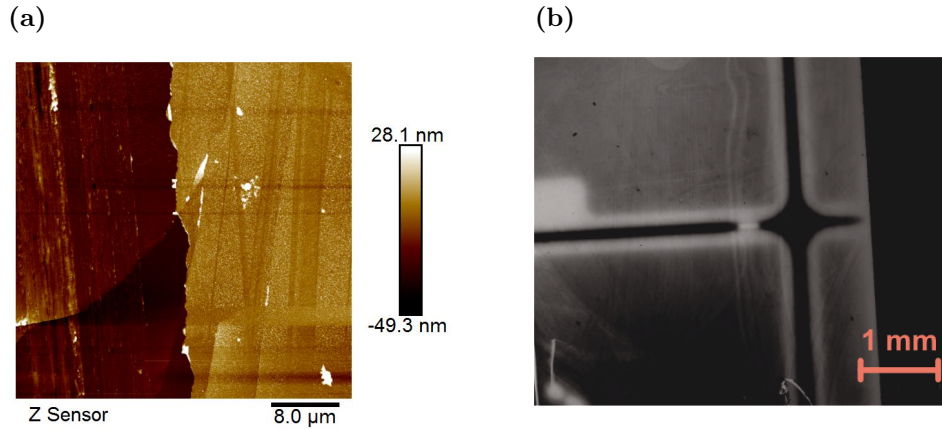


Figure 3.19: (a) AFM image of polypyrrole film electropolymerised via cyclic voltammetry. No structure is visible. (b) Light microscopy image of polypyrrole film electropolymerised via light illumination. The macroscopic implant structure is clearly reproduced.

of the implants (see Figure 3.19b). This was visible by light microscopy, SEM, TEM and partially AFM. No structuring in film thickness was measurable, but the conducted measurements lead to the conclusion that the apparent structure is most probably due to variations in doping of the conductive polypyrrole during the electropolymerisation. This result might prove useful for the fabrication of conductive polymer films with structured doping, as used in organic electronic applications. Here, the varying doping levels could be used to produce electronic devices in the organic thin film^[148–151].

Upon carry-over of the light induced polymerisation process to samples with top epitaxial layer, polymerisation was again successful, but no structuring could be observed. It stands to reason, that the resistance difference measured with SSRM is strong enough only on samples without the homogeneously doped epitaxial layer on top. On samples with this layer, the difference is too small to impact the polymerisation process in a way that yields a structured polymer film.

3.4 Light Induced Selective Etching - LISE

3.4.1 Introduction

As no successful self-alignment was possible using the previously described methods, further experiments were planned in order to improve the observed results. While preparing and cleaning one particular sample batch, the substrates were, as usual, stored in ultrapure water, immediately after the Standard Clean 1-step, which consists of treatment in a 5:1:1 mixture of $\text{H}_2\text{O}:\text{NH}_4\text{OH}:\text{H}_2\text{O}_2$ at 60°C for 20 min. After four days of storage, when samples were taken for further experiments, it became obvious that some samples were unexpectedly structured, as visible on the photograph in Figure 3.20b, perfectly replicating the chip structure shown in Figure 3.20c.

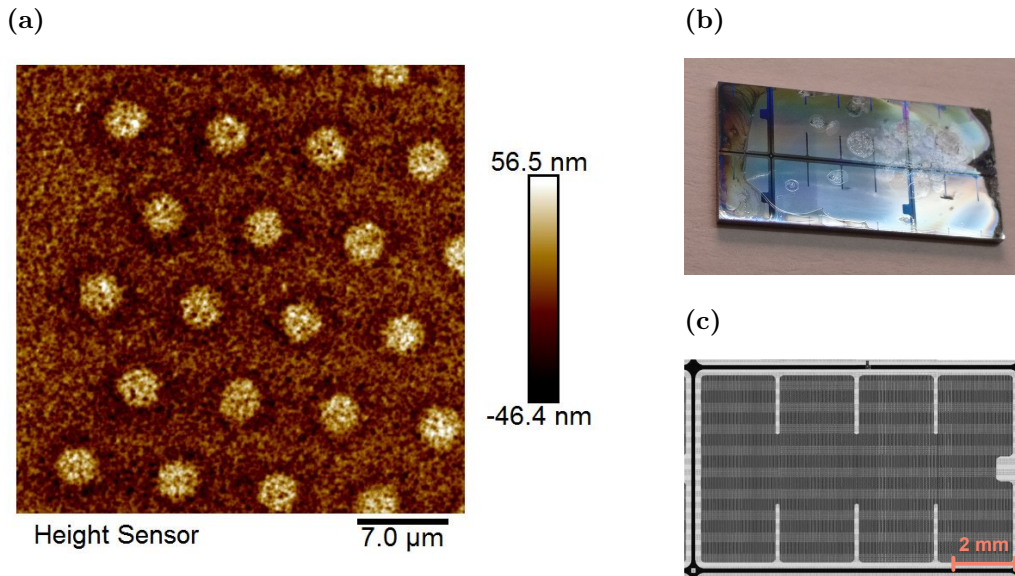


Figure 3.20: Analysis of sample showing patterning after cleaning with Standard Clean 1 and storage in ultrapure water. (a) AFM height image. (b) Photograph of visible structure, showing chip structure. (c) Mask image of the chip structure.

It appeared, that only those samples, which were oriented towards the brighter front of the laboratory showed the structuring. This partial illumination therefore seems to play an important part. All samples in this batch did not have a top epitaxial layer, meaning that the implants were immediately at the sample surface. Upon investigation with AFM, the image in Figure 3.20a was taken, clearly showing a structuring as a height difference. The structure of the implants is replicated as small dots oriented after the hexagonal pattern of the implantation mask. The dots are of increased height, protruding around 30 nm from the surface. The diameter of the dots of around $3.3\mu\text{m}$ and the distances between the dots suggest that these represent the smaller diameter

implants. From the AFM results it appears reasonable that either a deposition of some material took place selectively over the implant areas, or that an etching process removed the parts surrounding the implants. From the overall appearance of the samples, and the surface roughness before and after it was deduced, that an etching process is likely responsible. The surface roughness of the areas around the dots is around 10 nm Root mean squared (RMS), as compared to around 300 pm immediately after cleaning. As the samples were stored in ultrapure water, it was not immediately obvious what had induced this etching process. After analysing the cleaning steps, consisting of ultrasonic cleaning in various solvents and the subsequent Standard Clean 1, it was determined that the most likely reason for the observed etching are traces of NH_4OH remaining in the storage solution. It is known that alkaline solutions, in contrast to the other cleaning components, can etch silicon even at low concentrations, albeit with a slow etch rate. This also explains the long time before the structure was visible on the samples. This hypothesis could be confirmed after a number of tests, showing that etching in NH_4OH -solutions leads to patterning of the substrates, if the samples are illuminated with a 50 W halogen lamp at the same time. Partial illumination during the sample storage was hypothesised previously for the reason while only some and not all of the samples showed evidence of this structuring.

From these unexpected results, it appears that the variation in doping on the sample surface can be exploited for selective etching under light illumination in basic solutions. In order to further characterize this process and investigate its suitability for self-alignment above buried implant structures, more experiments were conducted. Initially, samples without top epitaxial layer were again used in order to study the apparent effect.

3.4.2 Self-Replication of Implant Structure through Selective Etching

After it could be determined which process leads to the visible structuring of the samples further investigations were performed to determine the cause of the structuring and how it can be influenced. First, simple time dependence experiments were conducted by immersing samples in dilute NH_4OH -solutions (0.6 wt%) for 20 min, 40 min and 60 min, respectively. During these time intervals the samples were illuminated as before with a 50 W halogen broadband lamp. The reaction initially proceeded without any visible change to the sample. Only after an induction time of around 10 min the surface appearance changed, looking more rough. Simultaneously, gas bubbles evolved from the sample, presumably hydrogen gas released during the etching. During this time the macroscopic chip structure also became visible on the surface. For a sample with 20 min overall etching time AFM images of the resulting structures are shown in Figure 3.21a and Figure 3.21b.

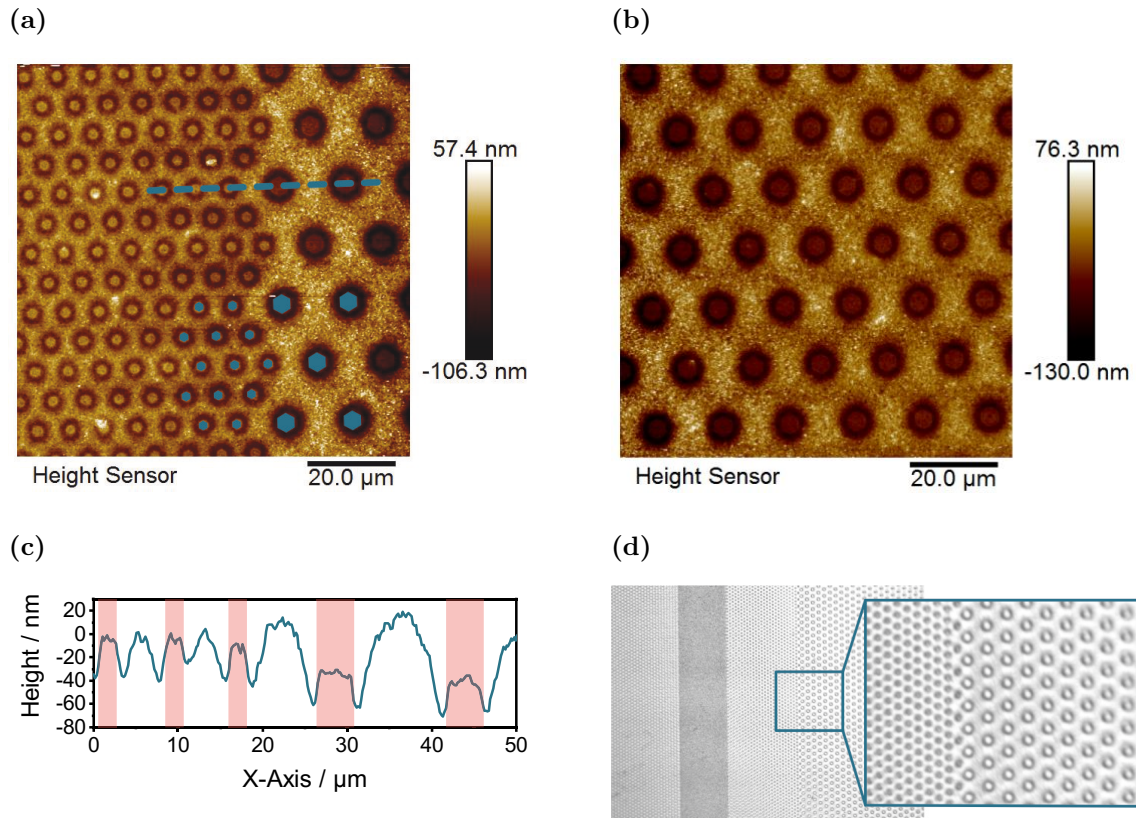


Figure 3.21: Etching results for a sample without top epitaxial layer etched under illumination for 20 min. (a), (b) AFM height images showing strong selective etching as rings and pillars located at the p-Si implants (c) Cross section taken from (a). The areas marked in red represent the regions with p-type implant underneath. (d) Light microscopy images showing an overview of the resulting structure.

The images show that the etching process leads to the reproduction of the implant areas as height differences. The hexagonal layout of the implants can be seen as indentations into the surface with rings around it which are etched even deeper. The overlay of the implant structure on Figure 3.21a shows the perfect localisation of the etched features in accordance with the implants. Overall, three differently etched areas can be found: First, the area without underlying p-Si implants appears the least strongly etched, constituting the highest point for each image. Next, directly above the p-Si implants the height is significantly lower, presumably due to faster etching in these areas. Lastly an even stronger etch effect can be found as rings immediately around the p-Si implants. For further clarification, a cross-section taken from Figure 3.21a is shown in Figure 3.21c, where the areas with underlying implants are marked in red. For the larger implants the measured height difference between the area directly above the p-Si and the bulk n-Si areas is (57.8 ± 7.2) nm and for the ring and the bulk n-Si it is (84.5 ± 8.8) nm. The actual diameter of these pillars inside the area of deep etching is $4.22 \mu\text{m}$ (-3% from the reference value) at the top and $5.04 \mu\text{m}$ ($+16\%$) at the bottom. This means, that the sidewalls of the pillars are not perfectly vertical, but have a small angle, which can be calculated as 8.2° . This deviation is too small to be due to anisotropy of the silicon etch rate, for which an angle of 54.7° on (100)-Si is expected (see section 1.2.2). As the top parts of the columns are exposed to the etchant longer and have a larger surface area in contact with the etchant, the difference in diameter is most likely due to increased etching at the top.

For the smaller implants, the height difference between the center, above the implants, and the area with pure n-doping is small, measuring only (5.8 ± 1.9) nm, meaning that effectively these areas are level. Only the ring is etched deeper into the silicon with an etch depth of (36.2 ± 3.4) nm. As for the diameter, the pillars inside the ring are $2.16 \mu\text{m}$ (-1%) at the top and $3.22 \mu\text{m}$ ($+48\%$) at the bottom. As before this small sidewall angle of 4.1° can be explained by the difference in exposure time and exposed surface area to the etchant. On AFM phase images (see Appendix, Figure A.3a) no contrast between the differently etched areas was found, indicating no material contrast. Accordingly, it appears the variation in etch-rate was not externally influences, e. g. via an etch mask, except for the illumination. On other samples with longer overall etch time, e. g. 40 min and 60 min, it was visible that the structuring was destroyed with further etching. After 60 min the structure was only barely visible, indicating that lower process times are preferable. Therefore, 20 min was chosen as the process time for further experiments.

As is visible in the illustrations of the sample cross section (Figure 3.1a) pn-junctions exist between the p-implants and the surrounding n-type bulk. In the theoretical part,

the high sensitivity of pn-junctions to illumination, e. g. by a 50 W halogen lamp, leading to the formation and separation of charge carriers, was described. It stands to reason that these carriers, electrons and holes, could potentially influence the etch reaction, as was demonstrated in the literature via bias-controlled etch stop techniques (see paragraph 1.2.2). In a first step to investigate this further, the theoretical width of the pn-junction was compared to the deeply etched rings around the p-implant areas, as seen in Figure 3.21a. As described in section 1.3.1, in order to calculate the theoretical width W_d , the built-in voltage V_0 first needs to be calculated via:

$$V_0 = \frac{kT}{q} \ln \left(\frac{N_A N_D}{n_i^2} \right) \quad (3.1)$$

$$= \frac{1.38 \cdot 10^{-23} \text{ J K}^{-1} \cdot 300 \text{ K}}{1.602 \cdot 10^{-19} \text{ A s}} \ln \left(\frac{2 \cdot 10^{15} \text{ cm}^{-3} \cdot 4 \cdot 10^{14} \text{ cm}^{-3}}{10^{20} \text{ cm}^{-6}} \right) \quad (3.2)$$

$$= 0.589 \text{ V} \quad (3.3)$$

with k being the Boltzmann constant, T the temperature, q the elemental charge, N_A the acceptor doping concentration, N_D the donor doping concentration and n_i the intrinsic carrier concentration of silicon^[67]. With the obtained result, the depletion width can then be calculated as

$$W_d = \sqrt{\frac{2\epsilon_{Si} V_0}{q} \left(\frac{1}{N_A} + \frac{1}{N_D} \right)} \quad (3.4)$$

$$= \sqrt{\frac{8.854 \cdot 10^{-12} \text{ A s V}^{-1} \text{ m}^{-1} \cdot 11.9}{1.602 \cdot 10^{-19} \text{ A s}} \cdot 0.589 \text{ V} \cdot \left(\frac{\text{cm}^3}{2 \cdot 10^{15}} + \frac{\text{cm}^3}{4 \cdot 10^{14}} \right)} \quad (3.5)$$

$$= 1.52 \mu\text{m} \quad (3.6)$$

where ϵ_{Si} is the permittivity of silicon. As the doping levels are not equal, the junction is not equally distributed between p- and n-Si, but shifted towards n-Si due to the higher level of p-doping. The proportion of the depletion region stretching into each region can be calculated via these equations^[67]:

$$x_n = W_d \frac{N_A}{N_A + N_D} = 1.52 \mu\text{m} \cdot \frac{2 \cdot 10^{15}}{2.4 \cdot 10^{15}} = 1.27 \mu\text{m} \quad (3.7)$$

$$x_p = W_d \frac{N_D}{N_A + N_D} = 1.52 \mu\text{m} \cdot \frac{0.4 \cdot 10^{15}}{2.4 \cdot 10^{15}} = 0.25 \mu\text{m} \quad (3.8)$$

This results in the depletion region stretching out into the n-Si over 1.27 μm and into the p-Si over 0.25 μm . From Figure 3.21b the width of the deeply etched ring can be measured as $(1.31 \pm 0.13) \mu\text{m}$, fitting well to the expansion of the depletion region in-

side the n-Si volume. This indicates that the variation in etch rate depending on the underlying doping state correlates to the depletion region and potentially its behaviour upon illumination. Photons with energy higher than the band gap of silicon ($E_g = 1.12 \text{ eV}^{[67]}$), meaning with wavelength shorter than 1100 nm, are able to excite electrons from the valence band to the conduction band, therefore generating electron-hole pairs in the crystal lattice. If these carriers are generated in or close to the junction, they will be swept into the corresponding doping region (i. e. electrons to n-Si, holes to p-Si), due to the built in electric field. This changes the concentration of majority carriers in the p- and n-type regions, without changing the concentration of dopant ions in the crystal lattice, creating a charging effect, as illustrated in Figure 3.22^[67–69]. These charging effects can potentially influence the etching behaviour via electrostatic attraction and repulsion. The increased etch rate on the p-type area is due to the negatively charged OH^- ions being attracted to the positively charged p-Si surface, leading to a locally increased etchant concentration and higher etch rate. Conversely, over the n-type silicon the negative charge repels the etchant ions, decreasing the local concentration and therefore etch rate. The highest etch rate inside the ring on the other hand can not easily be explained by charging effects due to majority charge carriers, as these are constantly swept into the quasi neutral regions and only the fixed dopant ions remain inside the junction region. The n-type part contains positively charged phosphorus ions and the p-type part negatively charged boron ions. As measured from AFM images, the deeply etched ring is in good agreement with the dimension of the depletion region inside the n-type bulk of the substrate. Here the large abundance of fixed, positively charged phosphorous ions can increase the local etchant concentration and consequently the etch rate via electrostatic attraction, similar to the effect due to holes on the bulk

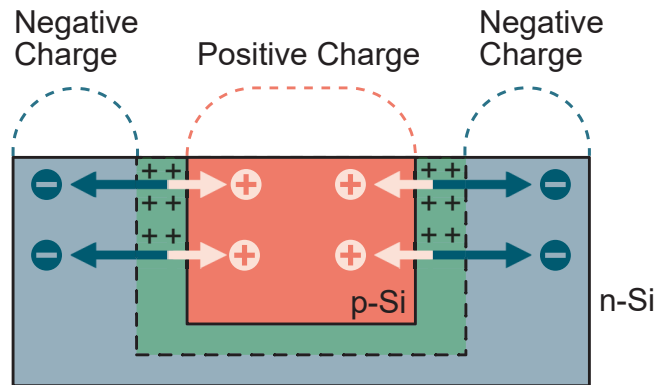


Figure 3.22: Model representation of proposed mechanism responsible for etch selectivity in basic etchant under illumination. The depletion region is shown in green, separating electrons and holes to p- and n-Si respectively. Here, the charging effects due to carrier accumulation change the etch behaviour at the surface.

p-type surface, but to a greater extent.

Subsequent experiments were carried out to determine how the various conditions change the resulting structure. Firstly, samples were etched under identical conditions as before, but in dark under exclusion of any light source. At room temperature, no etching was observed within the same time frame as before. In contrast, at elevated temperature of 40 °C, chosen as the measured temperature inside the etching solution after 15 min of illumination with a 50 W halogen lamp, again selective etching was observed, albeit with a greatly differing resulting structure, exemplary shown in Figure 3.23.

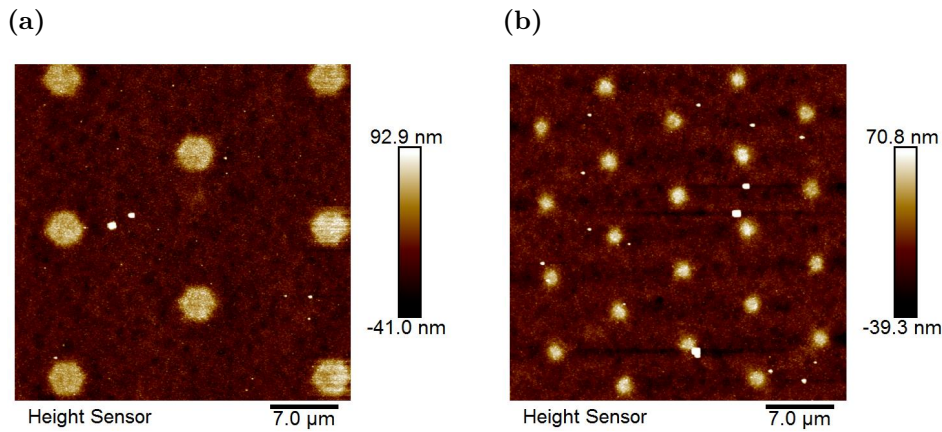


Figure 3.23: AFM images of a sample etched under full light exclusion at 40 °C for 20 min. (a) 4.36 μm implants, (b) 2.18 μm implants. The sample shows clear evidence of p-Si etch stop like etching.

This type of etching under light exclusion but at elevated temperature results in the formation of columns or pillars in the areas where the p-implants are located, i. e. the area without p-implants is selectively removed. This result is in good agreement with the expected result on a sample exhibiting p-Si etch stop behaviour (see paragraph 1.2.2). In Figure 3.23a, the columns of mostly p-silicon on the surface are (56.1 ± 4.0) nm high with a diameter of 4.34 μm (-1%) at the base. The etching did not result in a very large height difference, but a clearly measurable, repeatable structuring. The general layout of the pillars is a precise reproduction of the implant layout and the size of the columns at the base is very close to the reference value of 4.36 μm, based on SSRM images. Notably, the diameter of the columns changes towards the top, resulting in a mean diameter of 3.56 μm (-18%). This is possibly due to the upper parts of the columns being less stable as they have more surface area and longer exposure to the etchant compared to the lower parts. A similar result can be found for the smaller implants, as shown in Figure 3.23b. Here the mean height is (64.4 ± 3.6) nm with 2.14 μm (-2%) base diameter and 1.64 μm (-25%) top diameter. Generally the results from these experiments are in agreement

with the typical p-etch stop behaviour, indicating no other influence on the etching. In particular these experiments show that the results achieved from experiments with illumination are not due to the heating of the reaction solution alone, as this yields an entirely different result.

Continuing from these results, it was investigated, if the structuring result seen in Figure 3.21 is possible with illumination at room temperature, excluding the heating due to the halogen light source. For this, the etching solution was cooled during the illumination inside a beaker with cold water. Within a similar time frame as before (10 to 20 min), no etching and specifically no structuring was observable for such experiments, demonstrating that illumination as well as heating is necessary to achieve the initially shown structuring result.

As noted before, all samples were covered with around 1.3 nm of native oxide after the cleaning steps. In order to investigate if this layer plays a role for the observed etch selectivity, it was removed from some samples immediately prior to the etching experiment, otherwise carried out under identical conditions as before. Removal of the native oxide layer was achieved with a dip in a Buffered Oxide Etch (BOE, 7:1 $\text{NH}_4\text{F}:\text{HF}$) solution. After placing these samples in the etching solution, immediate evolution of gas bubbles and change in surface reflectivity was visible, indicating that the etching starts without the induction period seen on samples with native oxide. The macroscopic structure was not immediately visible on these samples, but AFM images show a structured surface, as illustrated in Figure 3.24. Due to the high reactivity of the bare silicon in the basic etchant large pits and surface irregularities are formed as well, overlaying parts of the structure. Due to this, the structuring can not be found over the whole surface, but only in certain spots.

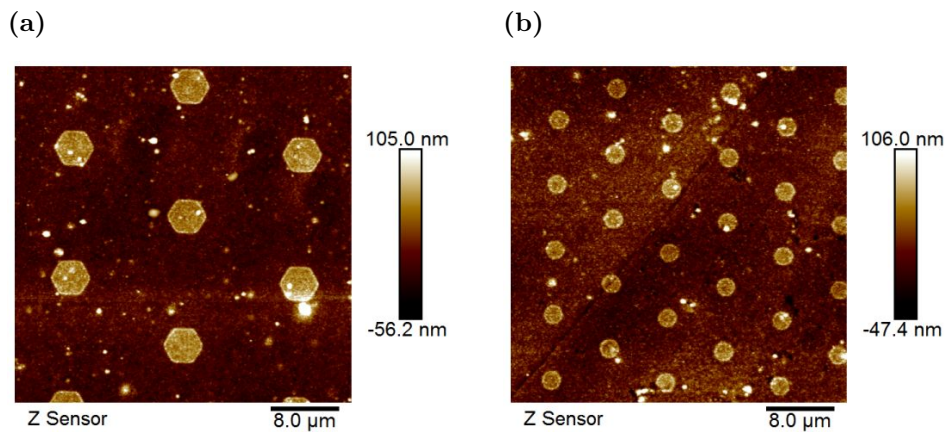


Figure 3.24: AFM images of a sample without top epitaxial layer and removed native oxide layer etched under illumination for 10 min. (a) 4.36 μm implants, (b) 2.18 μm implants. The sample shows clear evidence of p-Si etch stop like etching.

The AFM images show, that these samples are etched in a p-etch stop-like manner as well, visible as pillars of p-Si with the surrounding n-Si being etched away. The etch depth here is (60.4 ± 2.3) nm for the larger implants and (48.2 ± 4.9) nm for the smaller implants. The diameter of the large pillars is $4.60\text{ }\mu\text{m}$ (+5 %) at the top and $4.72\text{ }\mu\text{m}$ (+8 %) at the bottom. For the smaller implants these values are $2.37\text{ }\mu\text{m}$ (+9 %) and $2.46\text{ }\mu\text{m}$ (+13 %) at the top and bottom, respectively. Again the resulting sidewall angles are likely not due to crystallographic reasons, but exposure to the etchant. As a control experiment, further samples were also etched in dark, after the BOE removal of the native oxide layer. Here, the same p-etch stop-like structure was achieved, indicating that illumination does not significantly influence the etching result, if no native oxide layer is present.

These experiments clearly show the necessity of a native oxide layer on the surface in order to achieve the selective etching, as seen in Figure 3.21. Without such a layer, selective etching is still possible, but the resulting structure is not due to the illumination, but solely due to the abundance of p-dopant atoms, i. e. an etch-stop effect. It appears that the charge effect induced by the illumination can not efficiently act upon the silicon alone, but influences the etching behaviour by altering the oxide layer. Possibly, the Si-OH bonds on the silicon surface are able to successfully project the charging effect in a way that repels the etchant ions, whereas the same is not possible on bare silicon. Additionally, silicon oxide is known to etch very slow in alkaline solutions, compared to bare silicon, allowing for the usage of silicon oxide as an etch mask^[39,152–156]. The charging effect induced by illumination then presumably reduces the oxide stability in the areas with p-Si implants, whereas the surrounding areas of n-Si are protected and etched even slower. This essentially creates a quasi-mask of native silicon oxide self-aligned in accordance with the buried implants. With this information, the initially proposed mechanism can be extended to include the silicon oxide layer, as shown in Figure 3.25a. Additionally shown in Figure 3.25 are the proposed steps resulting in the formation of the observed structure. In the first step, as described before, the illumination leads to the evolution of charging effects on the differently doped areas (Figure 3.25b). Directly above the implants, generated holes induce a positive charge, which can attract etchant ions, thereby weakening the native oxide layer in this region. On surface areas which cover the extent of the pn-junction, particularly the part in the n-Si region, fixed positive charges act on the oxide layer in the same way, only to an apparently larger extent. Lastly, in the surrounding n-type area, electrons induce a negative charge, which repels etchant ions and subsequently enhances the oxide stability. This spatial difference in stability then leads to different etch speeds of the native oxide

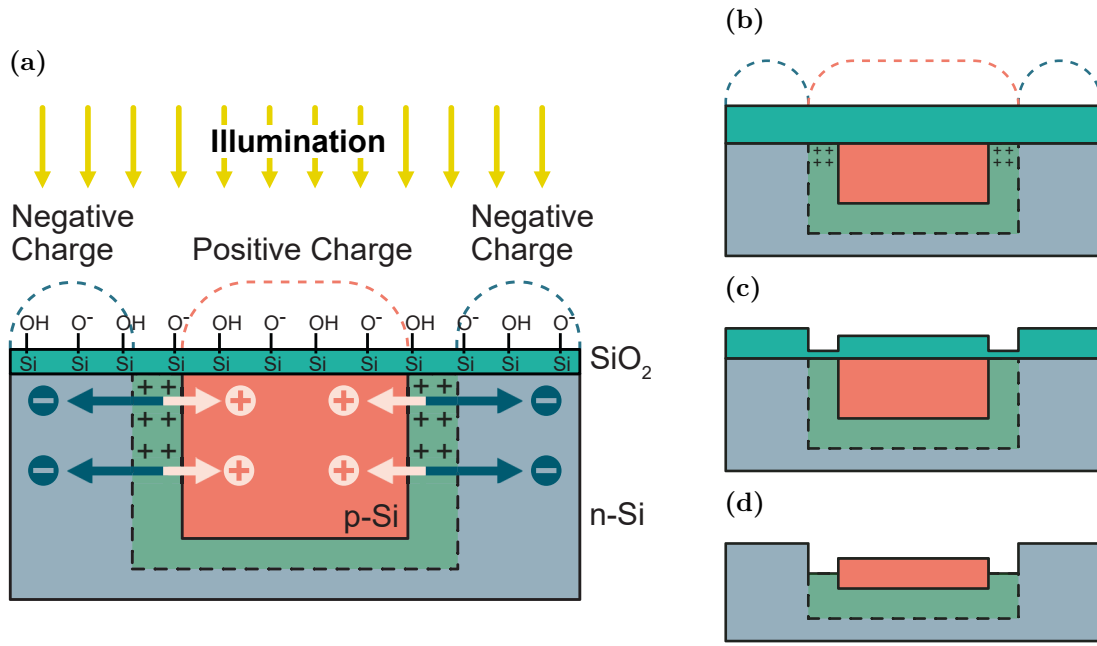


Figure 3.25: (a) Model representation of proposed mechanism responsible for etch selectivity in basic etchant under illumination with native oxide layer. (b) to (d) Process steps for the generation of the observed structures: (b) Generation of charges, modulating the oxide stability, (c) Removal of the native oxide layer at different speeds, (d) Etching of silicon, controlled by the oxide quasi-mask.

layer in the etchant solution, creating a in-situ masking aligned with the implants. Due to the varying time it takes to remove the oxide layer from the different regions, these regions are subsequently etched for varying times, resulting in the evolution of the observed height difference, replicating the structure of the p-Si implants.

3.4.3 Self-Replication via Etching with Implant Structure Buried Under a Homogeneous Epitaxial Layer

After this new selective etching effect, named Light Induced Selective Etching (LISE), was characterised extensively on samples with different doping regions immediately at the surface, the next step was to investigate the effect on samples with the implants buried beneath a homogeneous n-type silicon layer. For this, various samples were available, either with differing size of the implants or with different top epitaxial layer thickness (see section 3.1).

First, samples with the same implant structure as before, but with 250 nm top epitaxial layer were investigated. Applying the same etching process in a 0.6 wt% NH_4OH -solution under illumination by a broadband halogen lamp for 20 min again an immediately visible structuring was achieved. The sample appeared visually very similar to the

previous results and investigation with AFM and light microscopy yielded the images shown in Figure 3.26, showing a different reproduction of the buried implant structure compared to the previous results.

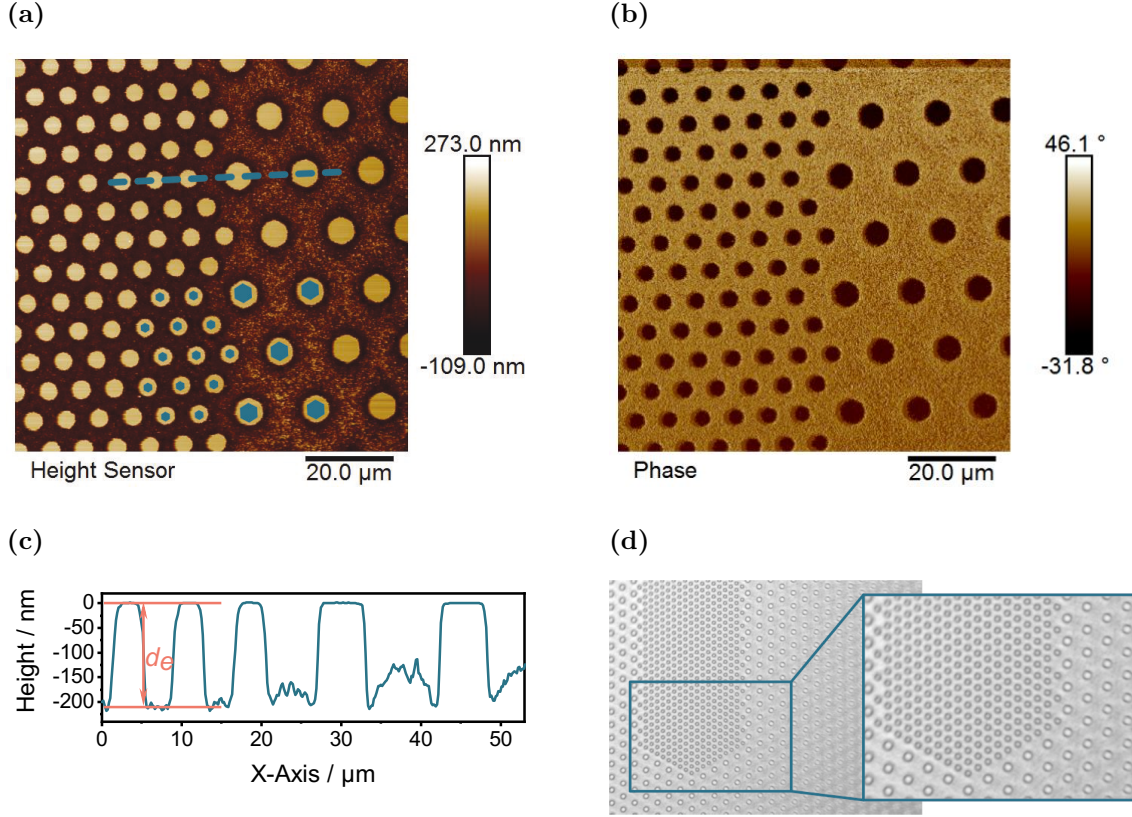


Figure 3.26: Etching results for a sample with 250 nm top epitaxial layer etched under illumination for 20 min. (a) AFM height image showing the implant reproduction as columns. The overlay at the bottom shows the alignment of the pillars in accordance with the implant structure. (b) AFM phase image showing the phase contrast between the top of the columns and the surrounding area. (c) Cross section taken from (a), showing exemplary how the etch depth d_e was determined from AFM images. (d) Light microscopy images showing an overview of the resulting structure.

The structure of the buried p-Si implants is clearly reproduced as columns, while the surrounding area is etched with high selectivity, similar to the previous results showing a p-Si etch-stop. In contrast to these previous results, the samples etched here were completely homogeneous in regards to the surface doping. This means, that the visible result is not simply due to an etch-stop effect. Both implant sizes are well resolved and differentiated from the surrounding material over a large area, as light microscopy images at smaller magnifications (Figure 3.26d) show. For the used sample size of $20 \times 20 \text{ mm}^2$ the process resulted in very even self-aligned etching over the full area. From the overlay

of the implant structure in Figure 3.26a, it can be seen that the column structure is exactly overlayed, albeit with an increase in the diameter of the structures. Noticeably, the etched area around the larger implants is less deeply and homogeneously etched, compared to the area around the smaller columns. This is also evident on the cross section seen in Figure 3.26c and it becomes clear that a thin area surrounding the large columns is etched deeper, visible as a ring, similar, but less pronounced, to the results from samples without any top epitaxial layer. This ring is level with the etched area between the smaller columns. The etch depth, measured as illustrated in Figure 3.26c as the difference between the top pillar surface height and the mean bottom surface height, for the ring around the larger columns and the area between the smaller columns are (193.0 ± 6.6) nm and (205.0 ± 5.9) nm, respectively. In contrast, the height difference between the top of the larger pillars and the area outside the deeply etched rings around the larger columns is only (135.0 ± 15.4) nm. It appears that the etching is slightly faster immediately around the columns, compared to the remaining areas. Between the smaller columns, no rings are visible, possibly because the distance is small and the areas of higher etch rate overlap. Accordingly, the whole area between the smaller columns etches evenly. As the thickness of the top epitaxial layer on these samples is 250 nm, the structuring here protrudes deep into this layer, almost penetrating through it. As for the diameter of the columns, the smaller ones are larger than the theoretical value at $3.93 \mu\text{m}$ (+80 %) and $4.61 \mu\text{m}$ (+111 %) at the top and bottom, respectively. For the larger pillars these values are $6.00 \mu\text{m}$ (+38 %) for the top and $6.73 \mu\text{m}$ (+54 %) for the bottom diameter. The selectivity inducing effect therefore is not confined precisely by the dimensions of the implants, but can influence a larger surface area. As the larger implants are exactly twice the diameter of the smaller ones it becomes apparent, that the absolute increase in diameter is essentially identical, regardless of the implant size. Another notable feature of the resulting structure is the top surface of the columns, which is very flat with a low roughness below 2 nm RMS. Additionally, from AFM phase images (Figure 3.26b) a strong contrast can be found between the top surfaces and the surrounding etched areas, indicating a material contrast. This suggests that the top surface retains the native oxide layer, which shows a similarly low roughness prior to etching experiments. This notion was further supported by simple masked experiments, where one half of the sample was protected from the etchant solution with a thin polystyrene film. After the etching process, these samples showed that the top of the columns is level with the original, unetched surface, as illustrated in Figure 3.27.

To summarize, during the light-induced selective etching achieved on this sample, the area directly above the buried implants etches negligibly slow, whereas the surrounding

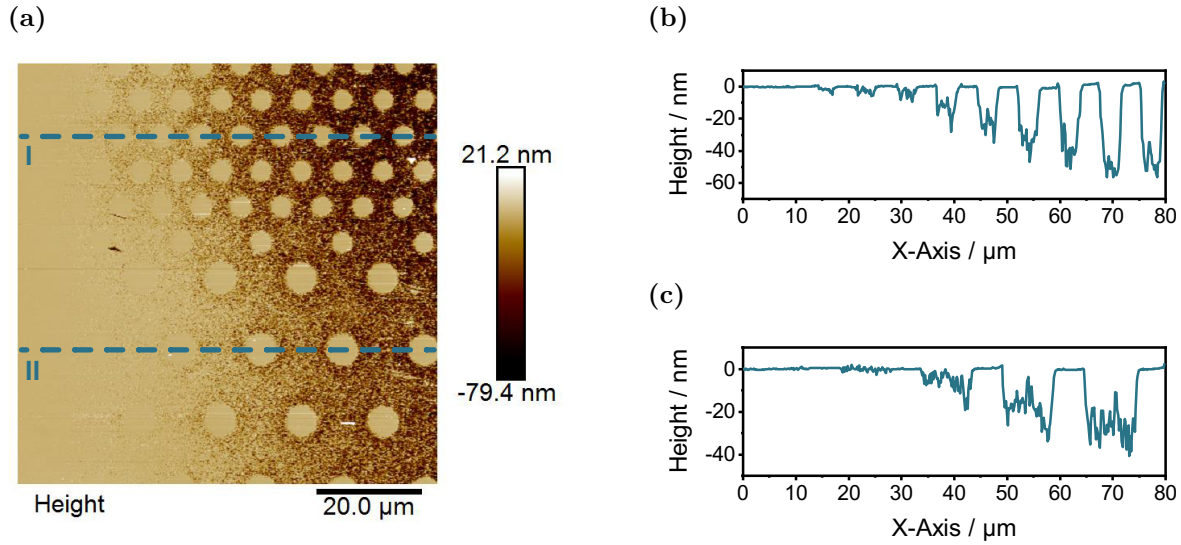


Figure 3.27: Results of masked etching on samples with 500 nm top epitaxial layer, showing that the top surface of the columns is level with the original surface. (a) AFM image after etching in 0.6 wt% NH_4OH under illumination. The left side of the images surface was protected from etching by a thin polystyrene layer, which is why it retains the original surface. (b) Graph of the cross-section I in (a). (c) Graph of the cross-section II in (a).

area etches much faster. This leads to a clear patterning of the homogeneously n-doped epitaxial layer according to the buried implant structure, without any additional masking, as is typically necessary for such microstructuring. A schematic illustration of this process is shown in Figure 3.28.

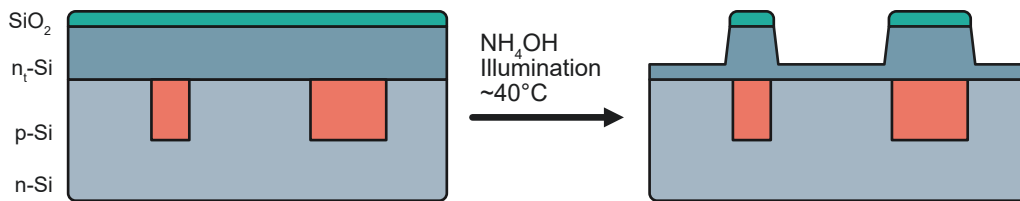


Figure 3.28: Schematic cross-section illustration of selective etching process on samples with top epitaxial layer. Notably, the homogeneously doped top layer is selectively etched solely due to the buried implants.

Following experiments addressed the influence of the top epitaxial layer thickness on the selectivity. First, samples with 500 nm top epitaxial layer thickness were used for this purpose. The process was repeated under identical conditions in ammonia solution under light illumination for 20 min. Again, obvious structuring was visible on the sample surface after an induction period of around 10 min. The results of the sample analysis are shown in Figure 3.29. The etch depth from AFM height images (Figure 3.29a) is very high, measuring (540.0 ± 8.9) nm for the larger and (578.0 ± 2.9) nm for the

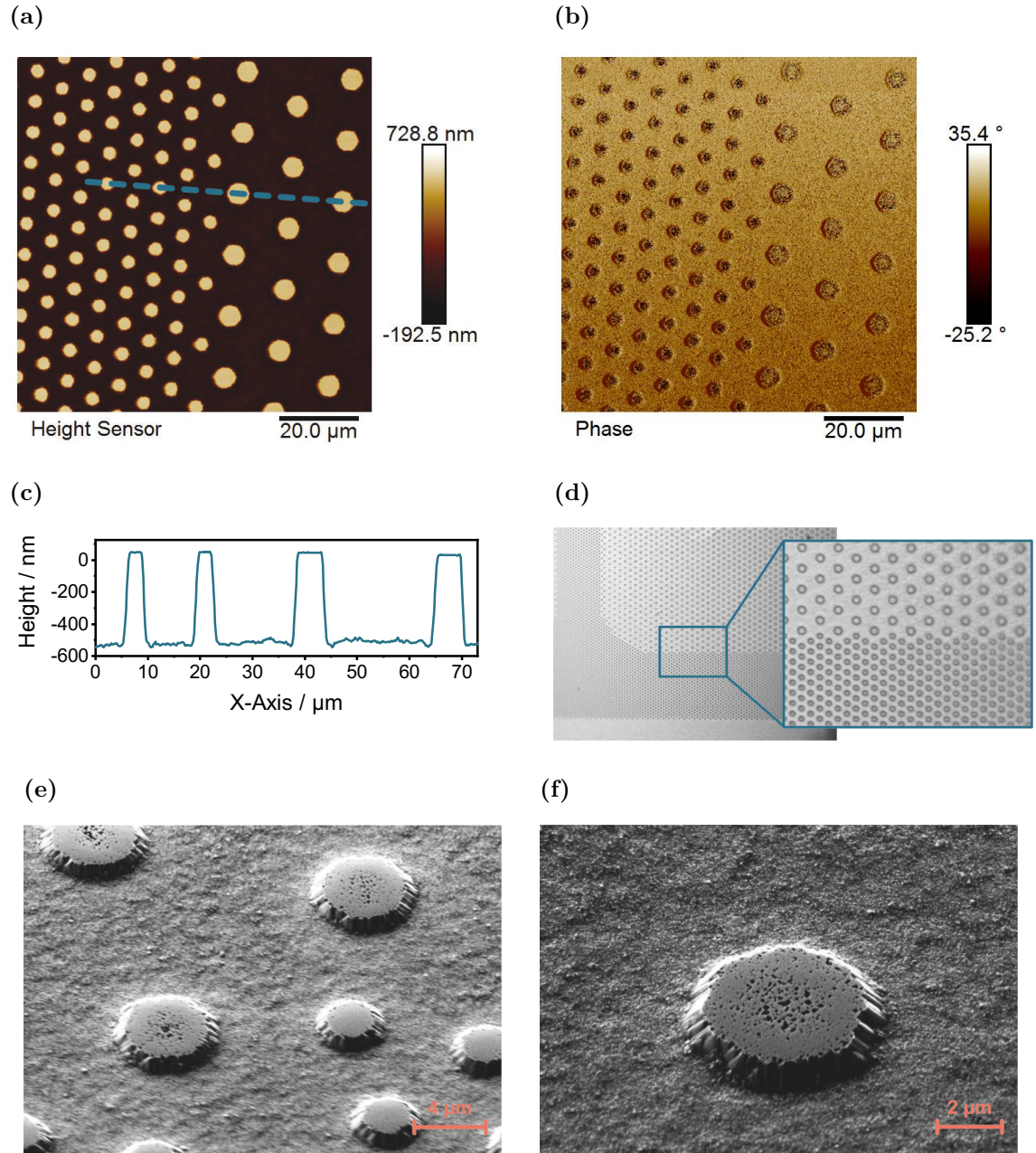


Figure 3.29: Etching results for a sample with 500 nm top epitaxial layer etched under illumination for 20 min. (a) AFM height image showing the implant reproduction as columns. The overlay at the bottom shows the alignment of the pillars in accordance with the implant structure. (b) AFM phase image showing the phase contrast between the top of the columns and the surrounding area. (c) Cross section taken from (a). (d) Light microscopy images showing an overview of the resulting structure. (e), (f) SEM images of etched sample with 500 nm top epitaxial layer. The slanted sidewall angle of around 35.4° can be seen.

smaller diameter columns. Therefore, on this sample the etch depth is independent of structure size and only a very shallow ring of deeper etching is formed around the larger pillars, contrary to what was seen on the sample with 250 nm top epitaxial layer thickness. This is also evident from the cross section marked in Figure 3.29a and shown in Figure 3.29c. Furthermore, the etch depth is larger than the thickness of the top epitaxial layer, showing that the etching has progressed through this layer, continuing inside the bottom epitaxial layer.

The etched area around the columns has a roughness of 22.0 nm RMS, whereas the top surfaces apparently remain essentially unchanged with a low roughness of around 3 nm RMS. For the illustrated sample a phase contrast was measurable again (Figure 3.29b), but the difference is slightly smaller. Still, these results indicate that also in this case the native oxide layer remains on the top surface of the columns.

Regarding the column diameters, the values are increased compared to the theoretical values, as before. For the smaller pillars the diameter is 2.94 μm (+35 %) at the top and 4.56 μm (+109 %) at the bottom. For the larger pillars the diameters are 4.95 μm (+14 %) at the top and 6.45 μm (+48 %) at the bottom. Again it is visible, that the increase does not scale with the structure size, but is within a small margin identical at around 600 to 700 nm at the top and 2.1 to 2.4 μm at the bottom. Due to scaling effects, the sidewalls of the columns appear almost vertical in the cross section, but are in fact slanted with angles of 35.7° and 35.4° for the large and small columns, respectively. When imaged with SEM the real appearance becomes easily visible, as shown in Figure 3.29e and Figure 3.29f. These results are likely due to the anisotropy of (100) silicon etching, leading to sidewalls with slack angles, instead of perfectly vertical sides (see section 1.2.2). The variation in the sidewall angle with regard to the expected value of 54.7° for (100)-silicon is likely due to the measurement from AFM images, on which the actual crystal faces can not be distinguished. The measured value is then a mean between different faces, offset from one another.

Further investigations into the influence of the top epitaxial layer thickness were carried out on samples with 1000 nm top epitaxial layer thickness. Two different sample types were available with this thickness; one with the typical hexagonal structure, and the other with much larger square implants, where the mask holes measured 5 \times 5 mm. The results for both types are shown in Figure 3.30. For the sample with hexagonal implants (Figure 3.30a) a significant structuring can again be achieved, resulting in columns with mean height of (627.5 ± 14.5) nm for the larger and (655.5 ± 9.6) nm for the smaller structures. Hence, for this sample the etching also progressed deep into the top epitaxial layer. Visible on this sample is a reduced fidelity of the structure

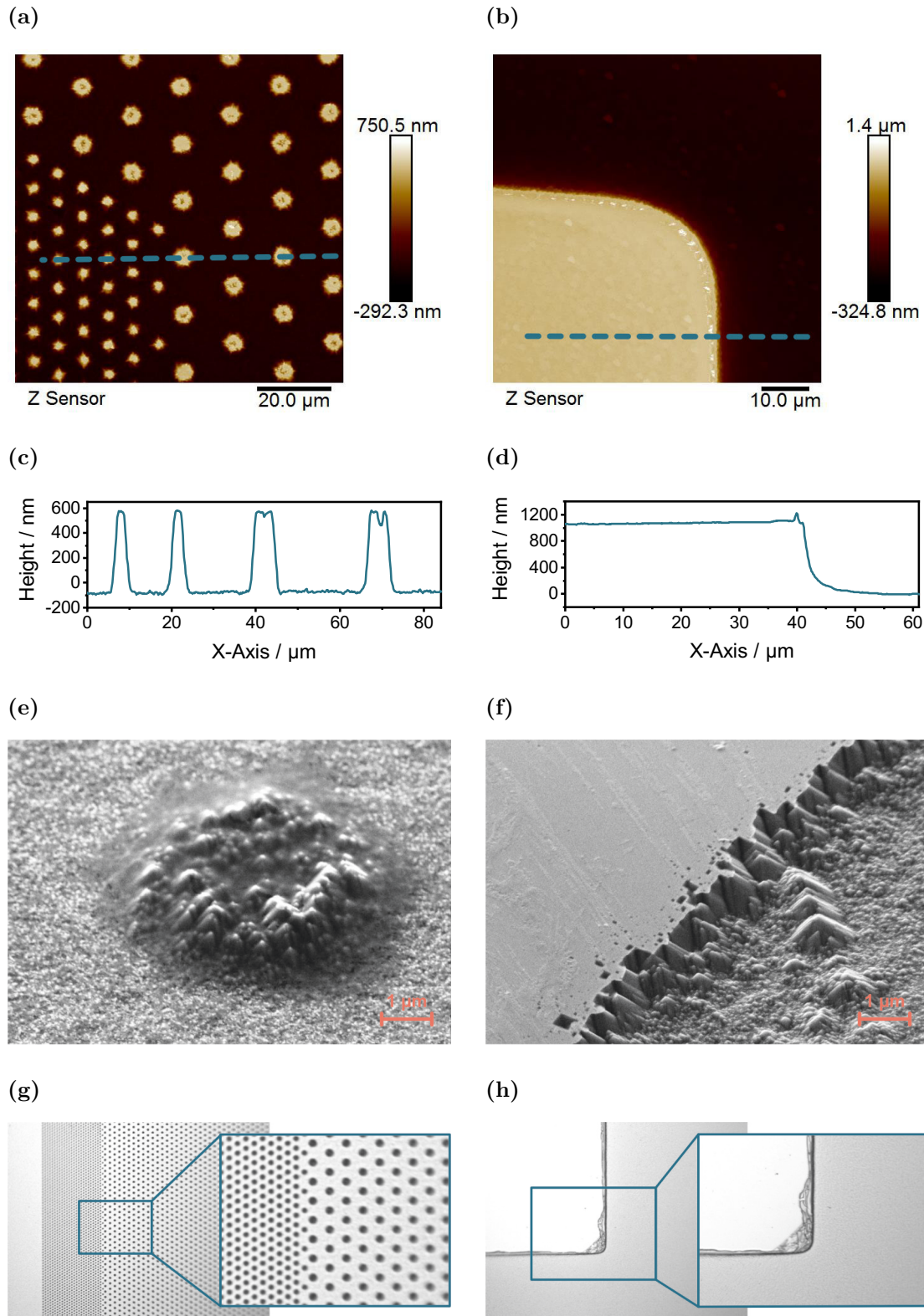


Figure 3.30: Etching results for samples with 1000 nm top epitaxial layer etched under illumination for 20 min. (a) Sample with hexagonal implant structure (b) 5×5 mm implant structure. (c) Cross section taken from (a). (d) Cross section taken from (b). (e), (f) SEM images of samples with hexagonal and 5×5 mm implant structure, respectively. (g), (h) Light microscopy images of samples with hexagonal and 5×5 mm implant structure, respectively

reproduction regarding the shape of the implants. The columns are frayed without smooth edges and side surfaces. This change is also evident in the column diameters. For the larger columns, this value is $4.01\text{ }\mu\text{m}$ (-8%) at the top and $6.54\text{ }\mu\text{m}$ ($+50\%$) at the bottom. For the smaller columns these values are $2.10\text{ }\mu\text{m}$ (-4%) and $4.29\text{ }\mu\text{m}$ ($+97\%$), respectively. Whereas the values for the bottom diameter are similar to the results on samples with thinner top epitaxial layer, the top diameter is actually smaller than the determined diameter of the p-implants. Furthermore, the top surface of the columns is much rougher, measuring 29.3 nm RMS . The roughness is similar to that of the etched surfaces, indicating that the etchant has also attacked the top surfaces. This is also evident from the cross section, shown in Figure 3.30c. Compared to the cross section of previous samples the top surfaces are more rounded and show pitting, indicating etching. AFM phase images also support this notion, as no strong phase contrast can be found, indicating no material contrast between SiO_2 and etched silicon (see Appendix, Figure A.3b). As the top of the columns can therefore not be used as a height reference to the original surface, as before, it is unknown how deep the etching actually progressed into or below the thickness of the top epitaxial layer.

For the sample with $5 \times 5\text{ mm}$ implants the resulting structure, as imaged by AFM, is shown in Figure 3.30b. Here, the boundaries of one of the large unetched areas is shown, demonstrating a sharp contrast between the area with buried p-implant underneath and the remaining surface. The etch depth here is greatly increased with a mean value of $(1082.1 \pm 18.3)\text{ nm}$. This step is also shown in the cross section graph in Figure 3.30d. When analysing sidewall angles on the sample with hexagonal implants values of 26.4° for the larger and 31.0° for the smaller pillars can be found, which deviates from the results of samples with thinner top epitaxial layer. Possibly this is due to the etching of the top surface, leading to a shallower sidewall angle, as the height of the pillars is reduced. From SEM images, as shown in Figure 3.30e and Figure 3.30f, it can be seen that the etching results in hillocks in the form of square-based pyramids as is expected for anisotropic etching on (100) silicon substrates. These hillocks are also evident at the perimeter of the larger $5 \times 5\text{ mm}$ areas. This indicates that the etching generally follows the behaviour expected for anisotropic etching, namely in the varying etch speed depending on the crystal plane, as expected for a (100)-Si surface. Despite this degradation in reproduction fidelity, light microscopy images (Figure 3.30g and Figure 3.30h) show that the implant structure was reproduced homogeneously over the full sample surface.

These results show that even with p-implants buried beneath 1000 nm of homogeneously doped n-type top epitaxial layer a selective etch process can be achieved. With-

out any additional masking step the buried structure can be reproduced reliably via a very simple process by illuminating the sample in a dilute etchant solution.

As was done before for samples without top epitaxial layer, etching experiments were carried out immediately after removal of the native oxide layer with a short buffered oxide etch. The samples were cleaned as usually, but subjected to the oxide-removing 7:1 $\text{NH}_4\text{F}:\text{HF}$ solution for 15 s immediately prior to the illumination-assisted etching experiment. This was carried out with the same conditions of 0.6 wt% NH_4OH -solution under illumination with a 50 W halogen lamp. Immediately upon insertion of the sample into the etchant solution, strong gas evolution and discolouration and dulling of the surface could be observed. This indicates the immediate onset of silicon etching, as expected without the oxide layer. On these samples, no structure was observable during the etch process, even after the previously employed 20 min of process time. Upon further investigation after the sample was removed from the solution, no structuring could be found visually, with light microscopy or AFM. The same result was achieved for all top epitaxial layer thicknesses (250 nm, 500 nm and 1000 nm). This indicates again that the native oxide layer plays a key role for the light-assisted, strongly selective etch process. Whereas on samples without any top epitaxial layer the expected p-etch stop effect was achieved, on samples with this burying layer, no selectivity is achievable, as the surface is absolutely homogeneous, preventing etch selectivity. Only with a native oxide layer present, the illumination is able to induce strong selectivity.

3.4.4 Mechanism Hypothesis

Based on the results achieved, a mechanism explaining the origin of the selective etching on samples with buried p-type implants in n-type silicon can be proposed. Evidently, the buried implants, together with the illumination play an important role. Therefore, the mechanism proposed for samples with implants immediately at the surface, as described in section 3.4.2, is modified, taking into account the homogeneously doped top epitaxial layer. A process as illustrated in Figure 3.31 can be envisioned. As before, it is assumed that the illumination leads to charge carrier generation in the silicon substrate. If the carriers are generated within or close to the pn-junction (marked in green) surrounding the p-implants, they are separated by the built-in electric field and swept into their corresponding quasineutral regions (electrons into the n-type - blue arrows - and holes into the p-type silicon - white arrows -, respectively). The electrons then diffuse inside the n-bulk, reaching the surface of the sample, as illustrated in Figure 3.31a. Here, they can influence the native oxide layer by inducing a charging effect, leading to the evolution of a dipole of positive charges at the Si-SiO₂ interface and a highly negatively

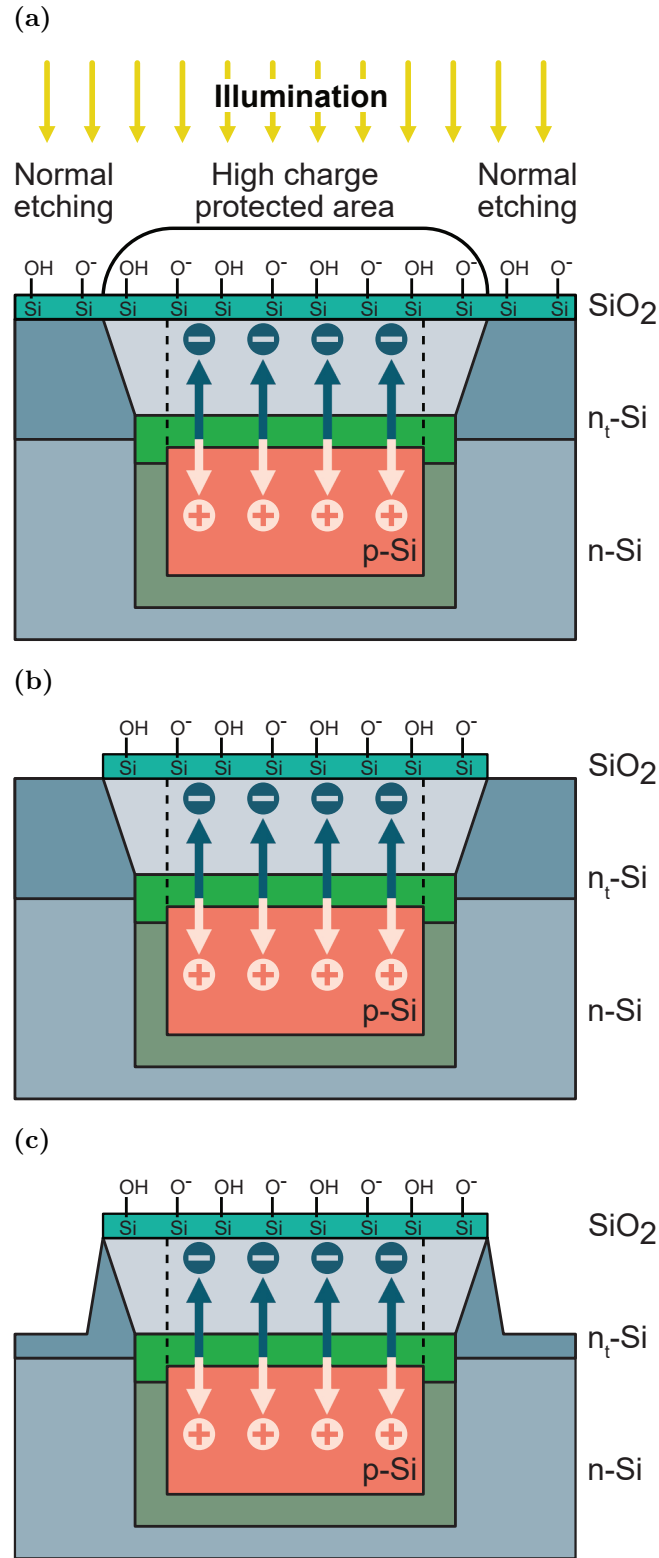


Figure 3.31: Model representation of proposed mechanism upon illumination in etchant solution. (a) Initial process of charge generation at surface from buried implants, generating protected areas. (b) Removal of silicon oxide layer selectively outside of protected areas. (c) Subsequent etching of unprotected areas by etchant solution, generating the self-replicated pattern.

charged surface at the SiO₂-solution interface. By itself, the silicon oxide surface charge is greatly dependant on the solution pH, reaching a neutral charge point around pH 2.5 and exhibiting a more and more negatively charged surface with increasing pH. This was also confirmed by zeta potential measurements of the provided samples, yielding an isoelectric point of around pH 2.6 (See Figure 3.6)^[138,139]. Accordingly, at the pH value of the basic etchant solution (pH \approx 10), the surface is negatively charged, but can still be etched by hydroxide ions. If the sample is then irradiated and a significant number of electrons diffuse to the surface, an even stronger negative surface charge is induced, possibly hindering the diffusion of hydroxide ions to the surface due to electrostatic repulsion. A similar effect was described by Seidel *et al.*, explaining the decreasing etch rate of silicon oxide in KOH solutions with increasingly high concentrations. Whereas the etch rate initially increases with KOH concentration up to 35 %, a maximum is then reached and the rate decreases again. This decrease is rationalised by an increase in negative surface charge due to rising pH. This inhibits etching by hindering the diffusion of hydroxide ions^[39]. In the present case of illumination controlled selectivity, in a presumably similar way, the diffusing charges are able to slow down the etch rate, inducing a passivating effect on the silicon oxide layer. Accordingly, at a certain point, the oxide in areas without buried implant beneath is removed, while it remains in the areas above the buried implants(Figure 3.31b). This effectively creates an in-situ self-aligned oxide etch mask, which directs the further removal of silicon by the etchant (Figure 3.31c). This results in the structure found on the samples after etching, consisting of columns above the implants, retaining the native oxide layer and etched silicon in between these structures.

An alternative mechanism envisions the direct etching of the silicon atoms by photo-generated holes, which diffuse to the silicon-etchant interface after initially being injected into the volume of the p-Si implants. The holes can oxidize the surfacial silicon atoms, increasing the speed of their removal. As the areas with directly underlying implants are saturated with electrons, the holes can only diffuse to the surfaces between the implants, leading to the observed patterning effect. In order to properly test these hypotheses, the process is first further characterised with regards to optimal process conditions. This then allows for the extensive investigation of the proposed mechanism.

3.4.5 Process Parameters

In the initial experiments, the etching was carried out in a 5 mL vial containing a 0.6 wt% solution of NH₄OH. The sample was immersed in the solution and the vial illuminated by a 50 W halogen lamp. This yielded the previously shown selective etching after

around 20 min. During this time, an increase in solution temperature to 40–50 °C could be measured, induced by the thermal radiation of the light source, placed 15 cm from the vial. Further experiments could show that this temperature increase was in fact necessary in order to achieve the etching result in the given time frame. Accordingly, the solution temperature appears to play a significant part and should be optimized. In addition to this, the etchant composition and illumination are expected to influence the result to a great extent.

From the initial experiments it was furthermore apparent that the reaction proceeds in two phases:

Phase I: **Induction** - No observable change on the sample

Phase II: **Etching** - Visible etching and structuring on the sample

Generally, the induction period was identical in length under equal conditions, while the result obtained from etching varied with the length of the etching period, apparent in etch depth and fidelity. It is therefore furthermore necessary to find the ideal process time. To ensure comparability between different samples, not the overall process time was used to determine equal conditions, but the length of the etching period. For each sample, the time when first signs of selective etching were observed over the full sample surface was recorded and taken as the baseline for the etching period, further denoted as active etch time. For most optimization experiments, a consistent active etch time of 60 s was chosen.

In order to ensure identical parameters during the optimization, the experimental setup was changed for all following experiments. Instead of a simple glass vial, the process was carried out inside a quartz cuvette placed in a custom made aluminium heater block, allowing for easy temperature control on a lab hotplate with temperature sensor (see Appendix, Figure A.4). The halogen lamp was furthermore replaced by an LED light source with a narrow wavelength distribution and no significant thermal radiation, which would influence the solution temperature. A 730 nm LED source in combination with 50 °C solution temperature was found to produce etching results similar to the previously reported, which is why these parameters were chosen as starting points for further optimization.

In summary, the optimization was concentrated on temperature, etchant composition, process time and illumination wavelength. The first three of these are equal to the significant parameters for standard anisotropic etching, as reported in the literature^[39,40,47]. The newly discovered light dependency of the etching is investigated here, as well.

3.4.5.1 Etchant Dependence

It stands to reason, that the etchant significantly impacts the result obtained by the selective etching process. In the literature, typical etchants for basic wet-etching are TMAH, KOH and ethylenediamine based mixtures, showing varying etch behaviour^[12,39,40].

Previously, only NH_4OH at a concentration of 0.6 wt% was tested. As this is already very low, for the other experiments, the value was increased stepwise. Specifically, 3.0 wt% and 6.0 wt% were tested, as at higher concentrations at 50 °C NH_3 boils out of the solution vigorously, preventing successful selective etching. Figure 3.32 shows AFM images for samples with 500 nm top epitaxial layer thickness, etched at the different NH_4OH -concentrations.

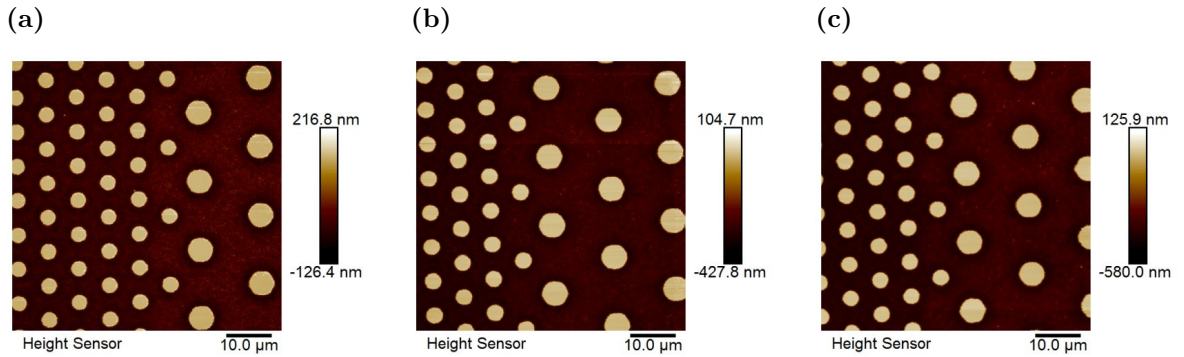


Figure 3.32: AFM images of samples with 500 nm top epitaxial layer etched in NH_4OH -solutions at different concentrations: (a) 0.6 wt%, (b) 3.0 wt%, (c) 6.0 wt%. All samples were etched at 50 °C for 60 s of active etch time under illumination with a 730 nm LED lamp.

Generally, the resulting structures are very similar at all three concentrations. On each sample, clearly resolved columns are visible, with flat top surfaces, representing the original native oxide sample surface. Accordingly, a strong phase contrast was measured between the silicon oxide on top of the columns and the etched areas. The diameter of the columns is similar, regardless of concentration. The smaller columns are between 3.3 to 3.5 μm (+51 to 61 %) and the larger between 5.3 to 5.4 μm (+22 to 24 %), each measured at the top. A difference can be found in the etch depth, which increases with increasing concentration, from (155.6 ± 18.9) nm at 0.6 wt% to (411.3 ± 22.8) nm at 6.0 wt%. Accordingly, if maximum etch depth is required, a high concentration should be used. The disadvantage of higher concentrations is a reduced homogeneity across the samples, as was visible in the form of strong colour deviations on the surface for the samples at 3.0 wt% and 6.0 wt%. As consistent etch results are more desirable than high etch depths for the further characterisation, 0.6 wt% was determined as the ideal concentration when using NH_4OH as etchant.

Alternative alkaline solutions, specifically consisting of TMAH or KOH, well described in the literature, were investigated as potential selective etchants as well. For the sake of reproducibility, similar concentrations of 0.5 wt%, 2.5 wt% and 5.0 wt% were chosen. AFM images of samples, again with 500 nm top epitaxial layer, etched in TMAH are shown in Figure 3.33.

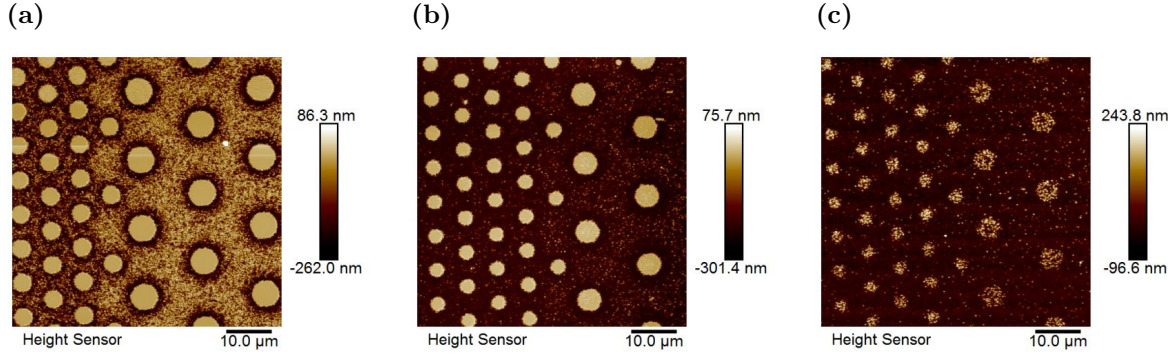


Figure 3.33: AFM images of samples with 500 nm top epitaxial layer etched in TMAH-solutions at different concentrations: (a) 0.5 wt%, (b) 2.5 wt%, (c) 5.0 wt%. All samples were etched at 50 °C for 60 s of active etch time under illumination with a 730 nm LED lamp.

For TMAH, a strong variation in the etch result, depending on the concentration, can be found. At low concentrations, the structures are not perfectly etched into the substrate, specifically for the larger columns, as the etch depth here is only (69.4 ± 18.4) nm, whereas the etching progressed to (145.0 ± 17.5) nm around the smaller columns. With increasing concentration at 2.5 wt%, the structures appear more similar to the results in NH_4OH , except for some fringing around the column perimeter, decreasing the etching fidelity. The etch depth is (192.8 ± 7.5) nm, evenly for both structure sizes. At 5.0 wt%, the selectivity appears to be reduced drastically and the columns do not exhibit an even top surface anymore, but instead appear to consist only of smaller hillocks. The etch depth is (85.8 ± 9.2) nm for the larger and (117.8 ± 6.6) nm for the smaller columns. When measuring the diameters of the columns, it can be found that they decrease with increasing concentration. Exemplary, at 0.5 wt%, the large structures are around $5.7 \mu\text{m}$ (+31 %), which decreases to around $4.8 \mu\text{m}$ (+10 %) at 2.5 wt% and finally $4.7 \mu\text{m}$ (+8 %) at 5.0 wt%. Accordingly, the structure size can be controlled via the concentration to a certain extent, before a breakdown in selectivity is induced. The strong difference in the etch result between NH_4OH and TMAH is most likely due to the lower stability of the native oxide layer in TMAH^[23,152,155]. If the mechanism presented previously is assumed, a lower SiO_2 -stability would lead to a faster removal of the protective quasi-mask, preventing perfect reproduction of the buried implant structure. This hypothesis

is reinforced by the variation in phase contrast, depending on the etchant concentration. Whereas all samples etched in NH_4OH show a strong phase contrast between the column top surface and the etched areas, only the TMAH sample etched in 0.5 wt% shows a significant contrast, indicating the removal of the silicon oxide layer on the other samples (see Appendix, section A.4).

KOH as etchant is frequently used in MEMS/MOEMS technology due to its high anisotropy^[14]. Outside of MEMS/MOEMS the usage of KOH is limited though, as it is not compatible with CMOS-technology^[14,32]. Nevertheless, KOH was investigated as a possible selective etchant. Figure 3.34 shows AFM images of two samples, etched in 0.5 wt% and 2.5 wt% KOH solution, respectively.

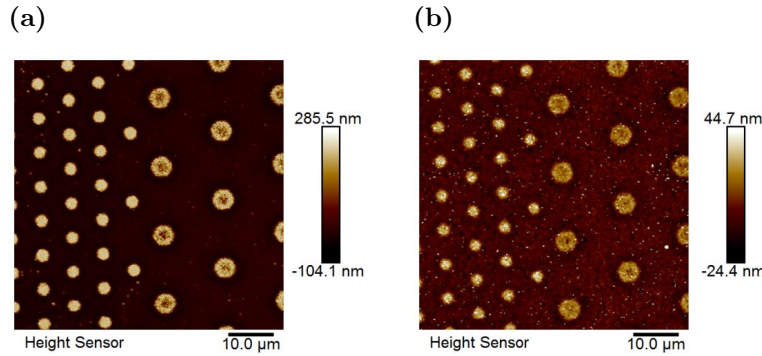


Figure 3.34: AFM images of samples with 500 nm top epitaxial layer etched in KOH-solutions at different concentrations: (a) 0.5 wt%, (b) 2.5 wt%. All samples were etched at 50 °C for 60 s of active etch time under illumination with a 730 nm LED lamp.

For both concentrations, a clear structuring is visible, but already at 0.5 wt% the fidelity of the generated structure is significantly lower than for the other etchants. This is particularly apparent on the larger columns, which do not exhibit an even top surface, but instead show deep divots in the center. On the smaller columns the surface appears more homogeneous, but the perimeter shows some fringing and decreased fidelity. Due to the uneven etching on the larger columns, the height of both column sizes is different, with the smaller reaching (233.0 ± 2.8) nm, while the larger only reach (175.3 ± 9.1) nm. This degradation of the columns is even stronger observed at 2.5 wt% KOH-concentration, where also the smaller columns show signs of etching and exhibit no clear outline anymore. Here, the column height is also greatly reduced, while retaining the diameter-dependent height difference. The smaller columns are (33.3 ± 1.3) nm high, while the larger only measure (21.2 ± 1.4) nm. Despite this apparent degradation in the structuring result, an improvement was measurable with regard to the column diameters. At 0.5 wt% the smaller columns had a diameter of $2.5 \mu\text{m}$ (+15 %) and the larger ones of $4.3 \mu\text{m}$ (−2 %). At 2.5 wt%, these values are $2.5 \mu\text{m}$ (+15 %) and $4.4 \mu\text{m}$

(+1 %), respectively. KOH therefore enables the reproduction of the buried implants with increased dimensional accuracy, but with largely decreased structure fidelity. As before for TMAH, this is most likely due to the decreased stability of SiO_2 in KOH, leading to a more rapid removal of the protective in-situ-mask. This was again apparent from phase images, showing no significant contrast between the columns and the surrounding etched areas for the sample etched in 2.5 wt% KOH-solution. For the lower concentration, which lead to an acceptable etch result, a phase contrast was measurable, albeit with opposite sign, likely due to differences in the resulting surface-properties after etching with KOH as compared to the other etchants (see Appendix, section A.4). Due to the already very low reproduction fidelity at 2.5 wt%, no further experiments at higher concentrations were conducted.

In summary, experiments regarding the etchant composition confirmed that NH_4OH is the ideal alkaline etchant for high quality structure reproduction. Based on the homogeneity of the resulting surface, 0.6 wt% is ideal in achieving homogeneous results, while higher concentrations are advisable if deeper etching is required. TMAH proved as a suitable etchant as well, but closer concentration control is required in order to achieve the desired result. Additionally, a material contrast between the column top surface and the surrounding, etched areas is not as easily achieved. Lastly, KOH showed selective etching behaviour as well, with high dimensional accuracy, at the cost of greatly reduced structure fidelity. Based on these results, it was decided to continue with the usage of etchant solutions containing 0.6 wt% of NH_4OH , as it resulted in the best structuring result, providing high fidelity self-replication of the buried implant structure. The large differences between the three etchants can be explained by varying SiO_2 -stability. If the oxide is more stable in a particular solution, the removal of the protective mask, above the buried implants, as hypothesised before, is slowed down, enabling deep silicon etching and subsequently a high quality reproduction of the buried structure. On the other hand, in the solutions in which the native oxide is less stable, the in-situ-mask is removed too fast and the selective etching can not proceed far enough to result in the desired reproduction quality.

3.4.5.2 Temperature Dependence

After establishing the ideal etchant composition, the process temperature was optimized between 30 °C and 70 °C. These limits were chosen, as previous experiments showed minimal reaction rate at room temperature, necessitating a certain minimum temperature. The upper limit was determined, so that excessive evaporation of NH_3 is avoided and to ensure the stability of the plastic sample holder. Samples were prepared at each

temperature and investigated with AFM in order to analyse the resulting structures.

Figure 3.35 shows three such AFM images for samples etched for 60 s active etch time at 30 °C, 50 °C and 70 °C, respectively.

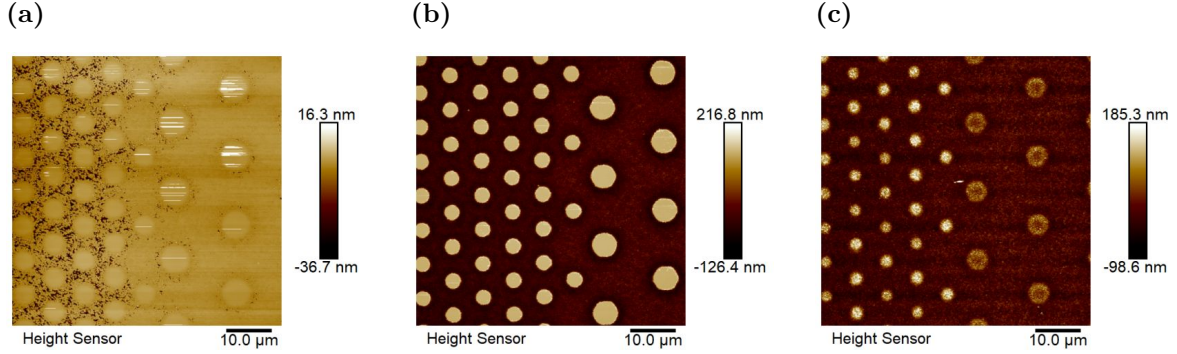


Figure 3.35: AFM images of samples with 500 nm top epitaxial layer etched at different solution temperatures: (a) 30 °C, (b) 50 °C, (c) 70 °C. All samples were etched in a 0.6 wt% NH_4OH -solution for 60 s of active etch time under illumination with a 730 nm LED lamp.

The sample etched at 30 °C, which took 69 min for visible etching to start, after which it was then etched for an active etch time of 60 s, shows a slight structuring, but with very low etch depth, especially around the area above the larger implants. Here, only a narrow ring with a depth of 5 nm can be found. Around the area above the smaller implants, the etching has visibly progressed further, but only to a mean depth of 5 nm, as well. Furthermore, the size of the implants is enlarged by around 2 μm . Overall, etching at 30 °C yields only a slightly structured surface and takes much longer than previous experiments to produce any structuring at all. In contrast, the sample etched at 50 °C, which had an onset time of 7 min shows much clearer structuring, very similar to the results previously achieved with a halogen lamp as light and heat source. Here, the etch depth was identical for both implant sizes at $(155.6 \pm 18.9) \text{ nm}$. The diameters of the etched columns are smaller, with an increase of only around 1 μm . Lastly, on samples etched at 70 °C, the structure is again clearly visible, with etching onset after only 2 min. The structure shows clear signs of degradation, namely in the loss of the even top surface and regular perimeter on the columns. Furthermore, the etching result was apparently dependent on the structure size, as the smaller implants were reproduced as higher columns. Compared to the columns above the larger implants, they differed by around 60 nm. Additionally, the larger implants showed a coronal structure of increased height at the perimeter. Notably though, the diameter of the columns was much closer to the theoretical values, being increased only by around 0.4 μm after 60 s active etch time.

In summary, these experiments show, that ideal etching results in a convenient process time window can be achieved in etchant solutions of 0.6 wt% NH_4OH at 50 °C. Significantly lower temperatures lead to much longer process times, with decreased reproduction fidelity, while higher temperatures decrease the necessary process time, but lead to a deterioration of the structures. Accordingly, 50 °C was chosen as the solution temperature for all further experiments.

3.4.5.3 Wavelength Dependence

As shown before, illumination of the samples during the etch process is the essential part in achieving the selective etching effect and it is therefore of great interest to investigate how the process is influenced by varying illumination wavelengths and intensities.

In order to investigate the influence of wavelength upon the selective etching process, LED light sources were used to screen a range from 365 to 1050 nm. All samples were etched under the same, previously established conditions (0.6 wt% NH_4OH , 50 °C) in order to ensure comparability. For evaluation, at least three AFM images were taken, spread over the sample surface. The etch depth was then measured as the height difference between the top of the pillars and the mean of the bottom surface, as before. This was carried out for samples with 250 nm, 500 nm and 1000 nm top epitaxial layer thickness to allow for simultaneous evaluation of the influence of the burying depth. The resulting graph, showing etch depth vs. wavelength, is shown in Figure 3.36.

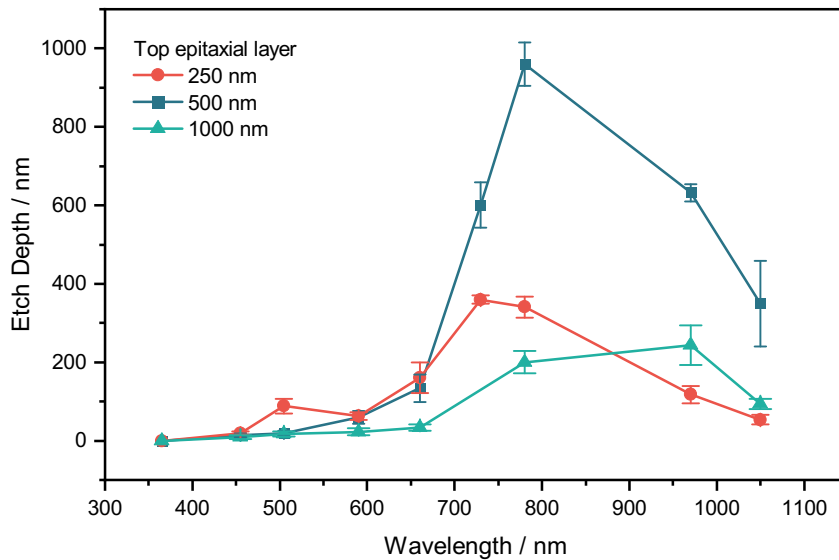


Figure 3.36: Wavelength dependent etch depth for samples with 250 nm, 500 nm and 1000 nm top epitaxial layer thickness. The samples were etched at 50 °C in a 0.6 wt% solution of NH_4OH .

As can be immediately seen, in all three cases the achieved etch depth is strongly dependent on the wavelength of the illumination source. For shorter wavelengths between 365 and 660 nm the etch depth follows a nearly identical course for all sample types, staying below 200 nm. For longer wavelengths the depth increases strongly up to around 800 nm, with the maximum value varying depending on top epitaxial layer thickness. For samples with 250 nm top epitaxial layer a maximum etch depth of (360.0 ± 11.2) nm was achieved at a wavelength of 730 nm. Accordingly, the etch process progressed significantly beyond the top epitaxial layer, etching more than 100 nm deep into the socket epitaxial layer in which the p-Si implants are situated. For the samples with 500 nm top epitaxial layer thickness the wavelength of maximum etch depth was slightly red-shifted to 780 nm, resulting in a maximum etch depth of (960.0 ± 56.0) nm. Here the etching progressed even further into the lower epitaxial layer, etching almost twice as deep as the top epitaxial layer thickness. In the case of 1000 nm top layer thickness, the maximum is again red-shifted to 970 nm, where an etch depth of (243.6 ± 50.7) nm results. Accordingly, the depth here is greatly reduced, likely due to a weakening of the protective effect with more deeply buried implants. In all cases, the etch depth decreases again for wavelengths further in the infrared, reaching a low value below 400 nm at a wavelength of 1050 nm for all sample types. An explanation for this strong wavelength dependence can be found in the absorption properties of silicon. The absorption depth of silicon increases with increasing wavelength in the UV to NIR range, meaning that short wavelength photons are absorbed close to the surface of the crystal without penetrating deeply. Conversely, longer wavelength photons can penetrate deep into the crystal, possibly even transmitting through a wafer sample, if the wavelength is long enough. This is also evident from absorption spectra of the unmodified silicon samples, showing that wavelengths above 1000 nm penetrate the full sample (see Appendix, Figure A.2a). The expected absorption behaviour of a given sample can be calculated from known silicon absorption characteristics and the theoretical depth within which generated charges can act upon the pn-junction, i.e. be split and subsequently act in the previously proposed way. All charges which are absorbed within the pn-junction or within one diffusion length of it are able to act in the way proposed in the mechanism^[67]. The diffusion length L can be calculated via

$$L = \sqrt{D\tau} \quad (3.9)$$

with D being the diffusivity and τ the carrier lifetime^[67]. These two values can be found from theoretical models, which will give a good estimate. For the diffusivity, a value of $35.24 \text{ cm}^2 \text{ s}^{-1}$ can be found from the n_t doping concentration of $8 \cdot 10^{14} \text{ cm}^{-3}$ ^[157–160]. For

the lifetime τ a value of 72 μs can be estimated, using the dopant concentration^[161,162]. With these values, the diffusion length can then be calculated as 504 μm or roughly half of the overall sample thickness. From this, in combination with the wavelength dependent absorption coefficient μ_λ (see Appendix, Figure A.2b), the theoretical absorption can then be determined via the the Lambert-Beer law as:

$$Abs_{504\mu\text{m}} = 1 - e^{-\mu_\lambda 504\mu\text{m}} \quad (3.10)$$

In addition, for every wavelength, the surface reflectance, i.e. the percentage of photons reflected on the sample surface, can be calculated from the wavelength dependent refractive index n_λ of silicon^[163,164]:

$$R = \left(\frac{1 - n_\lambda}{1 + n_\lambda} \right)^2 \quad (3.11)$$

With this, the actual absorption of photons within one diffusion length inside the sample can be calculated as:

$$Abs_{504\mu\text{m},r} = Abs_{504\mu\text{m}}(1 - R) \quad (3.12)$$

The resulting absorption plot from these calculations for various wavelengths is shown in Figure 3.37. This effectively models the response of the buried structures to illumination of different wavelengths.

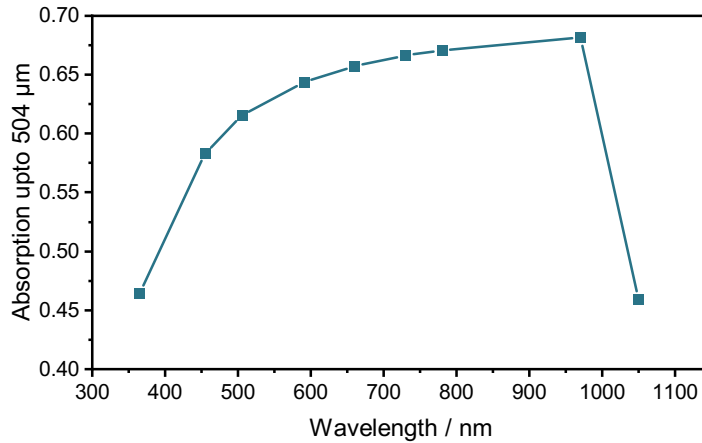


Figure 3.37: Calculated absorption through 504 μm , i.e. one diffusion length for the used samples, of silicon for varying wavelengths. The calculation takes into account the reflection of photons on the surface.

As seen before, the response is low in the UV region, with an increase towards red wavelengths and finally a strong decrease at 1050 nm. Different to the measured values is the overall higher response at shorter wavelengths. The lower response in the real

measurements is likely due to recombination effects for short wavelengths. It is known that charge carriers generated close to the surface are more prone to undergo surface recombination due to the proximity to this interface^[67,74,165,166]. Accordingly, shorter wavelengths, which are absorbed closer to the surface can not efficiently take part in the mechanism proposed before. In contrast, carriers generated from longer wavelength absorption are already located farther from the surface and are therefore more likely to reach the pn-junction to be separated and subsequently take part in the mechanism.

Interestingly, in the results for wavelength dependent etch depth, a shift in the maximum position can be found, depending on the thickness of the top epitaxial layer, i. e. a higher thickness leads to a more red-shifted maximum. Likely, the thicker epitaxial layer enhances the effect due to surface recombination, shifting the maximum towards longer wavelengths.

In contrast to the results for etchant and temperature dependence, the structure size varied much less with the different illumination wavelengths. The mean diameter over all measurements is $(4.66 \pm 0.27) \mu\text{m}$ for the larger structures and $(2.86 \pm 0.20) \mu\text{m}$ for the smaller structures. A significant variation in diameter always coincided with a large decrease in structure reproduction fidelity, indicating that the illumination wavelength does not significantly alter the dimensions of the reproduced structures. Overall, in order to achieve the maximum protective effect, it appears reasonable to apply IR wavelengths in the range of 660 to 870 nm. Accordingly, the wavelength for further experiments was set at 730 nm.

Light Intensity Dependence In the next step, the influence of the light intensity on the etch result was determined, using the variable power source of the ThorLabs LED lamps. At different power levels, samples with 500 nm top epitaxial layer were etched under otherwise equal conditions, in this case 50 °C, 0.6 wt% NH_4OH with an illumination wavelength of 730 nm. All samples were analysed with AFM with regard to the etch depth and structure dimensions. Figure 3.38a collects results for both parameters. The measured etch depth is relatively constant at around 170 nm, while the value at the lowest illumination current of 200 mA is significantly higher at a depth of $(200.8 \pm 8.1) \text{ nm}$. With higher illumination current the etch depth decreases to a small extent. This suggests an influence of the illumination on the etch speed, possibly reducing the etch rate slightly. This might be due to an inherent effect of photons on the n-type silicon or an extended protective influence in line with the proposed mechanism at higher illumination strengths. As for the structure dimensions, a much less significant variation in the column diameter for varying illumination currents was found. Again, all structure sizes are enlarged in comparison to the measured sizes of the implant structures. At 200

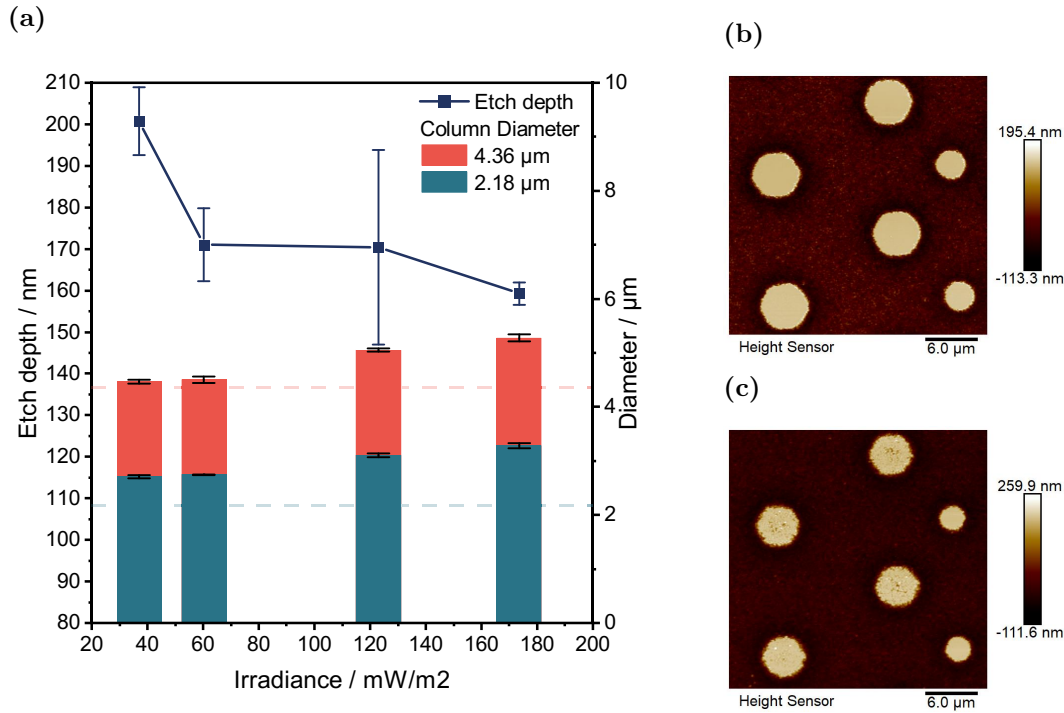


Figure 3.38: (a) Intensity dependent etch depth and structure size for samples with 500 nm top epitaxial layer. The real implant structure sizes are marked as dashed lines. The samples were etched at 50 °C in a 0.6 wt% solution of NH_4OH under illumination with a 730 nm wavelength LED source. AFM height images demonstrate the reduced structure fidelity with lower LED current: (b) 1000 mA LED current, (c) 200 mA LED current.

and 350 mA the structures are closer to the real implant size, with the enlargement of the diameter being around 500 nm for the smaller and 100 nm for the larger implants, whereas at 700 and 1000 mA these values are around 900 nm and 700 nm respectively. According to the proposed mechanism, a greater enlargement is expected with higher light intensity, as the protective effect would spread out farther due to the additional amount of generated carriers. From this, it seems advisable to choose lower illumination currents, as it seems to produce better results, but it was also found that the lower illumination currents lead to a decrease in structure fidelity, in particular in the smoothness of the column top surface and perimeter (see Figure 3.38b and Figure 3.38c). Similar to the results for the etchant composition, the highest possible illumination current was chosen for further experiments, as it induced the strongest protective effect.

3.4.5.4 Time Dependence

To gain further insight into the progression of the selective etching, experiments investigating the etch progress at specific time intervals were carried out. Here, especially the

start of the etching in the areas around the p-implants is interesting, as it can potentially give hints regarding the mechanism. Due to the nature and scale of the reaction, in-situ experiments investigating progress on a single sample are not feasible and instead multiple samples are etched, where the reaction is terminated at pre-specified durations. For this, the active etch time t_a was again used as the reference, instead of the overall process duration. This allowed for much more repeatable results, enabling comparisons between different samples. Usually, the time until a reaction was visible on the sample was in the range of 5 to 10 min. Images for some of the selected etch times on samples with 250 nm top epitaxial layer thickness are shown in Figure 3.39.

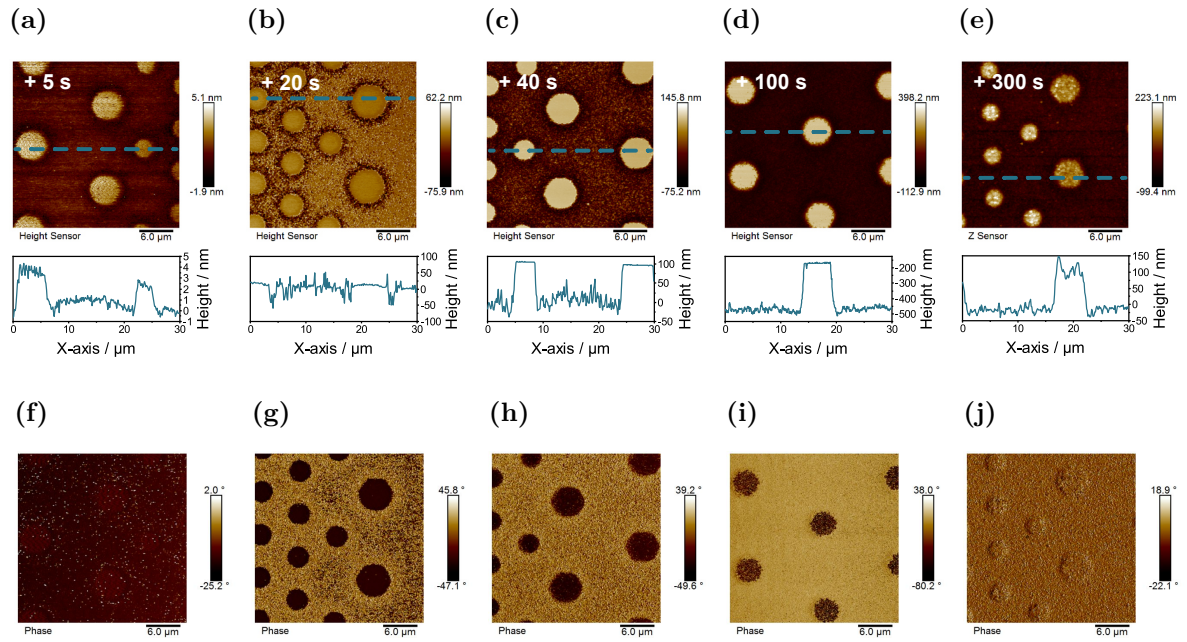


Figure 3.39: AFM images for samples with 250 nm top epitaxial layer etched for specific time intervals. (a) to (e) AFM height images with cross section, (f) to (j) corresponding AFM phase images. All time values counted from visibility of structuring on full sample surface.

The first image (a) is of a sample that was removed from the solution immediately when signs of etching were visible on the sample. This includes a visible pattern, small gas bubbles evolving and a dull looking surface. The AFM images already show a patterning as small columns with a height difference of (1.8 ± 0.9) nm, similar to the thickness of the native oxide layer. A ring of deeper etching can be seen immediately around the columns. On the phase image no contrast is visible, indicating no material difference between the columns top surfaces and the surrounding area. This suggests that the etching has not progressed through the native oxide layer yet, but the layer has been selectively etched. This essentially means that the influence of the illumination is

already apparent before the silicon bulk is actually etched. Possibly, the influence of the buried implants acts mainly during the induction period before the etching actually progresses to pattern the silicon substrate.

The next images (Figure 3.39b and Figure 3.39g) show the etch progress 20 s after the onset. Here the process has started to etch the silicon substrate, visible again as columns with smooth, seemingly unetched top surface surrounded by etched silicon. Especially clearly visible here are the rings of increased etching around the pillars, carrying on from the appearance at the onset of etching. The height difference between the pillars and the deep rings is (38.5 ± 7.0) nm, whereas the difference to the surrounding area is only (7.3 ± 5.4) nm. Also apparent on this sample was the effect that the etching varied depending on the size and distance of the columns around them. In between the smaller diameter columns the etching was deeper, essentially masking the presence of a deep ring. This is similar to the results from initial experiments on samples with 250 nm top epitaxial layer. Apparently, the distance between the smaller columns is short enough, so that no area of lower etch rate exists, as it does between the larger columns (see Figure 3.26a).

Continuing in the etch process, 40 s after the etch onset a clear patterning in the form of columns is visible. The area surrounding the columns is etched evenly between the smaller and larger pillars and the deeper etched ring around the structures is only barely visible. The etch depth after 40 s reaches a value of (94.9 ± 16.2) nm and a strong phase contrast is still visible between the top surface of the columns and the etched area. A similar appearance can be found for the samples with etch times of up to 100 s. The main difference here is the increase in etch depth up to (294.4 ± 2.7) nm at 100 s. Firstly visible on such samples were variations in the column surfaces, mainly as a loss in resolution of the column edges. For samples with shorter etch times these are straight and relatively smooth, but starting from 100 s they appear more frayed and uneven. Simultaneously, a large drop in phase contrast can be found. This suggests that the oxide layer on the top surface of the columns is removed, leaving behind bare silicon, which is also visible as a rounding of the edges and roughening of the surface. Despite this, the mean etch height increases to a maximum value of 401 nm after 180 s, albeit with a large standard deviation of 113.0 nm. The phase contrast on the other hand reaches a minimum after 160 s and remains at this value for all samples with even longer etch time. After 240 s the etch depth decreases again to a value of (187.4 ± 42.2) nm at 300 s and remains around this value also after 600 s. These changes, especially in the phase contrast indicate that the oxide layer initially covers the area over the buried implants and protects the silicon underneath from etching, leading to a patterning according to the implants. This oxide

layer is however not stable indefinitely and after around 100 s the layer is removed, visible as a structural change of the columns top surface and a strongly decreased phase contrast. Afterwards, as the protective effect no longer guides the etching, the etch depth decreases, but reaches a stable value due to homogeneous etching of all surfaces. The development of etch depth and phase contrast is also collected in graphical form in Figure 3.40.

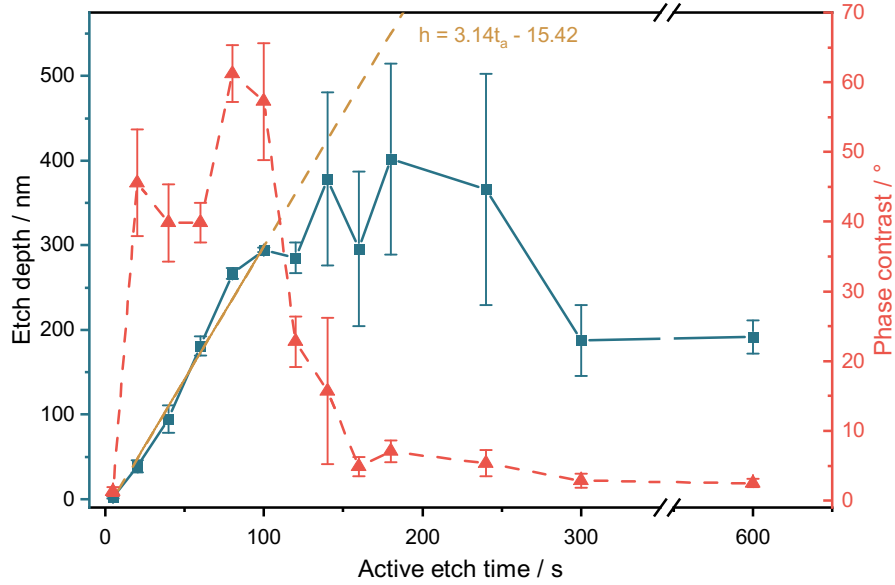


Figure 3.40: Figure of etch depth and phase contrast over time for samples with 250 nm top epitaxial layer. Measured from multiple AFM images for each sample/data point.

As described, a clear increase in phase contrast, indicating the onset of silicon etching after removal of the native oxide layer, is visible. The high phase contrast remains for around 100 s, while the etch depth increases in the same time linearly with a rate of $(3.14 \pm 0.28) \text{ nm s}^{-1}$. Afterwards, the phase contrast decreases strongly, indicating the removal of protective silicon oxide from the top surface of the pillars. Still, the etch depth increases further, albeit in a non-linear fashion and uneven over the sample surface, visible in the high standard deviation. Afterwards, the pillar height first remains constant, before it finally decreases to a low, but constant value, as the etch rate is even over the whole surface.

In summary, these results show that a certain etch time is necessary, before the structure of the buried implants is properly reproduced as etched columns. At least 20 s are necessary, before a significant etch depth is found, while times longer than 100 s produce lower quality results and should be avoided.

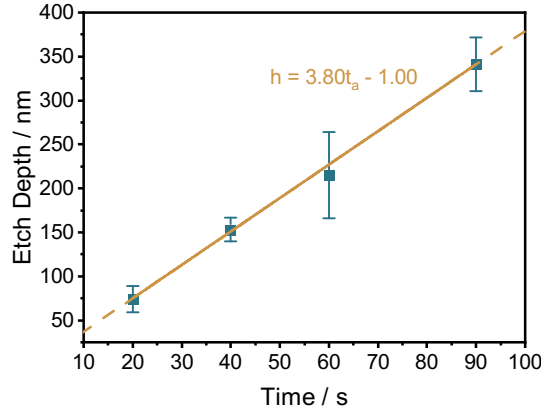


Figure 3.41: Figure of etch depth over time under dark conditions. Measured from multiple AFM images for each sample/data point.

After determining the etch rate under illumination, the same value in dark was determined as well. With this information, it is possible to determine if the illumination influences the silicon etch speed in a significant way. For this, the etch depth at certain time intervals, under otherwise identical conditions, was measured. A time frame from 20 to 90 s was chosen to correspond to the previously determined linear etch progress region. As no structures are etched into the silicon without illumination, the etch depth could not easily be measured from the column height, as before. Instead, an etch mask was prepared from SU-8 photo resist, using TEM grids as a simple photomask. This way, parts of the original surface remained unetched, which could then be used as a height reference to determine etch depth. The results are shown in Figure 3.41, showing an etch rate of $(3.80 \pm 0.10) \text{ nm s}^{-1}$. This is slightly higher than the etch rate under illumination, but quite similar, suggesting that the silicon etching is not influenced strongly by the illumination. It can be assumed, that the etching of silicon itself is not influenced by the buried implants, as apparently the silicon oxide layer is. Furthermore, the reduction in etch rate is in good agreement with reports from Glembocki *et al.*. They report that illumination of n-type silicon substrates during etching leads to a reduction of the etch rate as compared to etching in the dark^[53]. For the selective etching due to buried p-type implants this implies that the visible effect of column formation is not due to an influence on the actual etch rate of silicon, but is caused by another effect. From the time dependence under illumination it was possible to gain insight that selectivity is already measurable for the etching of the native silicon oxide layer before the silicon substrate itself is etched. Furthermore, large changes in phase contrast between the column tops and the surrounding areas during the etch process can be measured. The phase contrast can be attributed to a material difference between the etched silicon sub-

strate and the silicon oxide layer, which was detectable on the top surface of the pillars up to 100 s after the etch onset, whereas the oxide was removed from the remaining surface areas immediately upon etch onset. These results suggest that the oxide layer plays an important role in the mechanism and provides a means for selectivity. This is supported by previous results on samples where the native oxide was removed prior to the etch process. No selectivity could be found on such samples, but instead the surface was etched evenly.

3.4.5.5 Resolution Limit

From the previously shown time-dependent measurements, besides the structure-height, the dimensions of the structures in lateral direction can be investigated for the varying time steps and compared against the original implant sizes. As shown, the time frame of active etching from the onset until 100 s leads to properly resolved structures, which allow for a meaningful evaluation of structure size. As the structures do not exhibit perfectly vertical sidewalls, but are slanted, only the top diameter of the columns is evaluated, as this represents the unetched sample surface area. For every sample between 20 s and 100 s, the diameter at the top was measured and the structure size offset l_o calculated via

$$l_o = \frac{d_{etch} - d_{imp}}{2} \quad (3.13)$$

with d_{etch} and d_{imp} being the diameters of the etched structures and original implants, respectively. The resulting values, plotted against the active etch time are shown in Figure 3.42a. As previously described, the offset is always positive, meaning that the structure realised through etching is consistently larger than the buried implant. The measured offset is not constant, but decreases with increasing etch time. After 20 s of active etch time, the offset is around 900 nm, corresponding to almost a 50 % size increase for the smaller structures. This value decreases to a minimum value of around 100 nm after 100 s, which is a less than 10 % size increase. It becomes clear, that the selective etching effect does not perfectly replicate the dimension of the buried implants. Notably though, the offset is constant under identical process parameters, allowing for it to be factored into the fabrication of devices when using this selective etching process. Additional experiments were conducted to investigate how the offset varies between samples with different burying depth of the implants. For this, samples with 500 nm and 250 nm depth were etched for 40 or 80 s and the dimensional offset determined as described above. The results for these experiments are shown in Figure 3.42b. The samples etched for 40 s show an offset of around 500 to 600 nm, regardless of burying depth. After 80 s of active etch time, again no offset difference is discernible between the

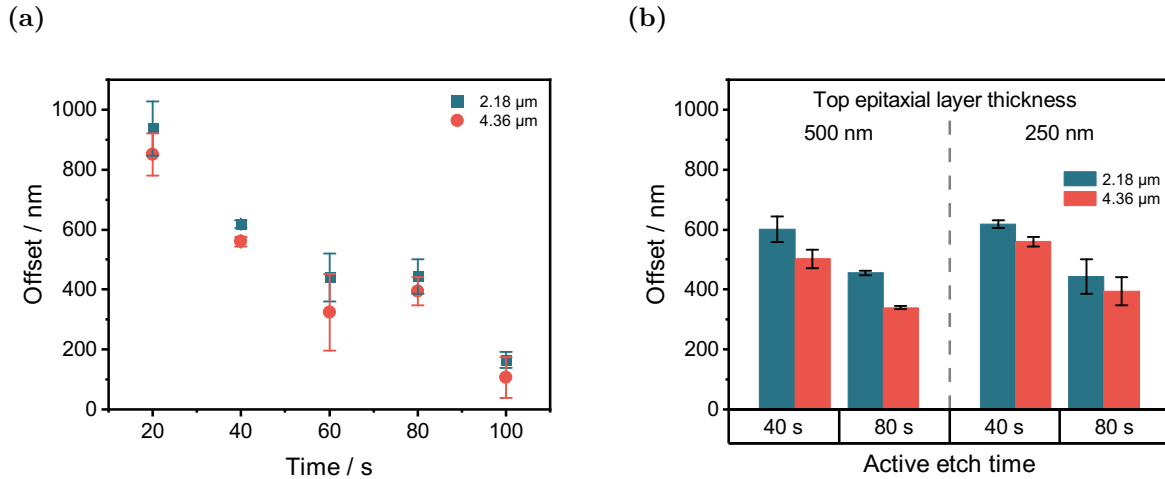


Figure 3.42: Figures for time dependent etching results on samples with 250 nm top epitaxial layer thickness. (a) Dimensional offset over time for both implant sizes. The offset is the difference in the radii of implants and resulting columns. (b) Figure of etch depth over time under dark conditions. Measured from multiple AFM images for each sample/data point.

two burying depths. For both, the value is between 300 to 400 nm, as was also measured before (see Figure 3.42a). This shows that the offset is not significantly influenced by the depth of the buried implants.

To further establish the resolution limit, samples with structures in varying sizes from around 7 to 0.3 μm were investigated. The implant structure on these samples contains various lines at different line widths and distances, as shown in Figure 3.2c. AFM images of such samples, etched in 0.6 wt% NH_4OH under 730 nm wavelength illumination are shown in Figure 3.43. Two different structure sizes are shown, etched under the same conditions, except for different time intervals. Figure 3.43a shows a sample position with a structure size of 1.8 μm. The value 1.500 visible in the structure represents the intended size, which was scaled up by 20 % due to the change in optical mask reduction from 5x to 4x. The image shows that the implant structure was reproduced clearly, with all features but the smallest hole at the bottom visible, as can be seen from the overlay of the theoretical structure. The width of the lines could be measured as $(2.05 \pm 0.11) \mu\text{m}$ at the top. This results in an offset value of 0.12 μm, calculated with equation 3.13. In comparison to the results on samples with hexagonal implants, this value is small, which might be due to variations in the actual doping concentration, depending on the structure and feature size. A smaller structure with a feature size of 0.72 μm is shown in Figure 3.43b, etched for 90 s. Here, the structure is much less clearly reproduced with most lines fused together. Only those lines with sufficient distance are recognizable. The visible lines measure $(1.10 \pm 0.09) \mu\text{m}$, yielding an offset value of 0.19 μm.

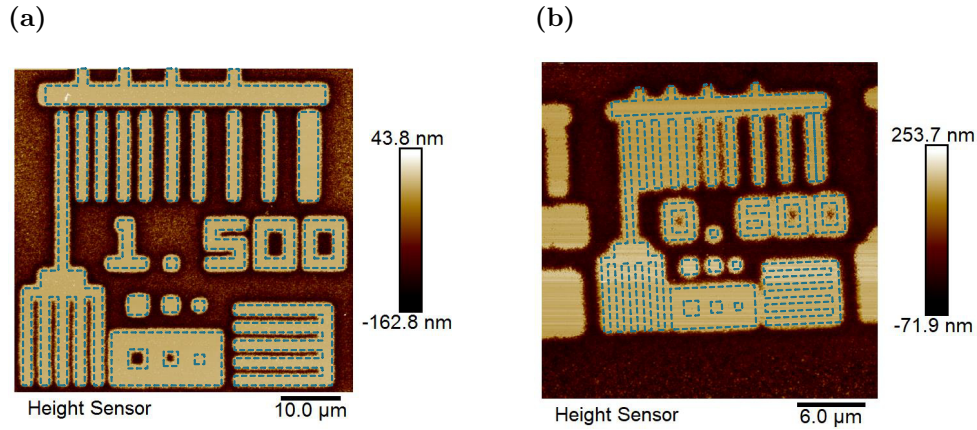


Figure 3.43: AFM height images of samples with 500 nm top epitaxial layer thickness and varying implant structure size. The theoretical implant structure is marked on both images with dashed blue lines. (a) Sample etched for 40 s active etch time, showing structure with 1.5 μm marked size. Real size is 1.8 μm due to optical mask reduction. (b) Sample etched for 90 s active etch time, showing structure with 0.6 μm marked size. Real size is 0.72 μm due to optical mask reduction.

The presented results suggest that the highest possible etch time should be chosen in order to achieve the best possible dimensional accuracy. Nevertheless, even with higher etch time, very small feature sizes are only achievable with sufficient distance. If features are too close to each other, the protective effect, spreading slightly outwards from each implant (see Figure 3.31), overlaps, making etching in between implant areas impossible. Accordingly, the selective etching process is not directly translatable to all structures, but allows for high fidelity reproduction of larger features, e.g. in MEMS/MOEMS applications.

3.4.6 Investigation of the Mechanism

From the previous optimization experiments, some important information about the evolution of the etch selectivity was already gained. In particular, the wavelength and time dependence provide some important information.

From the wavelength dependence, the general idea of illumination influence on the buried implants can be confirmed, as the measured dependence is in good agreement with the expected absorption behaviour. The maximum of etch depth around 800 nm means that at this wavelength the strongest protective effect was achieved, likely due to the largest number of absorbed photons. Furthermore, from the time dependence experiments, very useful information regarding the start of the selective etching and the overall progress could be gained. The first signs of selectivity were only found immediately after the visible onset of the etching progress, meaning, that within the 5

to 10 min of induction period, no measurable silicon etching takes place. Accordingly, the native oxide layer is first etched significantly in areas without underlying p-implants. Above these implants, the oxide is removed slower, leading to a structuring of the native oxide layer, replicating the buried implant structure. This was confirmed by AFM phase measurements, showing a large contrast, likely due to the material difference between SiO_2 and etched silicon. From this, it appears that the native oxide, rather than the silicon itself is influenced by the illumination, creating an in-situ etch-mask made of silicon oxide, which in turn directs the removal of silicon, creating the observed column structure. This hypothesis is also supported by the results obtained from etching of samples after removing the native oxide layer and the comparison of the etch rate under illumination and in dark. Samples without native oxide layer show no selectivity in regards to the buried implants, while the silicon etch rate is not significantly influenced by the illumination.

Furthermore the determined top epitaxial layer thickness dependence can be explained using the process described in the mechanism hypothesis. It was found that while thicknesses of 250 nm and 500 nm lead to perfect implant structure reproduction, a higher thickness of 1000 nm leads to a strongly decreased fidelity with a pitted surface of the column top surfaces. This is likely due to the variation of the extent of the pn-junction between the buried implants and the surrounding n-Si in vertical direction and how it influences the electron flow. With the equations shown in section 3.4.2 the extent of the pn-junction into the n-Si in the vertical direction can be calculated as 832 nm. This value varies from the extent in horizontal direction (1270 nm), as the n-doping concentration in the top and bottom epitaxial layer are slightly different. The calculated value shows that in the case of 250 nm and 500 nm top epitaxial layer thickness, the junction reaches all the way through the top epitaxial layer up to the surface. Electrons are therefore swept directly to the surface due to the built-in electric field. On the other hand, at a top epitaxial layer thickness of 1000 nm the junction does not reach all the way to the surface and the electrons therefore have to diffuse a certain distance to the surface. This potentially weakens the protective effect as not all photogenerated electrons reach the surface to induce the protective effect. Accordingly, the found dependence is in excellent agreement with the proposed mechanism.

In addition to these results, the previously proposed mechanism can be tested more intensely with a number of experiments. This includes the analysis of how varying etch regimes, such as variations in illumination duration and induction period change the etch progress and result, direct measurements of the illumination-induced charging and calculations regarding the photophysics of the proposed mechanism.

3.4.6.1 Variations in the Etch Regime

The experiments investigating the mechanism hypothesis were mainly concerned with how the etching progresses with and without light under different conditions. First, it was investigated if the illumination of the sample surface needs to be maintained for the duration of the active etching, i. e. the time in which silicon is actually removed. This should yield further information regarding a potential influence of the illumination on the silicon etching itself, in the form of photoassisted etching, i. e. increase in silicon etch rate due to illumination. For this purpose two sample sets were prepared, each with multiple samples with 50 s and 100 s active etch time. One sample set was subjected to the normal etch regime and illuminated during the whole process. For the other set, the illumination source was turned off and the setup covered to exclude any light, 10 s after the onset of the reaction was visible on the surface, i. e. the starting point of the active etch time. After the pre-determined active etch time, the samples were removed from the setup and cleaned as usual. From AFM images the topography and pillar height for all samples was measured to investigate how it changes depending upon illumination duration. Figure 3.44 shows the results of these experiments with exemplary AFM images and the mean column heights for all samples. As can be seen from the micrographs, the topography of the structures is identical, regardless of if the illumination is sustained for the full active etch time or only 10 s of it. Similarly, the column height results show that the etch depth does not change if the sample illumination is stopped shortly after the etching onset. For the respective etch times, the resulting pillar heights are essentially identical. After 50 s the column heights are around 180 nm, whereas after 100 s the etch depth reaches around 340 nm. Therefore, after the silicon etching onset, the illumination does not influence the etch process significantly, further supporting the previous results. It appears, that the illumination influences the substrate before the silicon is actually removed. This supports the mechanism hypothesis of a silicon oxide passivation, as this process would necessarily take place prior to the actual silicon etching.

The next step was to determine if an influence of the illumination on the oxide layer can be measured. For this, the length of the induction period was measured under illumination and in the dark. As the oxide layer prevents immediate silicon etching, the time it takes until clear evidence of the removal of silicon is visible (gas formation, changes in surface appearance) is equal to the time it takes to remove the oxide layer. If the selective effect is based upon passivation, there should be no significant variation in the onset time, as the effect would only influence the areas above the implants. The remaining surface is unchanged and therefore is expected to etch with identical rate,

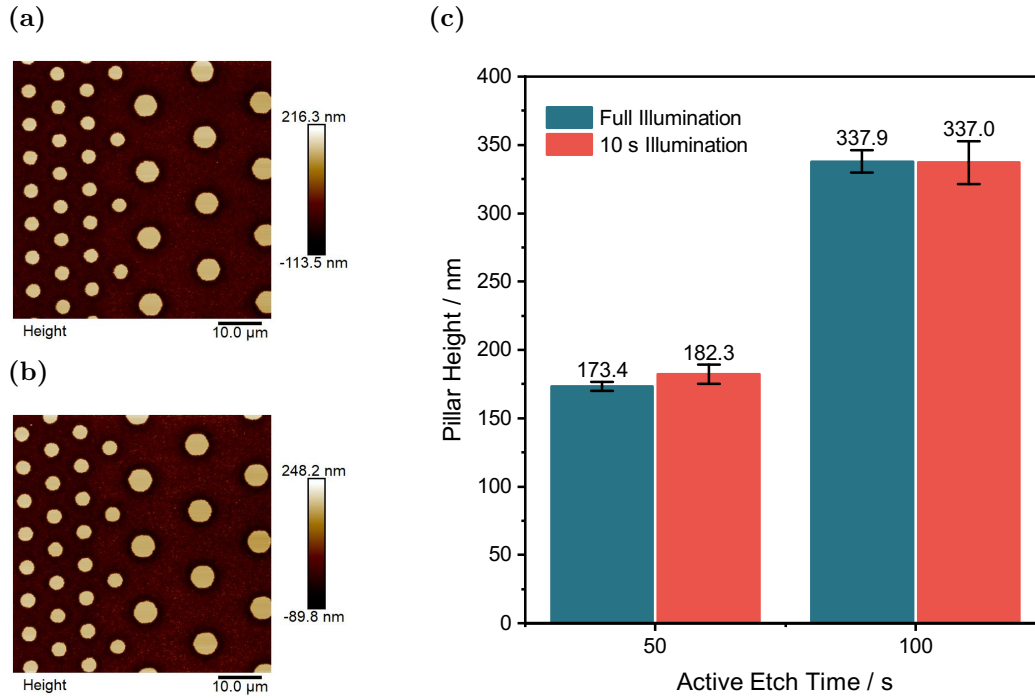


Figure 3.44: Results for samples with 500 nm top epitaxial layer fully and partially illuminated during etching. (a) Sample etched for 50s under full illumination, (b) Sample etched for 50s with only 10s illumination, (c) Graph showing the pillar height for all samples. No difference was visible for samples with full or only partial illumination.

regardless of illumination. If, in contrast, the onset time is significantly lower under illumination, compared to without illumination, it can be assumed that the illumination leads to an increase in oxide etch rate, specifically in areas without underlying p-implants, leading to the formation of an in-situ oxide-mask. The resulting onset times are shown in Figure 3.45a. For the three samples illuminated during etching, the mean onset time is (433 ± 33) s, while this value is (402 ± 30) s for the three samples etched in the dark. Accordingly, when etching samples under illumination, the onset is delayed slightly, i. e. the oxide etch rate is lowered. These experiments strongly suggest, that the in-situ-masking is induced by a passivating effect on the native oxide layer. As the oxide etch rate is essentially identical with and without illumination, the only explanation for the evolution of the in-situ etch-mask is the passivation of the oxide layer directly above the buried implants.

To further confirm the passivation hypothesis and determine how well the oxide layer is protected above the p-implants upon illumination, additional experiments with samples with full surface p-implants and without any implants, respectively, were conducted. For both sample types, the top epitaxial layer has thickness of 1000 nm (see Figure 3.1). On

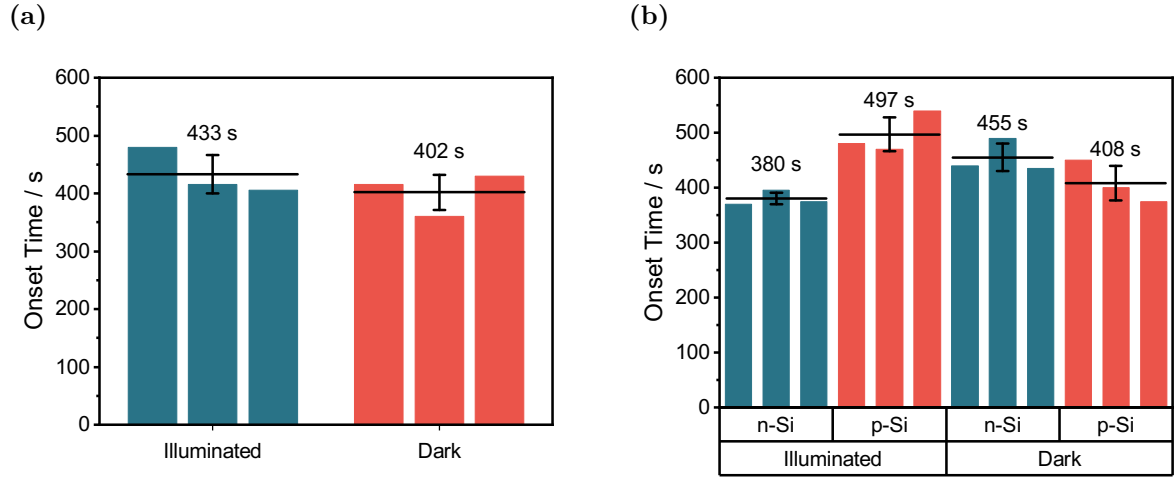


Figure 3.45: Results of the illumination dependent etch onset investigation. The black lines and numbers show the mean value for each sample group. (a) Comparison between onset in dark and under illumination for samples with hexagonal implant structure with 500 nm top epitaxial layer. (b) Variation in onset time for samples with full surface and no implant (1000 nm top epitaxial layer), respectively.

samples with full surface p-implant, it is expected that illumination during the etching process will lead to a significant delay of the etching onset, due to the passivating effect. On samples consisting only of n-type silicon, no such delay is predicted.

Figure 3.45b shows the measured values for onset time for three samples for each process regime, as well as mean values. For the samples with full area p-implant the mean onset time under illumination was (497 ± 31) s, whereas in dark the onset occurred after (408 ± 31) s. As expected, the onset was delayed significantly, due to the passivating effect, decreasing the oxide etch rate. Furthermore, the measured difference of 89 s fits well to the etching delay of the top of the columns, as previously determined during time dependence experiments, of around 100 s (see Figure 3.40). This gives further confirmation to the hypothesis that over the course of the light-induced selective etching process, the oxide layer over the areas with underlying, buried p-implants is removed slower than over the surrounding areas, leading to the formation of a thin oxide mask structured according to the implants. This in-situ mask then directs the basic silicon etching, leading to the formation of pillars.

On samples without any p-implant the etch onset in dark conditions is very similar to the value for samples with full surface implant, as expected. Interestingly, the samples without implant showed a distinctly shorter onset time when illuminated, compared to the results in dark. It appears that the illumination induces a higher oxide etch rate on fully n-type silicon samples. Possibly, positively charged hole charge carriers generated due to the illumination diffuse to the surface, reducing the negative charge

there, facilitating the etchant attack and subsequent removal of the native oxide layer.

With the information gained from these experiments it is possible to calculate the etch selectivity between Si and SiO₂ and compare them to theoretical values. The etch selectivity is simply the ratio between the etch rates of silicon and SiO₂ at the same conditions. For the time dependent experiments shown in Figure 3.40 the selectivity can be determined for the areas with and without underlying p-implants. In both cases the silicon etch rate is identical, as the etched volume is homogeneously doped n-Si and it was shown that the illumination does not change the etch speed of bare silicon. From the experiments, the silicon etch rate was determined as 3.14 nm s^{-1} over the first 100 s of active etch time. For the SiO₂ etch rate, the value varies, depending on the underlying doping structure. For the areas without underlying implants, the oxide was removed within the induction phase, i.e. the onset time. The mean onset time for all samples was $(390.5 \pm 37.8) \text{ s}$, yielding an oxide etch rate of $3.3 \cdot 10^{-3} \text{ nm s}^{-1}$ in combination with the known oxide thickness of 1.29 nm. Now, the same calculation can be used to find the SiO₂ etch rate above the buried implants by adding the known delay of 100 s, after which the oxide is also removed from the etched pillars, to the mean onset time. This results in an etch rate of $2.6 \cdot 10^{-3} \text{ nm s}^{-1}$. For both cases the selectivity can then be calculated as the ratio of silicon to SiO₂ etch rate. This yields a value of 950 for the areas with buried implants and 1194 for the surrounding areas.

In the literature, Lee *et al.* report a SiO₂ etch rate of around $3.2 \cdot 10^{-3} \text{ nm s}^{-1}$ at 50 °C and a NH₄OH concentration of 5 wt%. At the same conditions, the silicon etch rate is reported as 0.01 nm s^{-1} ^[155]. The reported oxide etch rate is identical to the measured value for areas without underlying p-implants, confirming the validity. As for the silicon etch rate, Lee *et al.* report a much lower value, as achieved in these experiments. When calculating the etch selectivity, a value of only 3.1 is achieved^[155]. In contrast, Van den Meerakker *et al.* report a silicon etch rate of 1.4 nm s^{-1} at 50 °C and a NH₄OH concentration of 3.2 wt%^[154]. With the previously used value for the SiO₂ etch rate, a selectivity value of 474 can be calculated. This is closer to the value obtained in this work, but nevertheless significantly smaller, indicating that the illumination does indeed increase the selectivity greatly. It has to be noted that Schnakenberg *et al.* report an etch selectivity of around 2000 in 3.7 wt% NH₄OH at 50 °C. This value is much larger, due to the reported very low SiO₂ etch rate of only $2.7 \cdot 10^{-4} \text{ nm s}^{-1}$ most likely because of the use of thermal oxide instead of a native oxide layer. Accordingly, this value is not comparable, unlike the reported values by Lee *et al.* and Van den Meerakker *et al.* With regards to the application of a thin oxide mask in typical structuring processes, e.g. in MEMS/MOEMS applications, a high etch selectivity of about 1000 is desirable,

as it allows for deep structuring, due to the high stability of the etch-mask^[39,156]. This can be achieved with the here presented LISE process, allowing for its potential use in a productive environment.

3.4.6.2 Photocurrent Measurements

With the previous investigations, the effect of the illumination on the etching process has been extensively determined, showing very good agreement with the hypothesised mechanism. Missing is the direct measurement of the charge carrier flow upon illumination. This is essentially the photocurrent at the pn-junction between the p-implants and the surrounding n-type sample bulk. One way of measuring the photocurrent are electrical measurements in solution under illumination. For this, samples were immersed in the typical etchant solution inside the previously employed electrochemical cell (see Figure 1.14). The sample was again attached to the working electrode using Ga-In-eutectic inside the custom-made PTFE holder, while the counter electrode was immersed in the electrolyte solution. The reference electrode was not used, as it was not needed for current measurements alone. The system was kept at room temperature, instead of 50 °C, in order to prevent etching of the sample during the measurement. Beneath the cell, orthogonal to the sample surface, a LED lamp with a wavelength of 730 nm was placed and turned on intermittently, inducing charge carrier generation in the sample. No external voltage was applied via the electrodes and the current flowing between the electrodes was measured over time using a potentiostat. As this setup results in the measurement of the average current over the full sample surface, samples with microscopic implant structure could not be used. Instead, samples with either full or no p-implant were used (see Figure 3.1), which had a top epitaxial layer thickness of 1000 nm. The measured current under illumination can then be compared to gain understanding about how generated charge carriers are influenced by the buried implants.

For each tested sample, the light source was activated after the same scheme, starting with 15 s of no illumination, followed by 15 s of active illumination. This cycle was repeated until an overall experiment time of 300 s was reached. This way, the resulting graphs of current over time allow for the direct comparison of the effect of illumination on the measured current between different samples. Figure 3.46 shows the results of current measurements for such samples, measured in the typical etchant solution of 0.6 wt% NH₄OH in water. As can be seen, a sample without buried implants (blue line) initially shows a negative current, regardless of illumination state. Upon illumination, a strong change in current to more positive values, i. e. an anodic current, is found^[167]. After around 100 s the negative current approaches zero, when not illuminated and fully

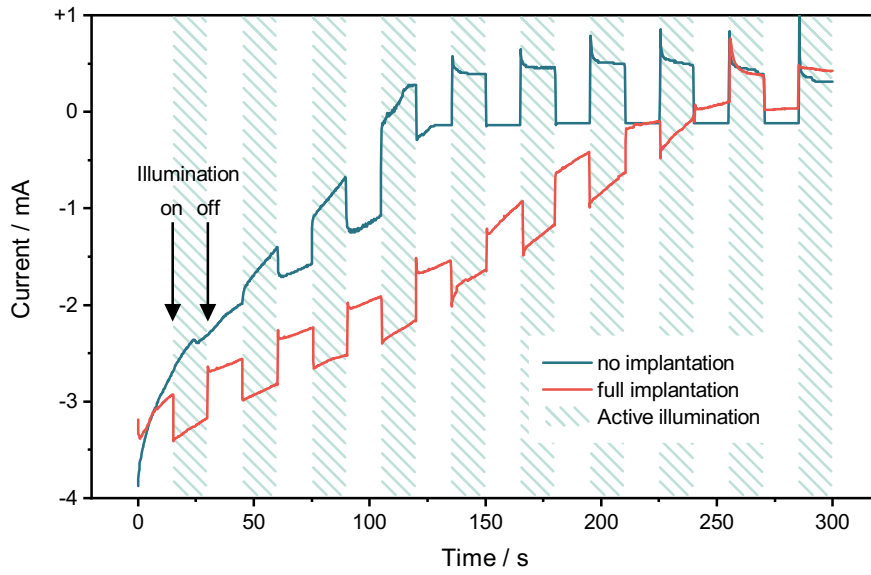


Figure 3.46: Figure of photocurrent over time in NH_4OH -etchant solution for samples with 1000 nm top epitaxial layer with and without full surface p-implant. The light source was turned on intermittently for 15 s over 300 s.

positive when the light source is active. The initially relative and later-on absolute positive current flow upon illumination indicates electrons flowing from the solution into the sample, to be then measured by the ammeter. The initially negative, but zero-approaching current is likely due to the build-up of charge on the surface, equilibrating the system. The charge likely blocks current flow from the sample into the solution leading to current flowing only in the opposite direction, measurable as positive sign current. This also explains the low impact of illumination on the current in the first two to three illumination cycles, as here the photocurrent can still flow equally in both directions, canceling itself out. After the equilibration, the driving force for current flow towards the solution (negative flow direction) is not strong enough to overcome the barrier, and only current in positive flow direction is measurable. Also notable in the positive region are spikes at the initial current increase upon illumination, which can be attributed to the rapid charging of junctions in the electrical system acting as capacitors^[167].

Samples with buried implants (red line) show an initial negative current as well, which is further increased by a strong negative sign, i. e. a cathodic current upon illumination^[167]. Thus, the current flow is opposite to the flow on samples without buried implant (blue line). Accordingly, the photocurrent here moves mainly from the sample into the solution and from there through the counter electrode to the ammeter, which coincides with electron flow from the buried implant to the surface, as proposed in the mecha-

nism. Here, the strong driving force due to the charge separation at the pn-junction is able to overcome the surface charge due to equilibration and photocurrent. Notably, after around 200 to 250 s the sign of the photocurrent changes when the dark current approaches zero, indicating that now the driving force is not strong enough to induce further electron flow from sample to solution, because the built-up charge is too high. Instead, only current flow in the opposite direction is measured, similar to the sample without buried implants. Also for these samples, spikes in the current flow were visible at the on-point in the photocurrent transient, again attributed to rapidly charging capacitances in the system^[167].

Additional experiments were then carried out to investigate how a change in electrolyte composition or surface properties affects the measured photocurrent. As the surface charge seems to influence the current flow to a large extent, any change in this property is expected to be easily measurable as a variation in photocurrent flow. First, experiments were carried out in a different electrolyte, consisting not of a basic NH_4OH -solution, but instead of hydrochloric acid in water at $\text{pH} \approx 2$. As was described before, silicon oxide exhibits a variable surface charge, depending on the solution pH. While the surface is strongly negative charged at the solution pH of around 10 in the standard etchant solution, at pH 2 the surface is instead positively charged. The results from such experiments on samples with and without implants beneath a 1000 nm top epitaxial layer are shown in Figure 3.47.

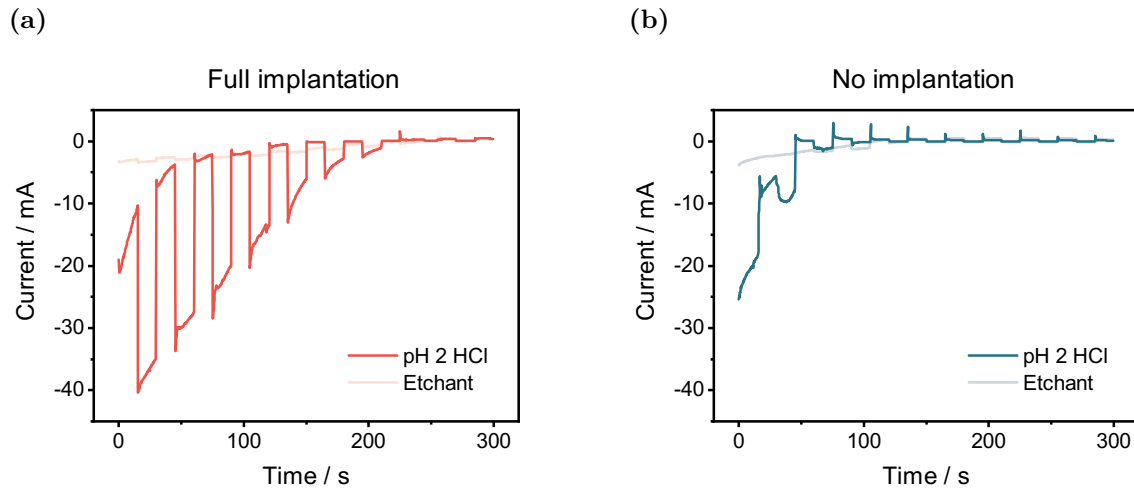


Figure 3.47: Figure of photo current over time in a pH 2 HCl-solution for samples with 1000 nm top epitaxial layer with (a) and without (b) full surface p-implant. The light source was turned on intermittently for 15 s over 300 s.

For both sample types, the overall behaviour is similar to samples in the basic etchant solution, but a strong increase in the initial dark current was measured, reaching values

of up to -25 mA , more than a 5-fold increase. This indicates that a much larger flow of electrons is possible, hinting at a smaller current barrier, due to the positive surface charge of silicon oxide in acidic solutions. This effect was especially apparent for the photocurrent on samples with buried implants, showing an 10-fold increase compared to the sample in basic solution, which supports the notion that a strong negative surface charge inhibits the flow of electrons. As before, a zero crossing with inversion of the current sign after around 200 to 250 s was observed. This indicates that even in acidic solutions a surface charge develops, which eventually poses a large enough barrier to prevent further electron flow from the sample to the surface. It is assumed that this charge builds-up due to charge-carrier generation, as proposed in the mechanism. For the samples without additional p-type implants, the behaviour is much closer to the effect in basic solutions, as the surface charge does not play such an important role.

In another experiment, the typical etchant solution was mixed with a small amount of hydrogen peroxide to provide readily reducible species. These species can potentially change the measured photocurrent as the generated electrons reduce them, leading to a decrease in measurable photocurrent. The results for these experiments are shown in Figure 3.48.

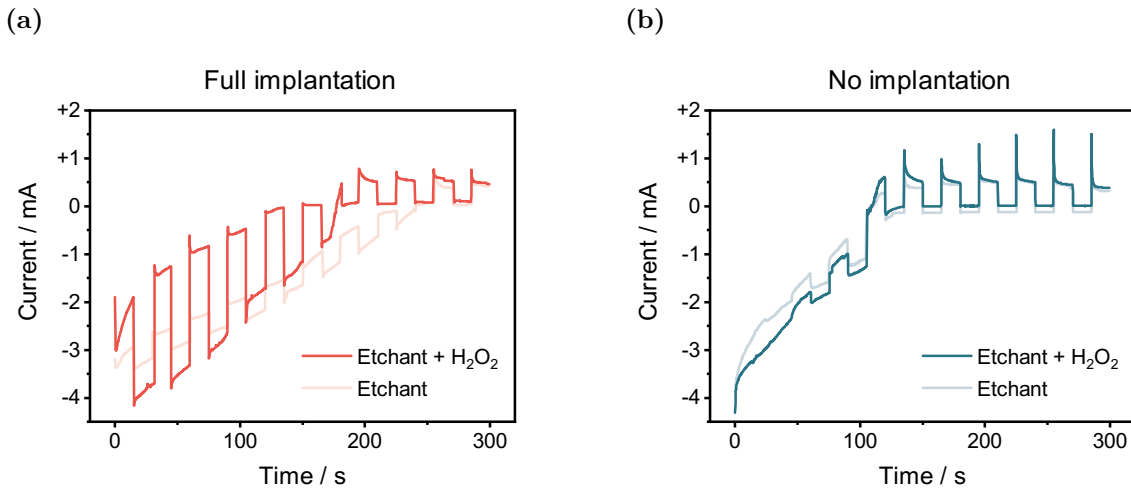


Figure 3.48: Figure of photo current over time in etchant solution with added hydrogen peroxide for samples with 1000 nm top epitaxial layer with (a) and without (b) full surface p-implant. The light source was turned on intermittently for 15 s over 300 s.

Samples with buried implants show a strong increase in the magnitude of the photocurrent. With added peroxide, the difference between dark current and photocurrent is as high as $2.5\text{ }\mu\text{A}$, where the same value in the normal etchant solution is only around $0.5\text{ }\mu\text{A}$. This increase might be attributed to electrons reducing the peroxide instead

of building up a surface charge as barrier. Notably, the magnitude of the positive sign current after the zero-crossing is similar to the results in unaltered electrolyte, as again this value is not affected by the solution as much. On samples without buried implants, the photocurrent behaviour is essentially identical to the case without added H_2O_2 . This is expected, as the measured current does not immediately flow through the solution in order to be registered at the ammeter.

The photocurrent experiments could demonstrate that upon illumination of samples with layered doping structures in electrolyte solutions, charge carrier flow is in very good agreement with the proposed mechanism, flowing from the pn-junction to the sample surface, where it can possibly influence the etching reaction. Furthermore, a strong influence of the surface charge on the photocurrent was determined, indicating that both interact. Apparently, the photocurrent is able to change the surface charge, modulating further carrier flow by inducing a charge barrier. This charging is what leads to the selective etching, as proposed in the mechanism.

3.4.6.3 Theoretical Photocurrent Calculation

In order to substantiate the experimental confirmations of the proposed mechanism with theoretical calculations, the generated photocurrent due to illumination, charge carrier generation and diffusion was determined. For this purpose, some experimental properties need to be known, namely the illumination source irradiance E_e and the irradiated sample surface A_a .

The irradiance E_e of the used 730 nm LED light source in the used CV cell at the correct distance to the sample was measured as 316 W m^{-2} at 730 nm wavelength. The photon irradiance E_q can then be calculated as:

$$E_q = \frac{E_e \lambda}{hc} = \frac{316 \cdot 730 \cdot 10^{-9} \text{ W m s}}{6.626 \cdot 10^{-34} \cdot 2.99 \cdot 10^8 \text{ J s m}^3} = 1.161 \cdot 10^{21} \text{ m}^{-2} \text{ s}^{-1} \quad (3.14)$$

with λ being the irradiation wavelength, h the Planck constant and c the vacuum speed of light. In combination with the illuminated surface area A_a of the sample the number of incident photons per second can be calculated as:

$$\Phi_i = E_q A_a = 1.161 \cdot 10^{21} \text{ m}^{-2} \text{ s}^{-1} \cdot 193.6 \cdot 10^{-6} \text{ m}^2 = 2.248 \cdot 10^{17} \text{ s}^{-1} \quad (3.15)$$

Due to surface reflection, not all incident photons can potentially be absorbed. The reflectance value can be calculated from literature values of the refractive index n_λ at

normal incidence of 730 nm light wavelength via^[163,164]

$$R = \left(\frac{1 - n_\lambda}{1 + n_\lambda} \right)^2 = \left(\frac{1 - 3.737}{1 + 3.737} \right)^2 = 0.334 \equiv 33.4\% \quad (3.16)$$

As the samples used for photocurrent measurements have a full surface implant, all of these incident photons are assumed to generate charge carriers, given that they are absorbed inside the pn-junction or within one diffusion length of it. As shown in section 3.4.5.3, the diffusion length is 504 μm , from which the absorbed ratio can be calculated using the absorption coefficient μ_{730} of silicon at a wavelength of 730 nm via:

$$Abs_{L,730\text{ nm}} = 1 - e^{-\mu_{730} 504\text{ }\mu\text{m}} \quad (3.17)$$

$$= 1 - e^{-1672.44\text{ cm}^{-1} \cdot 0.0503\text{ cm}} = 1 \quad (3.18)$$

Accordingly, all incident photons are absorbed within this region. It is now assumed that all of these photons generate carriers and all of the electrons diffuse to the surface. Therefore, the flow of charges q can be calculated as:

$$q = \Phi_i(1 - R)Abs_{L,730\text{ nm}} \quad (3.19)$$

$$= 2.248 \cdot 10^{17}\text{ s}^{-1} \cdot (1 - 0.334) \cdot 1 \quad (3.20)$$

$$= 1.498 \cdot 10^{17}\text{ s}^{-1} \quad (3.21)$$

Continuing from this value, the photocurrent is obtainable by division of q by the number of charges per coulomb C , leading to a value of $[\text{C s}^{-1}]$, which is equal to $[\text{A}]$:

$$I_{ph,730\text{ nm}} = \frac{q}{C} = \frac{1.498 \cdot 10^{17}\text{ s}^{-1}}{6.2415 \cdot 10^{18}\text{ C}^{-1}} = 0.0240\text{ C s}^{-1} = 24.0\text{ mA} \quad (3.22)$$

A theoretical photocurrent of 24.0 mA is induced due to the charge carrier generation upon illumination of a sample with full surface p-implant. This value is higher than the measured photocurrent in the typical etchant solution, as depicted in Figure 3.46, where the increase in current upon illumination is only around 0.5 mA. Here, the current barrier described for such samples is expected to reduce the measured value, compared to the actually generated photocurrent. Therefore, the calculated value appears reasonable, fitting well to the measured value. In contrast, the measured value in acidic solution, where the surface charge is positive, is around 30 mA (see Figure 3.47a), 25 % larger than the calculated photocurrent. This indicates that either the calculation is offset or that the measured current is influenced by another process than charge carrier generation. Possibly, the measured value for the incident power varies due to the sample placement

in the electrochemical cell, or the electrochemical setup influences the charge separation slightly. Nevertheless, the theoretical calculations fit to the measured photocurrent, confirming its accuracy.

Ratio of Absorbed Photons to Etched Silicon Atoms Based on the previous calculation, the ratio of absorbed photons to etched silicon atoms can be calculated as well. This value can provide further information about the participation of the charge carriers in the actual silicon etching process. In particular, in section 3.4.4, a possible enhancement of the silicon etch rate in areas surrounding the buried implants, induced by the photogenerated holes diffusing to the substrate-solution interface, was proposed. In order to investigate if this is reasonable, the number of etched atoms can be compared to the number of absorbed photons. In order to lead to the removal of silicon atoms by holes, the four binding electrons of each silicon atom need to be oxidized, i. e. four holes are needed per silicon atoms. The details of the calculation of both values are explained in the appendix, see section A.5. In short, the number of absorbed photons can be calculated as before, only differing in the active area, being only the area of the buried implants and the active etch time. As for the number of etched silicon atoms, this can be determined from the etch parameters, as measured from AFM images. With mean etch depth and etched surface area, the etched volume can be calculated. The number of silicon atoms can then be found via the atomical density, obtainable via the crystallographic parameters of silicon. These calculations yield ratios of around 0.25 absorbed photons, and subsequently generated holes, per etched silicon atom. This number is not sufficient to induce full photoetching, meaning that possibly only a small enhancement in etch rate is realistic. As shown in experiments regarding the time dependence (see Figure 3.42), a narrow ring of enhanced etching is visible at the perimeter of the area above the buried implants, which is possibly due to the proposed hole-enhanced etching. For this the calculated number of absorbed photons appears sufficient.

Overall, the calculations are in good accordance with previous etch results, showing that the silicon etch rate is not enhanced with illumination. Instead, the absorbed photons are only relevant for the enhanced protective effect of the silicon oxide. This further confirms the proposed mechanism, which envisions an influence of the generated charge carriers, in particular electrons, on the silicon oxide layer, enhancing its stability selectively above the buried implants, leading to the observed structuring in alkaline etchant solutions.

3.4.7 Summary

In this chapter, a light-induced selective etching process, discovered during the search for a self-alignment process, was investigated, characterized and a mechanism hypothesis formulated and tested. The discovered process, named LISE (Light Induced Selective Etching) allows for the easy and straightforward structuring of samples according to a buried implantation structure. In an unprecedented process, a structure can be introduced into a superficially homogeneous surface, showing no evidence of possible properties able to direct the etching process (see Figure 3.49a).

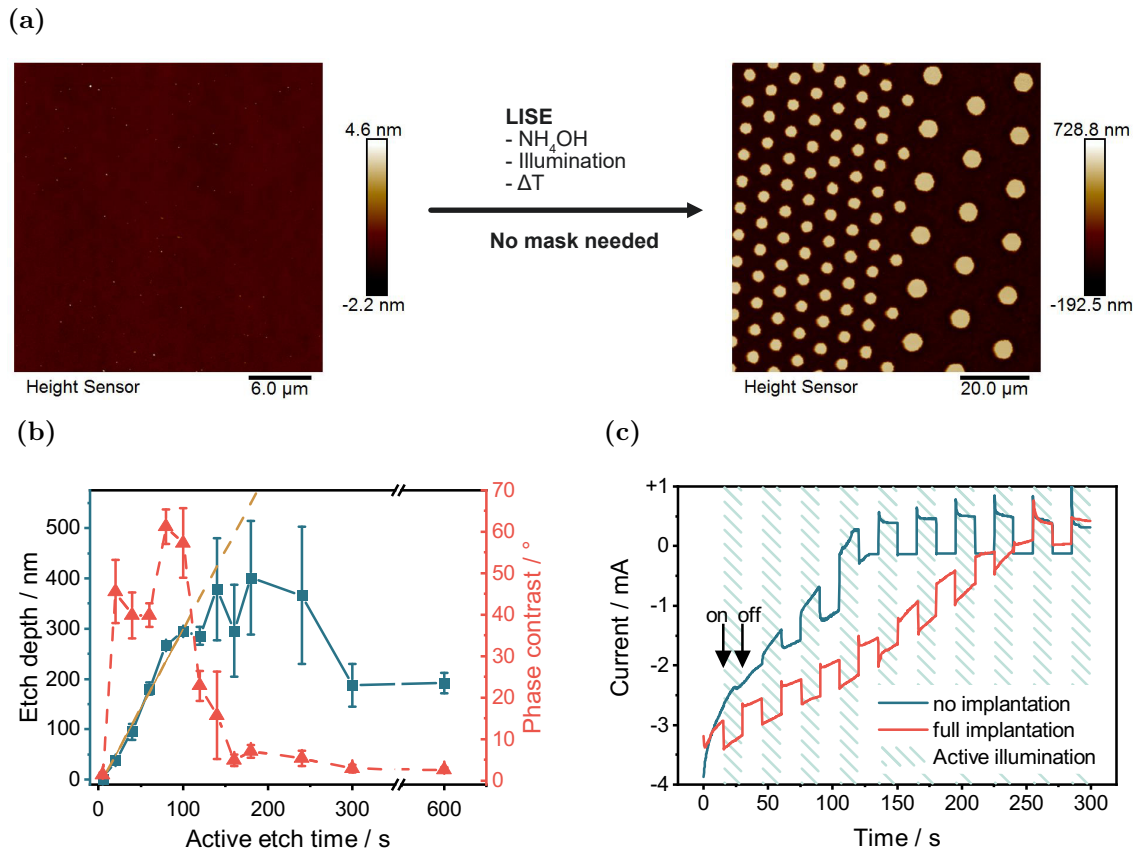


Figure 3.49: (a) By a simple process, samples with implants buried beneath a 500 nm top epitaxial layer can be structured, replicating the implant layout, without the need for lithography or other structuring methods. With only a light source and the etchant solution, high fidelity structuring is possible on otherwise completely homogeneous samples. Process investigations such as time dependency (b) and photocurrent measurements (c) confirm the mechanism hypothesis of an in-situ developed oxide etch-mask via charge induced protection.

Furthermore, no etch-mask is necessary. The process is based on the charge carrier generation due to illumination of the sample surface above the p-implants, buried beneath an up to 1000 nm thick top epitaxial layer. The charge carrier separation at the

pn-junctions in turn leads to the enhanced protection of the native oxide layer above the implant areas due to increased negative charging. It was found that while all investigated top epitaxial layer thicknesses lead to a successful reproduction of the buried structure with high fidelity. Only the hexagonal implant structure decreased in resolution at a top epitaxial layer of 1000 nm. In a multitude of experiments, the process was characterised in regards to etchant, temperature, wavelength and time dependence, as well as the achievable resolution limit. An ideal etchant composition of 0.6 wt% NH_4OH and ideal temperature of 50 °C and illumination wavelength around 700 nm was found. The proposed mechanism was tested extensively, proving that the illumination leads to an increase in silicon oxide stability against the alkaline etchant, likely due to electrostatic repulsion of the negatively charged OH^- -ions by the highly negatively charged oxide surface. This effect leads to the evolution of an in-situ etch mask of protected silicon oxide, while areas without underlying buried implants are etched normally (compare Figure 3.49b). In various experiments varying the process parameters, such as process time and illumination, and photocurrent measurements this was confirmed. The evolution of the in-situ mask could be shown from AFM height and phase images, demonstrating a sharp rise in phase contrast between etched and protected areas (see Figure 3.49b). It could also be shown, that illumination is not crucial during the actual etching period, but during the preceding induction phase, in which only the oxide layer is slowly selectively etched. The illumination also did not significantly change the length of the induction phase, indicating that no etch enhancing effect is apparent. This indicates, that the observed effect is mainly due to selective passivation of the areas above the buried implants. Photocurrent measurements further support the flow of electrons from the buried implants to the surface, as hypothesised (see Figure 3.49c).

3.5 Selective Polymer Deposition according to etched structure

3.5.1 Introduction

As was shown before, the structure resulting after the selective etching is not only apparent as a topography difference, but also as a material contrast between the etched areas and the top of the unaltered areas. Specifically, the contrast stems from the difference between bare silicon and remaining silicon oxide. Potentially, this opens pathways for the selective deposition of materials based on inhomogeneous surface properties. In the following part, such deposition of polymers in mainly two different ways is investigated. One is the direct deposition of polymers from solution and subsequent orientation of the polymer chains upon solvent evaporation or additional annealing steps. The second way is the selective surface polymerisation only on specifically modified areas of the etched substrate.

3.5.2 Deposition of Films

In the literature, a number of ways for the selective deposition of polymers from solution on inhomogeneous substrates are described. Generally, the most frequently used process is based on the uniform deposition of a polymer layer and a subsequent annealing step to induce a selective dewetting. Alternatively, a dropcasting process can be applied, inducing a selective material deposition during solvent evaporation. For both cases, polystyrene (PS) is frequently used as the material to be deposited. PS shows unfavourable surface interaction with silicon oxide layers, leading to dewetting, whereas the homogeneous deposition on H-passivated silicon, resulting from alkaline etching, is possible^[108].

Polystyrene Spincoating For spincoating experiments, PS with a molecular weight of $200\,000\text{ g mol}^{-1}$ was dissolved in toluene at varying concentrations from 0.1 to 10 mg ml^{-1} . This solution was spincoated on etched substrates at a rotation speed of 2000 rpm . Figure 3.50 shows AFM images of two samples, etched for 40 s of active etch time, spincast with a PS solution with concentration of 0.1 mg ml^{-1} and 10 mg ml^{-1} . No significant deposition took place for the lower concentration, only a small droplet of supposedly PS was found in the center of each column, indicating that during spincasting the material deposited here, dewetting slightly. In comparison, with a solution of $100\times$ higher concentration a thick layer is visible over the full surface and specifically on the column

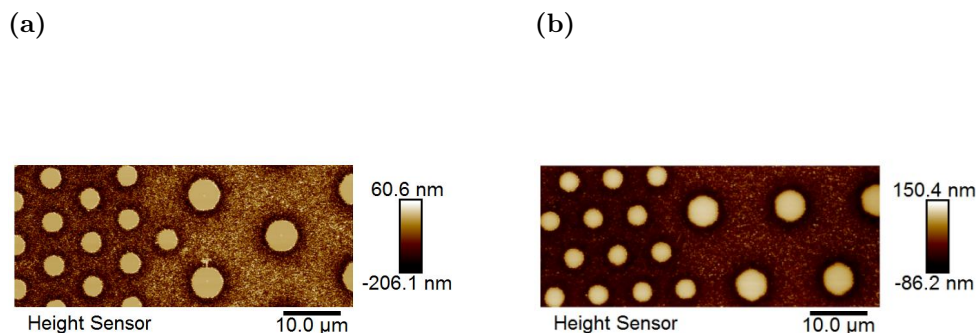


Figure 3.50: AFM images of samples spincoated and annealed with PS after etching. (a) PS-200k, 0.1 mg ml^{-1} , (b) PS-200k, 10 mg ml^{-1}

top surfaces, distorting the surface to a rounded shape, due to the surface tension of the polymer solution. Accordingly, the solution covered the surface unselectively and no significant dewetting took place, even after annealing at 120°C , well above the thin film glass temperature of PS at around 50°C ^[168]. Consequently, further experiments were carried out, varying the experimental parameters in order to achieve good dewetting. This included variation of the etching duration, polymer molecular weight, concentration, solvent and annealing parameters. None of these changes lead to successful selective deposition of the polystyrene. It was possible to deposit thicker, more homogeneous films, but again all samples showed the formation of small droplets of polystyrene on the top surfaces of the unetched areas, instead of dewetting and displacement of the polymer to the etched areas.

Polystyrene Dropcasting In a different approach, polystyrene was not spincoated, but dropcasted onto the etched substrates. In essence, a PS solution in a solvent with relatively low boiling point was dispensed onto the surface and left to evaporate in a small vial. The solvent chosen for these experiments was chloroform, as it evaporates with a suitable rate, if the sample is contained in a small vial. With this method, a final annealing step is not needed, as the slow evaporation and formation of a polymer film allows for enough mobility of the polymer chains to selectively deposit, according to the surface properties^[169,170].

Initial experiments were carried out with a 1 mg ml^{-1} PS-200k solution in chloroform. After dispensing the solution on the etched sample, it was covered and left to dry for at least 2 h. Afterwards the samples were investigated with AFM, as shown exemplary in Figure 3.51. Generally, the sample surface appears to be identical to the result im-

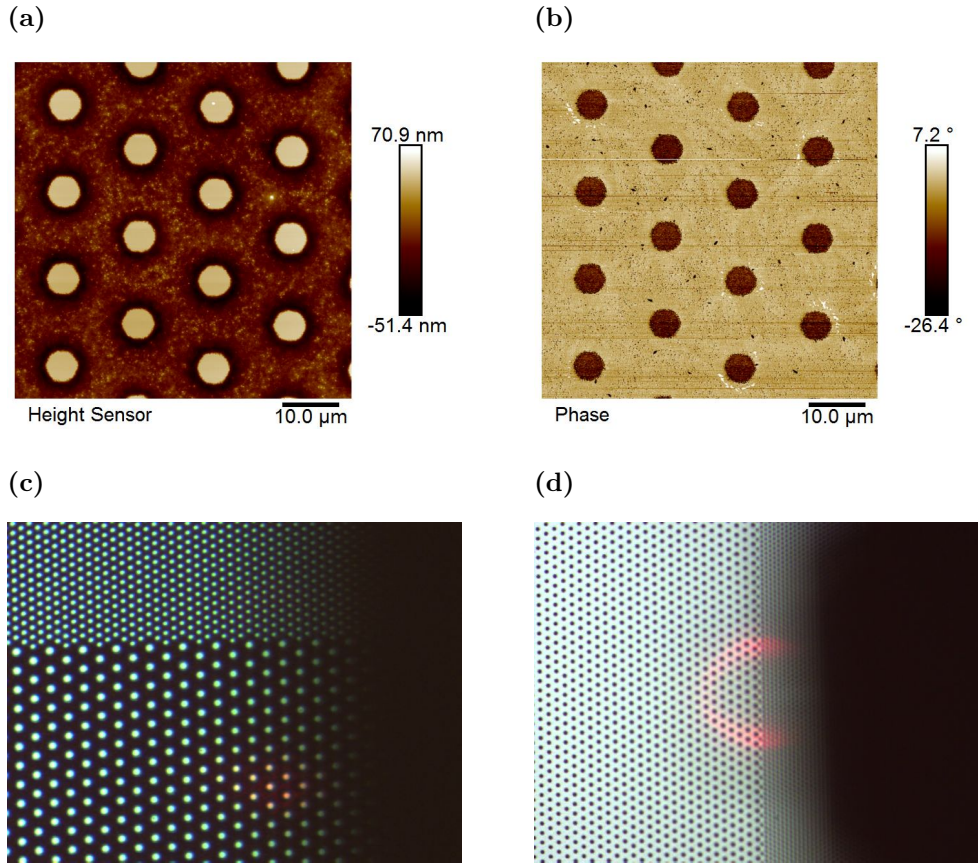


Figure 3.51: (a),(b) AFM images of samples with a dropcast PS film after etching. The PS-200k polymer was cast from a 1 mg ml^{-1} solution in chloroform. (a) Topography image, (b) corresponding phase image. (c),(d) Light microscopy images of samples with and without a dropcast PS film. The PS-200k polymer was cast from a 1 mg ml^{-1} solution in chloroform. (c) Sample with polymer film, (d) Sample after etching, without PS film.

mediately after etching. Upon closer investigation it becomes clear though that a PS film with a thickness of around 50 nm was deposited in the area between the columns. This was evaluated from the comparison to a sample after etching under identical conditions, showing a pillar height of around 126 nm, whereas the height on the sample with polymer film was around 75 nm. The selectivity of the deposition can be deduced from the change in surface topography in the etched areas, which can be found as a reduction in surface roughness (R_q) from 29.9 nm after etching to only 11.4 nm after the polymer deposition. Confirmation of the selective deposition only on the etched areas can be found in the strong phase contrast visible between the top of the columns and the polymer film (Figure 3.51b). Additionally, microscopic images of samples with and without deposited polymer layer show a clear change in reflectivity and light absorption in the areas between the columns (see Figure 3.51). It needs to be considered though

that, due to the low thickness, the achieved selective deposition might mainly be due to hydrodynamic effects of the polymer solution accumulating in the lower areas. During the final stages of the deposition the solution level might have been too low for the polymer to be able to deposit on top of the pillars. On the other hand, if no selectivity was actually achieved, at least a residue should be visible on the pillars, likely as variation in the phase image.

These initial results confirmed the general feasibility of selective deposition and further experiments were carried out aimed at increasing the film thickness. First, an increase in polymer concentration was investigated. For this, multiple samples were etched and solutions with concentrations of 2 mg ml^{-1} , 5 mg ml^{-1} and 10 mg ml^{-1} dropcast. AFM investigation showed no successful selective deposition, as on all samples a significant amount was deposited on top of the columns, as well as between them. Changes in the etch parameters, such as etchant and active etch time did not yield success as well. Only after a change of the polymer molecular weight to $35\,000 \text{ g mol}^{-1}$ selective deposition was achieved with a greatly increased layer thickness, as shown in Figure 3.52.

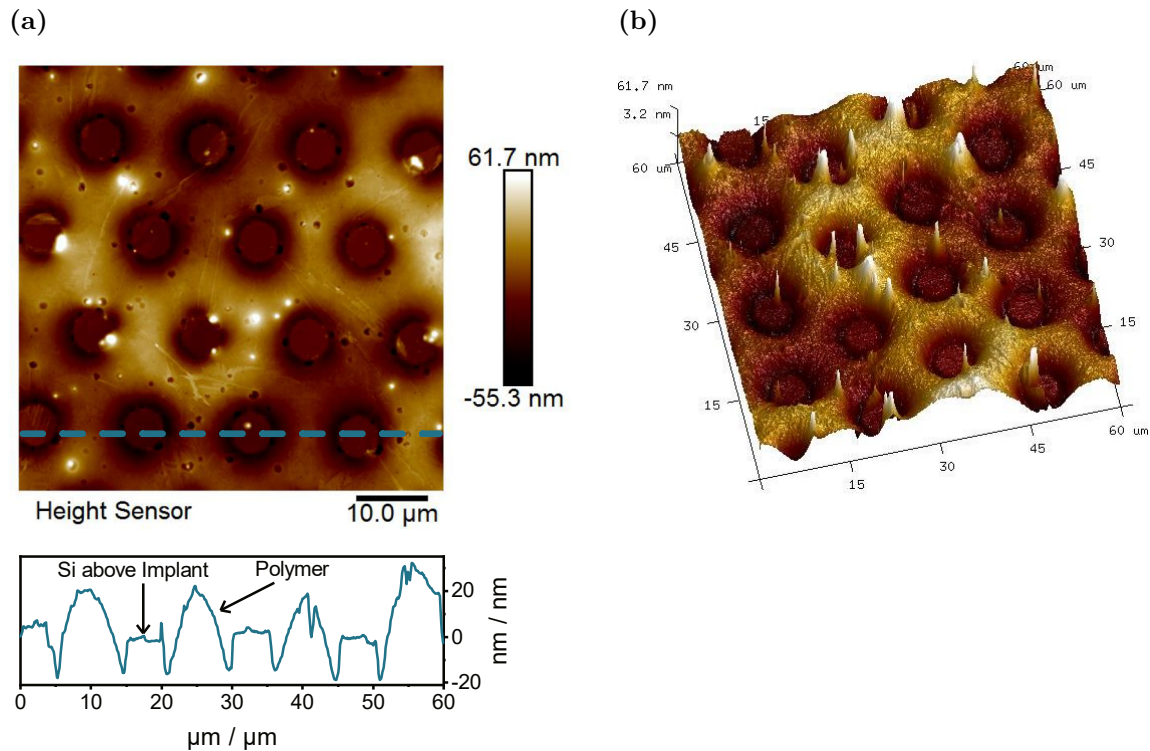


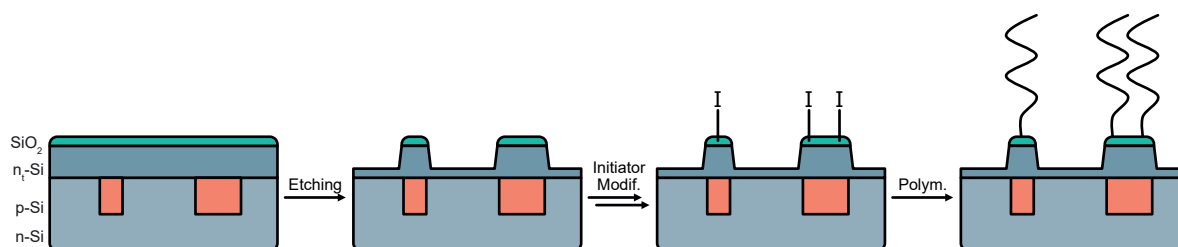
Figure 3.52: AFM images of samples with a dropcast PS film after etching. The PS-35k polymer was cast from a 1 mg ml^{-1} solution in chloroform. (a) Topography image and cross section, one Si-column and one polymer hill are marked as examples. (b) 3D representation of the topography highlighting the protrusion of the polymer film over the pillar height.

It is visible, that the polymer film is higher than the height of the pillars. Measurements of a scratch introduced after polymer deposition show a pillar height of around 60 nm, whereas the polymer film is up to 140 nm high, protruding significantly above the pillars. Furthermore, the film does not cover the pillars, but is instead confined to the etched areas. This experiment confirmed the possibility to selectively deposit a polymer according to the structure introduced by the selective etching process.

3.5.3 Surface Initiated Polymerisation

In an alternate approach, techniques for surface polymerisation using 'grafting-from' were tested, in order to create polymer brushes selectively only on the unetched or etched areas^[109–113]. Again, the difference in the surface properties between etched silicon and silicon oxide can be exploited for selectivity, in this case by modifying only one area with a suitable polymerisation initiator. Ma *et al.* used a technique based on the selective protection of a silicon oxide surface with micro contact printing, followed by silanization with a suitable initiator to finally grow patterns of a polymer from these initiator sites^[115]. Similarly, the result achieved after etching can potentially be silanized only in the unetched areas, enabling the selective growth of polymer brushes, as illustrated in Figure 3.53.

(a)



(b)

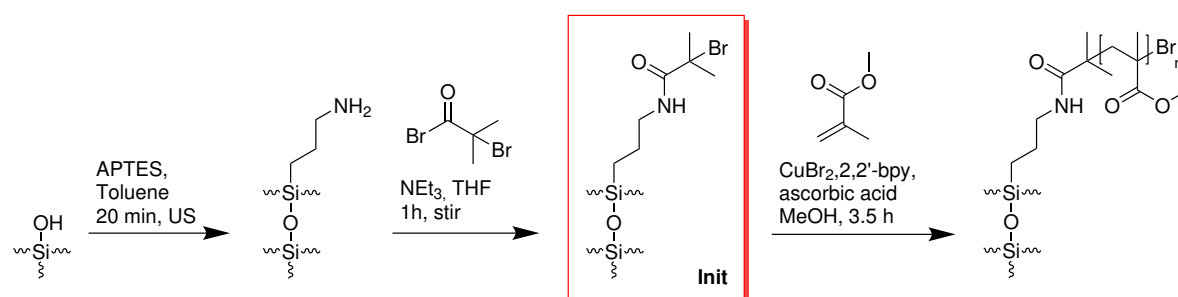


Figure 3.53: Illustration of the selective surface polymerisation process. (a) Illustration showing the three steps of etching, initiator attachment and polymerisation. (b) Reaction scheme for the two-step initiator formation and ARGET-ATRP surface initiated polymerisation.

In the first step of the reaction (see Figure 3.53b), the etched samples are modified with a Self-Assembled Monolayer (SAM) of (3-aminopropyl)triethoxysilane (APTES) to introduce reactive amino groups on the surface still covered with silicon oxide. Consequently, the SAM is modified further with α -bromoisobutyryl bromide (α -BiBB), establishing initiator groups on the surface. The polymerisation of methyl methacrylate (MMA) is then performed via ARGET-ATRP, employing ascorbic acid as regenerator for Cu(I), allowing for an easier polymerisation process^[121]. This then results in covalently attached brushes of poly(methyl methacrylate) (PMMA) only on surfaces which were still covered with silicon oxide after the etching process.

This process was verified in experiments, showing a significant change in the wetting behaviour between each surface modification step. The initially hydrophilic surface of the native oxide on top of the structures created after etching, first decreased significantly in water wettability after the APTES reaction. The next modification with α -BiBB decreased the wettability further, making the surface almost hydrophobic. Lastly, the result after polymerisation was investigated with AFM, as is shown in Figure 3.54. The images show a sample area of the selectively polymerised surface, where the polymer film was partially removed by scratching the surface, visible on the left side. The

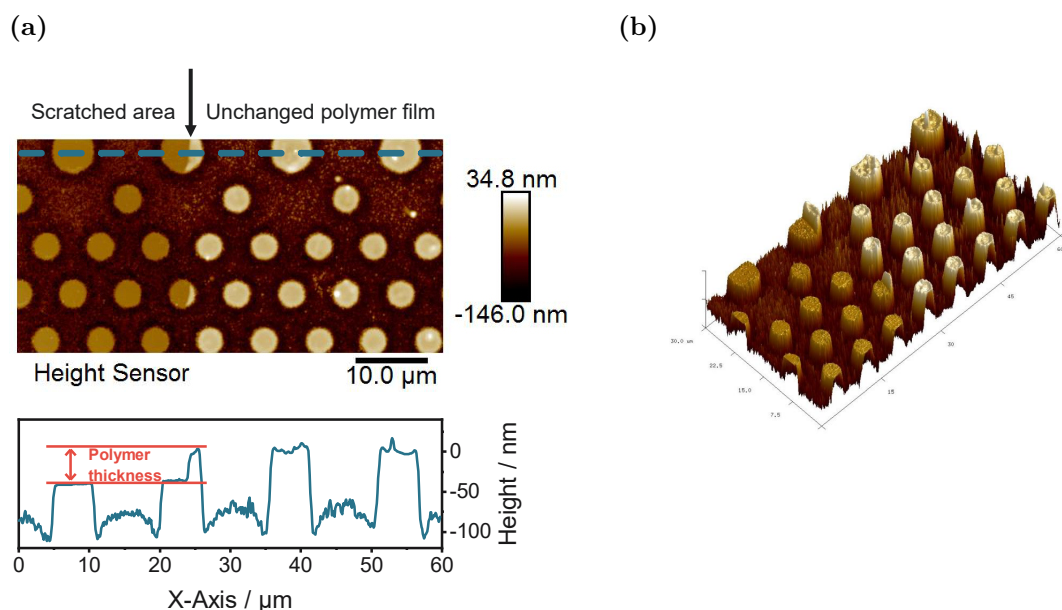


Figure 3.54: AFM images of samples with a selectively polymerised PMMA layer. The sample with 250 nm top epitaxial layer was etched with an active time of 40 s and polymerised for 3.5 h. On the left side the polymerised layer was removed by scratching, revealing the height difference on the top surface. (a) Topography image and cross section, demonstrating the thickness of the polymer film. (b) 3D representation of the topography highlighting the protrusion of the polymer film over the pillar height.

samples were also rinsed and treated in an ozone-cleaner shortly, in order to remove residues of the detached polymer. The partial removal allows for the evaluation of the polymer film thickness on top of the structures. Immediately visible is a significant contrast in height, measurable as a height difference of $(33.1 \pm 0.9) \text{ nm}$. Additionally, no height difference can be found between the etched areas, indicating a good selectivity for the polymerisation process. The surface of the polymerised parts shows a bowl-like shape, with a corona of increased height and decreasing film thickness towards the middle of the columns. In contrast, the scratched columns show the typical surface seen for selectively etched samples without further modification.

These experiments demonstrated the possibility to take advantage of the material contrast generated during the selective etching process, using it to selectively polymerise MMA on the unetched areas.

3.5.4 Summary

In this section, it was possible to demonstrate the feasibility of selective polymer deposition on samples previously etched with the LISE process. Due to the introduced surface inhomogeneity between etched silicon and the partially remaining native oxide layer, it was possible to deposit a polymer from solution, leading to the formation of a film only in the etched areas.

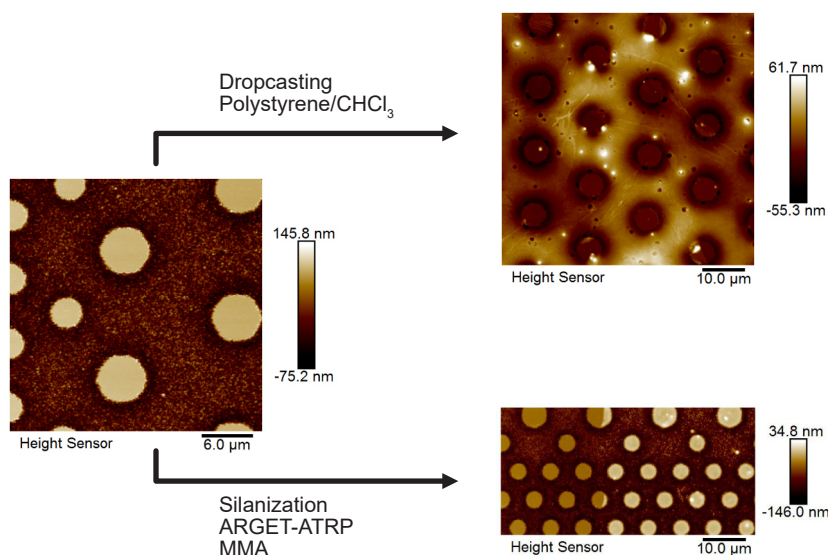


Figure 3.55: Summary of polymer deposition techniques on LISE etched samples. The top shows the polymer dropcasting pathway, selectively creating a PS layer on the etched areas. The bottom shows the surface polymerisation pathway, resulting in a covalently attached PMMA layer on the top surfaces of the columns.

The used polystyrene solution in chloroform dewetted selectively from the unetched, oxide covered areas, leading to the deposition of a PS film of around 140 nm protruding significantly above the column height of around 60 nm. Furthermore, the surface inhomogeneity could be exploited for selective surface polymerisation of MMA, initiated from selectively introduced initiator sites. These sites were covalently bound to the surface via silane bonding, which was only possible in the unetched areas. For this, first a reactive silane species was attached, which could then be modified by attaching an initiator functional group. Samples modified in such a way were then further submitted to ARGET-ATRP of MMA, creating a film of PMMA selectively on the modified areas, i.e. the top surfaces of the columns etched out of the substrate. Via partial mechanical removal of the polymer and subsequent AFM analysis, the thickness could be measured as (33.1 ± 0.9) nm. These two methods provide pathways for the further processing of samples etched with LISE, enabling further modification. In regards to the initial project goal of self-aligning photoresist, these results provide some possibilities of exploiting the previously created, heterogeneous surface in order to selectively deposit a polymeric material. For the use as e.g. implant masks, further improvements are necessary, but the overall goal seems feasible.

4 Conclusion and Prospects

The aim of this work was the development of a method for the generation of surface features on n-type silicon samples with deeply buried p-implants, in the form of heterogeneities aligned directly above the buried implants. This task was motivated by the realisation of a simpler process for the formation of superjunction transistors, which currently require the repeated creation of the same implantation structure over multiple steps of photolithography^[126,128]. These lithography steps can be potentially replaced, if a suitable process for the self-alignment in accordance to the buried implants can be found. The work on this goal was separated into three parts: the analysis of samples for suitable surface properties, the generation of surface heterogeneities using such a property and the analysis of the mechanism for the used process of contrast generation.

Surface property investigation

In a number of experiments, four different surface properties were investigated with regard to variations induced by the buried p-implants: Surface potential, surface charge, surface energy and sample conductivity. For this, samples with small hexagonal implant structures, as well as samples with either full surface or no implant at all were investigated. This allows for the macroscopic evaluation of the implant-influence when microscopically resolved measurements are not possible. For all properties a possible influence was evaluated not only on the bare silicon surface, but also on the native oxide layer, which inevitably forms on the surface, if silicon is exposed to air^[7]. For experiments on bare silicon, the native oxide was removed immediately prior via a HF-dip.

With surface potential measurements, performed via Kelvin Probe Force Microscopy, a variation could be measured on samples without top epitaxial layer, i.e. with the p-implants immediately at the sample surface and not buried beneath a homogeneous silicon layer. In contrast, on samples with such a layer, no variation was measurable, even at the lowest layer thickness or burying depth of 250 nm. Instead, the samples showed a constant surface potential over the measured surface, indicating no significant influence of the buried p-implants on the surface. This was found on samples with a bare silicon surface, as well as samples with a native silicon oxide layer.

From the surface charge, taken as zeta-potential measurements, no apparent variation between samples with and without buried implants could be found. With the native oxide layer present, both sample types showed the typical behaviour of increasing negative charge with increasing solution pH. A neutral charge point of around 2.5 was found, in good agreement with literature values for samples with silicon oxide layer^[138,139]. Measurements after removal of the native oxide layer showed a generally similar behaviour,

but overall shifted to more positive charge values. Again, no significant difference between samples with and without buried implants were found. This suggests, that surface charge is not a suitable surface property for the generation of self-aligned surface features in accordance with the buried implants.

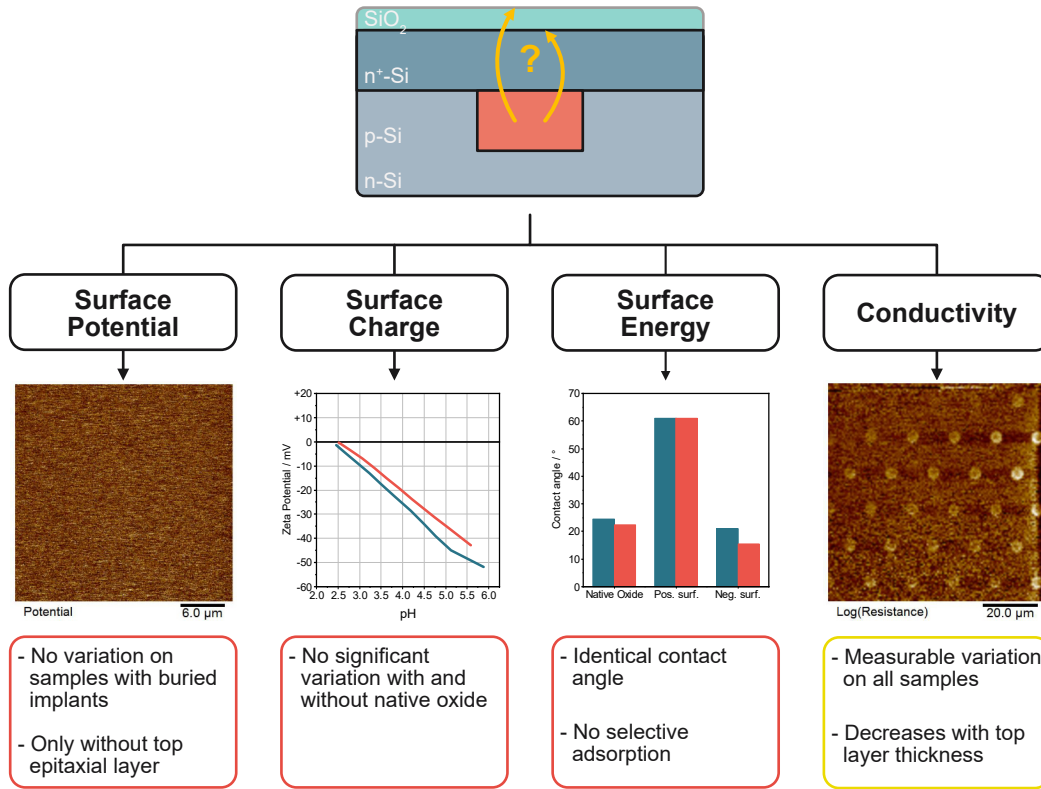


Figure 4.1: Summary of surface property investigations. The four properties shown in the image were investigated for variations corresponding to the buried p-implants. A potential influence was tested for samples with as well as without the native oxide layer.

Continuing in a similar direction, the samples were investigated for variations in the contact angle in neat state and after treatment with charged surfactants. Again, no significant variation was found between the angle measured on samples with and without buried implants over the full sample surface. The same was the case for samples treated with surfactants. After submerging the samples in a solution of a positively charged surfactant, the measured contact angle increased greatly, but in the same way for both sample types. This indicates an equally high degree of surfactant adsorption for both samples. The absorption itself is as expected due to the native negative surface charge. Further samples treated with a negative surfactant show no significant change in contact angle for both sample types, indicating negligible adsorption, as expected.

The last part of the surface property analysis investigated a variation in sample con-

ductivity, proposed to be due to the formation of pn-junction between the p-implants and the n-bulk. For this, SSRM measurements were evaluated, showing a very strong variation on samples without top epitaxial layer. On samples with such a layer, i.e. buried implants, the signal was reduced in magnitude, but still significant even with 500 nm epitaxial layer thickness. Furthermore, this was achieved on samples with a native oxide layer, measuring less than 2 nm in thickness, indicating that this layer does not influence the result significantly.

Pyrrole Electropolymerisation

Based on the measured resistance variation, the main goal of this work was further approached via electrochemical processes, primarily via the electropolymerisation of pyrrole. Upon oxidation, which can be induced electrochemically on semiconductor electrodes^[75–80], pyrrole is known to polymerise. Due to the measured variation in the through-sample resistance for the sample with buried implants, a concurrent variation in the polymerisation rate is expected, if these samples are used as the working electrode in a suitable electrochemical setup. For this, samples were initially subjected to a cyclic voltammetric procedure, varying the applied voltage between -0.5 to 1.5 V, as pyrrole will be oxidized in this range^[93–95]. Within the measured voltammograms, a significant signal for the oxidation of pyrrole is visible, confirming the overall possibility to oxidize and subsequently polymerise the monomer on the semiconductor surface. Furthermore, AFM measurements show a smooth polymer layer with around 30 nm thickness on the surface of the treated samples. Within this layer, no structuring in accordance with the buried implants could be found. The experimental parameters, such as CV settings or surface treatment were varied, but no improvement was realised. Also on samples without the top epitaxial layer, i.e. with the p-implants immediately at the sample surface, no successful patterning was achieved.

In a different approach experiments were conducted using the photo-induced electropolymerisation of pyrrole. Here, the oxidation of the monomer is not induced by an external current source, but via charge-carrier generation due to illumination of the semiconductor sample^[145,146]. These experiments were initially performed on samples without top epitaxial layer in order to maximize the possible influence of the implants. The experimental setup consisted of a glass vial with an electrolyte solution of acetonitrile containing pyrrole and silver nitrate in which the semiconductor sample is placed. The vial is then illuminated with a 50 W halogen lamp, leading to the formation of a polymer layer on the illuminated surface with a polymerisation rate of 2 nm min^{-1} .

Already for initial experiments, the macroscopic chip structure, created by variations in the implant size and density, was clearly visible as a dark-light contrast in the resulting polypyrrole film, as illustrated in Figure 4.2. Upon microscopic investigation, no evidence of the structure of the hexagonal implants was found, indicating that the implants did indeed affect the polymerisation, but apparently not precisely confined to their surface area. Instead, the surrounding areas were also modified, leading to only a macroscopic patterning of the polymer film. Improvements were achieved in further experiments, where it was found that an illumination time above 60 min results in films which show clear evidence of the microscopic implant-structure when imaged with a light microscope.

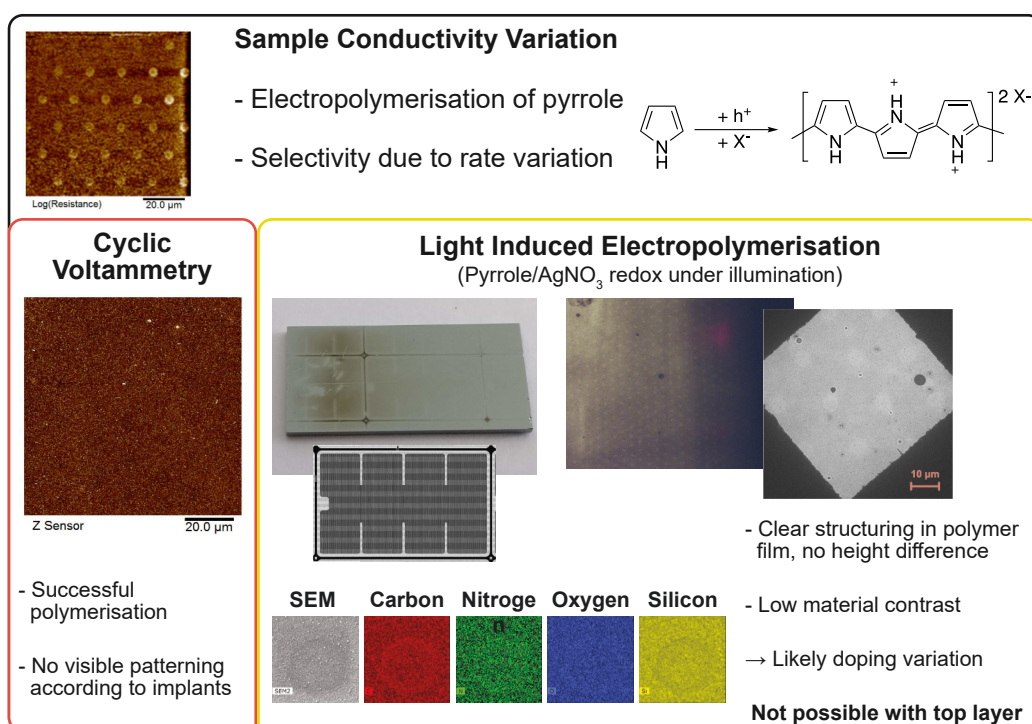


Figure 4.2: Summary image of electrochemical polypyrrole deposition. The resistance variation measured by SSRM was used first for cyclic voltammetric deposition, which resulted only in unstructured films. Used a light induced electropolymerisation it was then possible to create an optically structured PPy-film on samples without top epitaxial layer.

Here, the implant areas vary in colour, but no significant height contrast could be found from AFM images. The samples were also investigated with SEM, TEM and EDX, showing no significant height contrast, but a small material contrast, likely due to a different composition or density. From these results, it is assumed that the visible variation in the polymer film, reproducing the structure of the p-implants, is due to a difference in the doping of the conductive polypyrrole film.

Returning to the original aim of this work, the same process was investigated on samples with top epitaxial layer, i. e. with buried implants. Here a polypyrrole film is again deposited on the sample surface, but no structuring in accordance with the buried implants is found. This means that this process is not suitable for the reproduction of the buried structure in accordance with the aim of this work, but the results achieved on samples without top epitaxial layer appear promising for application in the realm of organic electronics, as the method likely allows for the selective doping of a film of conductive polypyrrole, useful in the fabrication of organic electronic devices^[148–151].

Light Induced Selective Etching

In a coincidental find during the sample cleaning process for further experiments a previously unobserved effect was then found, resulting in some samples being patterned in accordance to the implant structure. These samples, without a top epitaxial layer, were cleaned in a mixture of NH_4OH , H_2O_2 and water and afterwards stored in millipore water for several days. Closer investigation showed that the structure of the implants was etched into the surface, resulting in small hills located at the position of the p-areas, while the surrounding n-Si was etched deeper. It was found that residual NH_4OH from the cleaning process led to this etching, which acted in a selective way due to the influence of light, which only reached some of the samples during the storage. From this, a process for the doping selective etching of silicon under the influence of light was established. This simple process, consisting of alkaline etching in a 0.6 wt% aqueous solution of NH_4OH under illumination by a 50 W halogen lamp, leads to different etch speeds on the samples, depending on the doping properties. The pn-region around the p-implants is etched fastest, while the surrounding n-Si is removed relatively slowly. The p-implants themselves are etched with a rate between the other two. This results in deep rings surrounding the implants, which are etched as well, while the surrounding n-Si is etched more slowly. An exemplary image with cross-section is shown in Figure 4.3. The process behind this phenomenon was then further characterized, showing that a certain temperature, provided by the high power output of the light source, and the illumination itself are necessary to achieve the described result. A low temperature does not lead to any etching, due to the low silicon etch rate at these conditions. Conversely, if the samples are etched at elevated temperature of around 40 to 50 °C without any illumination, selectivity is still achieved, but with a different resulting structure. In this case, a p-etch stop effect determines the structuring, resulting in columns at the locations of the p-implants, while the surrounding n-Si is etched more strongly^[12,32,47–50]. An identical

result was achieved on samples on which the native oxide layer was removed immediately prior to the experiment. Again, columns at the p-implant locations were etched, showing that the oxide layer is essential to the formation of the ring-like structures.

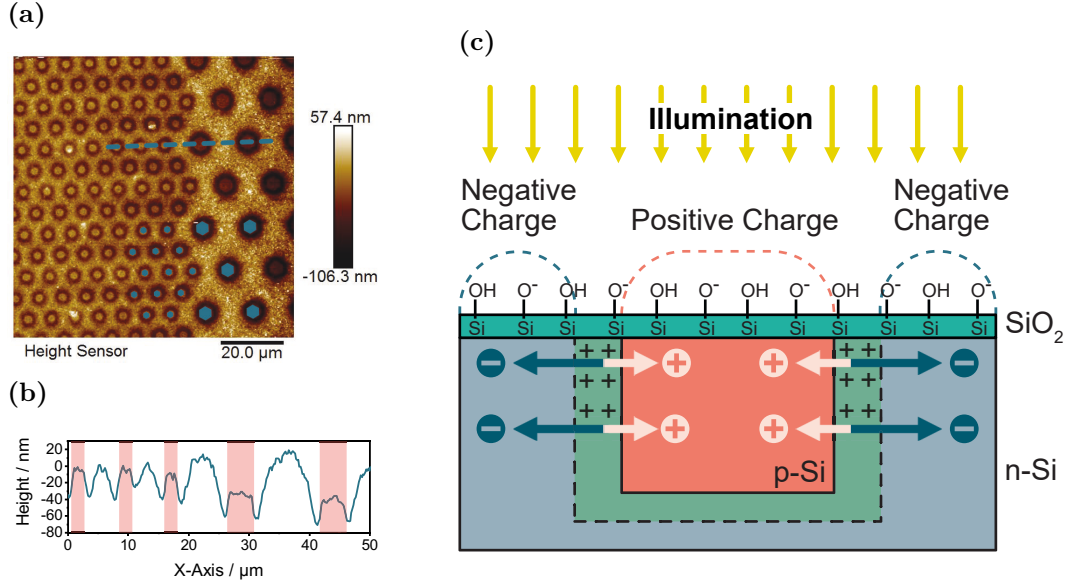


Figure 4.3: Summary of LISE results on samples without top epitaxial layer. (a) AFM image with implant overlay and cross section marker. (b) Cross section showing the selectivity of the etching, p-areas are marked in red. (c) Illustration of the proposed mechanism.

Based on these experiments, a mechanism hypothesis was proposed. It is assumed that the illumination leads to charge carrier generation and subsequent separation at the pn-junctions surrounding the p-implants. Here, the holes are swept into the p-Si, leading to an increased positive charge, which attracts the OH^- etchant ion, increasing the etch rate. Conversely, the electrons are swept into the n-Si, where they are able to reduce the etch rate via electrostatic repulsion of etchant ions. Lastly, at the pn-junction, which is located mostly in the n-Si due to the relative doping concentrations, a large number of fixed, uncompensated positive charges attract etchant ions, leading to an even higher etch rate than at the p-implants.

A different result is achieved on samples with top epitaxial layer, i.e. with buried implants. Here, the structure is reproduced as columns located above the buried p-implants, etched into the homogeneously doped top epitaxial layer. This appears to be similar to the p-etch stop effect observed for samples without the top layer, but as no p-Si is present at the sample surface, another process is responsible for the structure formation. In AFM phase images a strong phase contrast, indicating a material difference, was found between the top of the columns and the surrounding etched areas. As

no other material is introduced during the process, it is assumed that the native oxide layer remains on the top surface of the columns.

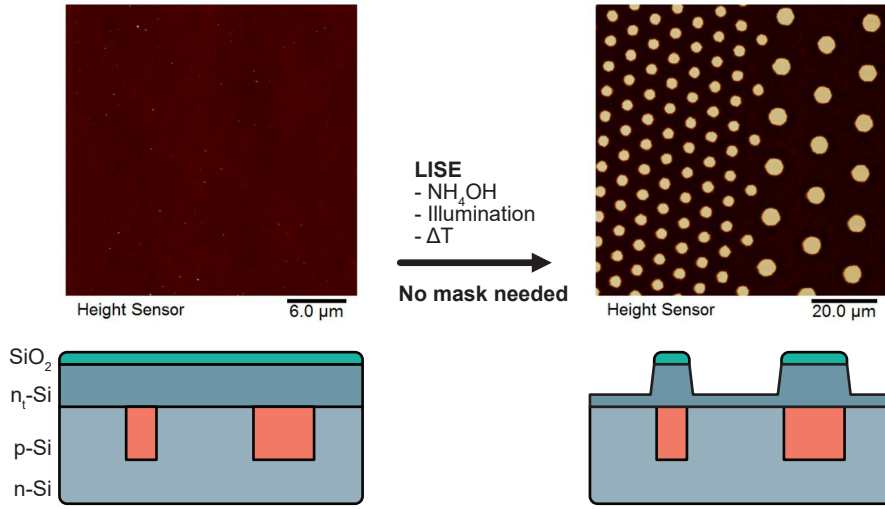


Figure 4.4: Illustration of the LISE result on samples with top epitaxial layer. The structure of the buried implants is reproduced as columns through selective etching on initially homogeneous surfaces. The schematic cross section shows the location of the columns directly above the buried implants.

In further test, it could be shown that this result is also attainable on samples with 1000 nm of epitaxial layer thickness, leading to a robust reproduction of the buried implant structure. From AFM images, the size of the resulting columns was compared to the real implant size, showing an increase in the radius of around 600 to 700 nm. Besides this offset, the location and overall layout of the implants was perfectly replicated with ideal overlay. This highly selective etching result was only possible with active illumination, as no selectivity is achieved at all, if samples are etched in dark under otherwise equal conditions. Similarly, if the native oxide layer was removed prior to the illumination in the etchant solution, no selectivity was achieved, indicating that the oxide layer plays an important role. Based on the apparent importance of the light influence, the name Light Induced Selective Etching (LISE) was chosen for this process.

The previously described mechanism hypothesis for samples without top epitaxial layer was then adapted to samples with this layer, resulting in the mechanism illustrated in Figure 4.5a. In essence, the generated electrons lead to a protective effect on the oxide layer directly above the buried implants, based on etchant ion repulsion. The holes on the other hand do not significantly influence the etching, as they are not able to reach the surface due to confinement in the p-implants. This essentially leads to the formation of an in-situ SiO_2 etch mask, which directs the etching progress. Consequently, the area directly above the implants is etched significantly slower, while the surrounding areas are

etched normally, leading to the formation of a positive image of the implant structure as a topography variation. In the present case, this leads to the observed columns etched into the substrate.

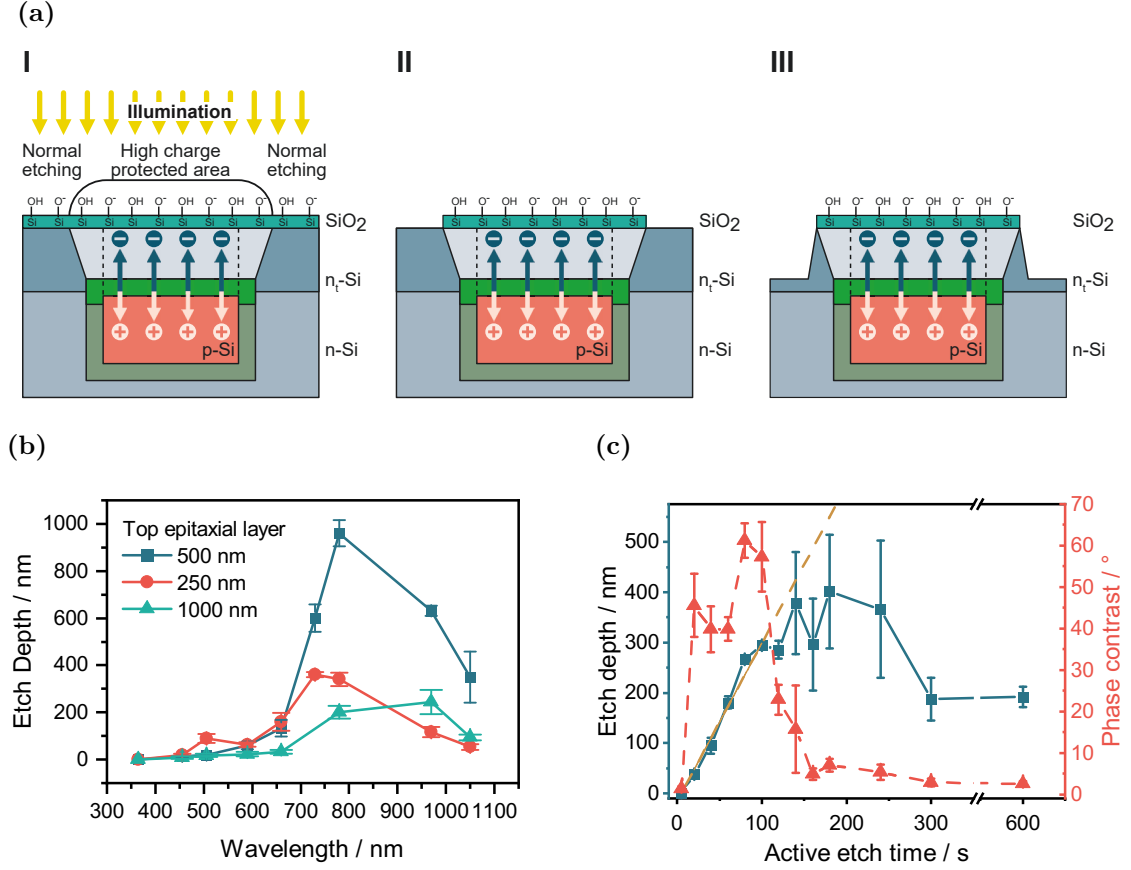


Figure 4.5: (a) Proposed mechanism of the selective etching process on samples with top epitaxial layer. The illumination-generated charge carriers lead to a negative charging of the surface above the implants, protecting these areas against etching. (b) Measured wavelength dependence for different top epitaxial layer thicknesses. (c) Time dependence of the etch depth and phase contrast.

Following this, the LISE process parameters were optimized in order to find optimal conditions for the subsequent evaluation of the mechanism hypothesis. From the initial experiments, the influence of the top epitaxial layer thickness could already be evaluated, showing that the process is possible with thicknesses ranging from 250 to 1000 nm. For the hexagonal implant structure the best results were achieved at lower thicknesses of 250 nm and 500 nm, while the structure fidelity was decreased at 1000 nm thickness. Conversely, larger implant structures allowed for a perfect reproduction also at this thickness. Due to these results, the condition optimisation experiments were performed on samples with 250 nm and 500 nm of top epitaxial layer thickness. It was found that NH₄OH-solutions with a concentration of 0.6 wt% resulted in ideal structure

reproduction, although other alkaline etchants, such as TMAH and KOH were suitable as well. A temperature of 50 °C is ideal, as the structure fidelity is diminished at higher temperatures, while the process time is too long without any improvement in the result at lower temperatures. For the wavelength dependence, the result is in good agreement with the expected behaviour based on the absorption properties of silicon, showing a distinct maximum at wavelengths of around 800 nm in the near infrared^[163,164]. For the time dependence it was found that the process proceeds in two parts. During the first around 6 min, no etching or other surface change is visible. After this induction period the etching then sets on visibly, leading to the formation of the structure under evolution of gas. Within this active etch time, the process leads to a linear increase in etch depth over the first 100 s. During this time, a strong phase contrast is detectable, due to the material contrast between etched silicon and the native oxide remaining on the top of the columns. Additionally, the dimensional offset of the column diameter decreases linearly within this time frame. Overall, the structures are larger than the buried implants, with the enlargement being smallest at 100 s of active etch time with around 200 nm. After this duration, the structure fidelity decreases significantly, as the oxide is also removed from the top of the columns.

Following the optimization, the mechanism was evaluated with several experiments. On samples with full surface implantation, it could be shown that the onset of the silicon etching was delayed under illumination, confirming the enhanced stability of the native oxide layer under these conditions. Other experiments showed that the in-situ mask is generated during the initial induction period without active etching and the illumination is not necessary during the actual removal of silicon. Using photocurrent measurements in electrolyte solutions, the flow of the generated charges was determined. Samples with either full surface, or no implantation at all, were connected to an ammeter and submerged either in the typical etchant solution or a hydrochloric acid solution at pH 2. During intermittent illumination of the samples the photocurrent was measured, yielding the results shown in Figure 4.6. It can be seen that the direction of electron flow for samples with p-implant is from the sample towards the solution, i. e. in agreement with the proposed electron flow to the sample/etchant interface. Conversely, samples without the implant show only a flow from the sample to the electrode. Additionally, it can be seen that the variation of the solution pH to pH 2 leads to a strong increase in the magnitude of the photocurrent on samples with implant. This is rationalised by the changing surface charge of the native oxide layer, allowing for easier electron flow. Overall, the investigations could confirm the proposed mechanism for the newly discovered selective etching process.

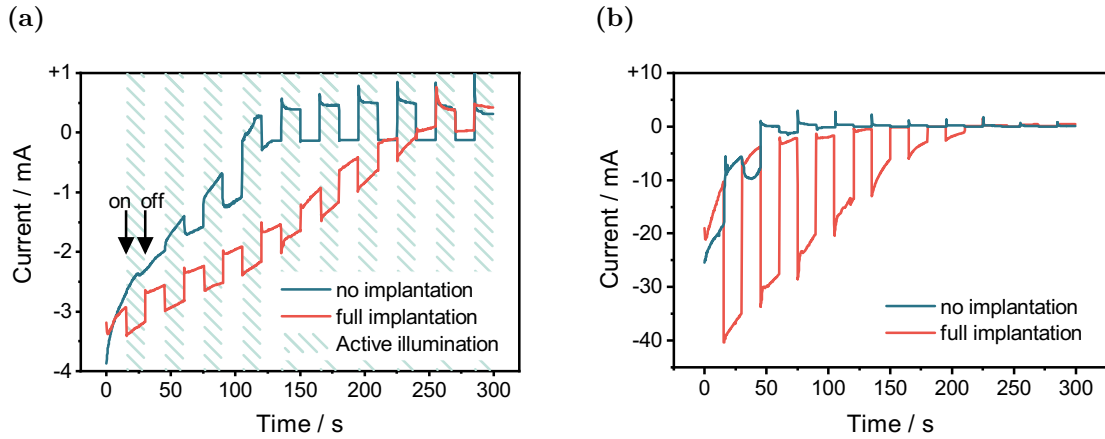


Figure 4.6: Photocurrent measurements showing the flow of electrons in good agreement with the proposed mechanism. (a) 0.6 wt% NH_4OH -solution. (b) pH 2 HCl solution.

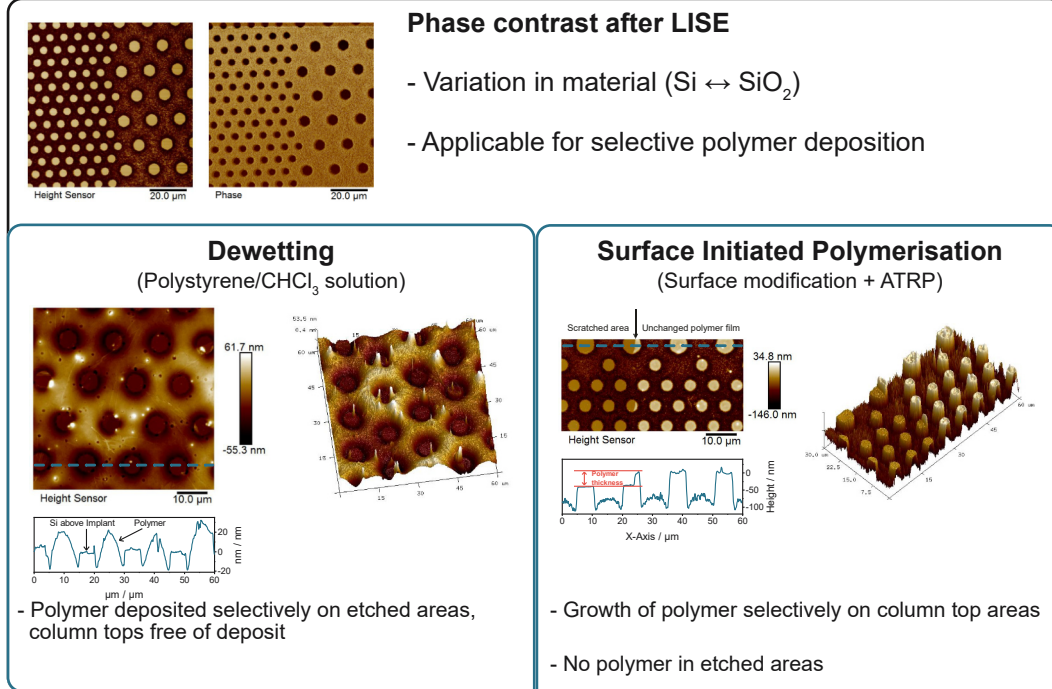
Selective Polymer Deposition

In the final part of this work, the material contrast between silicon oxide on the top of the columns and the etched silicon areas following the LISE process was used for the selective deposition of polymers. In literature sources, various methods for the selective deposition of polymer films via dewetting^[100–107] or surface polymerisation^[114,115] are described. In this work, the material contrast was successfully exploited via dropcasting of a polystyrene solution, as well as the surface initiated polymerisation of methyl methacrylate.

In the case of dropcasting, the polystyrene was dissolved in chloroform and dispersed on an etched sample, followed by slow evaporation of the solvent. This led to the formation of a polymer film, selectively deposited in the etched areas, while the top of the columns remained free of polymer. Due to unfavourable interactions, the polystyrene dewetted from the native oxide, displacing it to the etched surface. Upon total evaporation of the solvent, this structure solidified, further structuring the sample surface.

For the surface initiated polymerisation, etched samples were modified with a Self-Assembled Monolayer (SAM), incorporating an ATRP initiator group, in a two-step process. As the SAM only attaches to silicon oxide, the initiator functionalities are selectively deposited on the column top areas. Afterwards, methyl methacrylate was polymerised on the substrate via ARGET-ATRP, resulting in the growth of covalently attached PMMA chains. From AFM images it was determined that the polymer was successfully attached only to the column top areas. Partial removal of the polymer through scratching and washing showed that no polymer was attached in the etched areas, evident from a negligible height difference between the unscratched and scratched areas. In contrast, the partial removal leads to a significant height difference on the col-

umn top surfaces. The thickness of the polymer film was determined to be around 35 nm after 3.5 h of polymerisation time, in good agreement with the expected polymerisation rate of 10 nm h^{-1} ^[171].



Final Remarks and Outlook

Within this doctoral thesis, a before unseen method of selective etching on silicon was discovered and investigated. Hence, the overall aim of this work was successfully achieved.

- Samples containing buried p-implants inside a n-type silicon substrate were characterised with regard to various properties. Of these, the through-sample resistance showed a significant variation in accordance to the buried implants also through a homogeneous epitaxial layer.
- Various methods aimed at the usage of the resistance variation in order to generate a surface heterogeneity through electrodeposition failed to enable a suitable process. Instead, another method was found, which enables the replication of the implant structure via selective etching. This novel process enables the lithography-free patterning of the substrates through a simple alkaline etch process performed under illumination. This results in a surface heterogeneity as an alteration of the sample topography combined with a material contrast due to the formation of an in-situ SiO_2 etch mask. This material variation can also be used for the selective deposition of polymers, enabling further processing of the etched samples.
- For this new method, named Light Induced Selective Etching (LISE), a mechanism underlying the selectivity was proposed and through a number of experiments. In essence, the illumination during the etching process produces a flux of photo-generated electrons directed from the buried implants toward the surface, which increase the negative surface charge in the areas above these implants. The locally increased surface charge causes a local protection of the native silicon oxide layer against the alkaline etching, leading to the structuring of the substrate.

In essence, this novel method allows for the previously unreported self-adjusted structuring of silicon based on deeply buried implant structures. In general, even the characterisation of such implant structures is difficult^[134], whereas this method allows for structuring with regard to such buried structures with a very simple setup of only an etchant solution and a suitable light source. With regard to the introduction and motivation of this thesis, this process can possibly be applied for the intended purpose of creating a self-aligned resist in order to replace repeating lithography steps. This is the case in particular in combination with polymer deposition, as shown in the last part of the results. Certain limitations, such as the resolution limit and dimensional size increase exist, but can be circumvented by appropriate device design and further

optimisation of the process parameters. Furthermore, the LISE process appears applicable for the manufacturing of MEMS and MOEMS devices, as the typical feature sizes in these cases fit well to the achieved resolution of the LISE process^[12,13]. For devices needing a certain implant structure in combination with a corresponding topography, the new method allows for the elimination of at least one lithography step, including the necessary substeps such as alignment and measurement. Accordingly, LISE has the potential of simplifying the manufacturing process, enabling better and cheaper devices.

In addition to these achievements, experiments with the light induced electropolymerisation of pyrrole led to the discovery of a method which is assumed to enable the selective doping of a polypyrrole thin film, based on the doping structure of the used silicon substrate, acting as a template. Further research in this direction is necessary.

Considering future research, in particular on the topic of selective etching, more experiments regarding the nature of the observed effect are of interest. In particular, the mechanism can potentially be used for a different process, instead of etching. Here, the selective deposition of electroactive materials appears to be especially promising. This should enable the introduction of surface-heterogeneities without the need for the destructive modification of the substrate.

5 Experimental Part

5.1 Chemicals

All chemicals were used as received, unless noted otherwise.

Name	Purity	Supplier
Acetone	p.a.	Acros
Dimethylsulfoxide	>99.9 %	Acros
Potassium hydroxide	85 %	abcr
Pyrrole	98 %	Sigma
Dichloromethane	99.8 %	Acros
Diethyl ether	99 %	Fischer Scientific
Methanol	99 %	Fischer Scientific
Toluene	99 %	Fischer Scientific
<i>i</i> -Propanol	99.5 %	Fischer Scientific
Chloroform- <i>d</i>	99.8 % D	Euriso-Top
Allyl bromide	97 %	Sigma
Magnesium sulfate, anhydrous	99.5 %	Alfa-Aesar
Ammonium hydroxide solution	30 %	Acros
Hydrogen peroxide solution	30 %	VWR Chemicals
Ammonium fluoride solution, electronic grade	40 %	Honeywell/Fluka
Hydrofluoric acid	40 %	
N-[3-(Trimethoxysilyl)propyl]pyrrole (TMSPP)	95 %	abcr
(3-Aminopropyl)triethoxysilane (APTES)	98 %	abcr
Tetrabutylammonium hexafluorophosphate	99 %	Sigma
Gallium-Indium eutectic	99 %	Sigma
Acetonitrile, electronic grade	99 %	Sigma
Silver nitrate	99 %	Sigma
Tetramethyl ammonium hydroxide	25 %	Sigma
Polystyrene, 200k		Aldrich
Polystyrene, 100k		PSS
Polystyrene, 35k		Aldrich

Name	Purity	Supplier
Polystyrene, 2k		
Tetrahydrofuran, anhydrous	99.5 %	Acros
α -Bromoisobutyryl bromide (BiBB)	99 %	Sigma
Methyl methacrylate	99 %	Sigma
Ascorbic acid	99 %	Sigma
Copper(I)bromide	99 %	Sigma
2,2'-Bipyridyl	98 %	Sigma
Hydrochloric acid	80 %	VWR Chemicals

5.2 Silicon Substrates

The samples used for this work were provided by Infineon Technologies in pre-structured form. Generally, all samples consist of n-doped (100)-silicon wafer pieces. On all provided samples, a base epitaxial phosphorous n-doped ($N_D = 4 \cdot 10^{14} \text{ cm}^{-3}$) silicon layer, denoted as n-Si, with 17 μm thickness was deposited. On most wafers, boron ion implants were introduced into this layer, according to different structures, which are described extensively in the main text (see section 3.1). The p-doping concentration at the top of the implants was determined as $N_A = 2 \cdot 10^{15} \text{ cm}^{-3}$. Finally, on all but one sample type another phosphorous n-doped ($N_D = 8 \cdot 10^{14} \text{ cm}^{-3}$) epitaxial layer, denoted as n_t-Si, with varying thickness between 250 to 1000 nm was deposited, burying the implants beneath a homogeneous silicon layer. All samples were covered with a native oxide layer, due to silicon oxidation under atmospheric conditions.

5.3 Instrumentation

Light Induced Selective Etching Setup

The etching experiments were conducted with a specifically made setup, consisting of a LED light source, a custom heating block with sample holder and cuvette and a standard laboratory hotplate. The heaterblock is placed on the hotplate, allowing for temperature control via the temperature sensor. Inside the block a cuvette with custom sample holder and stir bar is located. 15 cm from the front of the cuvette, the LED light

source, allowing for wavelength and intensity control, is orientated in the optimal height and angle. An overview image of the setup is shown in the appendix, Figure A.4.

Atomic Force Microscopy (AFM)

Morphology and phase contrast images were taken on Dimension Icon and Dimension V (Bruker, USA) devices using Tapping Mode. Silicon cantilevers (Tap300Al, Budget-Sensors, Bulgaria) with around 40 N m^{-1} spring constant and around 300 kHz resonance frequency were used. The tip radius was below 10 nm. For surface potential measurements, a Dimension Icon with conducting cantilevers in KPFM mode was used.

The built-in optical microscope was furthermore used to capture overview images.

Scanning Electron Microscope (SEM)

SEM images were taken with a Neon40 SEM/FIB (Zeiss, Germany), typically at 3 kV accelerating voltage. Samples were used as-is without metal deposition. Images were taken with either a Secondary Electron (SE), InLens or backscattering detector. Additional EDX measurements were taken with 30 000 counts per spectrum on the Neon40 EDX device.

Transmission Electron Microscopy (TEM)

TEM images of polypyrrole films were taken with a Libra120 TEM (Zeiss, Germany). For this, the films had to be detached from the silicon substrate. This was either achieved by peeling for thicker films or with a short KOH-etch for thinner films. Afterwards, the films were placed on TEM-grids and investigated without further modification.

Ellipsometry

Ellipsometric measurements were taken on an alpha-SE ellipsometer (J.A. Woollam Co., USA) at an angle of 70° . The layer model was prepared from standard values and optimized with known samples. For the measurements of the silicon oxide thickness on the substrates a simple model of a native oxide layer with fixed optical properties on a silicon substrate was used.

For measurements of polypyrrole films, a more complex layer model was used. If the sample was surface modified this layer was set as cauchy layer with values determined from separate measurements. The polypyrrole layer on top was then modelled as a cauchy layer as well.

Nuclear Magnetic Resonance (NMR)

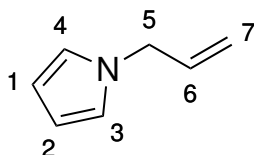
NMR experiments were performed on a Avance III 500 (Bruker, USA) spectrometer operating at 500.13 MHz. CDCl_3 was used as the solvent and the spectra referenced to this.

5.4 Synthetic Procedures

5.4.1 Allylpyrrole

To 200 mL of anhydrous dimethyl sulfoxide, 11.25 g (200 mmol, 1.72 eq) of potassium hydroxide are added and the solution is stirred for 15 min. To this, 7.82 g (116 mmol, 1 eq) of pyrrole are added, leading to a strongly yellow coloured solution. After stirring for 30 min, the solution takes on a dark green colour. 18.21 g (151 mmol, 1.3 eq) allyl bromide are then added and the solution is stirred for a further 30 min, after which the solution is of orange colour. The reaction is then quenched with 250 ml of water and the solution is extracted three times with 100 ml of diethyl ether, each. The combined ether extracts are washed three times with 50 ml of water each and dried over magnesium sulfate. In a distillation apparatus, the ether and unreacted allyl bromide are distilled off under normal pressure, followed by a vacuum distillation of the allyl pyrrole under 150 mbar at around 80 °C, resulting in a colourless liquid.

Yield: 6.02 g (56 mmol, 48 %)



^1H -NMR (CDCl_3 , 500 MHz)

δ (ppm) = 6.67 (t, $J=1.89$ Hz, 2 H, 1-H/2-H), 6.18 (t, $J=2.05$ Hz, 2 H, 3-H/4-H), 6.00 (ddt, $J=16.71, 10.48, 5.79, 5.79$ Hz, 1 H, 6-H), 5.05 - 5.25 (m, 2 H, 7-H), 4.45 - 4.56 (m, 2 H, 5-H)

5.5 Substrate Cleaning

Prior to any experiment on silicon, all samples were cleaned by a standardised procedure. If the samples were not already of $20 \times 10 \text{ mm}^2$, they were broken to this size utilizing a diamond-tipped scribe. Afterwards, the samples were loaded into a custom PTFE

holder with integrated stir bar, allowing for the parallel cleaning of up to 12 samples at once. The holder was itself placed inside a custom glass vial.

5.5.1 Solvent Clean

First, samples were submitted to a solvent cleaning procedure, consisting of ultra-sonic cleaning in CHCl_3 and acetone for 5 min each. Afterwards, the samples were rinsed with *i*-propanol and dried in a nitrogen stream.

5.5.2 Standard Clean-1

Subsequently, the samples were submitted to the RCA Standard Clean-1 process, consisting of treatment in a 5:1:1 mixture of millipore water: NH_4OH : H_2O_2 at 60 °C for 20 min. The solution was prepared by preheating 75 mL of millipore water in the custom glass vial, then adding 15 mL of 30 wt% NH_4OH and finally 15 mL of 25 wt% H_2O_2 . The samples holder containing the samples is then submerged in this solution and the mixture is stirred for 20 min. Afterwards, the solution is discarded and the holder is flushed 10 times with fresh millipore water. Finally, the samples are stored inside the holder in clean millipore water until used for experiments. Each sample is then removed when needed and dried in a stream of nitrogen.

5.6 Surface Modifications

For the surface modifications, cleaned samples were used. In some cases, the native oxide layer was removed prior to the reaction. For this, the sample was dipped in a 7:1 solution of 40 wt% NH_4F :40 wt% HF for around 15 s. Afterwards, the samples was quickly rinsed with millipore water and immediately used for the surface modification.

5.6.1 Silanisation Reactions

Silanisation was achieved from solution for N-[3-(trimethoxysilyl)propyl]pyrrole (TM-SPP) for pyrrole experiments and from gas phase for (3-aminopropyl)triethoxysilane (APTES) for the surface polymerisation experiments. For the solution procedure, TM-SPP was first dissolved in toluene to a concentration of 0.6 vol%. Afterwards, a cleaned sample was placed in this solution inside a small glass vial. The vial was then either submitted to ultrasonication for 20 min or left to react undisturbed for around 2 h. For the gas phase procedure, the samples were inserted into a vacuum container together with 0.5 ml of APTES in a small vial. The container was then evacuated to below 1 mbar

and left overnight. For both procedures, the work-up consisted of ultrasonic cleaning in fresh toluene and rinsing with toluene, acetone and *i*-propanol. Finally, the samples were dried in a stream of nitrogen.

5.6.2 Si-H Modification

For the direct Si-H modification of samples with allylpyrrole, samples without oxide layer were used. The modification was conducted via a photochemical hydrosilylation reaction. For this, the allylpyrrole was previously degassed by bubbling nitrogen for around 15 min. After placing samples in a small glass dish they were covered with a thin layer of allylpyrrole and subjected to illumination from a broadband halogen lamp providing UV-light. After around 1 h, the sample was removed, extensively rinsed and cleaned ultrasonically in CHCl_3 , acetone and *i*-propanol and finally dried in a stream of nitrogen^[87,144,172,173].

5.7 Polypyrrole Experiments

For the experiments depositing films of polypyrrole on the sample surface, two approaches were used. First, standard electrochemical deposition, as described extensively in the literature was used^[75–80,90,93,94,174]. Secondly, instead of supplying an external current, photo-current, generated upon illumination can be exploited as well^[145,146].

5.7.1 Electropolymerisation

The deposition of polypyrrole was performed using an electrochemical cell with three-electrode setup under control via a potentiostat. Inside the cell, the cleaned and for some experiments surface modified sample was placed in a custom made holder, allowing for the connection to the Pt-rod working electrode. In order to achieve good and ideally ohmic contact, the connecting area was covered with either a silver paste or Ga-In-eutectic. The cell also contained a counter-electrode made from Pt-wire and a Ag/AgCl reference-electrode. A typical experiment was conducted by first adding 25 mL of 0.1 mol L⁻¹ TBAFP in acetonitrile to the cell. To this 100 μL of pyrrole were added, bringing the concentration to 0.05 mol L⁻¹. After submerging the electrodes in this solution, it was deoxygenated by bubbling nitrogen for 15 min. Afterwards, the cell was kept under a flow of nitrogen to prevent oxygen from reaching the solution. At this point, the electrodes were connected to the nStat potentiostat (IVIUM Technologies) and the electrochemical experiment was started, typically as cyclic voltammetry

with the parameters given in the main text. After the experiment was finished, the sample was removed and rinsed carefully. After removal of the conducting paste or Ga-In-eutectic, it was dried in a stream of nitrogen and stored for further investigation.

5.7.2 Light Induced Polymerisation

For the light-induced electropolymerisation experiments, 5 mL of a solution of 0.1 mol L^{-1} AgNO_3 in acetonitrile were added to a small vial with septum. To this, $33.3 \text{ }\mu\text{L}$ of pyrrole were added, bringing the pyrrole concentration to 0.1 mL . The solution was then deoxygenated by nitrogen bubbling for 15 min. Under a counter stream of nitrogen, the cleaned and for some experiments surface modified sample was added to the solution. The vial with sample was placed in front of a 50 W halogen lamp, fixed in a custom holder to ensure good alignment. The vial was then illuminated for varying amounts of time. Afterwards, the sample was removed from the vial and rinsed carefully, followed by drying in a stream of nitrogen.

5.8 Selective Etching Experiments

The experimental setup and procedure for the newly established selective etching is very simple. In essence, only a vial with etchant and sample and a suitable lamp are necessary. For ideal experimental parameters, this baseline setup was extended as described above. In a typical experiment, 4.9 mL of preheated (usually 50°C) millipore water were added to the cuvette, typically followed by 0.1 mL of 30 wt% NH_4OH , whereas also TMAH and KOH were employed, resulting in an etchant concentration of 0.6 wt%. Following, the sample inside the custom holder was inserted into the solution under illumination and a timer was started. The sample was kept in the solution until a specified time after first signs of etching were visible. Typically, after the etched structure was visible over the full surface, the active etch time started. Afterwards, the sample older with the sample was removed and rinsed with fresh millipore water. The sample was removed from the holder and rinsed again, followed by drying in a nitrogen stream.

5.8.1 Polymer Film Deposition

Deposition of polymer films on selectively etched samples was performed via spin-coating, drop-casting and selective surface polymerisation.

5.8.1.1 Spincoating of Polystyrene

As described in the main text, spin-coating of polystyrene was performed primarily from toluene solutions. For this, the polymer, with varying molecular weight between $200\,000\text{ g mol}^{-1}$ and 2000 g mol^{-1} , was dissolved under stirring in 5 mL of toluene, creating varying concentrations between 10 mg mL^{-1} and 0.1 mg mL^{-1} . After complete dissolution, all solutions were filtrated with a $0.2\text{ }\mu\text{m}$ syringe filter before use. Spin-coating was performed on a POLOS BL-type spincoater (SPS-Europe), typically at 2000 rpm for 40 s with 1000 rpm/s acceleration. $100\text{ }\mu\text{L}$ of the polymer solution were pipetted onto the sample, prior to the program start. Afterwards, for some samples, annealing was performed on a hotplate at at least $100\text{ }^{\circ}\text{C}$ for varying time periods.

5.8.1.2 Dropcasting of Polystyrene

For the drop-casting of polystyrene films, the polymer was dissolved in CHCl_3 at a typical concentration of 1 mg mL^{-1} . As for spin-coating, the polymer molecular weight was varied between $200\,000\text{ g mol}^{-1}$ and 2000 g mol^{-1} . After filtration of the polymer solution with a $0.2\text{ }\mu\text{m}$ syringe filter, $1000\text{ }\mu\text{L}$ of the solution were pipetted onto a etched sample placed inside a small glass dish. The sample was covered with another small glass dish and left for several hours, until all of the solvent had evaporated and a film of polystyrene formed on the surface.

5.8.1.3 Surface Initiated Polymerisation

The selective surface polymerisation of methyl methacrylate (MMA) was carried out over several steps. First, samples were etched, as described previously, and immediately afterwards modified with an APTES SAM, also as described previously. For the introduction of the initiator functionality, three samples inside a custom PTFE-holder were added to a schlenk tube and the apparatus degassed and backfilled with nitrogen. To this, 30 mL of dry THF were added, followed by 0.75 mL of α -bromoisobutyryl bromide (BiBB)) and 0.9 mL of dry triethylamine. The mixture was stirred for 1 h, resulting in a white, cloudy solution. The samples were removed and rinsed extensively with THF, methanol and water.

For the ATRP procedure, each sample was polymerised separately. For this, the sample was placed inside a 5 mL test tube, which was degassed and backfilled with nitrogen. In a separate flask 8 mL methanol, 2 mL millipore water and 10 mL of Methyl methacrylate were degassed by nitrogen bubbling for 20 min. To this were then added 3.9 mg (17 mmol, 1 eq) CuBr_2 , 26.2 mg (168 mmol, 10 eq) 2,2'-bipyridyl and 30.1 mg

(170 mmol, 10 eq) ascorbic acid and the solution was stirred until all solids were dissolved. 5 mL of this solution were then transferred to the test tube containing the sample and the reaction left to proceed for 3.5 h. Afterwards the sample was removed and extensively rinsed with THF, methanol and water.

5.8.2 Photocurrent Measurements

The photocurrent measurements were carried out in the same setup as the cyclic voltammetric pyrrole experiments. Initially, a cleaned sample was attached to the custom sample holder and contacted to the Pt-working electrode using Ga-In-eutectic. Additionally, the Pt-wire counter electrode was inserted in the cell. The cell was filled with 25 mL of the appropriate electrolyte, either the typical 0.6 wt% NH_4OH or a 0.01 mol L^{-1} HCl solution. In some cases 5 drops of H_2O_2 were added to the NH_4OH electrolyte. The potentiostat was connected to the electrodes and these submerged in the electrolyte. Immediately afterwards the measurement was started. The typically used 730 nm LED lamp was used as the illumination source. The lamp was turned on intermittently for 15 s interrupted by 15 s of dark time, until an overall experiment time of 300 s was achieved. Sample cleaning consisted of rinsing with water and drying in a nitrogen stream. The electrolyte solution was renewed for every sample.

A Appendix

A.1 Sample Properties

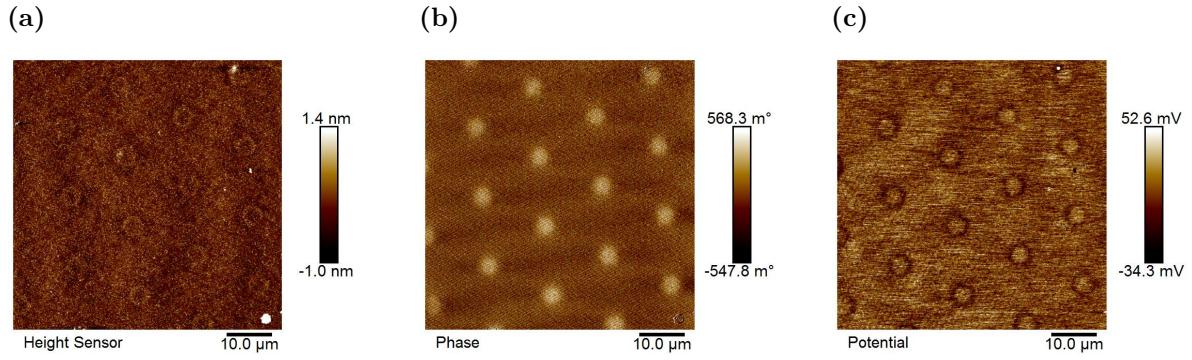


Figure A.1: AFM images for a sample without top epitaxial silicon layer, i. e. with implantations immediately at the surface. (a) Height image, (b) Phase image, (c) Surface potential.

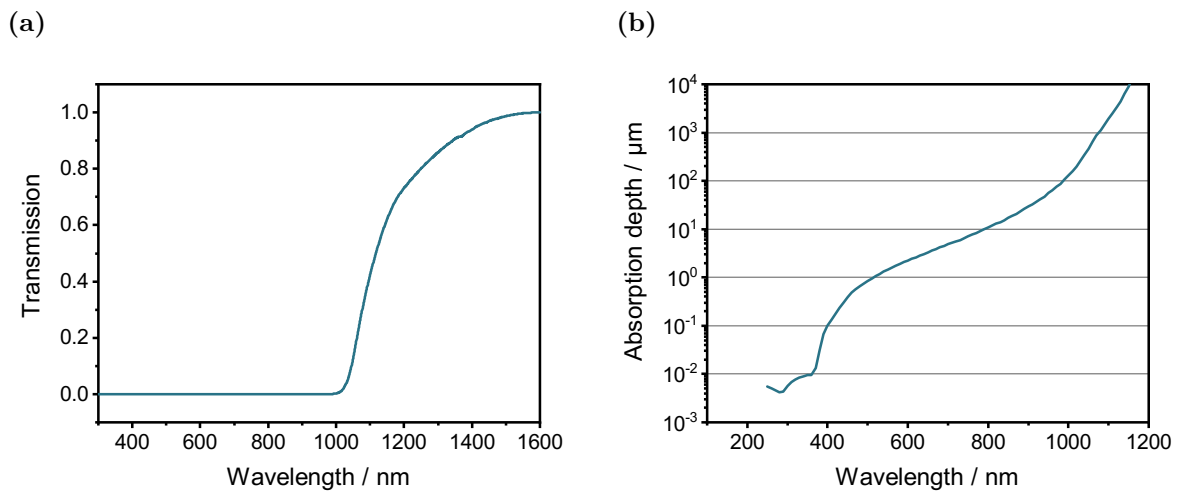


Figure A.2: (a) Measured UV/VIS transmission spectrum for a sample with 500 nm top epitaxial layer thickness. (b) Calculated absorption depth spectrum for silicon. Data points taken from^[163]

A.2 Self-Replication Results

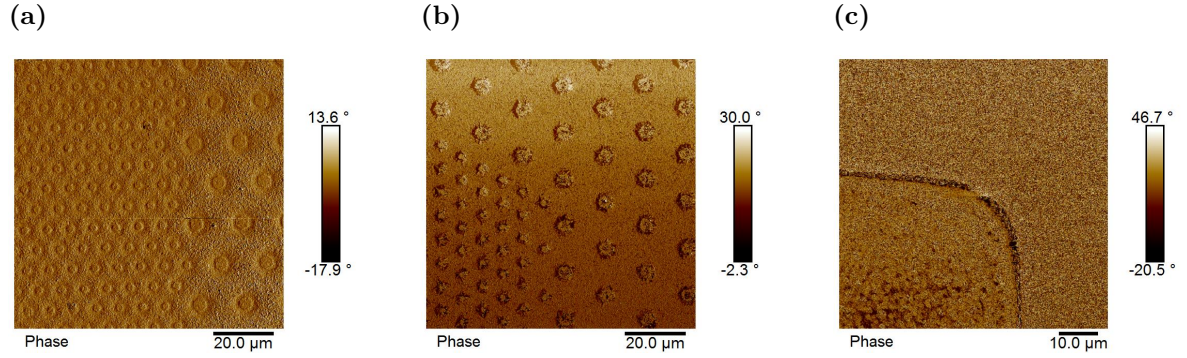


Figure A.3: AFM phase images for a sample with (a) 0 nm and (b), (c) 1000 nm top epitaxial silicon layer. (b) Sample with hexagonal implantation structure, (c) Sample with 5×5 nm implantation structure.

A.3 Experimental Setup

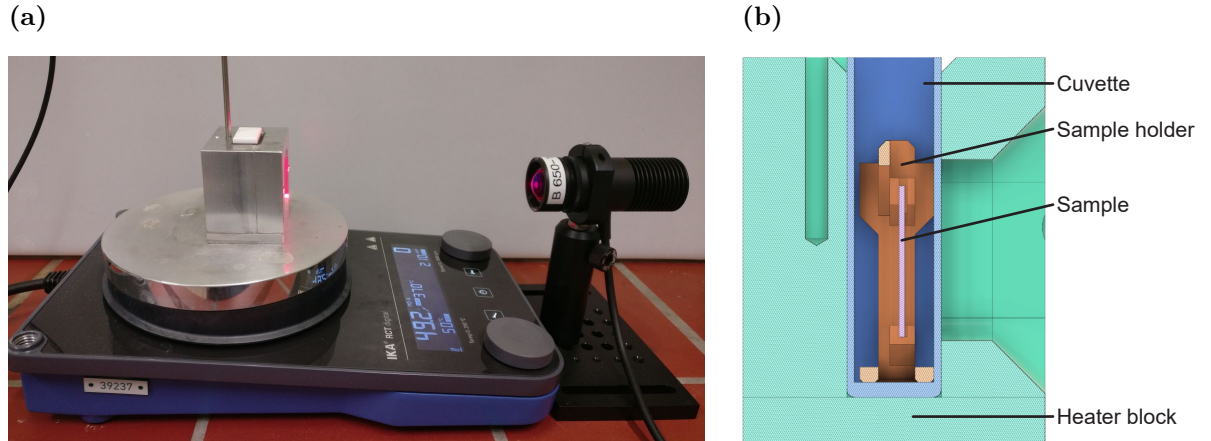


Figure A.4: (a) Photograph of experimental setup for LISE, consisting of a LED lamp, hot-plate with sensor, blockheater, cuvette, sample holder and sample. (b) CAD cross-section drawing of heaterblock with cuvette, sample holder and sample. The hole at the left is used for inserting a temperature sensor, connected to the hot plate.

The experimental setup for LISE experiments was successively varied in order to provide increasing parameter control during the experiments. The final version, consisting of a LED lamp, hotplate with sensor, blockheater, cuvette and sample holder is shown in Figure A.4a. In this setup, a sample is placed inside the 3D-printed (PETG filament) sample holder, which is then inserted into the cuvette filled with etchant. The cuvette itself is placed inside a custom machined aluminium heaterblock, which allows for precise

temperature control via a hotplate with temperature sensor, which can be inserted into the block via a separate hole (see Figure A.4b). The front of the heater block is cut out, allowing light from an LED lamp to reach the sample. Typically, ThorLabs mounted LEDs were used, fixed to a height variable mounting foot. Overall, this setup allowed for precise control and ideal repeatability of the experimental parameters.

A.4 Etchant Dependence

As described in the main text, different etchants lead to significantly differing resulting structures. Very notable here was the variation in AFM-phase contrast on the resulting structures. For NH_4OH a strong contrast between the top surface of the columns and the surrounding, etched areas is visible at all investigated concentrations, whereas in TMAH-solutions this is only the case at concentrations below 2.5 wt%, at higher values, the surfaces show only small differences. For KOH-solutions, at low concentrations a difference is visible, which is inverted in the signal compared to the previous results, possibly due to a different surface bond capping in this case. Figure A.5 collects AFM phase images for the three different etchants.

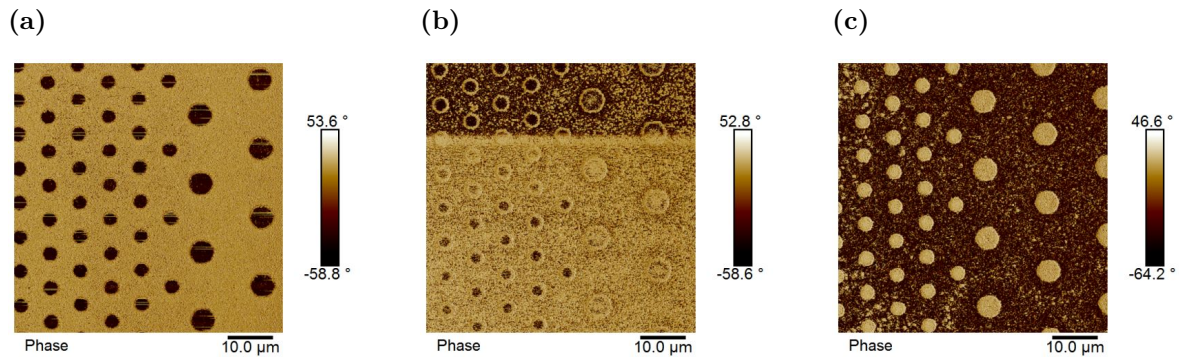


Figure A.5: AFM phase images for samples etched in different etchants: (a) 0.5 wt% NH_4OH , (b) 2.5 wt% TMAH, (c) 0.5 wt% KOH. All samples were etched at 50 °C with 730 nm LED illumination.

A.5 Ratio of Absorbed Photons to Etched Silicon Atoms

The previous experiments, investigating the origin of the selective etching, support the proposed mechanism strongly. A proposed alternative to this mechanism envisions not only the protective effect of the generated carriers but also an increase in etch speed in the areas surrounding the buried implants, due to diffusing holes, oxidizing the silicon atoms. Although a number of previous experiments do not show any evidence for this

kind of etch speed enhancement, calculations of the ratio of generated carriers to etched silicon atoms can further the understanding of the processes taking place during the illumination and etching. In order to calculate this ratio, several parameters need to be measured and taken into account. First, the light power of the illumination source and photon flux can be obtained as shown in section 3.4.6.3. Different here is the active surface area though, as these experiments are executed on samples with structured p-implant, i.e. with hexagonal implant pattern. This means, that only these areas are possible photoactive with regard to the proposed mechanism. Accordingly, only the photons incident on these areas are taken into account. As before, reflection and absorption is taken into account as well. Particularly, the absorption until 800 nm is calculated, as this represents the extent of the pn-junction on samples with 500 nm top epitaxial layer. It is also necessary to measure the active etching time and with it calculate the total number of incident photons during the actual etch time. After completion of the etching step, the sample needs to be investigated with AFM in order to measure the mean etch depth and size of the remaining unetched columns. With this, the etched volume of Si and subsequently the number of etched silicon atoms can be calculated.

Experimental Properties The samples used for these investigations have a surface area of 200 mm^2 ($20 \times 10 \text{ mm}$). As parts of the samples were obstructed by the sample holder it is necessary to subtract the blocked area to obtain the active area A_a during the experiments. The blocked area can be measured as 6.4 mm^2 , making the active area 193.6 mm^2 or $1.936 \cdot 10^{-4} \text{ m}^2$. To calculate the area with underlying p-implants the numbers of implants (n_G, n_A) per sample and their respective areas per implant (Gate: $3.14 \mu\text{m}^2$, Array: $12.57 \mu\text{m}^2$) are used. This yields the new active area for this case, called $A_{a,Imp}$.

Silicon Properties In order to calculate the number of silicon atoms during the etching, it is firstly necessary to determine the atomic number density of silicon atoms per volume unit. As silicon is a crystalline material this can be achieved using the crystallographic properties of the unit cell. As silicon crystallises in the diamond structure, each unit cell contains 8 Si-atoms with a lattice spacing a_0 of 0.543 nm. With this, the number density can be calculated as:

$$n_{Si} = \frac{N_{uc}}{V_{uc}} = \frac{8}{a_0^3} = \frac{8}{0.1602 \text{ nm}^3} = 49.937 \text{ nm}^{-3} \quad (\text{A.1})$$

Sample Etch Properties Next, the etched volume of each sample needs to be determined, which can be calculated as the product of etch depth and etched sample area. Etch depth can be directly taken from AFM measurements as the height of the unetched columns, as illustrated in Figure A.6. The etched area can be calculated as the difference

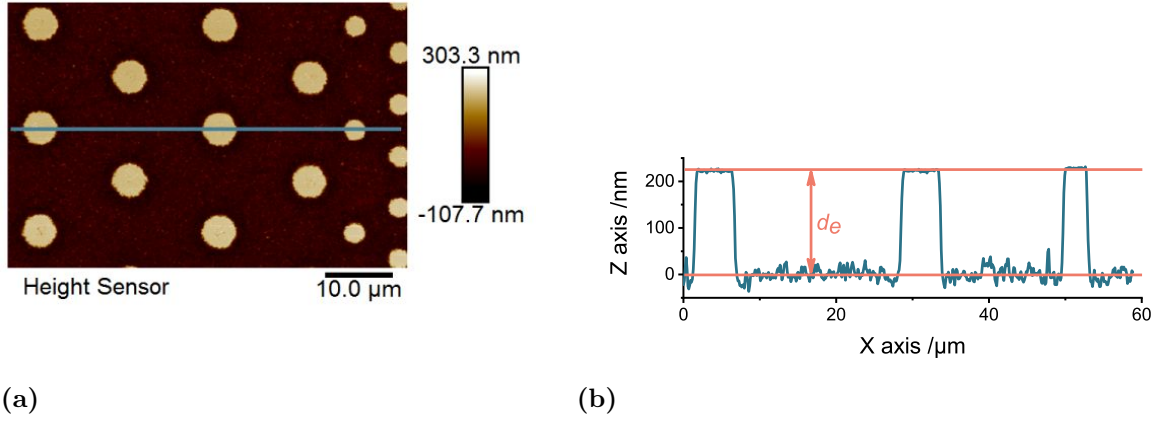


Figure A.6: (a) AFM image of a sample used for quantum yield estimations (b) Height profile of the marked region with measured value d_e .

of the active area and the sum of the areas of all columns. This sum can be obtained from the number of implants per sample (Gate: $n_G \approx 440\,000$, Array: $n_A \approx 780\,000$) and the measured areas, taken again from AFM measurements.

$$V_e = d_e A_e = d_e (A_a - (n_G A_G + n_A A_A)) \quad (\text{A.2})$$

Together with the previously determined atomic number density of silicon n_{Si} it is now possible to calculate the number of etched atoms N_{Si} simply as the sum:

$$N_{Si} = V_e n_{Si} \quad (\text{A.3})$$

Results Finally, the obtained values for incident photons and etched silicon atoms can be set in relation to one another, as shown in Table A.1. These results show, that for every etched silicon atom only around 0.25 photons were absorbed on the sample surface (see Figure A.7). If carrier generation outside of the areas with underlying implants is not taken into account, these results imply that much less than one photon is absorbed per etched silicon atom. As four holes are needed to oxidise the four binding electrons of each silicon atom, this result leads to the conclusion that only around 6% of the observed etching could potentially be attributed to photoetching due to charge carrier

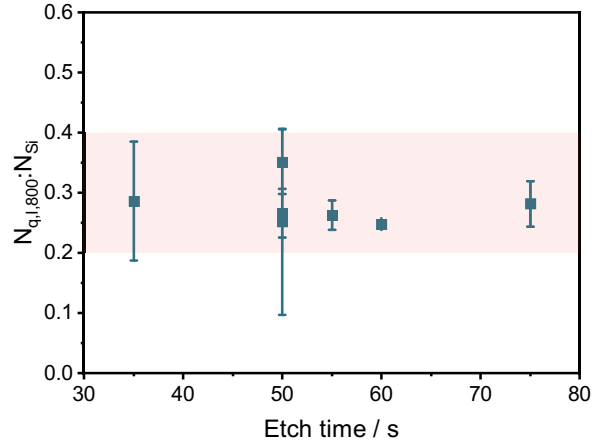


Figure A.7: Dependency of ratio of absorbed photons in areas with underlying p-implants to etched silicon atoms from etch time. Error bars are based on the deviation in measured etch depth.

generation at the pn-junction of the buried implants. Therefore, it can be concluded, that the charge carrier generation in the pn-junctions does not significantly contribute to etching silicon atoms directly. Instead, the generated charge carriers, specifically electrons, protect the areas immediately above the buried implants from etching, thus leading to a selective etching effect.

Table A.1: Table of data obtained from quantum yield measurements

Sample	Time t_a s	Photons $N_{q,I,800}$ $\cdot 10^{17}$	Si-atoms N_{Si} $\cdot 10^{18}$	Ratio $N_{q,I,800} : N_{Si}$
CSW106-02-2	50	3.861	1.452	0.266
CSW106-02-3	60	4.632	1.868	0.248
CSW106-02-5	50	3.861	1.534	0.252
CSW107-02-1	50	3.861	1.098	0.352
CSW107-02-2	55	4.247	1.618	0.262
CSW107-02-3	75	5.791	2.056	0.282
CSW107-02-4 ^a	35	2.702	0.945	0.286

^a Evaluated from step height around columns, due to low etch progress

List of Abbreviations and Symbols

$R_{DS(on)}$	On-Resistance	MEMS	Micro-Electro-Mechanical Systems
AFM	Atomic Force Microscopy	MMA	Methyl methacrylate
APTES	(3-Aminopropyl)triethoxysilane	MOEMS	Micro-Opto-Electro-Mechanical Systems
ARGET	Activators Regenerated by Electron Transfer	MOS	Metal-Oxide-Semiconductor
ATRP	Atom Transfer Radical Polymerisation	PS	Polystyrene
B\dot{i}BB	α -Bromoisobutyryl bromide	RCA	Radio Corporation of America
BOE	Buffered Oxide Etch	RIE	Reactive Ion Etching
CMOS	Complementary Metal-Oxide Semiconductor	RMS	Root mean squared roughness
DNQ	Diazanaphthoquinone	SAM	Self-Assembled Monolayer
DUV	Deep Ultra Violet	SEM	Scanning Electron Microscopy
EDX	Energy-dispersive X-ray spectroscopy	SMM	Scanning Microwave Microscopy
EUV	Extreme Ultra Violet	SSRM	Scannning Spreading Resistance Microscopy
HNA	Hydrofluoric nitric acetic	TBAFP	Tetrabutylammonium hexafluorophosphate
IC	Integrated Circuit	TEM	Transmission Electron Microscopy
KPFM	Kelvin Probe Force Microscopy	TMAH	Tetramethylammonium hydroxide
LED	Light Emitting Diode	TMSPP	N-[3-(Trimethoxysilyl)propyl]pyrrole
LIDAR	Light Detection and Ranging	ToF-SIMS	Time of Flight-Secondary Ion Mass Spectroscopy
LISE	Light Induced Selective Etching	VLSI	Very Large Scale Integration

Bibliography

- [1] J. S. Kilby, Miniaturized electronic circuits, **1959**.
- [2] R. Noyce, Semiconductor device-and-lead structure, **1961**.
- [3] K. Lehovec, Multiple Semiconductor assembly, **1962**.
- [4] K. H. Yeap, H. Nisar, *Very-Large-Scale Integration*, (Eds.: K. H. Yeap, H. Nisar), InTech, **2018**, DOI 10.5772/65525.
- [5] J. Lohmer, C. Flechsig, R. Lasch, G. Schneider, D. Eberts, B. Zettler, *Digital Transformation in Semiconductor Manufacturing*, (Eds.: S. Keil, R. Lasch, F. Lindner, J. Lohmer), Springer International Publishing, Cham, **2020**, pp. 64–71, DOI 10.1007/978-3-030-48602-0.
- [6] Deloitte, Semiconductors – the Next Wave, Opportunities and winning strategies for semiconductor companies, tech. rep. April, **2019**, pp. 1–58.
- [7] H. Xiao, *Introduction to semiconductor manufacturing technology: Second edition*, SPIE, **2012**, pp. 1–665, DOI 10.1117/3.924283.
- [8] A. N. Saxena, *Invention of integrated circuits: untold important facts*, **2009**, p. 523.
- [9] P. Rai-Choudhury, *Handbook of Microlithography, Micromachining, and Micro-fabrication. Volume 1: Microlithography*, SPIE PRESS, **1997**, DOI 10.1117/3.2265070.
- [10] B. J. Lin in *Optical Lithography: Here Is Why*, SPIE, Bellingham, **2010**, pp. 133–212, DOI 10.1117/3.821000.ch5.
- [11] L. Li, X. Liu, S. Pal, S. Wang, C. K. Ober, E. P. Giannelis, *Chemical Society Reviews* **2017**, 46, 4855–4866, DOI 10.1039/c7cs00080d.
- [12] P. Pal, K. Sato, *Silicon Wet Bulk Micromachining for MEMS*, (Eds.: P. Pal, K. Sato), Jenny Stanford Publishing, **2017**, DOI 10.1201/9781315364926.
- [13] P. Rai-Choudhury, *MEMS and MOEMS Technology and Applications*, (Ed.: P. Rai-Choudhury), SPIE, **2017**, DOI 10.1117/3.2265068.

- [14] P. Rai-Choudhury, *Handbook of Microlithography, Micromachining, and Micro-fabrication, Volume 2: Micromachining and Microfabrication*, SPIE PRESS, **1997**, DOI 10.1117/3.2265071.
- [15] J. W. Faust, *Journal of The Electrochemical Society* **1983**, *130*, 1413–1420, DOI 10.1149/1.2119964.
- [16] J. Williams, *Materials Science and Engineering: A* **1998**, *253*, 8–15, DOI 10.1016/S0921-5093(98)00705-9.
- [17] I. Ahmad, *Ion Implantation - Research and Application*, (Ed.: I. Ahmad), InTech, **2017**, DOI 10.5772/65528.
- [18] G. S. May, C. J. Spanos, *Fundamentals of Semiconductor Manufacturing and Process Control*, **2006**, p. 463, DOI 10.1002/0471790281.
- [19] G. M. Moore, *Electronics* **1965**, *38*, 114.
- [20] E. Strubell, A. Ganesh, A. McCallum, Energy and Policy Considerations for Deep Learning in NLP, **2019**.
- [21] H. Cai, C. Gan, T. Wang, Z. Zhang, S. Han, Once-for-All: Train One Network and Specialize it for Efficient Deployment, **2019**.
- [22] B. Johnstone, Processing Power in autonomous vehicles, **2018**.
- [23] M. Tilli, *Handbook of Silicon Based MEMS Materials and Technologies*, Elsevier, **2015**, pp. 71–88, DOI 10.1016/C2013-0-19270-7.
- [24] J. R. Mallon, F. Pourahmadi, K. Petersen, P. Barth, T. Vermeulen, J. Bryzek, *Sensors and Actuators: A. Physical* **1990**, *21*, 89–95, DOI 10.1016/0924-4247(90)85018-Y.
- [25] B. Liang, W. Chen, Z. He, R. Yang, Z. Lin, H. Du, Y. Shang, A. Cao, Z. Tang, X. Gui, *Small* **2017**, *13*, 1–7, DOI 10.1002/smll.201702422.
- [26] L. Xu, S. Wang, Z. Jiang, X. Wei, *Microsystems and Nanoengineering* **2020**, *6*, DOI 10.1038/s41378-020-0170-2.
- [27] Y. Dong, P. Zwahlen, A. M. Nguyen, R. Frosio, F. Rudolf, *2011 16th International Solid-State Sensors Actuators and Microsystems Conference TRANSDUCERS'11* **2011**, 695–698, DOI 10.1109/TRANSDUCERS.2011.5969218.
- [28] C. Honglong, X. Liang, Q. Wei, Y. Guangmin, Y. Weizheng, *Sensors* **2008**, *8*, 2886–2899, DOI 10.3390/s8042886.

-
- [29] H. W. Yoo, N. Druml, D. Brunner, C. Schwarzl, T. Thurner, M. Hennecke, G. Schitter, *e & i Elektrotechnik und Informationstechnik* **2018**, *135*, 408–415, DOI 10.1007/s00502-018-0635-2.
- [30] W.-J. Mao, C.-L. Cheng, S.-C. Lo, Y.-S. Chen, W. Fang in 2017 19th International Conference on Solid-State Sensors, Actuators and Microsystems (TRANSDUCERS), IEEE, **2017**, pp. 1037–1040, DOI 10.1109/TRANSDUCERS.2017.7994229.
- [31] S. Mallik, D. Chowdhury, M. Chhstopadhyay, *Innovations in Systems and Software Engineering* **2019**, *15*, 17–25, DOI 10.1007/s11334-019-00325-7.
- [32] W. Lang, *Materials Science and Engineering R: Reports* **1996**, *17*, 1–55, DOI 10.1016/0927-796X(96)00190-8.
- [33] H. J. Levinson, *Principles of Lithography, Fourth Edition*, SPIE, Bellingham, **2019**, pp. 1–505, DOI 10.1117/3.2525393.
- [34] R. R. Dammel, *Diazonaphthoquinone-based Resists*, SPIE, **1993**, DOI 10.1117/3.2265072.
- [35] H. Ito, *Journal of Photopolymer Science and Technology* **1998**, *11*, 379–394, DOI 10.2494/photopolymer.11.379.
- [36] L. Wu, M. Baljovic, G. Portale, D. Kazazis, M. Vockenhuber, T. Jung, Y. Ekinici, S. Castellanos, *Journal of Micro/Nanolithography MEMS and MOEMS* **2019**, *18*, 1, DOI 10.1117/1.jmm.18.1.013504.
- [37] T. Kozawa, S. Tagawa, *Japanese Journal of Applied Physics* **2010**, *49*, 19, DOI 10.1143/JJAP.49.030001.
- [38] M. Shikida, K. Tokoro, D. Uchikawa, K. Sato, *Journal of Micromechanics and Microengineering* **2000**, *10*, 522–527, DOI 10.1088/0960-1317/10/4/306.
- [39] H. Seidel, *Journal of The Electrochemical Society* **1990**, *137*, 3612, DOI 10.1149/1.2086278.
- [40] I. Zubel, *Journal of Micromechanics and Microengineering* **2019**, *29*, 093002, DOI 10.1088/1361-6439/ab2b8d.
- [41] P. J. Hesketh, C. Ju, S. Gowda, E. Zanoria, S. Danyluk, *Journal of The Electrochemical Society* **1993**, *140*, 1080–1085, DOI 10.1149/1.2056201.
- [42] P. Pal, S. S. Singh, *Engineering* **2013**, *05*, 1–8, DOI 10.4236/eng.2013.511a001.
- [43] I. Barycka, I. Zubel, Silicon anisotropic etching in KOH-isopropanol etchant, **1995**, DOI 10.1016/0924-4247(95)00992-2.

- [44] J. T. Thong, W. K. Choi, C. W. Chong, *Sensors and Actuators A: Physical* **1997**, *63*, 243–249, DOI 10.1016/S0924-4247(97)80511-0.
- [45] M. M. Moslehi, Pattern formation in the fabrication of microelectronic devices, **2003**.
- [46] N. G. Einspruch, *VLSI Electronics, Volume 4*, 1st Editio, (Ed.: N. G. Einspruch), Academic Press, **1982**, p. 392.
- [47] H. Seidel, *Journal of The Electrochemical Society* **1990**, *137*, 3626, DOI 10.1149/1.2086278.
- [48] Y. Lindén, L. Tenerz, J. Tirén, B. Hök, *Sensors and Actuators* **1989**, *16*, 67–82, DOI 10.1016/0250-6874(89)80006-X.
- [49] E. D. Palik, V. M. Bermudez, O. J. Glembocki, *Journal of The Electrochemical Society* **1985**, *132*, 135–141, DOI 10.1149/1.2113747.
- [50] E. D. Palik, J. W. Faust, H. F. Gray, R. F. Greene, *Journal of The Electrochemical Society* **1982**, *129*, 2051–2059, DOI 10.1149/1.2124367.
- [51] Z. Ma, Y. Liu, L. Deng, M. Zhang, S. Zhang, J. Ma, P. Song, Q. Liu, A. Ji, F. Yang, X. Wang, *Nanomaterials* **2018**, *8*, 77, DOI 10.3390/nano8020077.
- [52] J. Hsieh, W. Fang, *Journal of Micromechanics and Microengineering* **2002**, *12*, 574–581, DOI 10.1088/0960-1317/12/5/310.
- [53] O. J. Glembocki, R. E. Stahlbush, M. Tomkiewicz, *J. Electrochem. Soc.: SOLID-STATE SCIENCE AND TECHNOLOGY* **1985**, *132*, 145–151, DOI 10.1016/0924-4247(92)80188-9.
- [54] L. Wallman, J. Bengtsson, N. Danielsen, T. Laurell, *Journal of Micromechanics and Microengineering* **2002**, *12*, 265–270, DOI 10.1088/0960-1317/12/3/311.
- [55] R. Voss, H. Siedel, H. Baumgartel in Transducers '91, IEEE, **1991**, pp. 140–143, DOI 10.1109/sensor.1991.148821.
- [56] R. Mlcak, H. L. Tuller, Electrochemical Etching Process, **1994**.
- [57] R. L. Smith, S. D. Collins, *Journal of Applied Physics* **1992**, *71*, DOI 10.1063/1.350839.
- [58] G. Barillaro, A. Nannini, F. Pieri, *Journal of The Electrochemical Society* **2002**, *149*, C180, DOI 10.1149/1.1449953.
- [59] M. Tanenbaum, D. E. Thomas, *Bell System Technical Journal* **1956**, *35*, 1–22, DOI 10.1002/j.1538-7305.1956.tb02371.x.

-
- [60] D. M. Chapin, C. S. Fuller, G. L. Pearson, *Journal of Applied Physics* **1954**, *25*, 676–677, DOI 10.1063/1.1721711.
- [61] D. C. Jacobson, A. Kamgar, D. J. Eaglesham, E. J. Lloyd, S. J. Hillenius, J. M. Poate, *Nuclear Inst. and Methods in Physics Research B* **1995**, *96*, 416–419, DOI 10.1016/0168-583X(94)00531-1.
- [62] J. Mayer in 1973 International Electron Devices Meeting, IRE, **1973**, pp. 3–5, DOI 10.1109/IEDM.1973.188633.
- [63] L. Rubin, J. Poate, *Industrial Physicist* **2003**, *9*, 12–15.
- [64] U. Littmark, J. F. Ziegler, *Physical Review A* **1981**, *23*, 64–72, DOI 10.1103/PhysRevA.23.64.
- [65] J. Gibbons, *Proceedings of the IEEE* **1968**, *56*, 295–319, DOI 10.1109/PROC.1968.6273.
- [66] J. Gibbons, *Proceedings of the IEEE* **1972**, *60*, 1062–1096, DOI 10.1109/PROC.1972.8854.
- [67] S. Sze, *Physics of Semiconductor Devices*, 2nd, John Wiley & Sons, Inc, **1981**, p. 868.
- [68] B. Lipovšek, F. Smole, M. Topič, I. Humar, A. R. Sinigoj, *AIP Advances* **2019**, *9*, DOI 10.1063/1.5092948.
- [69] G. P. Smestad, *Optoelectronics of Solar Cells*, SPIE, **2009**, DOI 10.1117/3.446028.
- [70] A. Einstein, *Annalen der Physik* **1905**, *322*, 132–148, DOI 10.1002/andp.19053220607.
- [71] H. Hertz, *Annalen der Physik* **1887**, *267*, 983–1000, DOI 10.1002/andp.18872670827.
- [72] W. Hallwachs, *Annalen der Physik und Chemie* **1888**, *270*, 731–734, DOI 10.1002/andp.18882700809.
- [73] T. Otanicar, D. DeJarnette, *Solar Energy Harvesting: How to Generate Thermal and Electric Power Simultaneously*, **2016**, DOI 10.1117/3.2256722.
- [74] J. L. Gray, *The Physics of the Solar Cell*, **2011**, pp. 82–129, DOI 10.1002/9780470974704.ch3.
- [75] G. Sabouraud, S. Sadki, N. Brodie, *Chemical Society Reviews* **2000**, *29*, 283–293, DOI 10.1039/a807124a.

- [76] S. Asavapiriyant, G. K. Chandler, G. A. Gunawardena, D. Pletcher, *Journal of Electroanalytical Chemistry* **1984**, 177, 229–244, DOI 10.1016/0022-0728(84)80225-9.
- [77] A. Pike, S. Patole, N. Murray, T. Ilyas, B. Connolly, B. Horrocks, A. Houlton, *Advanced Materials* **2003**, 15, 254–257, DOI 10.1002/adma.200390060.
- [78] M. Zhou, J. Heinze, *Electrochimica Acta* **1999**, 44, 1733–1748, DOI 10.1016/S0013-4686(98)00293-X.
- [79] J. M. Ko, *Journal of The Electrochemical Society* **1990**, 137, 905, DOI 10.1149/1.2086576.
- [80] a.F. Diaz, J. I. Castillo, J. Logan, W.-Y. Lee, *Journal of Electroanalytical Chemistry and Interfacial Electrochemistry* **1981**, 129, 115–132, DOI 10.1016/S0022-0728(81)80008-3.
- [81] R. D. McCullough, *Advanced Materials* **1998**, 10, 93–116, DOI 10.1002/(SICI)1521-4095(199801)10:2<93::AID-ADMA93>3.0.CO;2-F.
- [82] G. Schopf, G. Kößmehl, *Polythiophenes - Electrically Conductive Polymers*, Springer Berlin Heidelberg, Berlin, Heidelberg, **1997**, p. 167, DOI 10.1007/BFb0111619.
- [83] J. Roncali, R. Garreau, A. Yassar, P. Marque, F. Garnier, M. Lemaire, *Journal of Physical Chemistry* **1987**, 91, 6706–6714, DOI 10.1021/j100311a030.
- [84] Z. Chen, H. Lv, X. Zhu, D. Li, S. Zhang, X. Chen, Y. Song, *Journal of Physical Chemistry C* **2014**, 118, 27449–27458, DOI 10.1021/jp509268t.
- [85] J. L. Camalet, J. C. Lacroix, T. D. Nguyen, S. Aeiach, M. C. Pham, J. Petitjean, P. C. Lacaze, *Journal of Electroanalytical Chemistry* **2000**, 485, 13–20, DOI 10.1016/S0022-0728(00)00080-2.
- [86] G. Zotti, S. Cattarin, N. Comisso, *Journal of Electroanalytical Chemistry* **1988**, 239, 387–396, DOI 10.1016/0022-0728(88)80293-6.
- [87] N. Y. Kim, P. E. Laibinis, *Journal of the American Chemical Society* **1999**, 121, 7162–7163, DOI 10.1021/ja990260k.
- [88] I. Chikouche, A. Sahari, A. Zouaoui, *Surface Review and Letters* **2014**, 21, 1–8, DOI 10.1142/S0218625X14500826.
- [89] J. H. Jin, E. C. Alocilja, D. L. Grooms, *Journal of Porous Materials* **2010**, 17, 169–176, DOI 10.1007/s10934-009-9277-4.
- [90] I. E. Vermeir, N. Y. Kim, P. E. Laibinis, *Applied Physics Letters* **1999**, 74, 3860–3862, DOI 10.1063/1.124204.

-
- [91] T. V. Vernitskaya, O. N. Efimov, *Russian Chemical Reviews* **1997**, *66*, 443–457, DOI 10.1070/RC1997v066n05ABEH000261.
- [92] E. Genies, G. Bidan, A. Diaz, *Journal of Electroanalytical Chemistry and Interfacial Electrochemistry* **1983**, *149*, 101–113, DOI 10.1016/S0022-0728(83)80561-0.
- [93] P. Rapt, A. Neudeck, A. Bartl, L. Dunsch, *Electrochimica Acta* **1999**, *44*, 3483–3489, DOI 10.1016/S0013-4686(99)00119-X.
- [94] S. B. Saidman, M. E. Vela, *Thin Solid Films* **2005**, *493*, 96–103, DOI 10.1016/j.tsf.2005.07.308.
- [95] E. H. Yu, K. Sundmacher, *Process Safety and Environmental Protection* **2007**, *85*, 489–493, DOI 10.1205/psep07031.
- [96] F. S. Damos, R. C. Luz, L. T. Kubota, *Electrochimica Acta* **2006**, *51*, 1304–1312, DOI 10.1016/j.electacta.2005.06.019.
- [97] R. S. Hutchins, L. G. Bachas, *Analytical Chemistry* **1995**, *67*, 1654–1660, DOI 10.1021/ac00106a002.
- [98] C. B. Gorman, H. A. Biebuyck, G. M. Whitesides, *Chemistry of Materials* **1995**, *7*, 526–529, DOI 10.1021/cm00051a013.
- [99] B. Fabre, S. Ababou-Girard, F. Solal, *Journal of Materials Chemistry* **2005**, *15*, 2575–2582, DOI 10.1039/b504019a.
- [100] K. M. Ashley, J. C. Meredith, E. Amis, D. Raghavana, A. Karim, *Polymer* **2002**, *44*, 769–772, DOI 10.1016/S0032-3861(02)00779-6.
- [101] K. M. Ashley, D. Raghavan, J. F. Douglas, A. Karim, *Langmuir* **2005**, *21*, 9518–9523, DOI 10.1021/la050482y.
- [102] P. Volodin, A. Kondyurin, *Journal of Physics D: Applied Physics* **2008**, *41*, DOI 10.1088/0022-3727/41/6/065306.
- [103] P. Volodin, A. Kondyurin, *Journal of Physics D: Applied Physics* **2008**, *41*, DOI 10.1088/0022-3727/41/6/065307.
- [104] M. Ghezzi, S. C. Thickett, C. Neto, *Langmuir* **2012**, *28*, 10147–10151, DOI 10.1021/la301773h.
- [105] A. Sehgal, V. Ferreiro, J. F. Douglas, E. J. Amis, A. Karim, *Langmuir* **2002**, *18*, 7041–7048, DOI 10.1021/la0201801.
- [106] R. Seemann, S. Herminghaus, K. Jacobs, *Journal of Physics Condensed Matter* **2001**, *13*, 4925–4938, DOI 10.1088/0953-8984/13/21/319.

- [107] Z. Zhang, Z. Wang, R. Xing, Y. Han, *Surface Science* **2003**, *539*, 129–136, DOI 10.1016/S0039-6028(03)00785-4.
- [108] S. Lee, W. Lee, N. L. Yamada, K. Tanaka, J. H. Kim, H. Lee, D. Y. Ryu, *Macromolecules* **2019**, *52*, 7524–7530, DOI 10.1021/acs.macromol.9b01284.
- [109] S. Wang, Z. Wang, J. Li, L. Li, W. Hu, *Materials Chemistry Frontiers* **2020**, *4*, 692–714, DOI 10.1039/c9qm00450e.
- [110] K. Matyjaszewski, D. Hongchen, W. Jakubowski, J. Pietrasik, A. Kusumo, *Langmuir* **2007**, *23*, 4528–4531, DOI 10.1021/la063402e.
- [111] S. Berger, A. Synytska, L. Ionov, K. J. Eichhorn, M. Stamm, *Macromolecules* **2008**, *41*, 9669–9676, DOI 10.1021/ma802089h.
- [112] S. J. Sofia, V. Premnath, E. W. Merrill, *Macromolecules* **1998**, *31*, 5059–5070, DOI 10.1021/ma971016l.
- [113] W. Feng, J. Brash, S. Zhu, *Journal of Polymer Science Part A: Polymer Chemistry* **2004**, *42*, 2931–2942, DOI 10.1002/pola.20095.
- [114] S. Edmondson, V. L. Osborne, W. T. Huck, *Chemical Society Reviews* **2004**, *33*, 14–22, DOI 10.1039/b210143m.
- [115] H. Ma, D. Li, X. Sheng, B. Zhao, A. Chilkoti, *Langmuir* **2006**, *22*, 3751–3756, DOI 10.1021/la052796r.
- [116] J. D. Jeyaprakash, S. Samuel, R. Dhamodharan, J. R  he, *Macromolecular Rapid Communications* **2002**, *23*, 277–281, DOI 10.1002/1521-3927(20020301)23:4<277::AID-MARC277>3.0.CO;2-U.
- [117] J. S. Wang, K. Matyjaszewski, *Journal of the American Chemical Society* **1995**, *117*, 5614–5615, DOI 10.1021/ja00125a035.
- [118] T. E. Patten, K. Matyjaszewski, *Advanced Materials* **1998**, *10*, 901–915, DOI 10.1002/(SICI)1521-4095(199808)10:12<901::AID-ADMA901>3.0.CO;2-B.
- [119] H. Shinoda, K. Matyjaszewski, L. Okrasa, M. Mierzwa, T. Pakula, *Macromolecules* **2003**, *36*, 4772–4778, DOI 10.1021/ma034064g.
- [120] K. Matyjaszewski, *Macromolecular Symposia* **1998**, *134*, 105–118, DOI 10.1002/masy.19981340112.
- [121] P. Shivapooja, L. K. Ista, H. E. Canavan, G. P. Lopez, *Biointerphases* **2012**, *7*, 1–9, DOI 10.1007/s13758-012-0032-z.

-
- [122] E. M. Benetti, C. Acikgoz, X. Sui, B. Vratzov, M. A. Hempenius, J. Huskens, G. J. Vancso, *Advanced Functional Materials* **2011**, *21*, 2088–2095, DOI 10.1002/adfm.201002569.
- [123] S. Nadel, *Current Sustainable/Renewable Energy Reports* **2019**, *6*, 158–168, DOI 10.1007/s40518-019-00138-z.
- [124] C. Murphy, T. Mai, Y. Sun, P. Jadun, M. M. B. N. R. Jones, Electrification Futures Study: Scenarios of Power System Evolution and Infrastructure Development for the United States, tech. rep., National Renewable Energy Laboratory, Golden, CO, **2021**.
- [125] A. Hopkins, N. McNeill, P. Anthony, P. Mellor, *2015 IEEE Energy Conversion Congress and Exposition ECCE 2015* **2015**, 3788–3793, DOI 10.1109/ECCE.2015.7310195.
- [126] G. Deboy, N. Marz, J.-P. Stengl, H. Strack, J. Tihanyi, H. Weber in International Electron Devices Meeting 1998. Technical Digest (Cat. No.98CH36217), IEEE, **1998**, pp. 683–685, DOI 10.1109/IEDM.1998.746448.
- [127] S. Havanur, P. Zuk, Power MOSFET Basics Understanding Superjunction Technology, tech. rep., Vishay Siliconix, **2015**, p. 5.
- [128] R. Higgelke, CoolMOS – Hintergründe und Ausblicke einer Erfolgsstory, **2017**.
- [129] J. A. Liddle, G. M. Gallatin, *Nanoscale* **2011**, *3*, 2679–2688, DOI 10.1039/c1nr10046g.
- [130] Y. Jiao, D. Djurdjanovic, *IEEE Transactions on Semiconductor Manufacturing* **2011**, *24*, 404–417, DOI 10.1109/TSM.2011.2142329.
- [131] W. H. Arnold, *Optical Microlithography XXI* **2008**, *6924*, 692404, DOI 10.1117/12.782311.
- [132] G. Masetti, M. Severi, S. Solmi, *IEEE Transactions on Electron Devices* **1983**, *30*, 764–769, DOI 10.1109/T-ED.1983.21207.
- [133] G. Gramse, A. Kölker, T. Lim, T. J. Z. Stock, H. Solanki, S. R. Schofield, E. Brinciotti, G. Aeppli, F. Kienberger, N. J. Curson, *Science Advances* **2017**, *3*, e1602586, DOI 10.1126/sciadv.1602586.
- [134] G. Gramse, A. Kölker, T. Škereň, T. J. Z. Stock, G. Aeppli, F. Kienberger, A. Fuhrer, N. J. Curson, *Nature Electronics* **2020**, *3*, 531–538, DOI 10.1038/s41928-020-0450-8.

- [135] M. Nonnenmacher, M. P. O’Boyle, H. K. Wickramasinghe, *Applied Physics Letters* **1991**, *58*, 2921–2923, DOI 10.1063/1.105227.
- [136] W. Melitz, J. Shen, A. C. Kummel, S. Lee, *Surface Science Reports* **2011**, *66*, 1–27, DOI 10.1016/j.surfrep.2010.10.001.
- [137] L. Polak, R. J. Wijngaarden, *Physical Review B* **2016**, *93*, 195320, DOI 10.1103/PhysRevB.93.195320.
- [138] L. Bousse, S. Mostarshed, B. Van Der Shoot, N. F. de Rooij, P. Gimmel, W. Göpel, *Journal of Colloid And Interface Science* **1991**, *147*, 22–32, DOI 10.1016/0021-9797(91)90130-Z.
- [139] M. Kosmulski, *Chemical Properties of Material Surfaces*, 1st, Boca Raton: CRC Press, **2001**, Marcel Dekker Inc., New York, NY, DOI 10.1201/9780585418049.
- [140] L. Cui, Z. Zhang, X. Li, Y. Han, *Polymer Bulletin* **2005**, *55*, 131–140, DOI 10.1007/s00289-005-0404-3.
- [141] M. Böltau, S. Walheim, S. Mlynek, G. Krausch, U. Steiner, *Nature* **1998**, *391*, 877–879, DOI 10.1038/36075.
- [142] A. Budkowski, A. Bernasik, P. Cyganik, J. Rysz, R. Brenn, *E-Polymers* **2002**, *2*, 1–21.
- [143] P. Andrew, W. T. S. Huck, *Soft Matter* **2007**, *3*, 230–237, DOI 10.1039/B613593E.
- [144] R. L. Cicero, M. R. Linford, C. E. D. Chidsey, *Langmuir* **2000**, *16*, 5688–5695, DOI 10.1021/1a9911990.
- [145] T. Kobayashi, Y. Taniguchi, H. Yoneyama, H. Tamura, *The Journal of Physical Chemistry* **1983**, *87*, 768–775, DOI 10.1021/j100228a015.
- [146] H. Yoneyama, M. Kitayoma, *Chemistry Letters* **1986**, *15*, 657–660, DOI 10.1246/cl.1986.657.
- [147] L. Reimer, *Image Formation in Low-Voltage Scanning Electron Microscopy*, SPIE, **2017**, DOI 10.1117/3.2265074.
- [148] P. Lv, Y. Meng, L. Song, H. Pang, W. Liu, *RSC Advances* **2021**, *11*, 1109–1114, DOI 10.1039/D0RA08040C.
- [149] B. Wang, H. Cheng, J. Zhu, Y. Yuan, C. Wang, *Organic Electronics* **2020**, *85*, 105819, DOI 10.1016/j.orgel.2020.105819.

-
- [150] J. S. Kim, S. Y. Ku, N. J. Economou, W. Jang, D. H. Wang, *Nanoscale and Microscale Thermophysical Engineering* **2019**, *23*, 222–234, DOI 10.1080/15567265.2019.1586804.
- [151] Z. Ma, W. Shi, K. Yan, L. Pan, G. Yu, *Chemical Science* **2019**, *10*, 6232–6244, DOI 10.1039/c9sc02033k.
- [152] U. Schnakenberg, W. Benecke, D. Löchel, *Sensors and Actuators A: Physical* **1990**, *23*, 1031–1035, DOI 10.1016/0924-4247(90)87084-V.
- [153] U. Schnakenberg, W. Benecke, B. Löchel, S. Ullerich, P. Lange, *Sensors and Actuators A: Physical* **1990**, *25*, 1–7, DOI 10.1016/0924-4247(90)87001-Y.
- [154] J. E. A. M. van den Meerakker, *Journal of The Electrochemical Society* **1990**, *137*, 1239, DOI 10.1149/1.2086639.
- [155] K. T. Lee, S. Raghavan, *Electrochemical and Solid-State Letters* **1999**, *2*, 172–174, DOI 10.1149/1.1390773.
- [156] F. S. Chien, C. L. Wu, Y. C. Chou, T. T. Chen, S. Gwo, W. F. Hsieh, *Applied Physics Letters* **1999**, *75*, 2429–2431, DOI 10.1063/1.125037.
- [157] C. H. Wang, K. Misiakos, A. Neugroschel, *IEEE Transactions on Electron Devices* **1990**, *37*, 1314–1322, DOI 10.1109/16.108194.
- [158] W. R. Thurber, R. L. Mattis, Y. M. Liu, J. J. Filliben, *Journal of The Electrochemical Society* **1980**, *127*, (Ed.: D. R. Lide), 2291–2294, DOI 10.1149/1.2129394.
- [159] W. R. Thurber, R. L. Mattis, Y. M. Liu, J. J. Filliben, *Journal of The Electrochemical Society* **1980**, *127*, 1807–1812, DOI 10.1149/1.2130006.
- [160] C. Honsberg, S. Bowden, General Properties of Silicon.
- [161] M. J. Kerr, A. Cuevas, R. A. Sinton, *Journal of Applied Physics* **2002**, *91*, 399–404, DOI 10.1063/1.1416134.
- [162] C. Honsberg, S. Bowden, Bulk Lifetime.
- [163] M. A. Green, *Solar Energy Materials and Solar Cells* **2008**, *92*, 1305–1310, DOI 10.1016/j.solmat.2008.06.009.
- [164] C. Schinke, P. Christian Peest, J. Schmidt, R. Brendel, K. Bothe, M. R. Vogt, I. Kröger, S. Winter, A. Schirmacher, S. Lim, H. T. Nguyen, D. MacDonald, *AIP Advances* **2015**, *5*, 067168, DOI 10.1063/1.4923379.
- [165] W. D. Eades, R. M. Swanson, *Journal of Applied Physics* **1985**, *58*, 4267–4276, DOI 10.1063/1.335562.

- [166] *McEvoy's Handbook of Photovoltaics*, (Ed.: S. A. Kalogirou), Elsevier, **2018**, p. 1340, DOI 10.1016/C2015-0-01840-8.
- [167] K. Szaciłowski, W. Macyk, G. Stochel, *J. Mater. Chem.* **2006**, *16*, 4603–4611, DOI 10.1039/B606402G.
- [168] S. Herminghaus, K. Jacobs, R. Seemann, *European Physical Journal E* **2001**, *5*, 531–538, DOI 10.1007/s101890170036.
- [169] H. R. Tseng, H. Phan, C. Luo, M. Wang, L. A. Perez, S. N. Patel, L. Ying, E. J. Kramer, T. Q. Nguyen, G. C. Bazan, A. J. Heeger, *Advanced Materials* **2014**, *26*, 2993–2998, DOI 10.1002/adma.201305084.
- [170] R. A. Segalman, *Materials Science and Engineering R: Reports* **2005**, *48*, 191–226, DOI 10.1016/j.mser.2004.12.003.
- [171] B. Zhu, S. Edmondson, ARGET ATRP: Procedure for PMMA Polymer Brush Growth.
- [172] D. K. Aswal, S. Lenfant, D. Guerin, J. V. Yakhmi, D. Vuillaume, Self assembled monolayers on silicon for molecular electronics, **2006**, DOI 10.1016/j.aca.2005.10.027.
- [173] G. Riveros, G. González, B. Chornik, *Journal of the Brazilian Chemical Society* **2010**, *21*, 25–32, DOI 10.1590/S0103-50532010000100005.
- [174] J. Heinze, A. Rasche, M. Pagels, B. Geschke, *The Journal of Physical Chemistry B* **2007**, *111*, 989–997, DOI 10.1021/jp066413p.

List of Publications

Journal publications

1. Self-Replication of Deeply Buried Doped Silicon Structures, which Remotely Control the Etching Process: A New Method for Forming a Silicon Pattern from the Bottom Up; C. Schutzzeichel, N. Kiriya, A. Kiriya, B. Voit; *Adv. Func. Mat.*, 2021, 31, 2100105, DOI 10.1002/adfm.202100105

Patents

1. Verfahren zur Strukturierung von oberflächennahen Bereichen eines Bauteiles aus Silizium; C. Schutzzeichel, N. Kiriya, A. Kiriya; Patent published on 08.04.2021, Number: DE 10 2020 103 821 B3

Conference contributions

Poster presentations

1. **21st International Vacuum Congress (IVC-21)** in Malmö, Sweden 2019; C. Schutzzeichel, N. Kiriya, A. Kiriya, B. Voit; Light-Induced Deposition of Polypyrrole on Semiconductor Surfaces

Versicherung

Hiermit versichere ich, dass ich die vorliegende Arbeit ohne unzulässige Hilfe Dritter und ohne Benutzung anderer als der angegebenen Hilfsmittel angefertigt habe; die aus fremden Quellen direkt oder indirekt übernommenen Gedanken sind als solche kenntlich gemacht. Die Arbeit wurde bisher weder im Inland noch im Ausland in gleicher oder ähnlicher Form einer anderen Prüfungsbehörde vorgelegt.

Die vorliegende Dissertation wurde in der Zeit von Januar 2018 bis Februar 2021 am Leibniz-Institut für Polymerforschung Dresden e.V. unter wissenschaftlicher Betreuung von Frau Prof. Dr. Brigitte Voit angefertigt.

Frühere Promotionsverfahren fanden nicht statt.

Ich erkenne die Promotionsordnung des Bereichs Mathematik und Naturwissenschaften der Technischen Universität Dresden vom 23.02.2011 und deren Änderung durch Beschlüsse des Fakultätsrates vom 15.06.2011 und 18.06.2014 sowie des Bereichsrates vom 23.05.2018 an.

Dresden, den 23. Februar 2021

Christopher Schutzeichel